AN INVESTIGATION OF NI AND CU ISOTOPIC FRACTIONATION IN BASAL DULUTH COMPLEX CU-NI-PGE MINERALIZATION, NORTHEASTERN MINNESTA

A THESIS SUBMITTED TO THE FACULTY OF THE UNIVERSITY OF MINNESOTA DULUTH
BY

Kristofer Asp

IN PARTIAL FULFILLMENT OF THE REQUIREMENTS FOR THE DEGREE OF MASTER OF SCIENCE

Advisers: Christian Schardt, James Miller

May 2016

Abstract

Cu-Ni-PGE magmatic sulfide-style mineralization occurs along the western margin of the Duluth Complex in northeastern Minnesota. Previous studies have demonstrated a notable fractionation of ^{60}Ni and ^{58}Ni in terrestrial materials, including both primary and secondary phases, with a total range of up to 2.1 ‰. Other work has indicated a fractionation of ^{65}Cu and ^{63}Cu, with pronounced differences between primary copper sulfides and secondary copper phases in a variety of deposit types. Prior to this study, no $\delta^{60/58}$Ni or $\delta^{65/63}$Cu values have been measured in Duluth Complex rocks. The primary goal of this study is to measure Ni and Cu isotope values in a variety of Duluth Complex samples, and develop a possible model for the $\delta^{60/58}$Ni isotopic system in this geologic terrane.

Based on the findings of previous studies, samples were collected to determine the isotopic differences between sulfide-bearing and sulfide-barren material. Samples were collected from a variety of locations in the basal Duluth Complex, including glacial till beds and surface outcrops in the vicinity of the I, II, Serpentine, Mesaba, and NorthMet deposits. Additional drill core material was obtained from the III, Wetlegs, and Wyman Creek deposits.

A detailed characterization of till, weathered surface, and primary drill core samples revealed three main sources of nickel in Duluth Complex material: silicate, sulfide, and secondary oxide. The 24 $\delta^{60/58}$Ni values have an overall range from -0.97 to 0.22 ‰, but are correspondingly distinct in each type of material: silicate (-0.03 ‰ average), sulfide (-0.36 ‰ average), secondary oxide (-0.50 ‰ average). Further geochemical and microprobe work, along with the isotopic values, indicate two main stages of Ni fractionation in basal Duluth Complex rocks: a high temperature stage during crystallization, and a low temperature stage during surficial weathering. High-T fractionation is defined by a preferential incorporation of ^{58}Ni into sulfide, while silicates, especially olivine, are reflective of the Bulk Silicate Earth value. Low-T fractionation results in a preferential incorporation of ^{58}Ni into secondary oxide, while ^{60}Ni possibly enters solution and leaves the system.

The 22 measured Duluth Complex $\delta^{65/63}$Cu values have an overall range from -1.28 ‰ to 0.36 ‰, with an overall average of -0.35 ‰. Further work is necessary to better define and interpret the involved fractionation processes in the Duluth Complex.

Acknowledgements

Many different individuals, organizations, and institutions have contributed to the final product below. First and foremost is my primary adviser Dr. Christian Schardt, who provided guidance, funding, and support during this process. Without his initial ideas, the results of this study would not have been possible. My co-adviser, Dr. Jim Miller, was also invaluable, especially as a resource for Duluth Complex and petrography-related questions. My other thesis committee members, Dr. Christina Gallup and Dr. David Saftner, provided an additional resource for questions, comments, and advice during this process.

Several individuals contributed their time and effort to the sample processing and analytical components of this study. These include Dr. Bryan Bandli, Dr. Lev Spivak-Birndorf and Dr. Laura Wasylenki (IU-Bloomington), Dr. Dan Asael (Yale University), and Dr. Audrey Bouvier (U-Western Ontario). A special thank you goes out to U of M emeritus professor Dr. Paul Weiblen for allowing me to use his EPD device.

A number of companies and organizations contributed sample material and local expertise in the early planning and sampling phases of this study. These include: Duluth Metals Ltd., Twin Metals LLC, Teck Resources Ltd., PolyMet Mining Inc., Encampment Minerals LLC, and the Minnesota DNR Drill Core Library. The following individuals were especially helpful during field and drill core sampling: Dr. Dean Peterson, Mark Severson, Andrew Ware, Harry Noyes, and Barry Frey.

The Earth and Environmental Sciences department at UMD provided me with ample space and equipment for the entirety of this process. Various faculty and staff members, undergraduate, and graduate students were helpful throughout this process. A special thank you goes out to my graduate student colleague, Paul Fix, who was always happy to discuss project ideas.

Finally, thank you to all my friends and family members. You were immeasurably supportive and willing (most of the time) to listen to me blather on about rock-related topics over the last two and a half years.

Table of Contents

List of Tables

Appendix Tables

List of Figures

Appendix Figures

1. Introduction

The 1.1 Ga Midcontinent rift event produced massive volumes of igneous rock that are currently exposed at the surface in Minnesota, Wisconsin, Michigan and southern Ontario, Canada (Miller et al., 2002). During this event, numerous intrusive units formed beneath the overlying volcanic sequences; these units are typically grouped and collectively called the Duluth Complex (figure 1). These intrusive units are generally gabbroic, and range in composition from olivine-rich troctolite to four-phase cumulate gabbro (Miller et al., 2002). This study will focus on two specific Duluth Complex intrusions, the South Kawishiwi and Partridge River intrusions, which host significant amounts of copper, nickel, and platinum group elements (PGE) in a number of high temperature magmatic sulfide-type deposits.

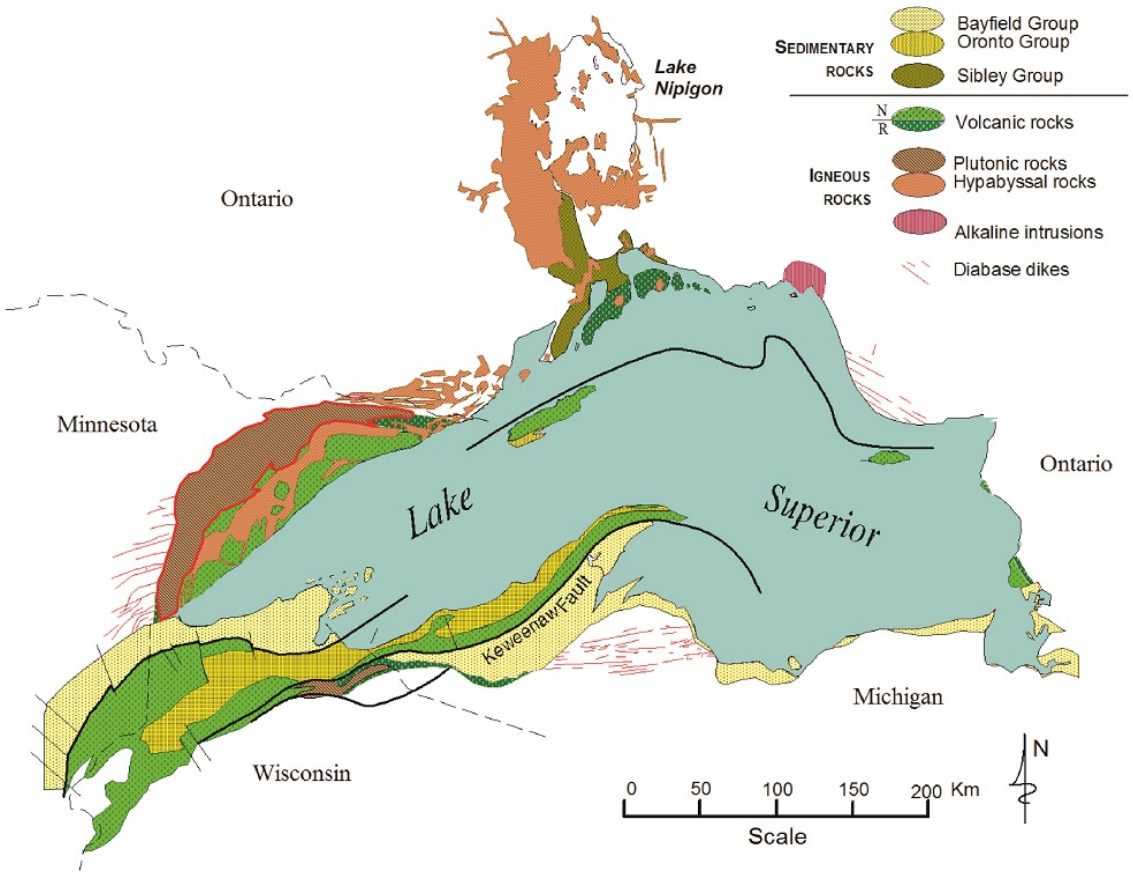

Figure 1: Generalized extent of Midcontinent rift related rocks in the Lake Superior area. The Duluth Complex is located at left in brown highlighted by the red outline. Image courtesy of Jim Miller (Personal Communication).

These deposits and the associated host rocks will be studied using a number of different techniques to evaluate the potential for the isotopic fractionation of nickel within primary Cu-Ni-PGE mineralization and weathered material at the surface. Specifically, how does nickel fractionate during these two processes and can this behavior be observed using the $\delta^{60/58}$Ni isotopic system?

Within the broad igneous and sedimentary stratigraphy of the Lake Superior region, various rock units contain economic amounts of base (Fe, Cu, Ni) and precious metals (Au, Ag, Pd, Pt; Severson et al., 2002). Historically, the region was known for native copper deposits in Michigan and Isle Royale, but recently, the Duluth Complex and other intrusive units in the Lake Superior area have seen a significant increase in exploration and development. In particular, the South Kawishiwi and Partridge River intrusions, which are located at the westernmost edge of the Duluth Complex, have been estimated to contain upwards of 7 billion tons of ore at grades of roughly 0.66% Cu and 0.2% Ni, along with accessory amounts of PGE's (Listerud and Meineke, 1977; Eckstrand and Hulbert, 2007; Peterson, 2010; Miller and Nicholson, 2013).

The formation of these magmatic sulfide deposits is hotly debated, with several competing theories put forward to explain the genesis of the mineralization. One hypothesis was published by Severson (1994), who evaluated the igneous stratigraphy of the South Kawishiwi Intrusion and speculated that a multiphase intrusive model could explain the creation of mineralization near the footwall contact with the Giants Range Batholith, Biwabik Iron formation, and Virginia Formation. Later, Peterson (2001) suggested an alternative hypothesis that involved a restricted, channelized flow of magma from a northern source, identified as the Nickel Lake Macrodike, that led to the creation of the "basal mineralized zone" (BMZ) in the lowermost stratigraphy of the South Kawishiwi Intrusion (figure 2). Both theories were evaluated in depth by White (2010), who used extensive drill logging and petrography to re-examine the stratigraphy presented by Severson (1994), and the models presented by both authors. White (2010) concluded that elements of each hypothesis were valid, but the Peterson (2001) model was best fit to explain the igneous stratigraphy in the South Kawishiwi Intrusion.

In addition to the work done by Severson (1994), Peterson (2001), and White (2010), many other studies have explored the origins and ongoing weathering of the Cu-Ni-PGE mineralization in the basal Duluth Complex and in other deposits around the world.

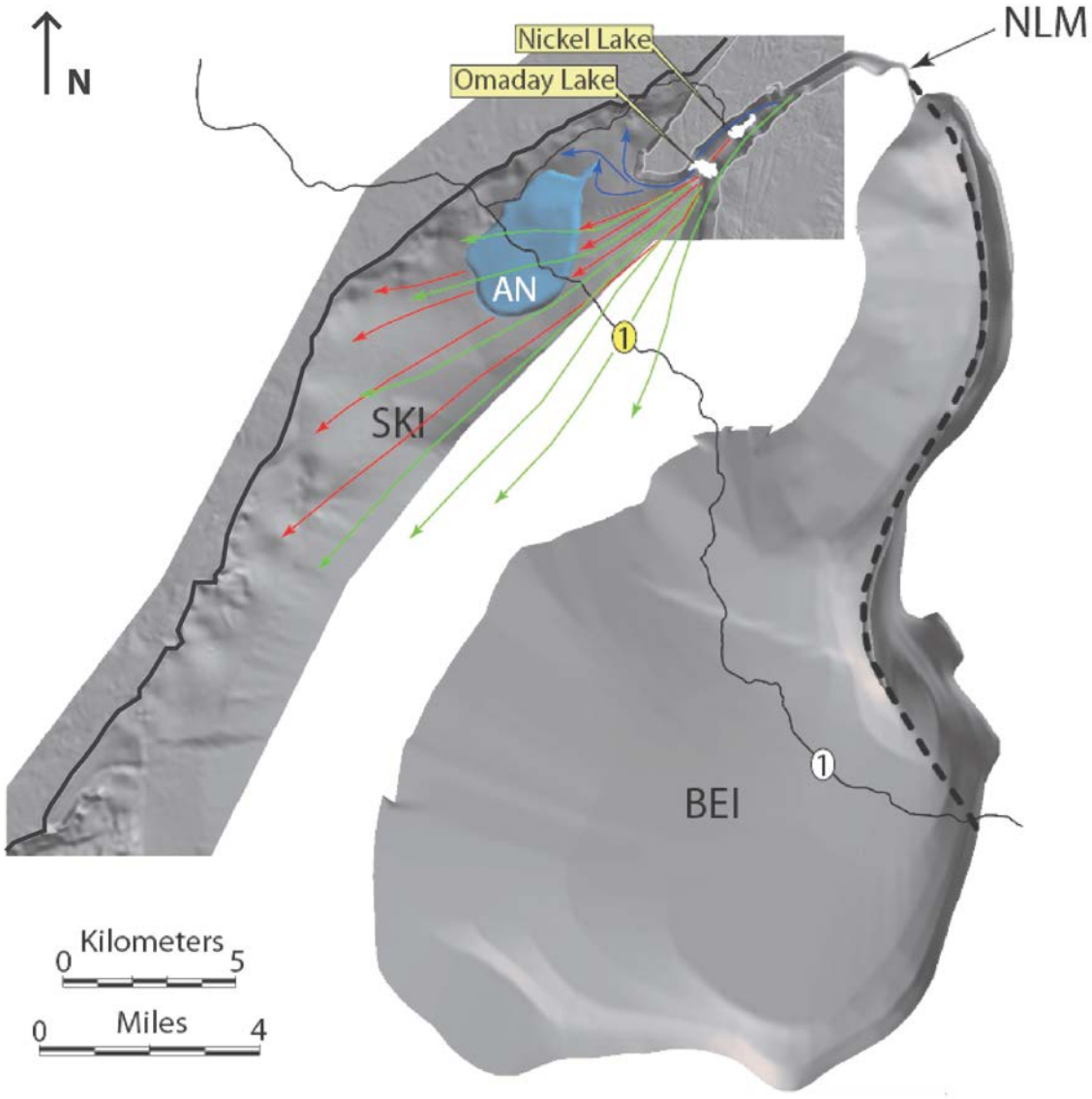

Figure 2: 3D Map showing the Peterson (2001) hypothesis of magma flowing from the Nickel Lake Macrodike (NLM) into the South Kawishiwi Intrusion (SKI). Image modified from Peterson (2008).

In particular, several studies by Ed Ripley and others have used $\Delta^{33}S$ and $\delta^{34}S$ values to identify the Paleoproterozoic Virginia Formation as the primary sulfur source for the Cu-Ni-PGE deposits of the basal Duluth Complex (Ripley, 1981; Li and Ripley, 2009; Ripley, 2013). Apart from sulfur isotopes, transition metal isotopic systems have been applied to scholarly and environmental work to evaluate primary and secondary processes within metal deposits. In particular, the $\delta^{60/58}Ni$ system has recently been used to interpret

processes in komatiite-hosted nickel sulfide deposits and nickel laterites (Hiebert et al., 2014; Hofmann et al., 2014; Ratie et al., 2015). Other studies have used this isotopic system to examine surficial processes, and a significant overall fractionation of up to 2.1 ‰ has been observed (Gall et al., 2011; Gueguen et al., 2013; Wasylenki et al., 2015; Cameron and Vance, 2014). These isotopes, which have never before been measured in Duluth Complex material, will be used to examine the Cu-Ni-PGE deposits in the basal Duluth Complex to see whether or not a significant fractionation can be observed in primary sulfide ore, unmineralized gabbroic host rock, and highly weathered, oxide-rich weathered material. Ideally, this will provide answers to the project goals described below.

2. Project Goals

Stable isotope systems have been used successfully by Ripley (1981) amongst others in the Duluth Complex to answer questions about the formation of the Cu-Ni-PGE mineralization. Up to this point in time, no $\delta^{60/58}$Ni values have been measured in Duluth Complex rocks. However, from previous studies, a fractionation of up to 2.1 ‰ has been observed in a variety of terrestrial materials. Based on these ideas, the overall question for this study is: Does fractionation of nickel occur in Duluth Complex rocks, and can it be attributed to specific processes?

In addition to the fundamental study question, a number of secondary questions will be pursued to try and gain a complete understanding of the nickel isotope system in the Duluth Complex. Some of these questions surfaced during the course of this study, while others were sourced from the results of other publications.

1. Does the amount of sulfide in Cu-Ni-PGE mineralization affect the $\delta^{60/58}$Ni value? Specifically, is there a difference isotopically between massive, semi-massive, and disseminated sulfide ore?

2. Are sulfide-barren rocks isotopically distinct from sulfide-bearing rocks?

3. Are there any differences isotopically between early and late-phase olivine cumulates? If so, can these differences be seen geochemically in sample material?

4. Do the $\delta^{60/58}$Ni values change based on geographic location in the basal Duluth Complex? Specifically, do these values change from deposit to deposit?

5. Does surficial weathering have an effect on $\delta^{60/58}$Ni values?

6. Based on question 5, do rocks rich in secondary oxides have distinct $\delta^{60/58}$Ni values from sulfide-bearing rocks?

7. Can $\delta^{60/58}$Ni values in glacial till be used as an exploration tool for mining companies?

8. How do $\delta^{60/58}$Ni values compare to $\delta^{65/63}$Cu values in Duluth Complex material?

Based on the results of this study and the answers to the above questions, a final goal for this project will be the development of a conceptual model for Ni fractionation in the basal Duluth Complex, including both the initial formation of the mineralization and subsequent surficial weathering. To address the questions, a variety of samples will be collected from the greater basal Duluth Complex, including all of the major Cu-Ni-PGE deposits, unmineralized South Kawishiwi and Partridge River rock, weathered surface material, and glacial till. In addition to measuring $\delta^{60/58}$Ni values, samples will be characterized in detail using petrography, reflected light microscopy, and bulk geochemistry, along with several other techniques described below in the methods section.

3. Geologic Background

This chapter contains relevant background information about the Midcontinent rift event that produced the extrusive and intrusive igneous rocks in northeastern Minnesota. Detailed information is provided about the Duluth Complex and several individual intrusions that contain known Cu-Ni-PGE mineralization.

3.1 Geologic Setting

The Midcontinent rift event that formed the Duluth Complex took place over a period of roughly 30 million years between 1115 Ma and 1086 Ma. The event has been divided up into four main stages of magmatism: the early magmatic stage (1115-1107 Ma), the latent magmatic stage (1107-1102 Ma), the main magmatic stage (1102-1094 Ma), and the late magmatic stage (1094-1086 Ma; Paces and Miller, 1993; Miller and Vervoort, 1996; Miller and Severson, 2002). Each stage produced distinctive rock units characterized by differing lithologies, magnetic polarities, thicknesses, volumes, and correlations to specific sedimentary units overlying individual flows. The early magmatic stage began with the initiation of rift activity, which generated primitive magmas that were sourced directly from the upwelling mantle. This initial sequence gradually gave way to more evolved and crustal-contaminated magmas, including several felsic units. These early rocks are noteworthy due to their reversed magnetic polarity in contrast to the normally polarized rocks of the later series' (Miller and Severson, 2002). The latent stage saw reduced rift activity, resulting in the creation of sedimentary units that overly the flows of the early stage. The few lava flows that were generated during this stage were felsic and highly contaminated by crustal material. The main magmatic stage coincided with a reinvigorated rift, resulting in generally uncontaminated basalts with a normal magnetic polarity (Miller and Severson, 2002). Several rhyolite flows were also generated during this stage. The late magmatic stage began with regional subsidence due to the massive volumes of magma generated during the first three stages and ended with the secession of rift activity around 1086 Ma (Miller and Severson, 2002). This stage is characterized by diverse flows that are commonly interbedded with sedimentary rocks, which were created in larger amounts due to higher-angle topography that resulted from subsidence (Miller and Severson, 2002). Generally, the rocks in the Lake Superior area and the Chengwatana volcanic group in the Taylors Falls area are characterized by a 10-15 km thick sheet of mafic to felsic extrusive

volcanic rocks interbedded with volcanic sandstones and conglomerates and cross-cut by the intrusive dikes and sills of the Duluth Complex (Miller et al., 2002; Ojakangas, 2009).

3.2 The Duluth Complex

Although it formed during the Midcontinent rift and has geochemical similarities to the extrusive rocks of the North Shore Volcanic Group (NSVG), the Duluth Complex, as a whole, is less-well exposed and is less-well understood. Extending in a wide arc from the Duluth area north to Ely, Minnesota, and east towards the Grand Portage reservation, the Duluth Complex is one of the largest mafic intrusive bodies in the world, comprising hundreds of individual intrusions of mafic rocks in addition to several felsic intrusions (figure 3). These rocks exhibit complex cross-cutting relationships with the overlying rocks of the NSVG, and also with each other, making it extremely difficult to piece together a conclusive, accurate formational history of the complex, along with a meaningful stratigraphy (Miller et al., 2002). Work by numerous researchers over the course of the 20th and 21st centuries has revealed much about the structure, mineralogy, texture, and stratigraphy of the Duluth Complex. For the purposes of this study, the overall characteristics of the Duluth Complex will be briefly discussed, along with more detailed information about a few specific intrusions that are essential to the understanding of the Cu-Ni-PGE mineralization.

The Duluth Complex includes a wide range of rock types that have been placed into four groups based on age, lithology, and the individual relationships with other units within the Duluth Complex as a whole (Miller and Severson, 2002). These groups are: the felsic series, the early gabbro series, the anorthositic series, and the layered series. Like the different magmatic stages of the Midcontinent rift, each group in the Duluth Complex is distinctive from the other groups based on certain defining characteristics.

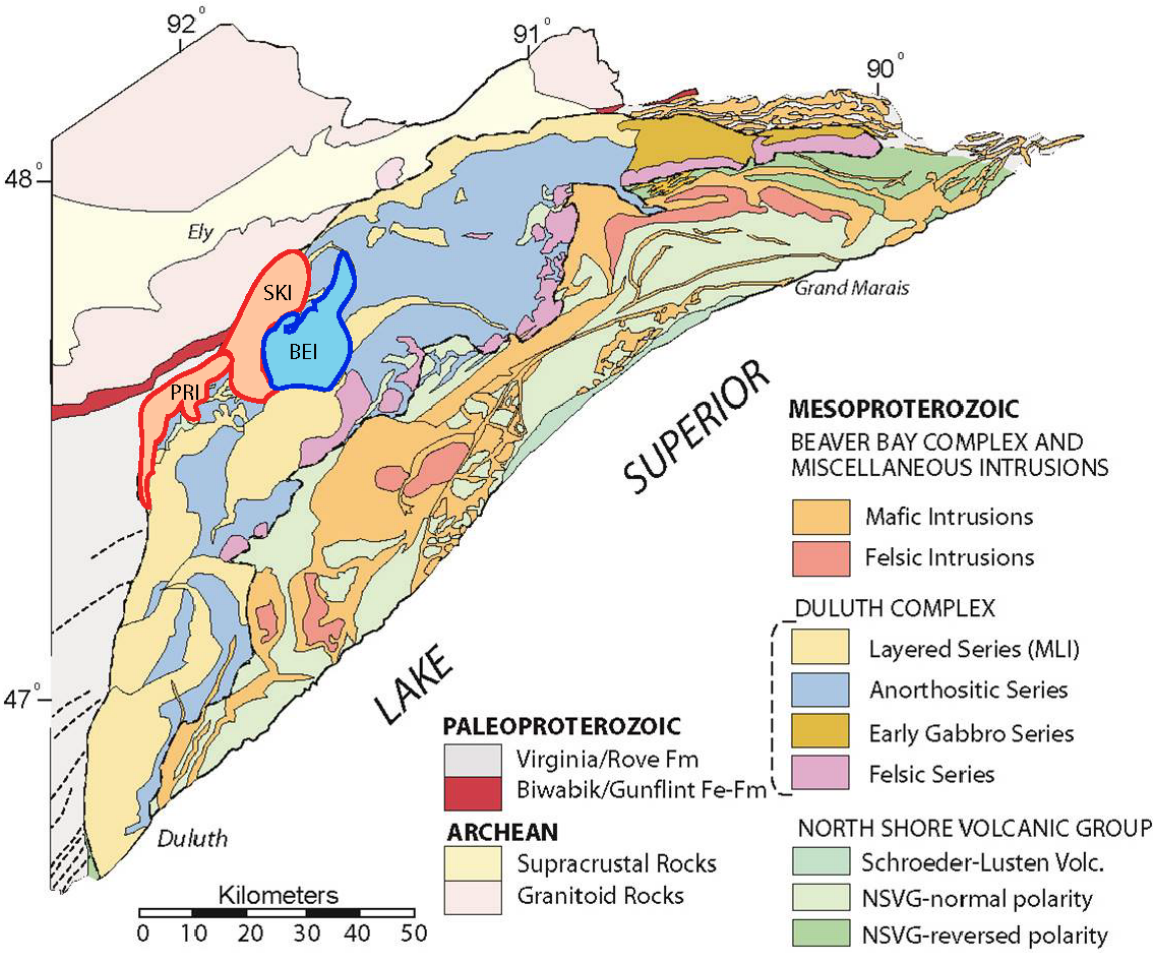

Figure 3: Generalized geologic map of northeastern Minnesota. Highlighted are the Partridge River intrusion (PRI), South Kawishiwi intrusion (SKI), and Bald Eagle intrusion (BEI). Figure modified from Miller et al. (2002).

The **felsic series** is composed of generally homogenous granophyre and intermediate rocks that are located stratigraphically above the rocks of the other groups. Its location in the northeastern part of the Duluth Complex, along with several documented textural relationships with other Duluth Complex rocks, show that this series was likely emplaced during the early magmatic stage (Miller and Severson, 2002). The **early gabbro series** is thought to be roughly contemporaneous with the felsic series, but is composed of very different rocks. This group, also located in the northeastern part of the Duluth Complex, includes layered, largely gabbroic cumulates that immediately underlie rocks from the felsic series. This stratigraphic relationship is reinforced by a gradational contact margin between a granophyre and a layered gabbro from the Poplar Lake intrusion, which was dated at 1106.9 ± 0.8 Ma (Paces and Miller, 1993; Miller and

Severson, 2002). This suggests that although both series formed during the early stage, the felsic series was emplaced first. The third group, the **anorthositic series**, consists of medium to coarse-grained, often foliated, plagioclase-rich gabbros and anorthosites located stratigraphically below the felsic and early gabbro series. This is indicated by a field relationship between an overlying granophyre unit of the felsic series and an underlying gabbroic anorthosite unit near the roof zone of the Duluth Complex (Miller and Severson, 2002). Furthermore, contacts between the anorthosite and overlying rocks, including the felsic series, are typically sharp, implying a significant time gap between the two intrusions. The final group, **the layered series**, is implied to have been emplaced last, although age dates obtained from both the anorthositic series and the layered series in the northwestern and southern Duluth Complex are nearly identical at 1099 ± 0.6 Ma (Paces and Miller, 1993; Miller and Severson, 2002). The layered series consists of moderately to well-foliated gabbros of varying compositions, ranging from olivine and plagioclase-rich troctolites to oxide-rich and apatite-bearing four phase cumulate gabbros. Iron and titanium-rich phases have also been described, including ferrodiorites and ferrogabbros. Included in the layered series are the two principal intrusions, located at the stratigraphic base of the Duluth Complex, that are host to extensive sulfide mineralization; these will be described in detail below (Miller and Severson, 2002; Miller et al., 2002).

3.2.1 The Partridge River Intrusion

The Partridge River Intrusion (PRI) is a roughly 2.5 km thick, largely troctolitic, mafic intrusion (figure 4) that dips gently to the southeast. The PRI is located along the western margin of the Duluth Complex where it is in contact with Paleoproterozoic rocks, including the 1.85 Ga Virginia Formation (metasedimentary slates and greywackes), and the 1.9 Ga Biwabik Iron Formation (Miller and Ripley, 1996). Geographically, the PRI is located on the southern end of the basal Duluth Complex between Hoyt Lakes, MN, and an area roughly three miles southeast of Babbitt, MN. The PRI lies to the south/southwest of the other two mineralized intrusions of the Duluth Complex: the South Kawishiwi Intrusion and the Bathtub Intrusion. The Bathtub Intrusion was once considered to be a stratigraphically unique part of the eastern PRI and was only recently classified as a separate intrusion based on detailed core logging by Severson and Hauck (2008).

The PRI has been broken up stratigraphically into a number of igneous units based on texture, mineralogy, and sulfide content, the latter of which helps to define the ore bodies (Miller and Ripley, 1996; Miller and Severson, 2002). The stratigraphically lowest unit of the PRI, called Unit 1, is defined by heterogeneous troctolite that contains abundant disseminated sulfides along with thin zones of massive sulfide. Additionally, Unit 1 contains numerous inclusions of the footwall Virginia formation, which have occasionally led to the formation of noritic rocks near the basal contact due to silica contamination during recrystallization (Severson et al., 2013). Unit 2, located directly above Unit 1, also contains some disseminated sulfide mineralization, but the troctolitic host rock is much more homogenous than in Unit 1. Other features in Unit 2 include infrequent, late-stage oxide ultramafic inclusions that share geochemical similarities with the footwall Biwabik Iron Formation (Severson and Hauck, 1990). Unit 3, located above Unit 2, is compositionally distinct from the underlying units and is characterized by a mottled appearance, which is due to randomly oriented olivine oikocrysts within a fine-grained, poikilitic leucotroctolitic host rock (Severson et al., 2013). This unit is not stratigraphically continuous, however, which helped to define the boundaries of the Bathtub Intrusion. Units 4-7 in the upper part of the stratigraphy are sulfide-barren and grade from augite troctolite to troctolitic anorthosite. Each unit is stratigraphically defined by a thin lens of ultramafic rock that implies the occurrence of several small magma injection events (Severson et al., 2013).

The igneous stratigraphy described above has been utilized by several mining companies to characterize the Cu-Ni-PGE deposits that are located within the PRI. These deposits include: Wyman Creek, Wetlegs, NorthMet, and the southern part of the Mesaba deposit, which is partly within the newly defined Bathtub intrusion. In addition to these deposits, there are several small ultramafic bodies within the PRI, known as Oxide Ultramafic Intrusions (OUI), that host prospective TiO_2-V deposits (Severson et al., 2002). These deposits are generally south of the Cu-Ni-PGE deposits in a “pearls on a string” formation. The southernmost TiO_2-V prospect, Waterhen, represents the far southern extent of the PRI, where other intrusions of the layered series extend southwards towards the Duluth area.

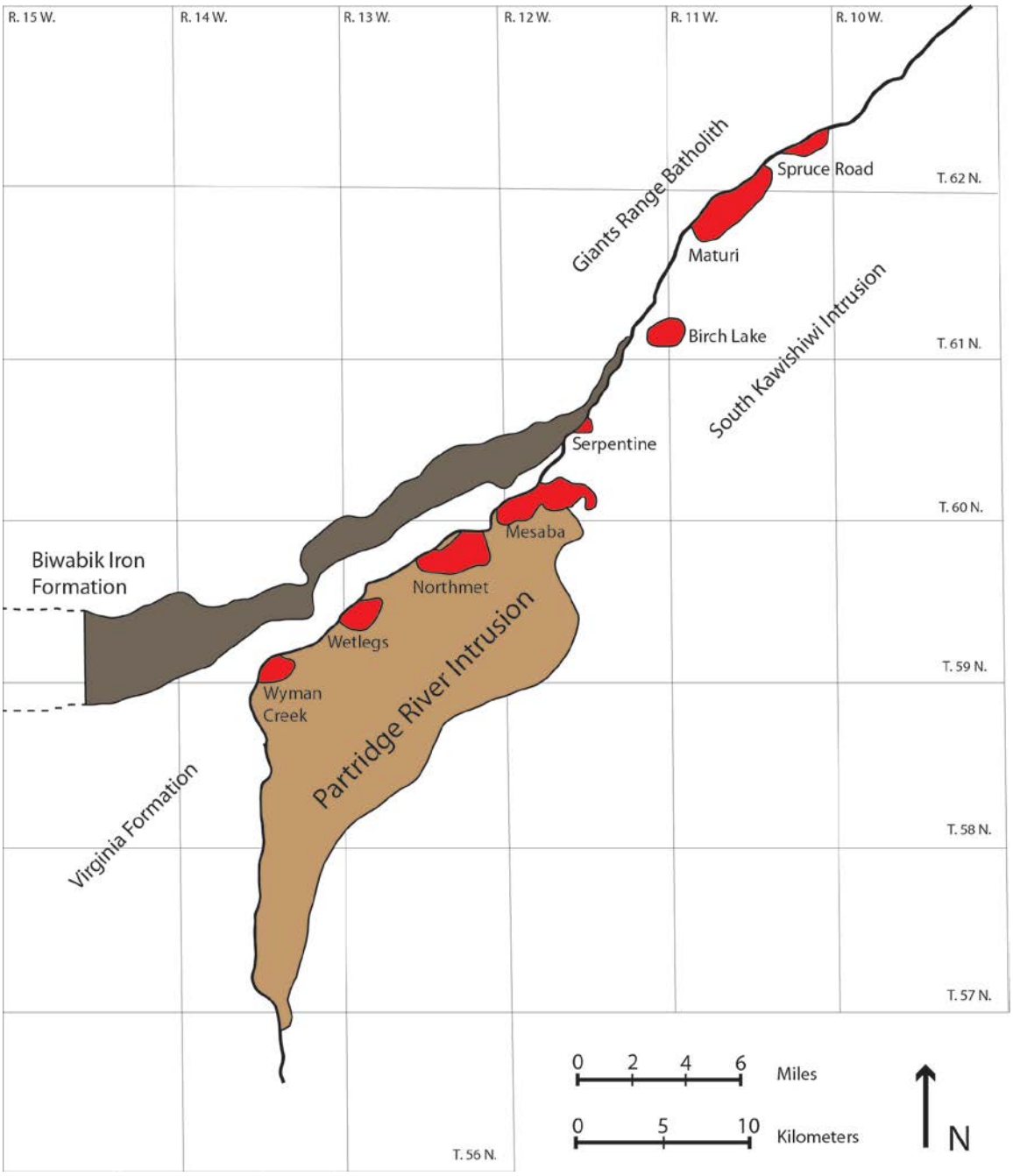

Figure 4: Location and simplified geologic map of the Partridge River Intrusion with approximate extent of Cu-Ni-PGE mineralization. Modified from Raič (2013) and Severson (in press).

3.2.2 The South Kawishiwi Intrusion

The South Kawishiwi Intrusion (figure 5), like the PRI, is a largely troctolitic mafic intrusion of the basal Duluth Complex that dips gently to the southeast. The SKI is located north of the PRI, extending in a roughly 30-kilometer, north-south arc between Babbit, MN, and the Nickel Lake area, southeast of Ely, MN (Miller and Severson, 2002). The SKI has a brief interval in basal contact with the Virginia Formation and the Biwabik Iron Formation, but the majority is in contact with the Archean Giants Range Batholith (GRB; ca. 2.7 Ga). Despite the observed stratigraphy, numerous inclusions of Virginia Formation and Biwabik Iron Formation within the SKI indicate that the initial intrusion of the SKI likely eroded and assimilated the preexisting bedrock, resulting in a significant unconformity between the GRB and the SKI that is not present in the stratigraphy further to the south (Miller and Severson, 2002; Severson et al., 2013). Additionally, the SKI is structurally separated from the PRI and Bathtub Intrusion by the Grano fault zone, which is present in the area where the Biwabik Iron Formation is in direct stratigraphic contact with the SKI and the PRI (Severson, 1994).

Apart from geographic and footwall contact differences, the SKI has a significantly more complex stratigraphy than the PRI, although the overall lithologies of the bedrock remain the same. In total, the SKI stratigraphy contains 17 distinct units that are unevenly distributed over the entire strike length of the SKI (Severson et al., 2013). Generally, the SKI is defined as being troctolitic in composition with irregular intervals of leucotroctolite, ultramafics, oxide gabbros, and contains numerous inclusions of volcanic and sedimentary hornfels (Miller and Severson, 2002). Like the PRI, sulfide mineralization is present in the lowermost stratigraphic units of the SKI, although the exact lithologies vary significantly from deposit to deposit. The sulfide mineralization is commonly massive in the lowest few meters of the intrusion, and becomes more disseminated higher up in the stratigraphy with occasional massive and semi-massive pockets associated with vein-like features. The units immediately above the footwall contact with the GRB that host the sulfide mineralization are: the Basal Heterogeneous Unit (BHU), the Basal Augite Troctolite and Norite Unit (BAN), the Updip Wedge Unit (UW), and the Ultramafic 3 Unit (U3). The BAN, UW, and U3 units contain the most significant mineralization and are typically grouped into a larger unit known as the Basal Mineralized Zone (BMZ). The U3 unit contains local massive oxide clots that are recognized as recrystallized xenoliths of Biwabik Iron Formation. In some areas, a pegmatitic unit (PEG) immediately overlies the BMZ, which is frequently used as a

marker bed during core logging to separate the lower and upper parts of the SKI stratigraphy. Above the PEG, the units are sulfide barren and grade from augite troctolite to anorthositic troctolite. In the Maturi area, there is a unique feature present known as the anorthosite “pillar.” This feature is theorized to be a massive inclusion that could be proximal to a large-scale vent or magma channel related to the Nickel Lake macrodike further to the east (Severson et al., 2013).

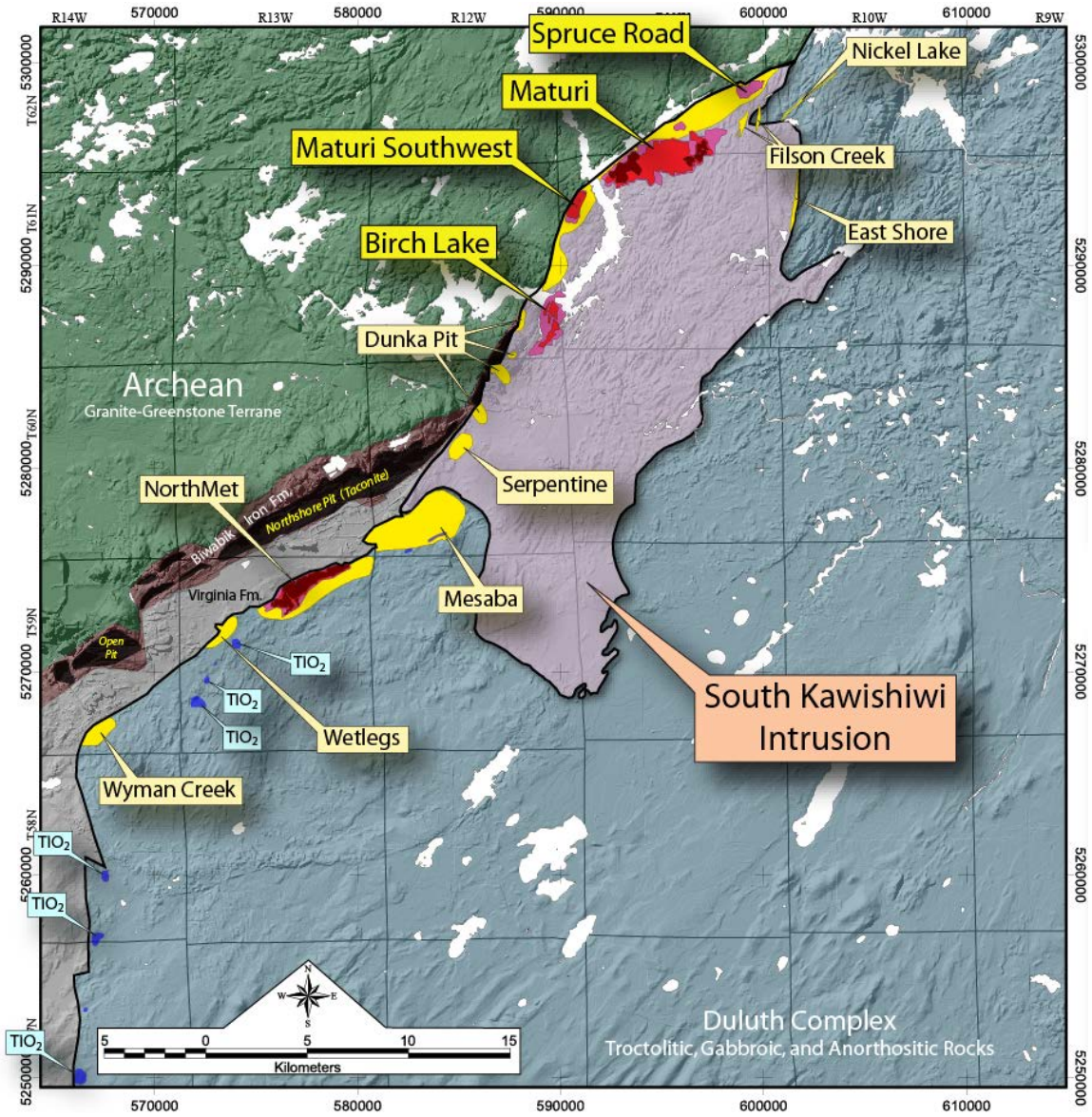

Figure 5: Location and simplified geologic map of the South Kawishiwi intrusion. Image courtesy of Duluth Metals (2013).

Like the PRI, the stratigraphy described above has been used by several mining companies to characterize the zones of Cu-Ni-PGE mineralization within the SKI. The deposits within the SKI include: Dunka Pit, Birch Lake, Maturi (including Maturi Southwest and Maturi Extension), Spruce Road, South Filson Creek, and Nickel Lake. Additionally, there is abundant mineralization within the footwall Giant's Range batholith (GRB) that has recently been characterized by Steiner (2014). This master's thesis project demonstrated that a significant exchange of material took place during the intrusion of the SKI due to the partial melting of the uppermost portion of the GRB. Effectively, sulfide droplets traveled downwards into the partially melted GRB, while felsic material moved upwards into the lower part of the SKI, resulting in irregular felsic dikes and pods within the BMZ. Further research is needed to characterize the exact effects that this exchange had on the existing Cu-Ni-PGE mineralization within the SKI.

3.2.3 The Bathtub Intrusion

The Bathtub Intrusion is significantly smaller in size than the PRI and the SKI and sits geographically in-between the two larger intrusions in the vicinity of Babbitt, MN, near the Northshore iron ore mine. Unlike the PRI and the SKI, the Bathtub Intrusion has only recently been characterized as a distinct intrusion within the basal Duluth Complex, largely as a result of the detailed research undertaken by Severson and Hauck (2008). Previously, it was thought that the igneous units present in the Bathtub intrusion stratigraphy were simply extensions of the PRI stratigraphy; however, a sharp transition to compositionally different facies in the central part of the Mesaba deposit led to the differentiation of the Bathtub as a unique intrusion.

Generally, the Bathtub Intrusion is separated into three different units: BT1, BT4, and the Bathtub Layered Interval (BTLI), which is broken up from the BT4 unit based on texture and mineralogy. The BT1 unit can be broken down into a number of different subunits that are roughly analogous to some of the features seen within Unit 1 of the PRI. These include: BT1-a (heterogeneous augite troctolite to olivine gabbro), BT1-c (norite to gabbro norite; indication of silica contamination), and BT1-uz (olivine-rich ultramafic zones). Like Unit 1 in the PRI, BT1 hosts most of the sulfide mineralization, which contains large zones of disseminated sulfide along with local massive sulfides. Unlike Unit 1, however, the BT1 contains zones of coarse to very coarse-grained, disseminated sulfides in the lowermost part of the stratigraphy. The BT4 and BTLI unit

form the upper part of the stratigraphy and grade from augite troctolite to anorthositic troctolite, although the BTLI is typically broken out from the BT4 due to the presence of ultramafic and modal-bedded zones related to a feature known as the “hidden rise” (Severson et al., 2013).

Apart from the stratigraphy described above, there are three features present within the Bathtub Intrusion that provide structural controls for the mineralization in the Mesaba deposit. These features include: a syncline-anticline complex at the base of the intrusion, a feature known as the “Hidden Rise,” and the Grano fault zone, which serves as the contact between the Bathtub Intrusion and the SKI to the north (Severson et al., 2013). The “Hidden Rise” is a lithological contact zone between the PRI and the Bathtub Intrusion, which is located above the crest of the basal anticline. This contact zone is generally characterized by the presence of numerous hornfels inclusions along with a massive sulfide zone called “Local Boy” that sits right at the crest of the anticline. The specific style of mineralization within the Mesaba deposit will described in greater detail below.

3.2.4 The Bald Eagle Intrusion

The Bald Eagle Intrusion (BEI; figure 3) sits directly to the east of the SKI, and has similar geochemical and mineralogical features to the SKI. The BEI is located stratigraphically between rocks of the anorthositic series (hanging wall) and rocks of the SKI (footwall). The BEI also shares a contact with the Greenwood Lake intrusion on its southern margin. Generally, the BEI is composed of two different units: a thick outer ring of troctolite and an inner core of olivine gabbro. Unlike other intrusions of the layered series, the BEI contains no cumulus oxide minerals, suggesting a different geochemical regime governed its crystallization. Miller and Severson (2002) suggest that either the BEI crystallized in open-system conditions where frequent pulses of magma recharged the system, or else oxide-rich facies formed and were subsequently eroded. Despite the recognized differences between the BEI and the SKI, field relationships and geophysical data point to a common origin for the BEI and SKI. Specifically, a feature at the far northern end of the BEI called the Nickel Lake macrodike seems to connect the northern BEI to the middle of the SKI. This macrodike is comprised of well-foliated troctolite and olivine gabbro along with thin lenses of sulfide-bearing augite troctolite that are geochemically similar to the mineralized units of the SKI (BMZ). The presence of very

large xenoliths of iron formation and anorthosite suggests that this macrodike could have served as a very energetic feeder dike, which allowed the sulfide-rich magmas to travel and spread out along the basal contact with the Paleoproterozoic footwall. Geophysical data collected in the area support this idea, and shows a distinct aeromagnetic and gravity anomaly in the vicinity of the macrodike (Weiblen and Morey, 1980; Peterson, 2001; Chandler, 2002).

Apart from the sulfide lenses within the Nickel Lake macrodike, the BEI is unique compared to the PRI, SKI, and Bathtub Intrusions because it contains no identified Cu-Ni-PGE deposits. This is possibly due to a lack of a sulfur source in close proximity to the BEI. Samples collected from the BEI will serve as a "background" Duluth Complex rock signature due to their typical gabbroic lithologies and pronounced lack of sulfide minerals.

3.3 Magmatic Cu-Ni-PGE Deposits

The three principal intrusions of the basal Duluth Complex are mineralized in a semi-continuous fashion from the far northern end of the SKI in the Nickel Lake area to the far southern end of the PRI in the Hoyt Lakes, Minnesota area (Severson et al., 2013) (Figure 6). The mineralization in this area has been broadly characterized as typical high temperature magmatic sulfide that hosts vast reserves of copper, nickel, and platinum group elements. Although the mineralization is semi-continuous along the entire strike length of the basal Duluth Complex, the grade of the mineralization changes significantly from area to area. Thus, the areas with the highest grades and tonnages of Cu-Ni-PGE mineralization will be discussed below, beginning with the deposits in the SKI. Samples were collected for this project from deposits listed in bold font (tables 1 and 2)

The **Spruce Road** deposit is located at the far northern end of the SKI in close proximity to the South Filson Creek deposit and the Nickel Lake Macrodike mineralization. According to estimates by Miller et al. (2002), Spruce Road contains roughly 500 Mt of ore at average grades of 0.43 wt. % Cu and 0.15 wt. % Ni. This mineralization is hosted within the BMZ, which varies in thickness from 30 to 450 meters in the deposit. At Spruce Road, the BMZ is relatively copper rich and nickel poor, with typical sulfide contents between 0.5 and 5 % in the disseminated ore zone (Gál et al., 2011). 0.1 to 0.5 meter pods of massive sulfide occur near the basal contact with the

GRB (Zanko et al., 1994; Hauck et al., 1997; Severson and Hauck, 2008; Benko et al., 2015). The sulfide mineral assemblage is typically chalcopyrite + pyrrhotite + cubanite, with pentlandite as an accessory phase.

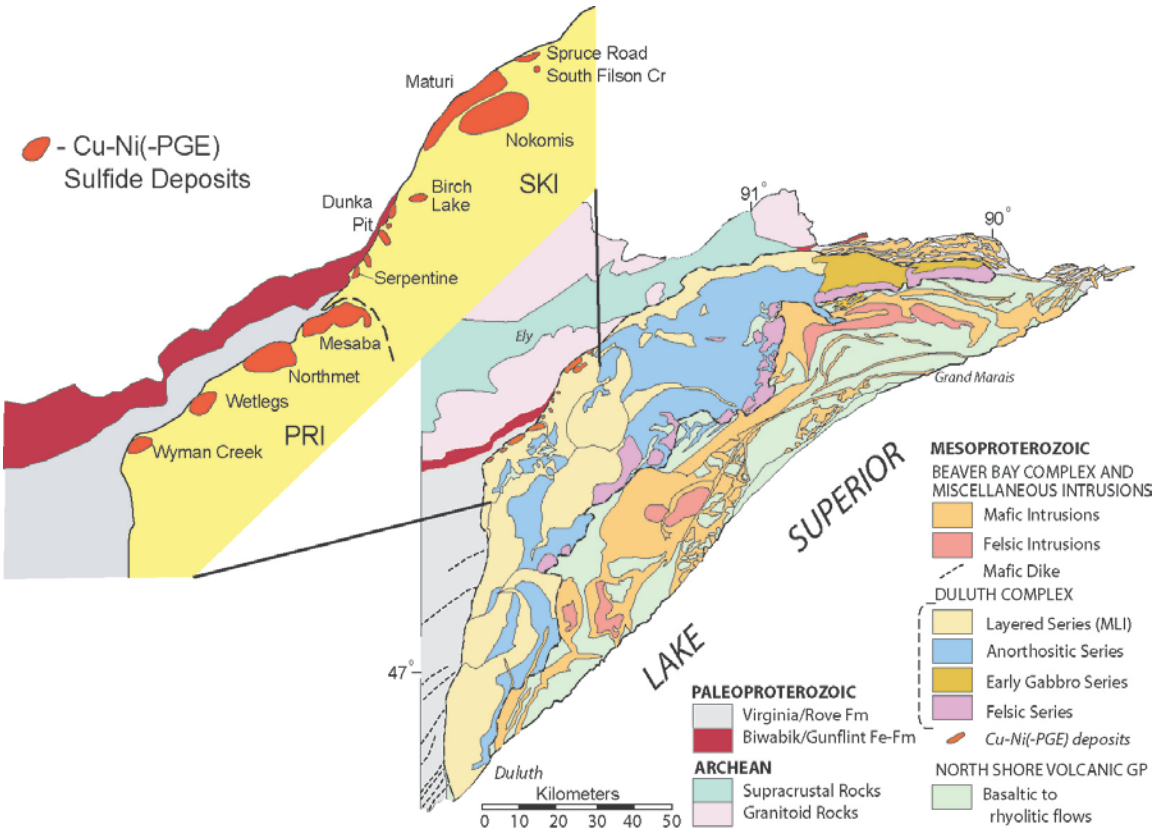

Figure 6: Location and extent of the major Cu-Ni-PGE magmatic sulfide deposits in the basal Duluth Complex. Image courtesy of Jim Miller (personal communication).

The **Maturi** deposit is located just to the south/southwest of the Spruce Road deposit in the vicinity of Highway 1 south of Ely, Minnesota. The Maturi deposit is significantly larger than the Spruce Road deposit, roughly 8 by 30 km in size, and has commonly been divided into two sub-deposits: Maturi, and Maturi West (also known as Maturi Extension or Maturi Southwest). The total indicated resource estimate for Maturi, based on a cut-off grade of 0.3 % Cu, includes 1,065 million tons at average grades of 0.59 % Cu, 0.19 % Ni, and 0.6 ppm TPM (Total Precious Metal; Au + Pt + Pd; Severson et al., 2013). Additionally, there are inferred resource estimates, based on the same cut-off grade, of 542 million tons at average grades of 0.51 % Cu, 0.17 % Ni, and 0.53 ppm TPM. Like Spruce Road, the mineralization is hosted within the BMZ, which has a more

consistent thickness of roughly 50 to 100m throughout the Maturi deposit. The mineralization is broadly similar to Spruce Road, with sulfide content ranging from 1 to 5 % in the disseminated ore zone. Unlike Spruce Road, however, there are significantly larger zones of massive sulfide associated with a down-dipping feature into the GRB called the “magma channel” (Severson et al., 2013). This feature could possibly have formed as a result of partial melting of the underlying GRB (Severson et al, 2013), although the exact mechanisms of its formation are still debated. The sulfide mineral assemblage is similar to Spruce Road, with chalcopyrite + pyrrhotite + cubanite + pentlandite as the main phases and talnakhite ($Cu_9(Fe, Ni)_8S_{16}$) as a significant accessory phase (Severson et al., 2013). Samples were collected from both the Maturi and Maturi West deposits for this study.

The **Birch Lake** deposit is located south of the Maturi deposit and is directly beneath Birch Lake. Unlike Spruce Road and Maturi, the Birch Lake deposit is poorly exposed at the surface, so efforts to evaluate the mineralization have been limited to drill core. A detailed investigation of the mineralization was undertaken by Marna (2004) to examine the relationship between sulfides and PGE concentration, which is unusually high in the Birch Lake deposit. By using the same cut-off grade of 0.3 %, the Birch Lake deposit includes 100 million tons of indicated mineral resources with an average grade of 0.52 % copper, 0.16 % nickel, and 0.86 ppm TPM (Twin Metals, 2014). The sulfide mineral assemblage is characterized as chalcopyrite + pyrrhotite + pentlandite, with minor talnakhite and bornite as accessory phases. Typically, elevated PGE concentrations occur as halos or skirts around chlorite that is adjacent to disseminated chalcopyrite, pentlandite and bornite (Marna, 2004). Due to the poor surface exposure of the Birch Lake deposit, the only samples for this project were collected from drill core.

The **Serpentine** deposit is within the southernmost portion of the SKI and is located to the southwest of the Birch Lake deposit just outside of Babbitt, Minnesota. Material from Serpentine is exposed in the pit wall of the operating Northshore iron mine. Unlike the other deposits describe above, the footwall rock to the Serpentine deposit is the Biwabik Iron formation. Additionally, between Serpentine and Birch Lake are a series of small pockets of Cu-Ni-PGE mineralization that are exposed in the Dunka Pit, the easternmost surface extent of the Biwabik Iron Formation, which was formerly mined to produce iron ore. These small deposits are broadly grouped together as the Dunka Pit deposit. According to estimates by Miller et al. (2002), the Serpentine deposit contains roughly 250 million tons of ore at average grades of 0.41 % Cu and 0.14 % Ni.

Unusually, some material from Serpentine exposed at the surface includes highly weathered massive sulfide. The sulfide mineral assemblage is described as pyrrhotite + chalcopyrite + cubanite + pentlandite, with no notable accessory phases. Disseminated sulfides are typically present within the BMZ, although unlike at other deposits, massive sulfide zones are commonly associated with hornfels inclusions located near the basal contact with the Biwabik Iron formation (Zanko et al., 1994).

The **Mesaba** deposit is located in a geologically complex area at the far northern end of the Partridge River intrusion just outside of Babbitt, Minnesota. The deposit is stratigraphically linked to both the northern end of the Partridge River intrusion and the newly differentiated Bathtub intrusion because of notable changes in rock textures from the western to the eastern ends of the deposit. Significant exploration has been conducted in the area by a number of companies over the years, including the development of an actual shaft and several drifts in the late 1970's to conduct underground definition drilling (Severson et al., 2013). Currently, the resource estimate for Mesaba are reported as 3,300 Mt of ore grading 0.46 % Cu and 0.12 % Ni, with a cut-off grade of 0.38 % Cu (Miller et al., 2002). The sulfide mineral assemblage at Mesaba has been characterized as chalcopyrite + cubanite + pyrrhotite + pentlandite, with minor talnakhite occurring in rock units in close proximity to the "Hidden Rise" stratigraphic feature. The sulfides are concentrated in the basal zone (especially BT1-c) and typically increase in concentration depending on the proximity to the footwall contact with the Virginia formation (Severson et al., 2013). At Mesaba, the thickness of the mineralized horizon beginning at the basal contact varies from 60 to 120 meters thick and varies from massive/semi-massive at the contact to disseminated further up in the stratigraphy (Severson et al., 2013).

The **NorthMet** deposit is located within the Partridge River intrusion just to the north of Aurora, Minnesota just southwest of the Mesaba deposit. Although they are adjacent, there are significant differences between the igneous stratigraphy of the two deposits, including the location of the primary mineralized zone. The total resource estimate for NorthMet, including measured, indicated, and inferred resources, includes 1,178 Mt of ore at an average grade of 0.25 % Cu, 0.07 % Ni, and 0.29 ppm TPM, with a total Cu equivalent value of 0.66 % (Severson et al., 2013). Like at Mesaba, the economic metals are hosted within a sulfide assemblage that includes pyrrhotite, chalcopyrite, cubanite, and pentlandite, with no notable accessory phases. Unlike Mesaba, however, the mineralization is concentrated in the upper part of the basal

mineralized zone (Unit 1) and is almost always semi-massive to disseminated with rare zones of massive sulfide concentrated in veins in fault zones (Severson et al., 2013).

The **Wetlegs** deposit is located within the Partridge River intrusion to the southwest of the NorthMet deposit. Wetlegs is significantly smaller than the other deposits described above and contains a maximum of 54 Mt of ore at an average grade of between 0.57 % and 0.94 % Cu equivalent. Significant petrologic and geochemical work has been done at Wetlegs recently by Raič (2013), who characterized the arsenic-rich Cu-Ni-PGE mineralization. The sulfide mineral assemblage is characterized by both primary and secondary sulfides that formed in hydrothermally altered zones. The primary sulfides include chalcopyrite, pyrrhotite, and pentlandite, while the secondary sulfides include digenite and covellite. Like other Partridge River deposits, the mineralization at Wetlegs is largely concentrated in the basal contact zone as semi-massive to disseminated sulfides, while mineralization higher up in the stratigraphy is strictly disseminated.

The **Wyman Creek** deposit is located within the far western end of the Partridge River intrusion to the southwest of the Wetlegs deposit. This deposit is notable for a mineralized sequence of Virginia formation and Biwabik Iron Formation defined by a thinly bedded pyrrhotite zone that directly underlies the typical Cu-Ni-PGE mineralization in the Partridge River gabbro. This well-defined layering demonstrates the significant chemical exchange that occurred between the Paleoproterozoic footwall and gabbro during the crystallization of the Partridge River intrusion (Miller et al., 2002). Samples were collected from the bedded pyrrhotite horizon to compare to the more typical mineralization found in the Partridge River intrusion.

4. Ni and Cu Isotopes Background

Stable isotopic systems have been used by scientists for many years to examine chemical and physical processes that occur on the Earth's surface. Commonly, these systems involve a given element and several stable isotopes of that element, which fractionate during specific processes, resulting in a greater concentration of one isotope relative to another. For each process, there can be several mechanisms that lead to the fractionation of an element. The most commonly observed mechanisms are: equilibrium fractionation and kinetic fractionation. In this study, two stable isotopic systems will be

utilized to investigate the processes involved in the initial formation and later weathering of the Cu-Ni-PGE mineralization in the Duluth Complex. The primary isotopic system used here is $^{60}Ni/^{58}Ni$ because these two isotopes are present in the highest overall abundance in nature. Furthermore, previous studies involving nickel isotopes primarily utilize this system, so the use of any other Ni isotopes would make comparisons between this study and other available data difficult. The copper isotopic ratio $^{65}Cu/^{63}Cu$ will also be used as an alternative source for data.

4.1 Ni Isotopes

In both terrestrial and extraterrestrial systems, nickel has five naturally occurring stable isotopes: ^{58}Ni, ^{60}Ni, ^{61}Ni, ^{62}Ni, and ^{64}Ni, which are present on average in the following abundances: 68 %, 26 %, 1.1 %, 3.6%, and 0.9 % (Gueguen et al., 2013). Additionally, nickel provides a unique avenue for investigating surficial processes because it has only one natural valence state (Ni^{2+}), so unlike other metals like Fe and Cu, it is unaffected by mass-dependent fractionations caused by oxidation-reduction reactions (Albarede and Beard, 2004; Anbar and Rouxel, 2007). Historically ^{60}Ni was first used to analyze iron meteorites in an effort to better understand the early history of the universe. Notably, ^{60}Ni is a daughter product of the radioactive decay of ^{60}Fe, which has a half-life between 1.5 and 2.62 million years (Bizzarro et al., 2007; Rugel et al., 2009). Because ^{60}Fe can only form during high-energy solar events, the presence of excess ^{60}Ni in meteorites could theoretically provide insight into the first 10 million years of planetary formation (Morand and Allegre, 1983; Shimamura and Lugmair, 1983; Tanimizu and Hirata, 2006; Moynier et al., 2007; Cook et al., 2008). Apart from these early cosmochemical investigations, nickel isotopes have only recently been used to examine terrestrial processes. Based on the work by Albarede and Beard (2004) and Anbar and Rouxel (2007), it was theorized that nickel would only fractionate as a result of biotic or chemical processes, the latter of which include both high and low temperature phenomena (Gueguen et al., 2013). Recent studies have conducted research involving nickel isotopes to test other processes that may induce a significant fractionation of nickel.

Tanimuzu and Hirata (2006) first speculated that significant fractionation of up to 0.4 ‰ could occur during the gradual cooling and crystallization of a high-temperature magmatic intrusion. Although their research was largely theoretical and involved several

other metals, this hypothesis was further tested by Lazar et al. (2012), who experimentally determined that kinetic fractionation between nickel metal and silicate (talc) occurs under specific temperature (500 ºC to 900 ºC) and pressure (8-13 kbar) conditions. More recently, several studies have used natural materials from high temperature volcanic and intrusive igneous rocks to further explore the potential for high temperature fractionation in natural systems. Gueguen et al. (2013) published the first comprehensive set of data points from a variety of terrestrial materials and discovered a total overall fractionation range of 2.1 ‰ for $\delta^{60/58}$Ni (figure 7). High-temperature samples measured included komatiite and sulfide-bearing komatiite, serpentinite, dunite, altered and fresh basalt, and pure olivine crystals. Interestingly, the sulfide-bearing komatiites revealed a significant fractionation spread from -1.1 to -0.1 ‰, unlike the other materials that were clustered much closer to 0 ‰ (total spread from -0.15 to 0.25‰). This result suggests that a unique process, specifically involving sulfide minerals, governs the fractionation of nickel within high temperature magmatic systems because the other high temperature systems without sulfides produced a much smaller fractionation. These results were later corroborated by studies by Hoffmann et al. (2014) and Hiebert et al. (2014), who specifically sampled sulfide-bearing komatiites in Canada and Zimbabwe to measure $\delta^{60/58}$Ni. Hoffmann et al. (2014) found a fractionation spread from -0.47 to -0.28 ‰, while Hiebert et al. (2014) found a much larger fractionation spread from -1.06 to 0.15 ‰. The spread recorded by Hoffmann et al. (2014) was significantly less than other studies because samples were very similar and collected in a small geographic area. Regardless of the exact methods or geographic location, these studies demonstrated that fractionation of nickel does occur at high temperatures within magmatic, komatiite-bearing nickel sulfide deposits; this idea will be utilized in this study.

Low-temperature fractionation of nickel was first theorized by Albarede and Beard (2004) and Anbar and Rouxel (2007), and first experimentally evaluated by Gall et al. (2011). During their initial experiment, Gall et al. (2011) tested out a method for measuring nickel isotopes using a variety of materials including black shale. Although the resulting $\delta^{60/58}$Ni values were not greatly different from basalt and peridotite samples measured at the same time, the vastly different formational processes for the shale suggested that another mechanism could result in the fractionation of nickel at low temperatures. Another study by Gall et al. (2013) determined the isotopic signature of another low temperature material, ferromanganese crust. These Fe-Mn crusts form on the ocean floor in low-temperature environments and have significant interactions with

the surrounding seawater, which has an average $\delta^{60/58}$Ni value of 1.44 ‰ globally (Cameron and Vance, 2014). The Fe-Mn crusts themselves have measured values from 0.9 to 2.5 ‰, which vary from ocean to ocean and depend also on depth (Gall et al., 2013). Effectively, these studies combine to demonstrate that secondary materials forming in aqueous environments may involve processes that cause a concentration of heavy nickel isotopes, in contrast to the isotopically depleted fractionation spread observed in high temperature rock samples.

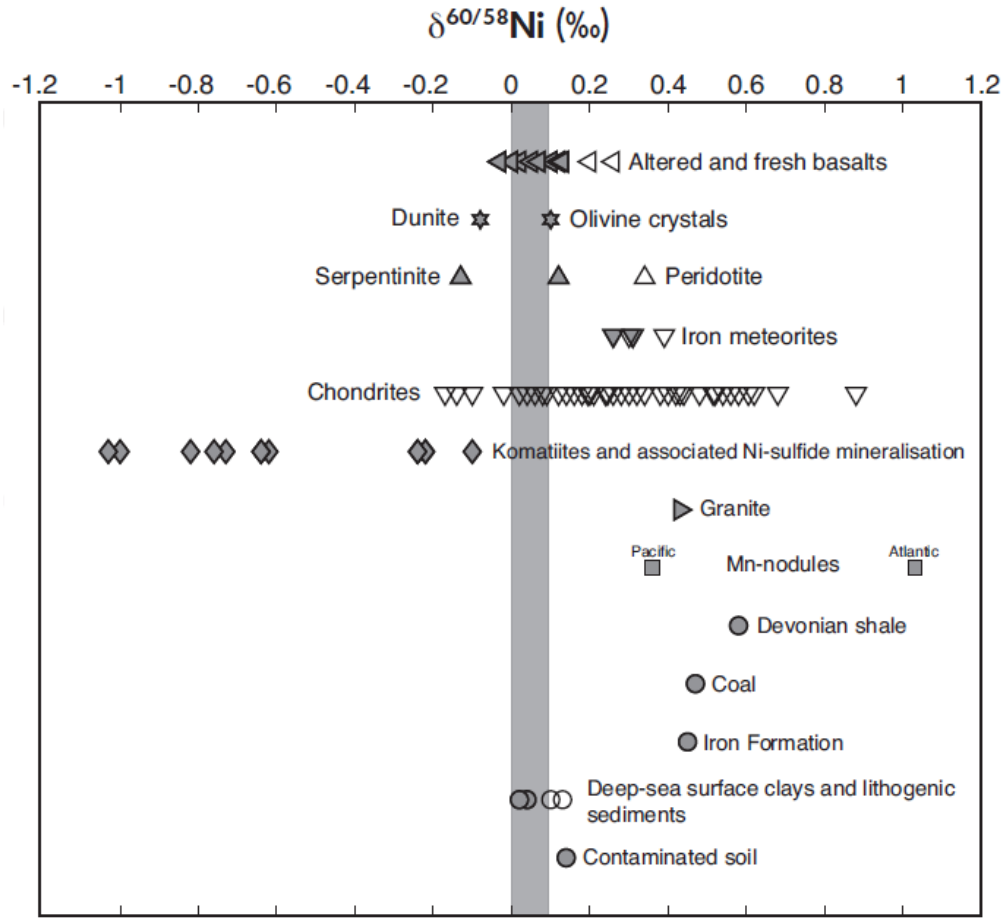

Figure 7: $\delta^{60/58}$Ni values published by Gueguen et al. (2013). Grey bar in the center represents the "bulk silicate earth" value for the $\delta^{60/58}$Ni isotopic system.

In addition to ferromanganese crusts, several other studies have examined surface weathering and the creation of secondary minerals as a potential mechanism for low-temperature fractionation of nickel. Along with examining Fe-Mn nodules, Gueguen et al. (2013) measured the $\delta^{60/58}$Ni values for several additional "low-temperature" materials, including deep-sea sediments (0 to 0.1 ‰), contaminated soil (0.14 ‰),

Devonian shale (0.59 ‰), coal (0.47 ‰), and iron formation (0.46 ‰). All of these materials, with the possible exception of deep-sea sediments, have positive $\delta^{60/58}$Ni values, suggesting that the heavy isotopes were preferentially incorporated into each material. Like the Fe-Mn crusts, these materials form at the surface and were likely affected by fluid flow and significant surficial weathering. Other studies built upon the preliminary work by Gueguen et al. (2013) and demonstrate the fractionation of nickel into secondary phases in specific environments. Ratié et al. (2015) measured $\delta^{60/58}$Ni values from a variety of materials in the Barro Alto complex in the Goiás state, Brazil, to determine if there is a preferential depletion of nickel isotopes during extreme, tropical weathering. Samples were collected from multiple horizons within the deep saprolitic and lateritic weathering profiles of the Barro Alto complex along with material from the bedrock and the soil to track the effects of weathering over the entire range of nickel-hosting products. In contrast to the findings by Gueguen et al. (2013), the data shows that there is an overall trend of heavy isotope depletion in secondary clay and oxide products, suggesting that light isotopes remain behind while the heavy isotopes are preferentially incorporated into fluid phases, which then leave the system. This uptake of relatively light nickel into secondary products and heavy nickel into solution was further examined in a study by Wasylenki et al. (2015), who measured $\delta^{60/58}$Ni values in laboratory-synthesized ferrihydrite. The results demonstrate that during adsorption and coprecipitation, the secondary oxide solid phase (-0.21 ‰ average) has a notably lighter isotopic signature than the Ni bearing solution (0.14 ‰ average). These results will be compared to data collected during the course of this study.

Although the studies described above examine low-temperature fractionation of nickel at the surface, to date no study has attempted to investigate the potential for a fractionation process that is biologically mediated. The presence of significant plant matter in nickel-rich weathering environments could possibly lead to an additional fractionation that is distinctly different from the chemical processes described above. A recent study by Juillot (2015) examined the possibility of mangrove swamps serving as potential metal sinks in the area of lateritic deposits in New Caledonia. Although this study did not measure nickel isotopes, it demonstrated a significant uptake of nickel by plant matter at the land-sea interface that is directly related to the stability of iron sulfides at the surface. Much more research is needed to determine the nature of this process, but it cannot be ruled out as a low-temperature fractionation process that potentially affects nickel isotopic signatures.

4.2 Cu Isotopes

The copper isotope system is defined by two naturally occurring stable isotopes, ^{63}Cu and ^{65}Cu, which are present in the crust on average in the following abundances: 69% and 31%. Unlike the nickel isotopic system, which has only one natural valence state, copper is significantly more complex and has several valence states: Cu^{2-}, Cu^{1+}, Cu^{2+}, Cu^{3+}, Cu^{4+}, of which Cu^{2+} is the most common due to its stability. As a result, copper is highly affected by redox reactions that commonly occur during surficial weathering. These reactions lead to a mass-dependent fractionation of copper, which leads significant depletions of heavy or light copper. Copper isotopes have been used extensively since the 1960's to study copper deposits for a variety of reasons including efforts to identify the source of copper in ore deposits, and attempts to monitor the source of contaminants in water runoff from massive Cu-porphyry deposits.

Unlike Ni isotope studies, where bulk isotopic values are commonly calculated for a whole rock sample, Cu isotopes are regularly measured for a known mineral phase within a given deposit type. Larson et al. (2003) measured $\delta^{65}Cu$ values from several different minerals in a number of different deposit types to try and determine the source of copper in hydrothermal systems. Isotopic values were measured in native copper from the Keweenaw peninsula in Michigan (0.22 to 0.36 ‰), bornite and chalcopyrite from porphyry and skarn deposits in Peru and the USA (-0.87 to 1.41 ‰), chalcopyrite from the Sudbury and Stillwater mafic intrusions (-1.06 to 0.16 ‰), and native copper, cuprite, and azurite from supergene deposits in the USA (-0.09 – 2.44 ‰). These values, along with additional measurements in secondary copper minerals from Markl et al. 2006, can be seen below in figure 8. These values represent a small percentage of the total amount of Cu isotope data available in the literature, but even in this small sample size, it is clear that $\delta^{65/63}Cu$ isotopic values change based on the mineralogy and the deposit type for copper ore. Specifically, values from high-temperature magmatic and hydrothermal systems are enriched in light copper (^{63}Cu), while more oxidized, secondary copper supergene and laterite deposits are highly enriched in heavy copper (^{65}Cu). These results are corroborated by Asael et al. (2007), who measured Cu isotopic values in sedimentary copper mineralization. Within that system, the basement quartz porphyry (-3.5 to -1.6 ‰) and the primary ore-hosting dolomite (-3.2 to -1.3 ‰) have significantly lighter isotopic values than the heavily oxidized rims of each unit (porphyry: -0.8 to 0.4 ‰; dolomite: -1.2 to -0.1 ‰). These values from previous work will be

compared to values obtained in this study to see whether or not similar values in both primary mineralized and weathered samples occur in the basal Duluth Complex.

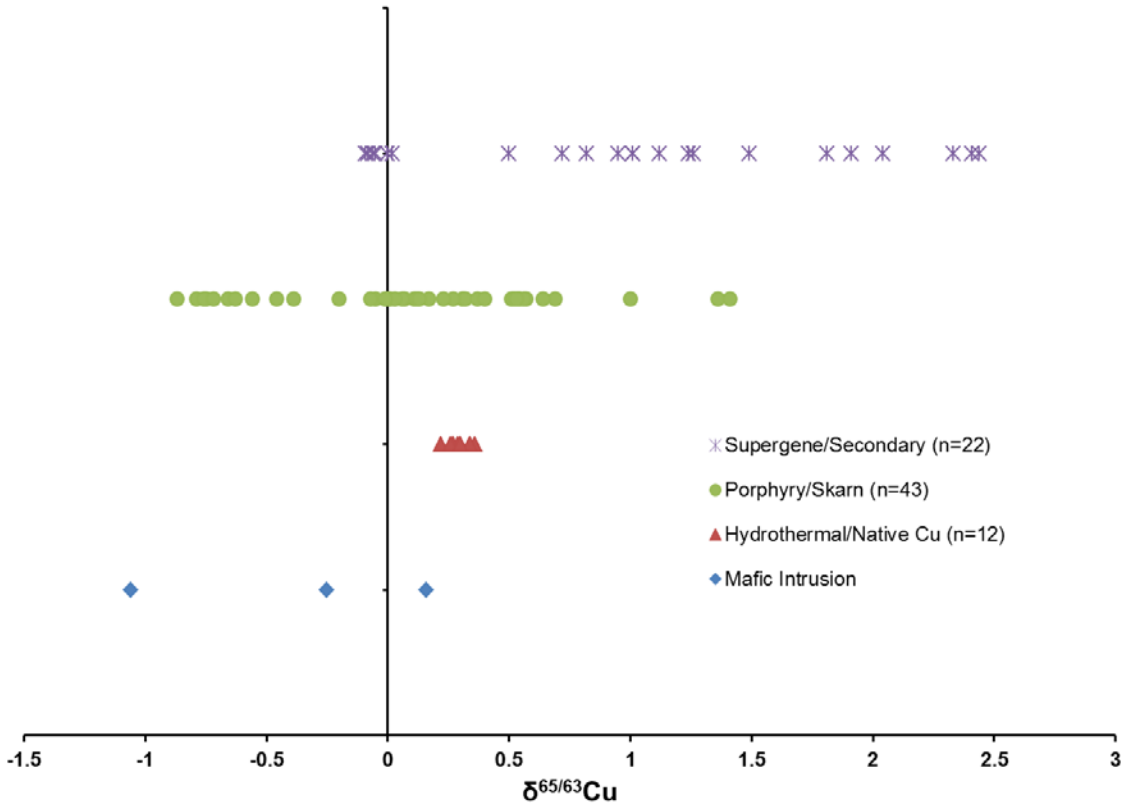

Figure 8: $\delta^{65/53}$Cu values for selected deposit types (data from Larson et al. 2003 and Markl et al. 2006). Dataset for Porphyry/Skarn includes measurements from chalcopyrite and bornite. Dataset for Supergene/Secondary includes measurements from native copper, cuprite, azurite, olivenite, malachite, and chrysocolla.

5. Methods

A variety of samples were collected from the basal Duluth Complex for this study. These samples were primarily chosen based on location and mineralogy, with the main focus on sulfide content and general proximity to the known Cu-Ni-PGE deposits described above. These samples were documented and processed for whole rock and trace element geochemistry, metal assay, Ni isotopes, and other methods; the exact type of processing differed depending on the specific analytical method. In addition to geochemistry and Ni isotopes, x-ray diffraction (XRD), transmitted and reflected light microscopy, scanning electron microscopy (SEM), microprobe, and Cu isotopic analyses were used to characterize the sample material. One unique processing technique, electric pulse disaggregation, was used to separate rock samples into their individual mineral components that were analyzed separately.

5.1 Sampling

5.1.1 Field Sampling

Surface samples were collected on field trips to the basal Duluth Complex area with the permission of several mining companies including Duluth Metals Ltd., PolyMet Mining Inc., Teck Resources Ltd., and Encampment Minerals LLC; specific guidance on selected sampling locations was provided by company geologists. In general, samples were taken from roadside outcrops, quarries or glacial till beds and were subdivided into four categories: sulfide-bearing rock, sulfide-barren rock, weathered rock, and till. Samples containing sulfide were targeted to study Ni isotopic signatures in sulfide-bearing rocks with varying degrees of weathering. Unmineralized rocks were also sampled to investigate the possibility of distinct isotopic signatures in sulfide-barren silicate and secondary oxide-rich rocks. Glacial till was also collected from sites in close proximity to sampled outcrops to determine if till has distinct isotopic signatures from mineralized and unmineralized bedrock. A complete list of all field samples is shown in table 1.

The first sampling trip took place in June 2014 with employees of Duluth Metals Ltd. (DM). Dean Peterson assisted in the collection of samples from several sites associated with the I deposit, the II deposit, and Jack's Rock, a location that contained notable nickel anomalies in glacial till previously sampled by DM. Other sites included

the Newton Belt and the Bald Eagle Intrusion, which are not associated with any known Cu-Ni-PGE deposits; sample material collected there serves as background samples. Three outcrops were visited that contained sulfide mineralization associated with the I deposit (figure 9). A total of eight samples were collected including glacial till and rock samples. A test pit into II deposit material was visited; four samples were collected including glacial till and surface rock samples. Since the anomaly associated with Jack's Rock is not related to any known outcrops, only a glacial till sample was collected. Two samples were collected from a road cut of the Archean-age Newton belt directly north of Ely, MN along the Echo trail. These samples included a till sample and a rock sample. Finally, a large quarry in the Bald Eagle intrusion was visited to collect samples that serve as background, unmineralized Duluth complex material (figure 10). At this quarry, five samples were collected including one glacial till and four rock samples. Additional drill core samples were also obtained from Duluth Metals and Twin Metals.

Figure 9: Outcrop of mineralized I deposit material. 8 cm scale card is shown in the center of the photograph.

Figure 10: Bald Eagle intrusion quarry where samples T7 and O11-O13 were collected.

The second sampling trip took place in late June 2014 in the area of the NorthMet deposit. This visit included field sampling and drill core sampling. Three field sites, suggested by Andrew Ware, chief geologist for PolyMet, were sampled. The first site, called “Test Pit 1,” is located off of Dunka Road near the northeastern end of the NorthMet deposit (figure 11). In this area, 5 samples were collected, including a till sample, a weathered sample, and three surface outcrop samples (figure 12). The second site was located in the woods roughly in the middle of the NorthMet deposit. Previously, this site had been extensively drilled in a dense grid pattern, producing about 60 drill holes in a 10,000 m^2 area. At this site, two samples were collected: a till sample, and a surface rock sample. The latter was not collected from a verified outcrop, but a weathered, oxide-rich boulder nearly identical to samples collected at Test Pit 1. The final site is located at the westernmost extent of the NorthMet deposit. No boulders or outcrops could be located, so only one till sample was collected.

Figure 11: NorthMet deposit “Test pit 1” location where samples T8 and PLM-1 to PLM-3 were collected.

Figure 12: Sampling procedure for till/highly weathered material at the test pit 1 site.

The third sampling trip took place in early July 2014 at a Mesaba deposit outcrop located on property leased to Teck Resources Ltd. This property is located on land owned and operated by Cliffs Natural Resources, but currently leased to Teck. Our contact was Mark Severson, who is a consulting geologist for Teck. Only one field site was visited; this site included exposed material adjacent to a former railroad grade that is currently a forest service road (figure 13). At this location, two sampling sites were used at either end of the long outcrop. At the beginning of the outcrop (site 1), two samples were collected: an outcrop sample and a weathered sample that resembled till. At the far end of the outcrop (site 2), two additional samples were collected.

Figure 13: Long outcrop of mineralized Mesaba deposit material. Sampling site 2 in the foreground of the image near the orange bucket; sampling site 1 is adjacent to the parked truck in the background.

The fourth sampling trip took place in mid-September 2014 at an exposure of the Serpentine deposit located at one end of the operating Cliffs Northshore mine. In this area, high-grade ore from the Serpentine deposit is exposed at the surface near the top of the pit wall in an area called “Block 0.” Three surface outcrop samples were collected at this site. The second sampling site was roughly 250 m southwest of the first site, one terrace down into the mine pit. In this area, the contact between the Serpentine-hosting

gabbro and the underlying Virginia formation was clearly visible in a zone of extreme weathering (figure 14). One surface outcrop sample was collected here.

The final sampling trip took place during the 2015 Precambrian Research Center field camp in late July of 2015. During mapping of the Nickel Lake macrodike area, five surface outcrop samples were collected including sulfide-bearing and sulfide-barren material.

Figure 14: Sampling site 2 in the second terrace of “block 0” of the Northshore iron mine. Contact between the Duluth Complex gabbro and the Virginia formation is visible in the center of the photo.

Table 1: Complete list of samples collected in the field. Samples are listed based on type and order collected.

Sample ID	Sample Deposit/Location	Sample Type
T1	Newton Belt	Glacial Till
T2	I	Glacial Till
T3	I	Glacial Till
T4	II	Glacial Till
T5	I	Glacial Till
T6	Jack's Rock	Glacial Till
T7	Bald Eagle	Glacial Till
T8	NorthMet	Glacial Till
T9	NorthMet	Glacial Till
T10	NorthMet	Glacial Till
O1 (B, C)	Newton Belt	Surface Outcrop
O2 (C, D)	I	Surface Outcrop
O3 (A, C, E, G, H, K)	I	Surface Outcrop
O4 (B)	I	Surface Outcrop
O5 (B)	II	Surface Outcrop
O6 (A, B)	II	Surface Outcrop
O7 (A, D)	II	Surface Outcrop
O8 (D)	I	Surface Outcrop
O9 (A)	I	Surface Outcrop
O11 (B, C, E)	Bald Eagle	Surface Outcrop
O12	Bald Eagle	Weathered Material
O13 (B, C*, D*)	Bald Eagle	Surface Outcrop
PLM-1	NorthMet	Weathered Material
PLM-2a (1*, 2, 3*, 4)	NorthMet	Surface Outcrop
PLM-2b (1, 2)	NorthMet	Surface Outcrop
PLM-3 (B)	NorthMet	Surface Outcrop
PLM-4 (A, B, C, D)	NorthMet	Surface Outcrop
TCK-1 (a, b, c, d, e, f*, g*)	Mesaba	Surface Outcrop
TCK-2	Mesaba	Weathered Material
TCK-3 (a, b*, c*, d*)	Mesaba	Surface Outcrop
TCK-4 (a*, b*, c*)	Mesaba	Surface Outcrop
SP-1 (a, b)	Serpentine	Surface Outcrop
SP-2 (a, b*)	Serpentine	Surface Outcrop
SP-3 (a, b)	Serpentine	Surface Outcrop
SP-4 (a, b*)	Serpentine	Surface Outcrop
NLM-1 (A, B, C)	Nickel Lake	Weathered Material
NLM-2 (A, B, C)	Nickel Lake	Surface Outcrop
NLM-3 (A, B, C)	Nickel Lake	Surface Outcrop
NLM-4	Nickel Lake	Surface Outcrop
NLM-5 (A, B)	Nickel Lake	Surface Outcrop

Note: analyses were not performed for each sample, but all samples are stored at the University of Minnesota-Duluth. *Sample has a small amount of material remaining

5.1.2 Drill Core Sampling

In addition to surface samples, drill core was collected to provide data for primary mineralized, unweathered rock from the Cu-Ni-PGE deposits. Drill logs were obtained from the Minnesota DNR online database and evaluated to select representative examples of mineralization from each deposit. Core material was sampled from the mining companies mentioned above, along with selected drill holes from the Minnesota DNR core facility in Hibbing, MN. A list of drill core samples can be seen in table 2.

The first drill core samples were collected from PolyMet, which holds material from the NorthMet deposit. Assistance was provided by Andrew Ware, who suggested drill holes to sample and provided access to company data and maps. Core was sampled from 6 different drill holes including two holes, 10-590d and 10-599d, where mineralization from the NorthMet deposit is very close to the surface. Segments of core were selected based largely on sulfide content, with secondary importance on silicate textures, weathering patterns, and volume of available core.

The second batch of drill core samples was collected from Teck Resources Ltd. Mark Severson from Teck was actively involved in the selection of drill holes. Core was obtained from 5 different holes chosen from his initial selection of nine drill holes. Like the samples from PolyMet, core segments were chosen based largely on sulfide content, weathering effects, and amount of available core.

The third group of samples was obtained on a visit to the Twin Metals core facility in Ely, Minnesota. Three pieces of drill core from a I deposit hole (KEA-1) were collected. These samples included two massive sulfide core segments from the high-grade intersect and a disseminated sulfide sample from several hundred feet above the massive zone.

The fourth batch of drill core samples was collected in late August 2014 from the Minnesota DNR core facility in Hibbing. Organizational and logistical support was provided by Barry Frey during sample collection. Drill core material kept at the DNR from II, III, Serpentine, Wetlegs, and Wyman Creek were selected and specific footages of drill logs were chosen for sampling based primarily on approximate sulfide contents from drill logs available on the MN-DNR online database. Eleven samples were collected from five drill holes that represent the five specified deposits (see table 2). Again, specific core segments were chosen based on sulfide content, available core material, and weathering patterns.

The final core segments came from the Serpentine deposit, and were provided by Harry Noyes of Encampment Minerals LLC. These include one surface sample and three pieces of drill core from two drill holes. Because these samples were provided by Mr. Noyes directly, selections based on sulfide content, host rock, and other characteristics were made by Mr. Noyes.

Table 2: Complete sample list for drill core material collected from mining companies and the Minnesota DNR.

Sample ID	Deposit/Location	Notes
05-420c	NorthMet	
07-536c	NorthMet	
07-537c (33')	NorthMet	
07-537c (574')	NorthMet	
07-537c (584.5')	NorthMet	
10-579c (15')	NorthMet	
10-579c (36')	NorthMet	
10-579c (1030 - 1031')	NorthMet	
10-590D (16')	NorthMet	
10-590D (151')	NorthMet	
10-599D (19')	NorthMet	
10-599D (165')	NorthMet	
MB-07-01	Mesaba	
MB-07-02	Mesaba	
MB-07-07 (4-5')	Mesaba	
MB-07-07 (390')	Mesaba	
MB-07-07 (1106')	Mesaba	
MB-07-07 (1110.5')	Mesaba	
MB-07-16	Mesaba	
MB-07-22	Mesaba	
KEA-1 (A')	I	
KEA-1 (B')	I	
KEA-1 (C')	I	
DNR-1	Serpentine	Sample completely used up
DNR-2	Wyman Creek	Sample completely used up
DNR-3	Wyman Creek	
DNR-4	Wyman Creek	
DNR-5	Wetlegs	Sample completely used up
DNR-6	Wetlegs	Sample mostly used up
DNR-7	Wetlegs	
DNR-8	II	Sample completely used up
DNR-9	II	Sample mostly used up
DNR-10	III	
DNR-11	III	
S1-11	Serpentine	
S4-11 (458 - 458.5')	Serpentine	
S4-11 (458.5 - 459')	Serpentine	

5.1.3 Comparative Ore Samples

In addition to the field and drill core samples described above, several other samples were selected to serve as proxies for different deposit types during nickel and copper isotopic analysis. These samples were obtained from the University of Minnesota-Duluth economic geology collection, and were chosen based on sulfide content and deposit type. A list of the samples and deposit types is provided in table 3.

Table 3: Ore samples used for Ni and Cu isotope analysis.

Sample ID	Sample Deposit/Location	Sample/Deposit Type	Notes
StE-1	St. Egidien, Germany	Secondary Ni	Ni Isotopes
Eagle-1	Eagle deposit, Michigan	Magmatic Cu/Ni	Cu Isotopes
Eagle-2	Eagle deposit, Michigan	Magmatic Cu/Ni	Cu Isotopes
SLC-88	Sturgeon Lake, Canada	VMS	Cu Isotopes
O-528	Bingham, Utah	Cu Porphyry	Cu Isotopes
O-574	Morenci, Arizona	Secondary Cu	Cu Isotopes
G-11	Greens Creek, Alaska	Magmatic Cu/Ni	Cu Isotopes
R-1	Rammelsberg, Germany	Banded/SEDEX Cu	Cu Isotopes

5.2 Sample Preparation

After samples were collected, drill core and surface outcrop samples were described with the focus on rock and sulfide mineralogy along with the effects of surface weathering. Till samples were processed using a series of four sieves from the US Standard Sieve Series to remove organic material. The four sieves used had the following mesh sizes: 14 (1400 µm), 25 (710 µm), 42 (355 µm), 170 (90 µm), and produced five grain size ranges for each sample: > 1400 µm (very coarse), 1400 µm > sample > 710 µm (coarse), 710 µm > sample > 355 µm (medium), 355 µm > sample > 90 µm (fine), and < 90 µm (very fine). The four mesh sizes were selected to produce different grain size fractions and were not selected based on any standardized processing procedures. Samples were chosen for analysis based on the descriptions and the location relative to the Cu-Ni-PGE deposits described above.

Samples were selected for bulk and trace element geochemical analysis, x-ray diffraction, and PGE fire assay in order to gain a general understanding of the Cu-Ni-PGE mineralization, the unmineralized gabbroic host rock, weathered material at the surface, and the glacial till overlying the surface material. A few other samples (see table

3) were chosen to represent rock units that are completely unrelated to the basal Duluth Complex. Samples for geochemical analysis were crushed to a fine powder (<100 µm) using a Spex Industries Shatterbox outfitted with both a ceramic and steel crusher assembly. The ceramic assembly was used to crush sulfide and metal-barren samples due to the potential for contamination with the steel assembly. The same setup was used to crush samples for XRD analysis, PGE assay, and Ni and Cu isotopic analysis.

5.2.1 Thick Sections

To characterize the sulfide mineralogy in the Cu-Ni-PGE deposits, several thick sections were prepared for reflected light microscopy. This method provides a unique way to examine the textures and paragenetic relationships between sulfide and oxide minerals that are opaque in standard transmitted light microscopy. Samples were chosen to represent each deposit as well as a wide variety of sulfide textures.

Initially, samples were cut into roughly 2.5 cm x 2.5 cm squares using an MK Diamond Rock Saw. These were placed on a flat surface in plastic molds and encased within a mixture of EpoxySet resin and hardener in a 10 g to 1.2 g ratio. A thin layer of release agent was added to the inside of the plastic molds to ensure a clean release for the epoxy pucks after 24 hours of hardening. The hardened pucks were ground down using a series of Carbimet paper discs in the following sizes: 180-grit, 320-grit, 400-grit, and 600-grit. The coarse grit sizes removed excess epoxy from the sample surface, and the finer grits began the polishing process. Following the 600 grit step, the epoxy pucks were polished using diamond compound of the following sizes: 9 µm, 3 µm and 1 µm. In total, 15 polished sections were produced that represent the varied sulfide minerals and textures found within the Cu-Ni-PGE deposits of the basal Duluth Complex.

5.2.2 Thin Sections

In addition to polished thick sections, several samples were selected for thin sections. Unlike the thick sections, samples were chosen based on typical gabbroic content, including the presence of olivine in contact with weathered oxide minerals and primary sulfides. Specifically, five surface samples and five drill core samples were selected. These were cut into roughly 5 cm x 2.75 cm pieces using the MK Diamond Rock Saw and sent off to Quality Thin Sections in Tucson, AZ to produce 10 polished

thin sections. These were used for transmitted light microscopy in addition to SEM and microprobe work.

5.2.3 Electric Pulse Disaggregation

Along with the traditional methods outlined earlier to prepare samples for geochemical and isotopic analyses, another method was used to isolate olivine and sulfide grains for Ni isotopic analysis. This method, known as electric pulse disaggregation (EPD), utilizes a strong pulse of electricity (200,000 volts) to effectively disintegrate a rock sample into its individual mineral components. A prototype EPD machine constructed by University of Minnesota emeritus professor Paul Weiblen was used to process 11 rock samples, including 2 weathered surface samples and 9 drill core samples (figure 15). One additional sample was mailed for processing to a Swiss company, Selfrag AG, that manufactures and sells high-performance, modern EPD machines. Of these 12 total samples, 3 were selected for Ni isotopic analysis and underwent further processing.

The original method for EPD was first pioneered by Soviet scientists in the 1940's, but not described in detail until the late 1960's (Maurer, 1968; Andres 1977; Andres and Bialecki, 1986; Andres, 1989; Finkelshtein et al., 1989; Kurets et al., 1989; Shuloyakov et al., 1989). More recent work by a variety of researchers (Weiblen, 1994; Saini-Eidukat and Weiblen, 1996; Cabri et al., 2008; Wang et al., 2011, 2012a, 2012b; Arribas et al., 2014) has revealed further insight into the physical phenomena that occur during this unique process.

In a standard EPD procedure, a rock sample is placed in a water bath inside a cylindrical chamber, and a pulse of electricity, up to 200,000 volts, is directed through a cathode towards an anode, located underneath the sample. The pulse preferentially moves into the rock sample rather than the surrounding water due to conductivity differences at high voltage, passes through it, and discharges through the anode (figure 16). While it moves through the rock sample, the high voltage pulse creates a thin layer of plasma along its pathways, which then explodes due to its unstable nature (Saini-Eidukat and Weiblen, 1996). These pathways form in the zones of greatest weakness within the rock sample, which are the grain boundaries between different minerals in addition to preexisting veins and fractures (figure 17).

Figure 15: Prototype EPD device at the University of Minnesota-Twin Cities used to process several samples for isotopic analysis.

To utilize this unique method of mineral separation, eleven 1 cm^3 samples were cut and brought to the prototype EPD device housed at the Minnesota Geological Survey (figure 15). Samples were placed into a plastic cylinder, which was then filled with water and sealed using two cylindrical steel discs. Attached to the insides of both discs were small metal tubes that serve as the anode and cathode assembly. The assembly was placed inside a large metal cage that housed the EPD device, which consisted of two large boxes and some extra circuitry including a grounding wire. One box held the capacitor array, which produced the high voltage pulse, and the second housed a control box that allowed the user to control how much voltage was produced by the capacitor array. The sample holder was attached to the capacitor array via a thick (~2mm) copper wire, the cage was sealed, and the control box was used to produce the electric pulses. Once the desired voltage level was reached, roughly 1 pulse was discharged through the sample per second for about 60 to 90 seconds, depending on the mineralogy of the sample.

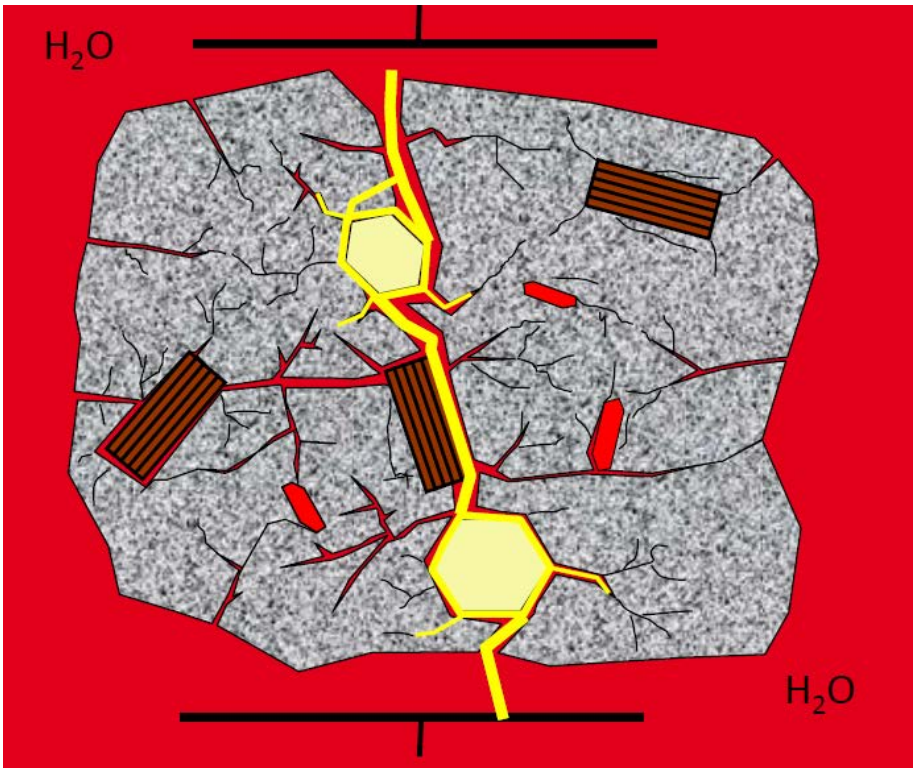

Figure 16: Visual representation of a pulse of electricity moving through a rock sample during disaggregation. Image courtesy of Selfrag AG (2014).

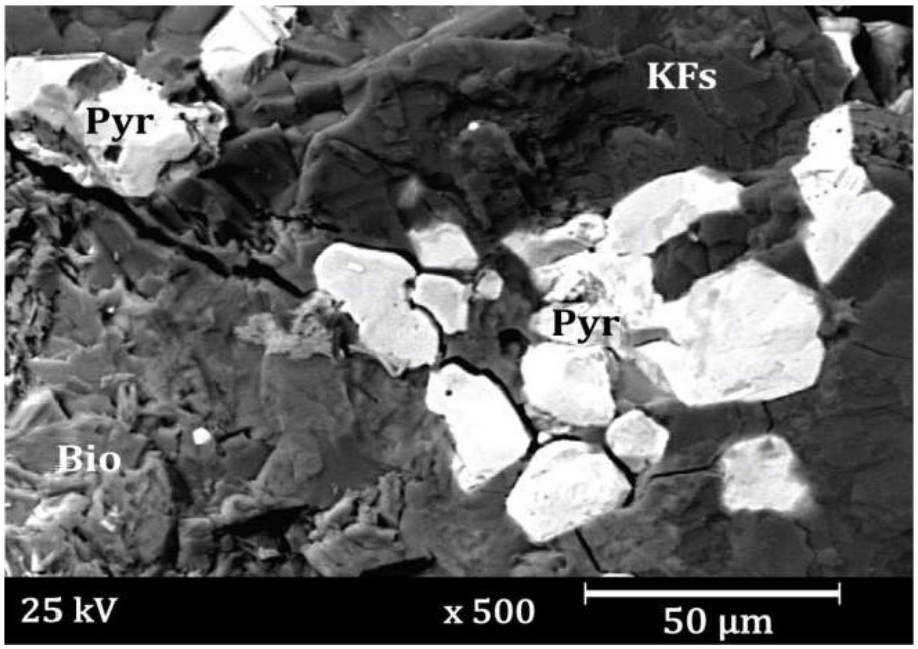

Figure 17: SEM image of a pulse pathway within a rock sample. Visible is a large crack between pyrite and potassium feldspar that formed during the EPD process. Image courtesy of Selfrag AG (2014).

As a result of this procedure, 11 vials of EPD-processed material were produced, although the quality of the mineral separation differed from sample to sample due to a fault that developed within the sample holder during processing. After examining the products through a binocular microscope, the three most well-separated samples underwent further processing to separate olivine crystals from the other phases present. This consisted of gravity separation, followed by picking of individual minerals using a fine paintbrush. The three samples chosen for isotopic analysis contained a pure olivine separate, with only a small potential for contamination by other minerals.

5.3 Analytical Methods

5.3.1 Geochemistry

Crushed material was sent to Activation Laboratories Inc. (ActLabs) in Hamilton/Ontario for bulk, minor, trace, and rare earth element geochemical analyses. These analyses were conducted using the following methods: INAA, TD-ICP, FUS-ICP, FUS-MS, and ICP-OES. Additionally, several other elements were measured that are not typically included in the standard analytical packages; these included precious metals (Au, Ag) and high technology metals (e.g. Ga, Ge).

A second batch of samples was sent to the University of Western Ontario for geochemical analysis. These samples were selected to provide more complete coverage of the study area and to ensure selected samples had both isotopic and corresponding geochemical data available. Samples were measured using ICP-MS. A complete list of all geochemical data (tables A2 to A7) can be found in Appendix 1.

5.3.2 X-Ray Diffraction

Crushed material was prepared in the Research and Instrumentation Lab at the University of Minnesota-Duluth for x-ray diffraction (XRD) analysis. 11 total surface outcrop samples were analyzed to identify mineral phases present within each sample in an effort to better understand the presence of secondary, weathered phases in sulfide-bearing gabbro at the surface in the Duluth Complex. Crushed material was backloaded into bulk analysis sample slides using a sieve to prevent a preferred orientation of the crystal grains. Some samples had limited amounts of crushed material, so they were

placed onto special crystal sample holders for a more limited analysis. Samples were analyzed with a Phillips XPert-MPD powder diffractometer; the machine was set to 40 kV and 40 mA, and a copper tube was employed to transmit the x-rays. The data were processed using the JADE microanalysis suite.

5.3.3 Petrography

Petrographic analysis of polished thin and thick sections was conducted using both reflected and transmitted light. Petrographic data obtained from reflected light microscopy includes: sulfide and oxide mineralogy, textures, and paragenetic relationships. Petrographic data obtained from transmitted light microscopy includes: silicate mineralogy, primary igneous textures, primary and secondary metamorphic and weathering effects, and approximate olivine modal percentages. This information was essential for selecting thin sections and thick sections to be analyzed in greater detail using a scanning electron microscope and electron microprobe. Specific data and images obtained through petrographic analyses are presented in the results section below.

5.3.4 Scanning Electron Microscopy

A JEOL JSM-G490LV scanning electron microscope was used to examine three thin sections and four polished thick sections. Samples were carbon coated to an approximate thickness of 20 to 25 nm using the bulk carbon coater in the Research and Instrumentation Lab at the University of Minnesota-Duluth. The specific machine settings used to collect images, mineral spectra, line scans, and element maps for each sample were generally 15 kV accelerating voltage, aperture 3, a spot size of 58 nm, and both the secondary and backscatter electron detectors. These settings changed slightly when collecting spectra for minerals containing high wavelength elements. Data were collected and processed using an EDS detector and INCA microanalysis suite. Functions used in INCA included Point & ID (mineral spectra), Analyzer (line scans), and Mapping (element maps). Before conducting analyses with an average process time of 5 seconds, a quant optimization was performed using copper tape as a standard.

5.3.5 Electron Microprobe

Although the scanning electron microscope described above provided preliminary data and high-quality images, the EDS detector was not precise enough to measure nickel values in silicate minerals that contain only a very small percentage of nickel. Thus, the JEOL JXA-8900R WD/ED combined microanalyzer housed in Pillsbury Hall at the University of Minnesota -Twin Cities was used to examine the chemical properties, including nickel, of samples with a much higher resolution than was possible on the SEM at UMD. In total, two visits were made to the probe lab during the summer and fall of 2015 and three types of data were collected from four thin sections and three polished thick sections: mineral chemistry from point analyses, mineral element spectra from bulk wavescans, and mineral chemistry from EDS analyses, linescans, and element maps. To obtain the highest precision mineral chemistry data, it was necessary to select specific elements for analysis and calibrate them to known standards based on the type of mineral that was being analyzed. During our visit, three analytical setups were used to examine the following minerals: olivine, clinopyroxene, and sulfide. The elements used in each setup can be seen below in table 4.

5.3.6 Ni Isotopes

Crushed material was sent to the Systematic Experimental Study and Analysis of Metals in the Environment lab (SESAME) at Indiana University-Bloomington where ^{60}Ni and ^{58}Ni isotopic values were measured. Because the nickel isotopic system in terrestrial materials is a relatively new field of research, a definitive procedure has not yet been developed to measure it. To produce the isotopic values for this project, Dr. Lev Spivak-Birndorf used a modified version of a procedure developed by Gueguen et al. (2013), which was further refined in Wasylenki et al. (2015).

In this modified procedure, powdered samples are first weighed, digested, and purified before beginning isotopic analysis. To separate the nickel from other transition metals with the same 2^+ valence state, a new column distillation method was utilized. Because this method is current unpublished, it will not be described in detail here. A nickel separate was produced that had consistent yields above 95 % purity, with corresponding blanks of ≤ 2 ng Ni. The nickel separate was measured for ^{60}Ni and ^{58}Ni using a Nu Plasma II MC-ICPMS, which was calibrated to measure nickel on masses 58 and 60.

Table 4: Element standards used for each mineral analysis package. Elements were selected based on their expected presence in the minerals of interest.

Standardized Element	Olivine Setup	Clinopyroxene Setup	Sulfide Setup
Si	X	X	
Al		X	
Fe	X	X	
Mn	X		
Mg	X	X	
Ca		X	
Na		X	
Ti		X	
S			X
Pb			X
Cu			X
Ni	X	X	X
Zn			X
Co			X

To conduct each analysis, 250 - 300 ppb Ni was introduced in a 0.32 M HNO_3 solution containing a desolvating nebulizer at an uptake rate of 100 µL/min. Instrumental mass bias was accounted for using the double-spike method, which involved bracketing with the SRM 986 nickel standard; this double-spike method was pioneered by Cameron et al. (2009), and has been used recently by Gueguen et al. (2013) and Wasylenki et al (2015). The final produced values are averages of 4 to 5 individual measurements, and are presented with an average 2 SD of ± 0.06 ‰. Further details of this analytical technique can be found in Wasylenki et al. (2015).

5.3.7 Cu-Isotopes

A total of 30 crushed samples were sent to Dr. Dan Asael at the Yale University Metal Geochemistry Center, where ^{65}Cu and ^{63}Cu isotopic values were measured. Unlike the Ni isotope measurements, a relatively standardized procedure for measuring Cu isotopes has been established; a complete version of the procedure can be seen in Marechal et al. (1999).

To measure $\delta^{65/63}Cu$ values, crushed samples are first digested in a mixture of HCl and HNO_3, followed by HNO_3 mixed with hydrofluoric acid. Next, the concentration of copper was measured using Element HR-ICP-MS. The material was then run through

a column separation procedure that was originally published by Marechal et al. (1999). In this method, digested, metal-rich fluid is purified to a single metal (copper) in an anion-exchange reaction involving a macroporous resin. During the course of this reaction, a 7 N HCl + 0.001 % H_2O_2 solution is added, during which Cu is eluted from the bulk solution and separated from the other transition metal cations. Several other solutions are then added, after which the purified Cu solution is dried and then dissolved into 0.05 N HNO_3 and mixed with the NIST SRM 976 and Pcal elemental Cu solution standards. The Cu standards were chosen based on previous analytical work and not specified in the Marechal et al. (1999) procedure.

After the column distillation, $\delta^{65/63}$Cu values were measured on a Neptune Plus high resolution multicollector ICP-MS using medium resolution and the APEX introduction system. In addition to the standards mentioned earlier, NIST SRM 3114 Cu was used as a bracketing standard during the measurements. The 28 values reported below in the results section are presented with an average 2 SD of ± 0.1 ‰. Two samples were not successfully measured due to difficulties encountered during the extraction of copper.

6. Results

Data were collected from samples in the basal Duluth Complex based on the procedures outlined in the methods section. These data includes detailed petrographic (transmitted and reflected light) descriptions of thin and polished sections along with geochemical, isotopic, and spectral/analytical data. Results obtained from bulk major, minor, and trace element geochemistry are presented in graphical and numerical form in Appendix 1. Selected SEM, microprobe, and isotopic data are presented below; numerical data and corresponding images are provided in the Appendix 1 & 2.

6.1 Sample Description - Thin Sections

The following pages contain information about the textures and mineral assemblages in several thin sections made from rocks of the basal Duluth Complex. These thin sections (table A1-a) include samples collected from rocks exposed at the surface and material collected from drill core material that has not been subjected to surficial weathering. The descriptions below were chosen as representative examples of certain textures and compositions observed within the thin sections, but do not describe every possible mineral assemblage or lithology in basal Duluth Complex material. Images shown below in figures 18 to 23 were collected using transmitted light microscopes in the University of Minnesota-Duluth microscope lab.

O6-A

Sample O6-A (figure 18) is an unfoliated, medium to coarse-grained gabbro containing plagioclase feldspar, olivine, clinopyroxene, and Fe-Ti oxides that was sampled from the test pit dug into II deposit rock. This sample is dominated by 250-500 µm subhedral plagioclase feldspar laths that are highly altered to secondary sericite and other jagged, angular phyllosilicate minerals. Clinopyroxene is typically ophitic and, along with olivine, is commonly altered to very fine-grained, unknown secondary phases. Sulfides are fine to medium grained, euhedral to subhedral, and are generally seen as individual crystals at plagioclase feldspar grain boundaries. Reflected light microscopy was used to determine the sulfide mineral assemblage, which includes pyrrhotite and chalcopyrite.

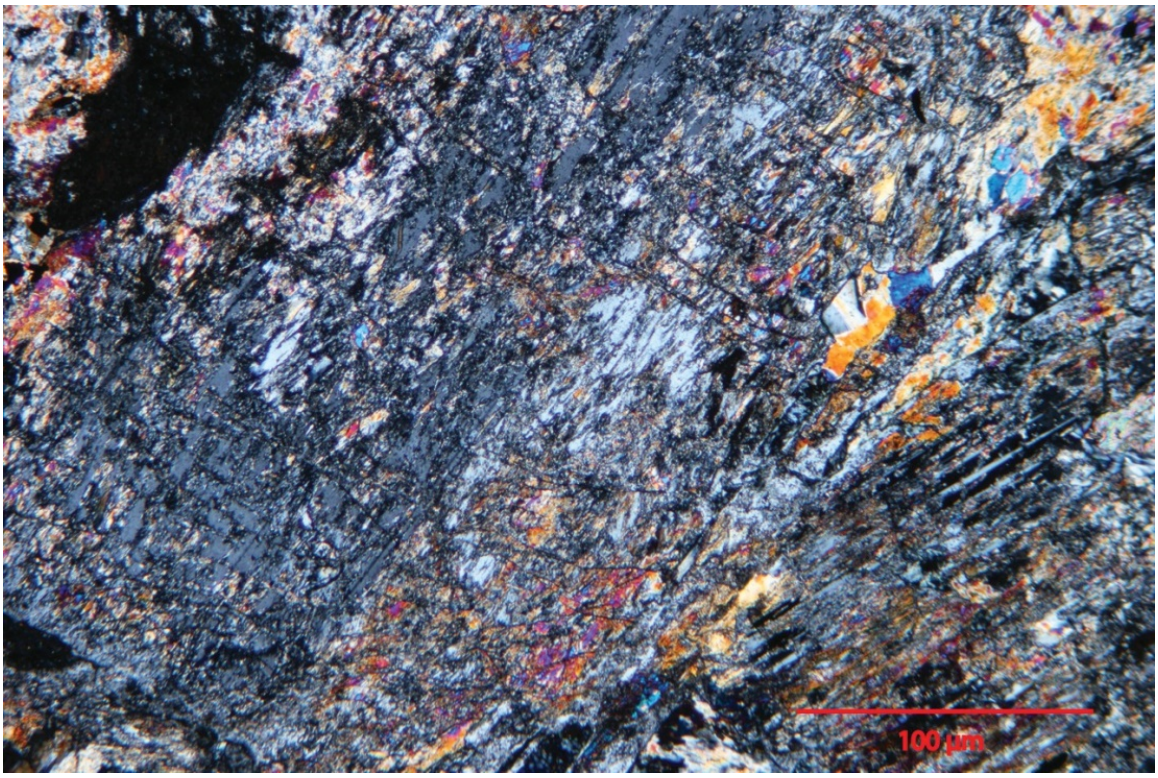

Figure 18: Transmitted light image of textures observed in sample O6-B. This image shows several plagioclase feldspar crystals (gray) that have undergone significant alteration to sericite and other unknown secondary phases. The opaque mineral in the upper-left corner is a sulfide grain that is surrounded by very-fine grained sericite fragments.

TCK-1c

TCK-1c (figure 19) is an unfoliated, medium to coarse-grained, sulfide-bearing gabbro that was sampled from an outcrop of Mesaba deposit material. Significant but not pervasive alteration can be seen at grain boundaries of large subhedral plagioclase feldspar laths and clinopyroxene crystals in addition to veins and fractures within olivine. Clinopyroxene occurs as distinct crystals, and is not ophitic; olivine is rare, and typically altered to serpentine or iddingsite. Biotite is present in notable amounts and occurs as medium-grained euhedral to subhedral crystals; other phyllosilicate minerals occur as very-fine to fine-grained crystals. The latter are commonly found near grain boundaries or in veins and fractures within plagioclase feldspar and clinopyroxene. Biotite commonly surrounds sulfides, which typically occur as fine to medium-grained crystals that are often found in association with clinopyroxene and plagioclase feldspar. Present sulfide minerals include pyrrhotite and chalcopyrite, with minor cubanite.

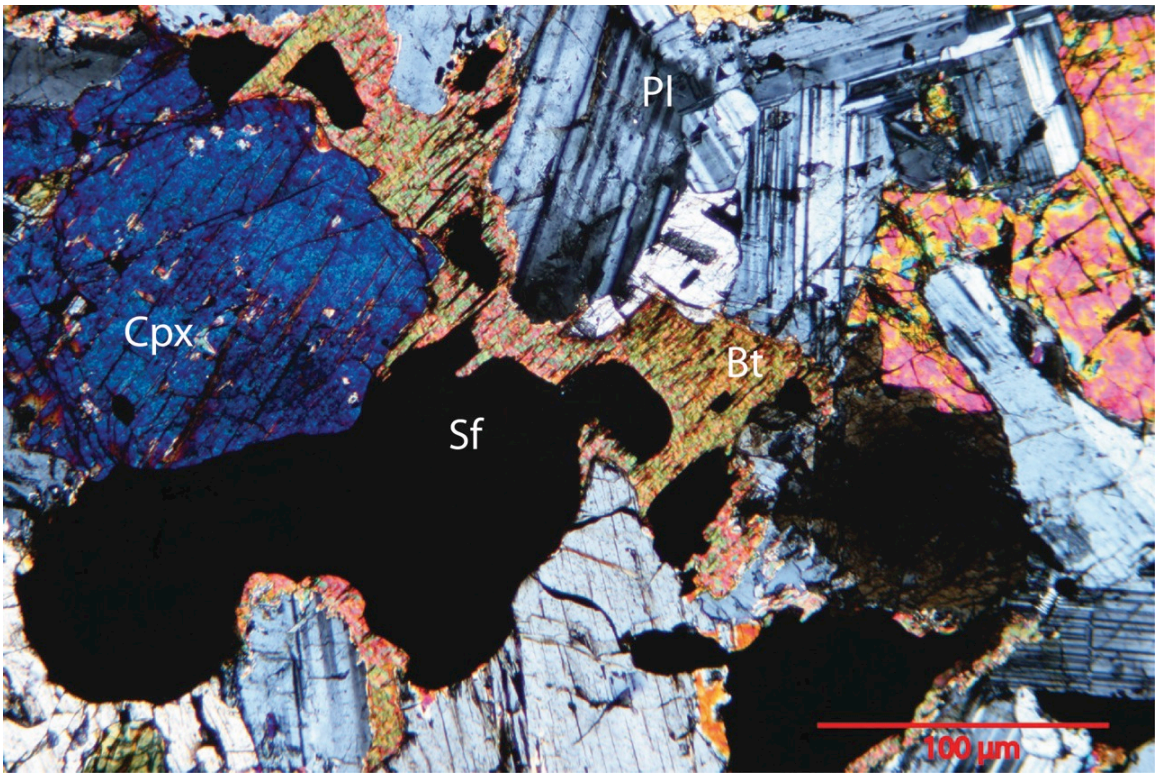

Figure 19: Transmitted light images of sample TCK-1c. This image shows plagioclase feldspar (Pl) in association with biotite (Bt) and clinopyroxene (Cpx). Medium-grained, anhedral biotite surrounds several small, opaque, sulfide crystals (Sf) in the center of the image.

05-420c

05-420c (figure 20) is an unfoliated, coarse to very-coarse grained, sulfide-bearing troctolite that has seen significant hydrothermal alteration. The mineral assemblage is dominantly plagioclase feldspar (70%) and olivine (15%), but also includes minor amounts of clinopyroxene, sulfide, and alteration minerals chlorite and epidote along with trace amounts of biotite. Plagioclase feldspar grains are very-coarse grained and are significantly altered to epidote, chlorite, and other phyllosilicate minerals. These alteration products are commonly concentrated in veins that form perpendicular to the long axis of the plagioclase grains. Olivine is coarse-grained and also highly altered. Fe-Ti oxides and biotite are rare and only present at plagioclase grain boundaries. Sulfide minerals are disseminated, very-fine to coarse-grained and include chalcopyrite, cubanite, and pyrrhotite. Commonly, these sulfides occur as very-fine grained crystals that invade plagioclase feldspar.

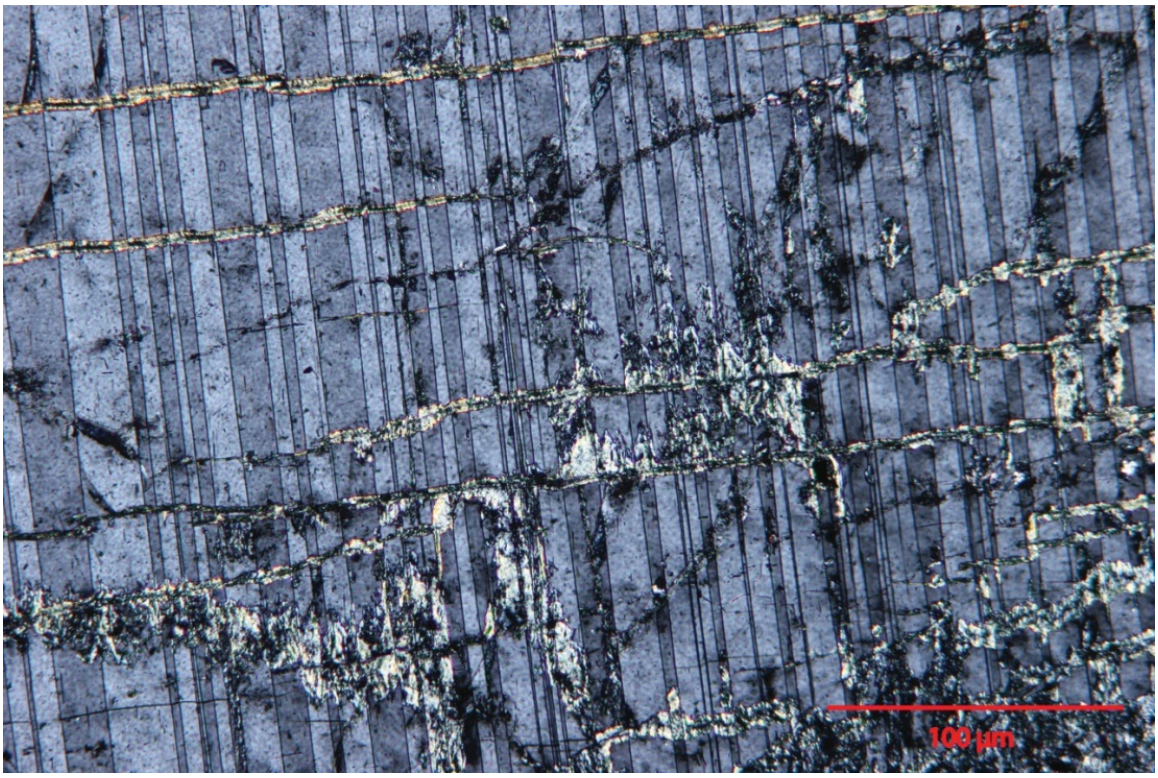

Figure 20: Image collected from sample 05-420c. This image shows veins containing an unknown secondary phase cross-cutting albite twins in plagioclase feldspar at roughly 90º angles.

KEA-1 (A')

KEA-1 (figure 21) is a medium to coarse-grained, unfoliated gabbro or melagabbro that is enriched in clinopyroxene relative to olivine at an approximate ratio of 3:1. Like 05-420c, KEA-1 has seen significant hydrothermal alteration that has resulted in the breakdown of plagioclase feldspar and clinopyroxene to secondary phases possibly including sericite or other phyllosilicate minerals. Clinopyroxene is subhedral to anhedral and is commonly weakly altered to secondary sericite or other unknown minerals, possibly uralite. Sulfides are common (~3-5 %) and typically occur as multi-phase grains. These grains include some combination of the following phases: pyrrhotite, chalcopyrite, and pentlandite.

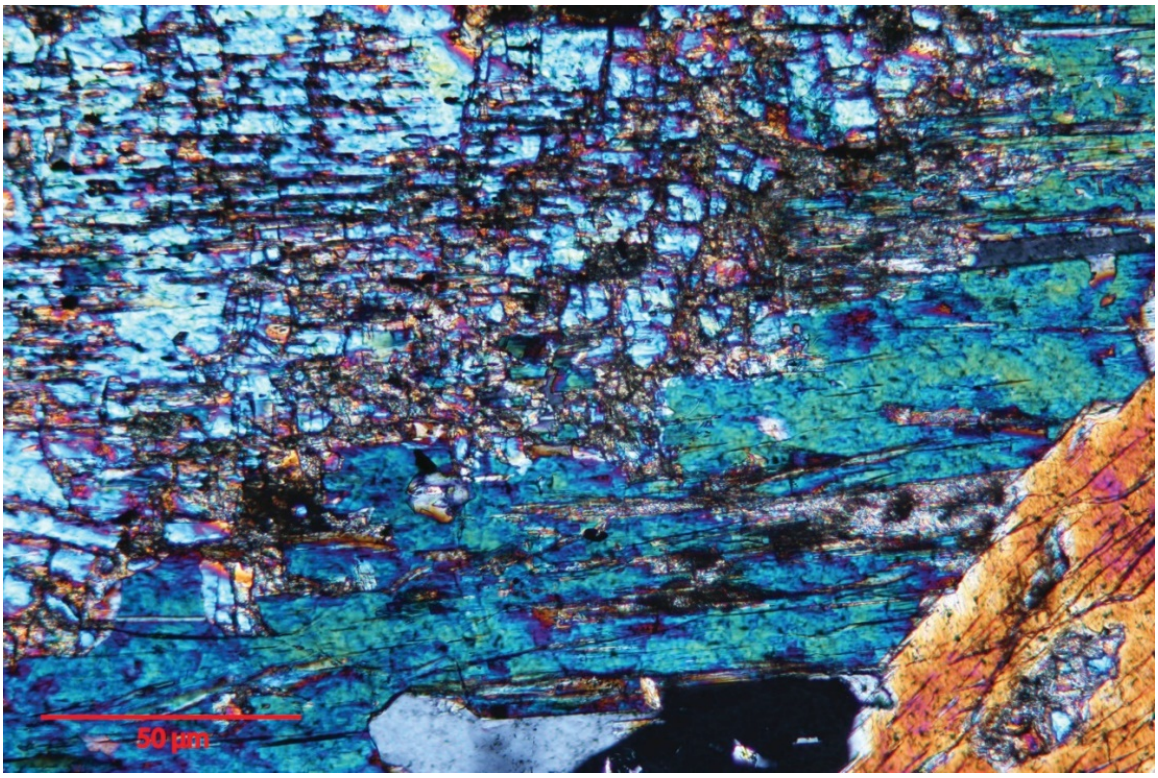

Figure 21: Image collected from KEA-1 (A'). This image shows the alteration of clinopyroxene to an unknown secondary phase – possibly uralite. Also visible is a second clinopyroxene in the bottom right corner of the image.

MB-07-02

MB-07-02 (figure 22) is an unfoliated, fine to coarse-grained melagabbro that was sampled in drill core from the Mesaba deposit-hosted gabbro of the Bathtub Intrusion. Plagioclase feldspar is the dominant mineral, forming subhedral, medium to coarse-grained crystals with minor clinopyroxene, orthopyroxene, and biotite. Notably, MB-07-02 is completely devoid of olivine. Clinopyroxene and orthopyroxene are typically euhedral, fine-grained crystals that occasionally occur within much larger plagioclase feldspar megacrysts. Biotite occurs as a euhedral, fine to medium-grained primary phase in a more typical textural relationship with plagioclase and pyroxene. Fine to very-fine grained sericite and other unknown minerals occur along grain boundaries and in veins and fractures. Sulfides are common and occur dominantly as fine-grained crystals within plagioclase feldspar or clinopyroxene.

MB-07-07 (390')

MB-07-07 (figure 23) is an unfoliated, medium to coarse-grained gabbroic rock that is difficult to assign a specific name to because it contains two very distinct mineral assemblages. The first assemblage is dominated by euhedral, moderately serpentinized, medium-grained olivine and euhedral to subhedral, moderately altered, medium-grained plagioclase feldspar. Minor amounts of serpentine, biotite and other secondary mica phases are present along grain boundaries. The second assemblage is largely coarse to very-coarse grained plagioclase feldspar megacrysts that are highly altered to secondary sericite and other micas. Other phases include minor clinopyroxene and primary biotite. Sulfides are consistently present in both lithologies and typically occur as fine to medium-grained crystals that occasionally invade plagioclase feldspar grains.

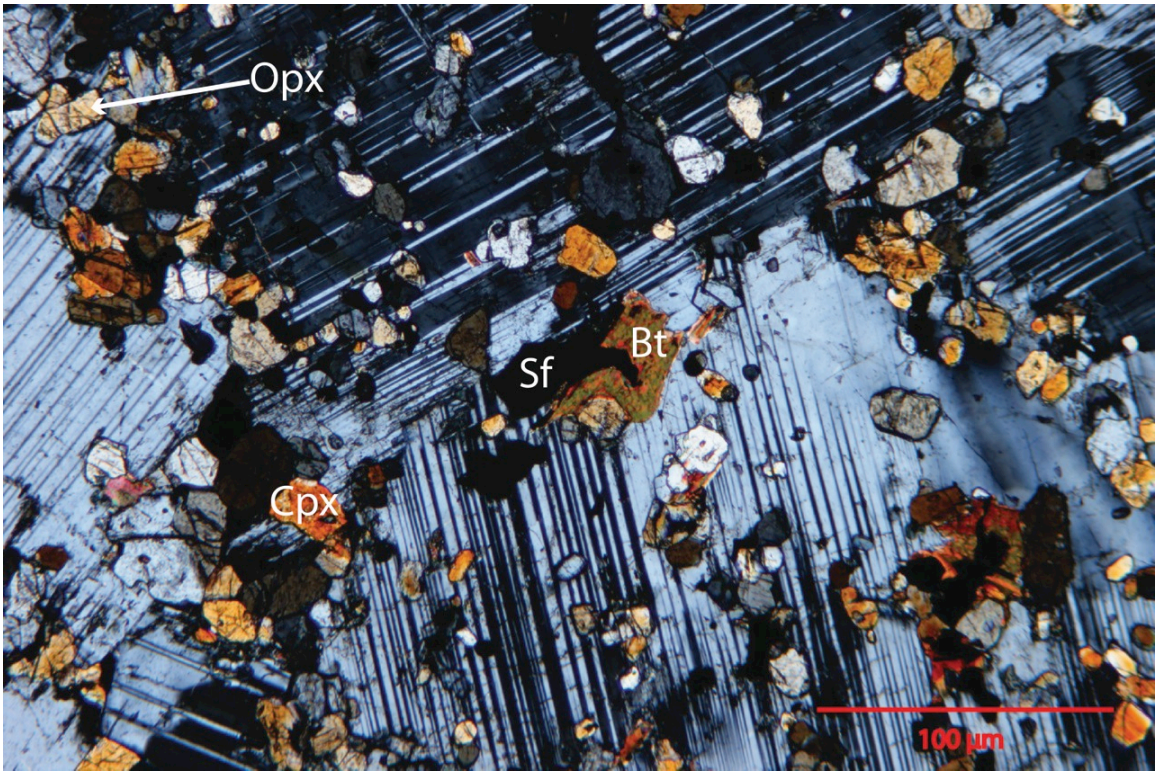

Figure 22: Image obtained from sample MB-07-02. This image shows fine-grained, euhedral clinopyroxene (Cpx), orthopyroxene (Opx), biotite (Bt), and sulfide (Sf) inside coarse-grained, anhedral plagioclase feldspar grains.

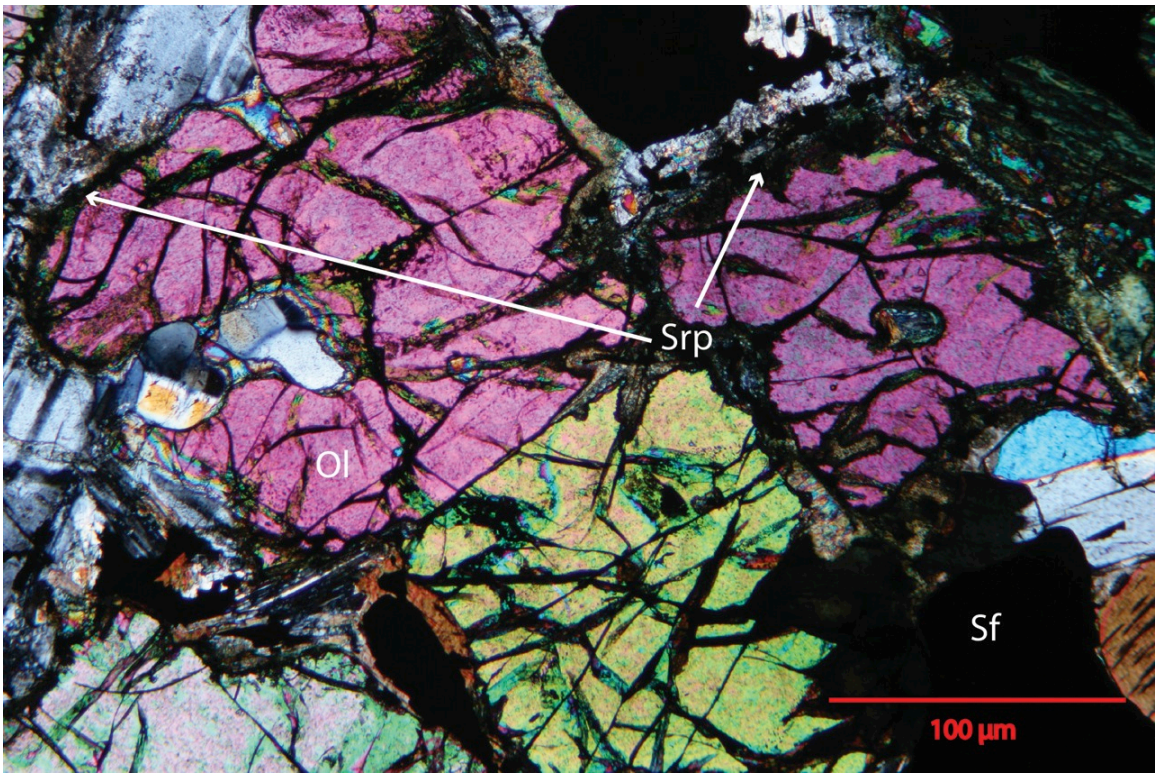

Figure 23: Transmitted light image collected from sample MB-07-07 (390'). This image shows the olivine-rich mineral assemblage described above. Several of the olivine (Ol) phenocrysts contain serpentine (Srp) rims. Several anhedral, medium-coarse grained sulfides (Sf) are adjacent to the olivine crystals.

6.2 Sample Description - Thick Sections

The following pages contain information about the textures and mineral assemblages in several of the fifteen polished thick sections created from the mineralized rocks of the basal Duluth Complex Cu-Ni-PGE deposits. Material was chosen for these thick sections (see table A1-a) to show the variety of sulfides and oxides in the basal Duluth Complex, along with the mineralogical and lithological relationships that can be found within the Cu-Ni PGE deposits. The descriptions are grouped based on similarity in textures and compositions seen within the polished sections, but do not include every possible sulfide/oxide texture or composition present within the basal Duluth Complex. The images shown below in figures 24 to 30 were collected using reflected light microscopes in the ore deposit laboratory at the University of Minnesota-Duluth.

Massive Sulfide

Samples SP-2b (figure 24) and KEA-1 (C') (figure 25) contain over 90% sulfide and were collected from drill core from the I deposit (KEA-1), and from exposed surface material of the Serpentine deposit (SP-2b). These samples represent a typical massive sulfide texture and as such are notable for the rarity of silicate minerals and the presence of a massive pyrrhotite groundmass. Other common sulfide minerals include pentlandite, which forms distinct channels and flame structures within the pyrrhotite groundmass, and chalcopyrite, which typically occurs as anhedral, fine to medium-sized distinct grains around magnetite/oxide inclusions. Additionally, very-fine grained chalcopyrite grains occur as "chalcopyrite disease" texture within oxide and silicate phenocrysts. Rarely, cubanite can be seen as very-fine to fine-grained crystals at the edges of chalcopyrite grains at the chalcopyrite-pyrrhotite interface. Sample SP-2b contains distinct banded oxide coatings in addition to other unique sulfide-oxide textures that formed as a result of surface weathering.

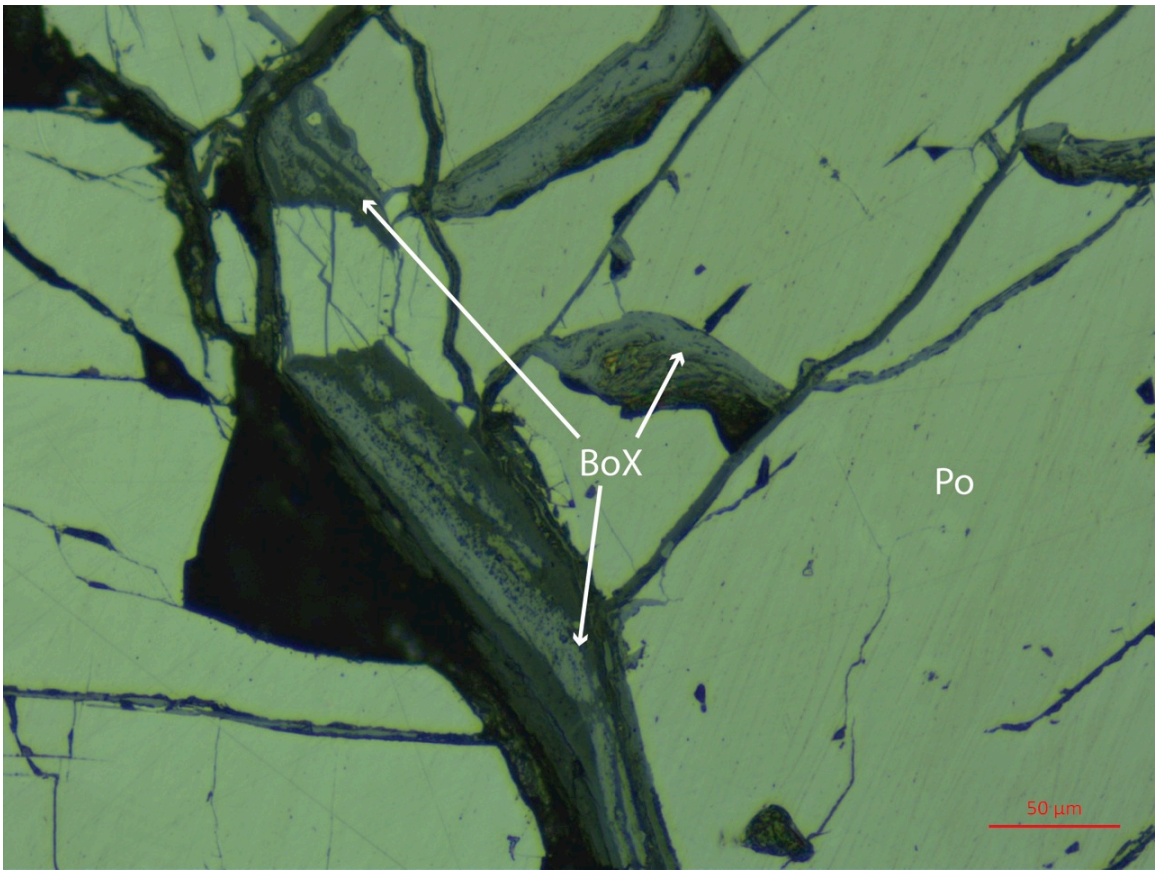

Figure 24: Reflected light image collected from sample SP-2b. This image shows banded oxide coatings (BoX) within a massive pyrrhotite (Po) groundmass.

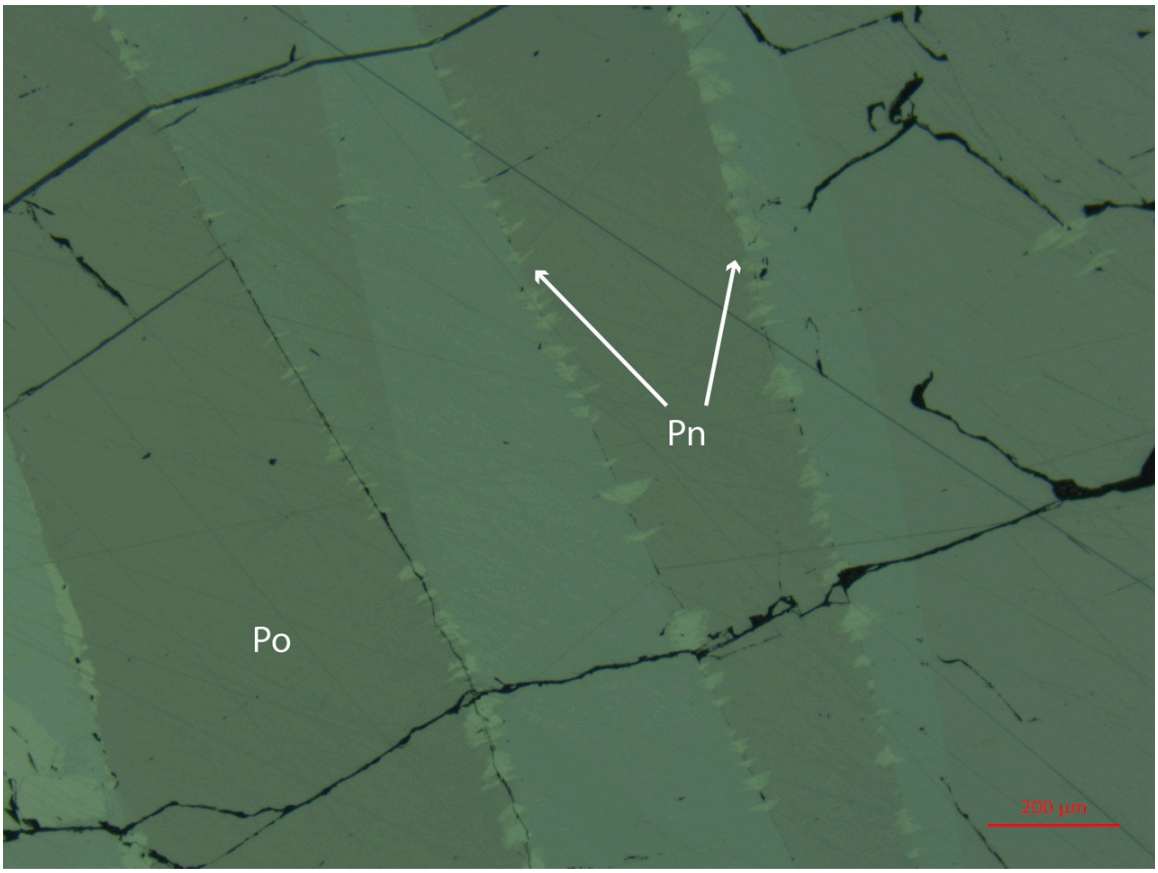

Figure 25: Reflected light images collected from sample KEA-1 (C'). This image shows pentlandite (Pn) flames forming at the edges of pyrrhotite crystals.

Semi-Massive/Globular Sulfide

Samples MB-07-07 (1106'), 10-599D, and MB-07-02b contain roughly 50-75 % sulfides and were collected from drill core from the Mesaba deposit (MB-07-07; MB-07-02b) and the Northmet deposit (10-599D). The semi-massive texture in these samples is generally defined by the presence of more than 50 % sulfide, but also a substantial amount of oxide and silicate minerals. Sample MB-07-07 (1106'; figure 26) contains two distinct textures in different halves of the polished section: massive sulfide and semi-massive sulfide, with a layer of pure sulfide (pyrrhotite) separating the two. The semi-massive assemblage is defined by globular net or web textured sulfides, including pyrrhotite, chalcopyrite and rare pentlandite, surrounding silicate minerals and spindly, needle-like oxides, possibly ilmenite. Sample 10-599D is defined by several very-coarse grained, multi-phase sulfides surrounded by fine-grained euhedral silicates and anhedral oxides. The large sulfide grains are typically composed of pyrrhotite and chalcopyrite,

but also contain minor pentlandite. Additionally, significant amounts of cubanite can be found within chalcopyrite in an exsolution texture. Finally, several locations within 10-599D contain globular magnetite exsolution into silicate phases.

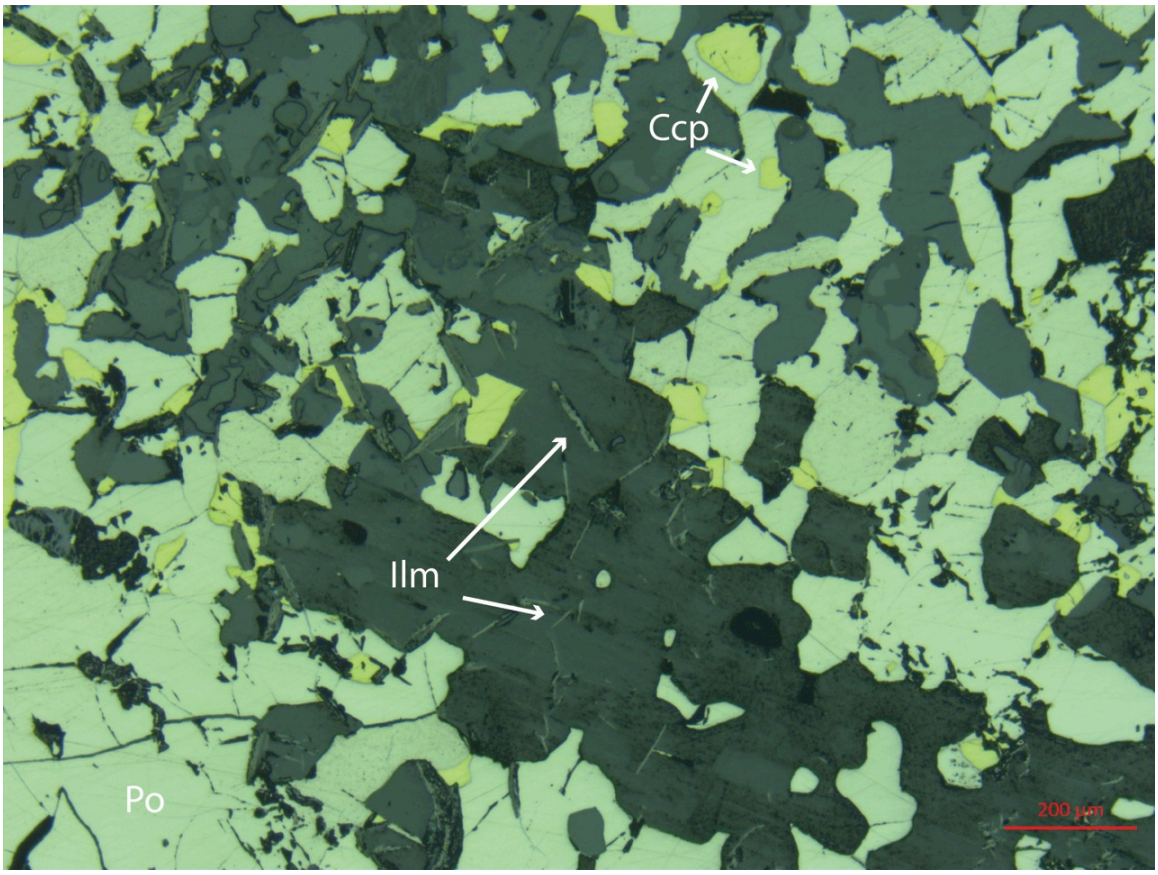

Figure 26: Reflected light image collected from sample MB-07-07 (1106'). Here sulfides surround silicate minerals in a typical web/net type texture. Sulfides present include pyrrhotite (Po), chalcopyrite (Ccp), and pentlandite (Po), which is too fine-grained to see here. Additionally, fine-grained ilmenite needles (Ilm) are present in the very center of the image.

Intergrown Sulfide

Samples MB-07-01, S4-11, and DNR-8 contain 25-40 % sulfides and were sampled from drill core in the Mesaba deposit (MB-07-01), Serpentine deposit (S4-11), and II deposit (DNR-8). Generally, these samples are defined by fine to coarse-grained sulfides in a complex, intergrown relationship with silicate and oxide minerals. Samples S4-11 (40-45 % sulfide) and MB-07-01 (25 % sulfide) exhibit a similar sulfide/silicate relationship, but differ in the amount of individual multi-phase sulfide grains. In both examples, coarse pyrrhotite/chalcopyrite aggregates surround and occasionally invade

oxides and silicates as fine-grained crystals. In sample S4-11, several of these coarse sulfides connect to form a large rim around a 1.5 mm large silicate grain. Additionally, in several locations, magnetite occurs within silicates along with fine-grained sulfides. In contrast, sample DNR-8 (figure 27) is defined by very-fine to fine-grained individual sulfide blebs that occur in a wormy web/net textured texture with silicate and oxide minerals. Unusually, sample DNR-8 is very pentlandite-rich, with major pyrrhotite and minor chalcopyrite. Commonly, pentlandite forms distinctive flames into pyrrhotite-rich crystals.

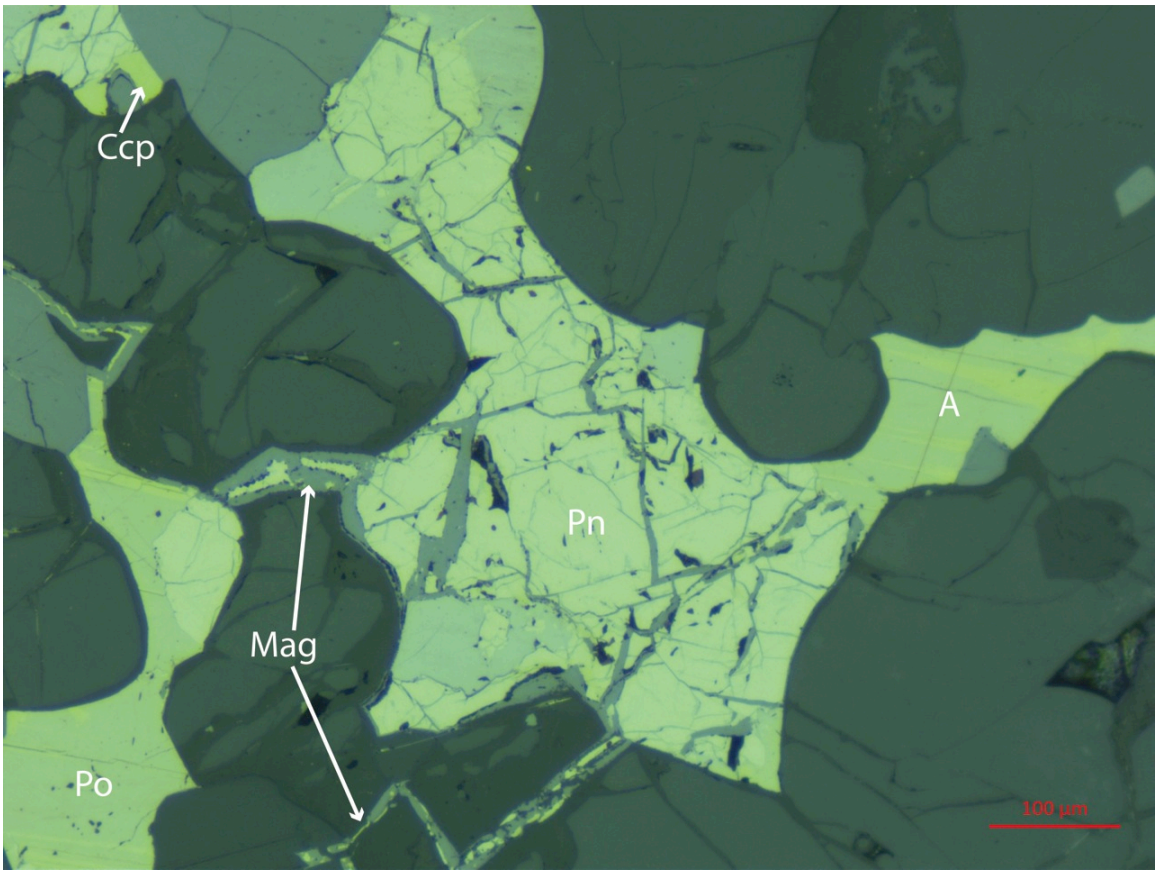

Figure 27: Reflected light image collected from sample DNR-8. This image shows a dominantly pentlandite (Pn) sulfide grain connected to several other sulfides through thin magnetite-rich veins (Mag). Other sulfides present include pyrhhotite (Po) and chalcopyrite (Ccp). Chalcopyrite occurs as distinct crystals and in exsolution inside pyrrhotite (Site A).

Disseminated Sulfide

Samples MB-07-02a, 05-420c, and DNR-6 contain 5-20% sulfide and were collected from drill core in the Mesaba deposit (MB-07-02), the Northmet deposit (05-420c), and the Wetlegs deposit (DNR-6). These polished sections are defined by typical

disseminated sulfide textures, although the exact sulfide mineralogy differs from sample to sample. Additionally, each sample contains distinctive textures that are not found within the other sections. Sample MB-07-02a (figure 28) contains a classic disseminated sulfide texture that is dominated by subhedral, very-fine to fine-grained pyrrhotite, but contains a significant amount of anhedral very-fine grained chalcopyrite that occasionally occurs in multi-phase aggregates with pyrrhotite. Oxide minerals are also common and occur as similarly sized crystals in a seemingly random relationship with sulfides. Sample 05-420c (figure 29) also exhibits by a disseminated texture, but is dominated by anhedral, fine-grained chalcopyrite along with pyrrhotite and pentlandite. Unlike the other samples, apart from KEA-1 (C'), chalcopyrite and pentlandite occur in the classic "chalcopyrite disease" texture within silicate minerals. Occasionally, chalcopyrite forms exsolution lamellae within pyrrhotite. Sample DNR-6 contains the least amount of sulfides (5%), but is also defined largely by a classic disseminated sulfide texture. Unlike the other samples, however, nearly every sulfide in DNR-6 is multi-phase, and contains several distinct minerals including bornite and cubanite. Additionally, DNR-6 contains a number of very thin sulfide veins that connect the disseminated sulfide grains.

Layered/Vein-Style Sulfides

Samples DNR-3 and DNR-10, collected from drill core in the Wyman Creek (DNR-3) and III deposits (DNR-10), contain unique textures distinct from those seen in any other polished sections. In particular, DNR-3 was sampled from a different host rock (layered Biwabik Iron Formation) than all other samples, so it is defined by a very different texture: layered sulfide and oxide. These layers alternate, and indicate a complex relationship between pyrrhotite and chalcopyrite-rich sulfides and magnetite-rich oxides during crystallization. DNR-10 (figure 30) is unique because it was sampled from a massive oxide section of drill core. The oxide assemblage is dominated by magnetite, but also includes a significant amount of ilmenite, which occurs as an exsolved phase. Sulfides are rare, and mostly occur in a single thin vein that extends completely across the polished section. Sulfides present include pyrrhotite, chalcopyrite, and pentlandite

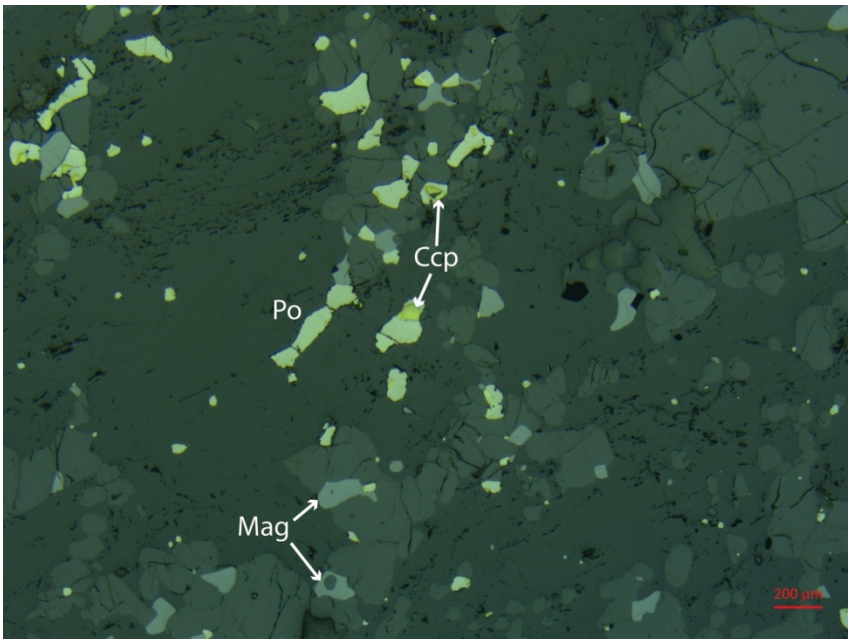

Figure 28: Reflected light image collected from sample MB-07-02a. This image contains a number of fine, well-rounded sulfides and magnetite (Mag) grains in association with numerous silicates in a typical disseminated texture. Sulfides present include pyrrhotite (Po) and chalcopyrite (Ccp).

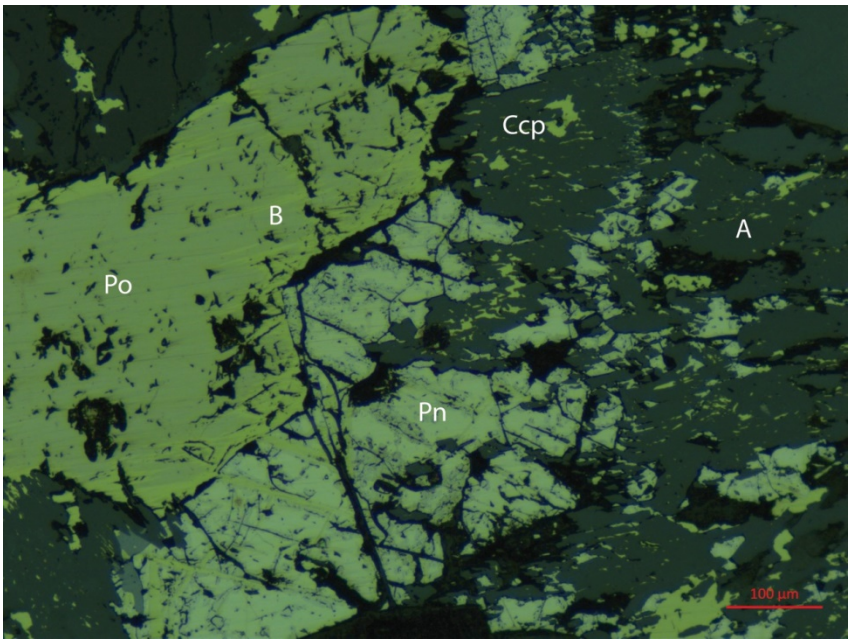

Figure 29: Reflected light images collected from sample 05-420c. Shown here are several large sulfide grains adjacent to very-fine grained chalcopyrite (Ccp) and pentlandite (Pn) in the “chalcopyrite disease” texture in the vicinity of site A and the right half of the images in general. Chalcopyrite exsolution into pyrrhotite (Po) is also visible at site B.

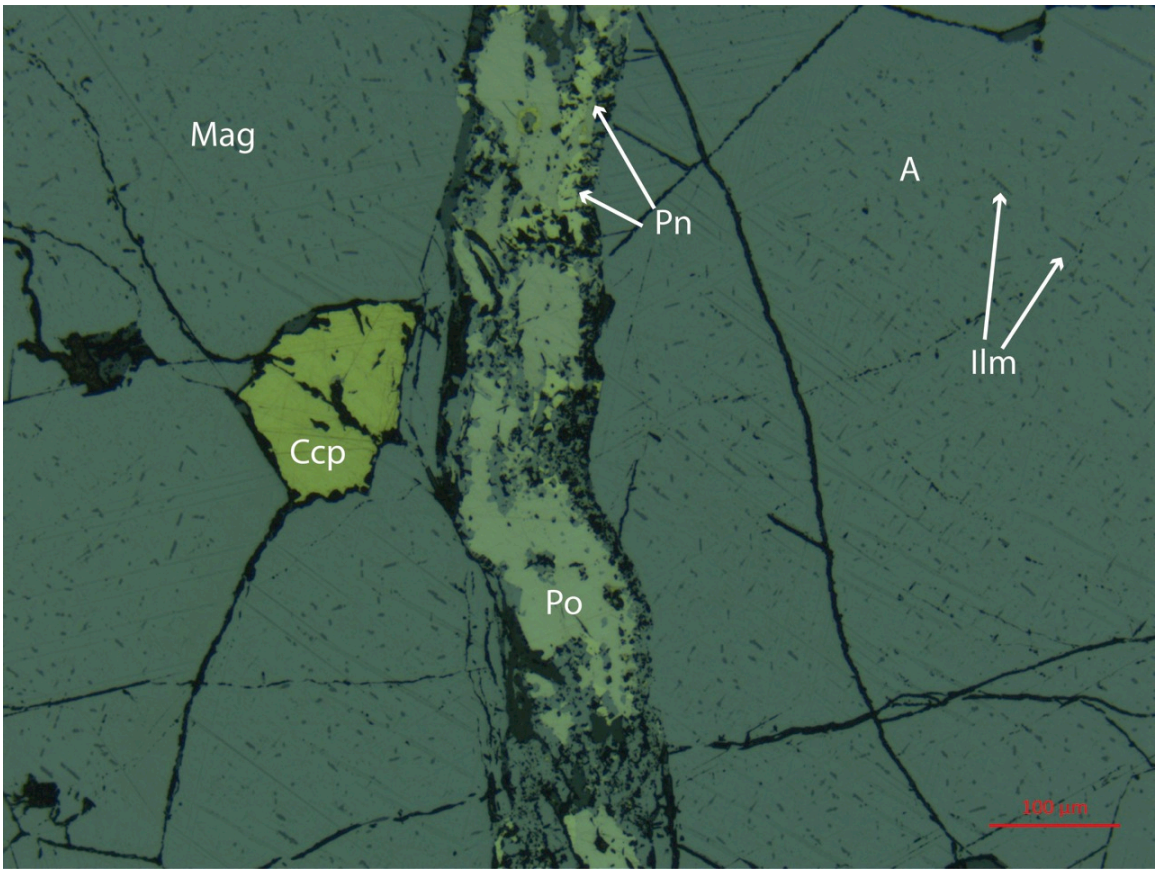

Figure 30: Reflected light image collected from sample DNR-10. This image shows a large, multi-phase sulfide and oxide vein that cuts across a massive oxide groundmass. The vein is most pyrrhotite (Po), but also contains very fine-grained, anhedral chalcopyrite (Ccp), pentlandite (Pn), and oxides. A single, relatively coarse chalcopyrite crystal can be seen in the middle-left of the image. The oxide groundmass is dominantly composed of magnetite (Mag), but also includes thin ilmenite (Ilm) needles as an exsolved phase as seen near site A.

6.3 Geochemistry

A total of 51 samples were analyzed for bulk geochemistry in two separate batches at ActLabs and the University of Western Ontario (UWO). The results of these analyses are shown in Appendix 1 in tables A2-A6. Analyses from ActLabs are in the A#-1 tables, while analyses from UWO are in the A#-2 tables. Elements at or near the detection limit are excluded. Whole rock geochemistry was obtained for major elements using inductively coupled plasma optical emission spectrometry (ICP-OES) and minor and trace elements using inductively coupled plasma mass spectrometry (ICP-MS). Transition metal data were obtained using total digestion inductively coupled plasma

optical emission spectrometry (TD-ICP). Gold and trace metals were analyzed using instrumental neutron activation analysis (INAA).

Rare earth element (REE) data are shown graphically below in Appendix 1 in figures A1 to A4 using the characteristic “spider diagram” method utilized by Rollinson (1993). The values are normalized to a chondrite standard published by McDonough and Sun (1995). Figure A1 shows the REE pattern for glacial till samples, followed by the REE pattern for surface outcrop samples (figure A2), and the REE pattern for drill core samples (figures A3, A4). The drill core samples are broken up based on relative europium enrichment or depletion.

A total of eleven samples, originally analyzed for bulk geochemistry, were also analyzed by ActLabs for platinum and palladium. This analysis was conducted using fire assay inductively coupled plasma optical emission spectrometry (FA-MS). The assay data are shown below in table A7, along with assay data for gold and silver produced during the initial bulk geochemical analysis.

6.4 X-Ray Diffraction

X-ray diffraction analysis was performed on 11 samples to identify the secondary oxide minerals in the weathered surface material collected. An analysis of x-ray spectra using the JADE analytical package identified typical gabbroic minerals along with a several sulfides, but was unable to determine the identity of any secondary oxide or hydroxide phases. Thus, XRD data will not be used in the discussion of results. The XRD raw data and spectra are available in the supplementary data file.

6.5 SEM

An analysis of two thin sections and four polished thick sections took place at the Research and Instrumentation Laboratory at the University of Minnesota-Duluth using a JEOL JSM-G490LV scanning electron microscope. The selection of these six samples was done using transmitted and reflected light microscopy. This helped determine the approximate olivine, clinopyroxene and nickel-sulfide content of each section. The primary goal of the SEM analysis was to collect high-resolution, backscatter detector images of olivine/clinopyroxene and sulfide textures and relationships in basal Duluth Complex mineralized samples to supplement the results of transmitted and reflected light microscopy. Additionally, EDS, element map, and line scan data were collected for olivine and clinopyroxene to establish which of the six samples would be analyzed in greater detail at the microprobe lab at the University of Minnesota-Twin Cities. Specifically, each sample was examined for locations where olivine is in close proximity to nickel sulfide; at these sites, EDS spectra were obtained to determine whether or not nickel could be identified above the detection limit within olivine. Additional EDS spectra were also collected for secondary silicate and iron oxide phases to determine whether or not nickel could be found in veins and fractures within the samples. Backscatter detector images can be seen below in figures 31 and 34 to 36. Element maps and a line scan with element count spectra can be seen in figures 32 and figure 33. Quantitative EDS data from spectra sites below can be seen in Appendix 1 (table A10). Additional images, line scans, element maps, spectra, and quantitative EDS data can be found in Appendix 2 and the supplementary data file.

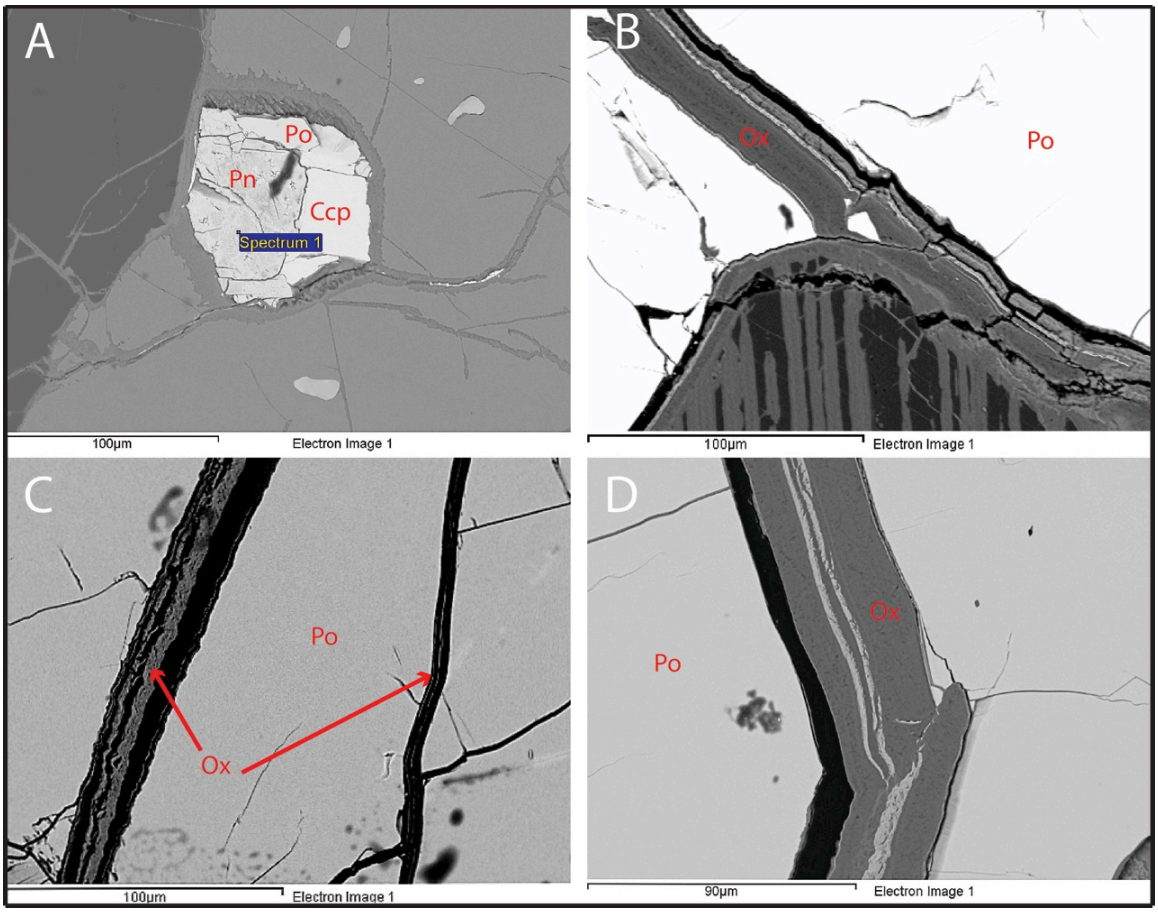

Figure 31: Thick section sample SP-2b. Image 31-A shows a multi-phase sulfide grain composed of pyrrhotite (Po), pentlandite (Pn), and chalcopyrite (Ccp) surrounded by a secondary silicate coating. Image 31-B shows two large pyrrhotite grains with a layer of secondary oxide (Ox) and sulfide between them. Images 31-C and 31-D also show secondary oxide that formed in a fracture between sulfide grains. The quantitative data for the spectrum in Image 31-A is shown below in Appendix 1 (table A10).

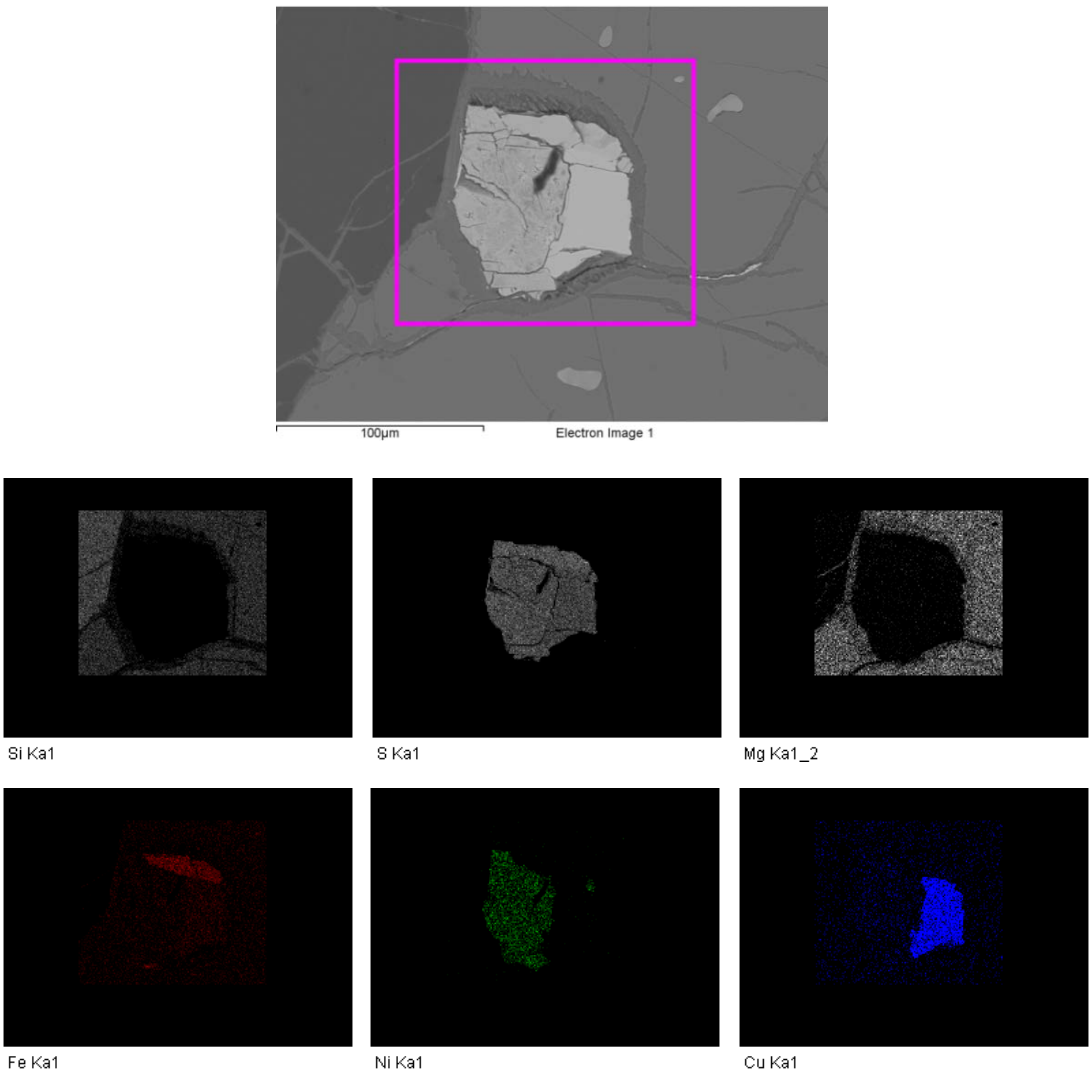

Figure 32: SEM/EDS element maps showing concentrations of Si, S, Mg, Fe, Ni, Cu in the multi-phase sulfide grain shown above in Figure 31-A. The area of analysis is indicated above highlighted by the pink box.

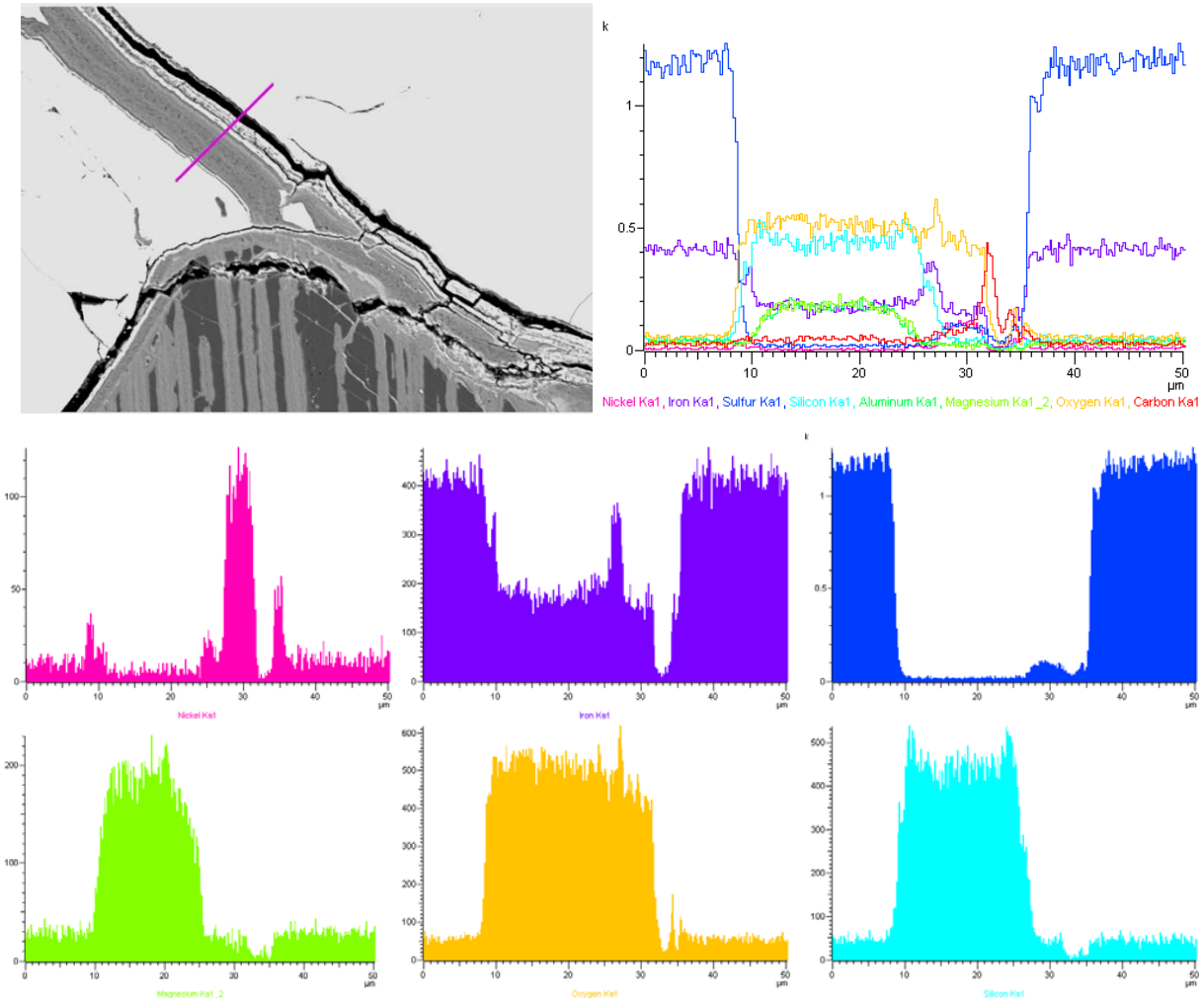

Figure 33: Line scan data for the secondary oxide coating shown above in Figure 31-B. The element count spectra include nickel (pink), iron (purple), sulfur (blue), magnesium (green), oxygen (yellow), and silicon (light blue). Not shown are aluminum and carbon.

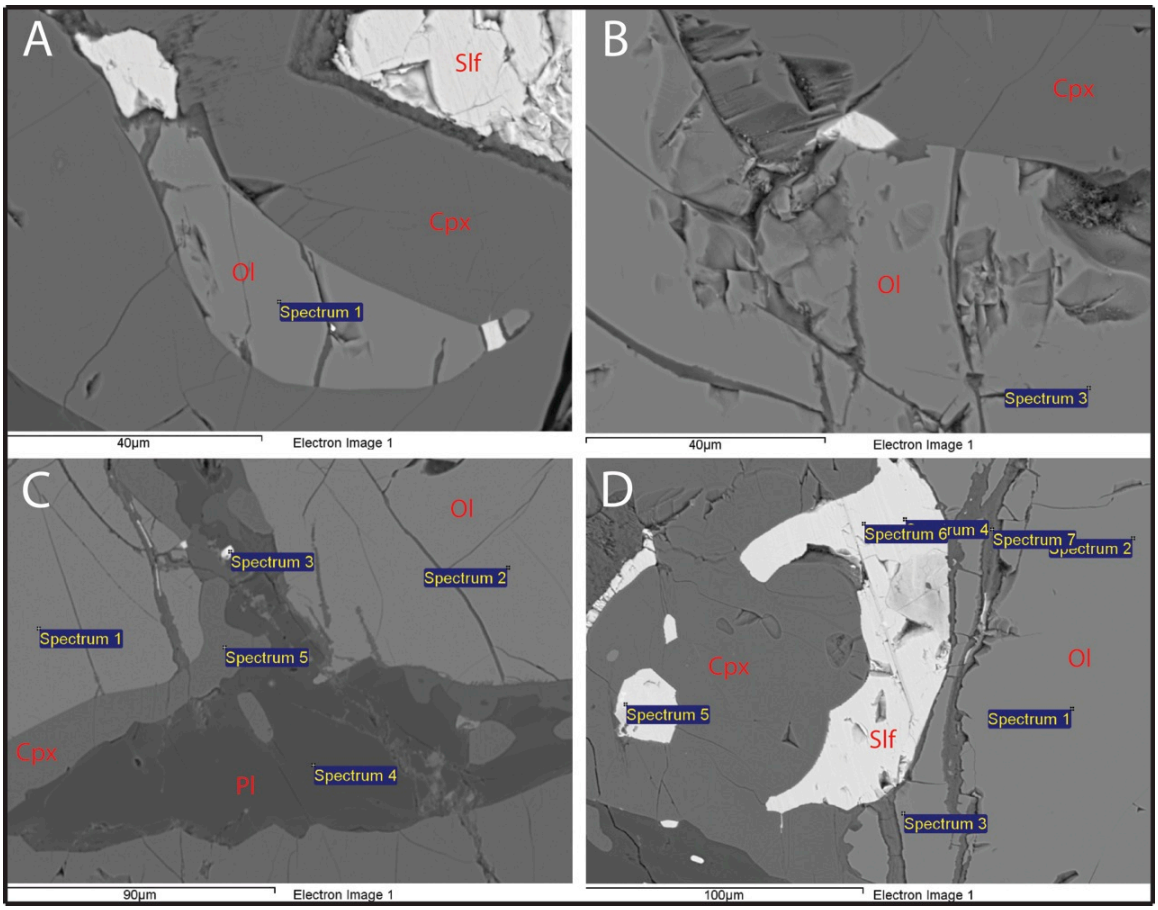

Figure 34: Thin section sample TCK-1c. Images 34-A and 34-B show olivine (Ol), clinopyroxene (Cpx) and sulfide (Slf) along with the location where a spectrum was collected. Image 34-C shows several silicates in a complex, intergrown texture including olivine, clinopyroxene, and plagioclase feldspar (Pl), along with small sulfide grains and spectra collection sites. Image 34-D shows olivine and clinopyroxene in close proximity to a sulfide grain, along with spectra collection sites. Spectra information can be found below in Appendix 1 (table A10)

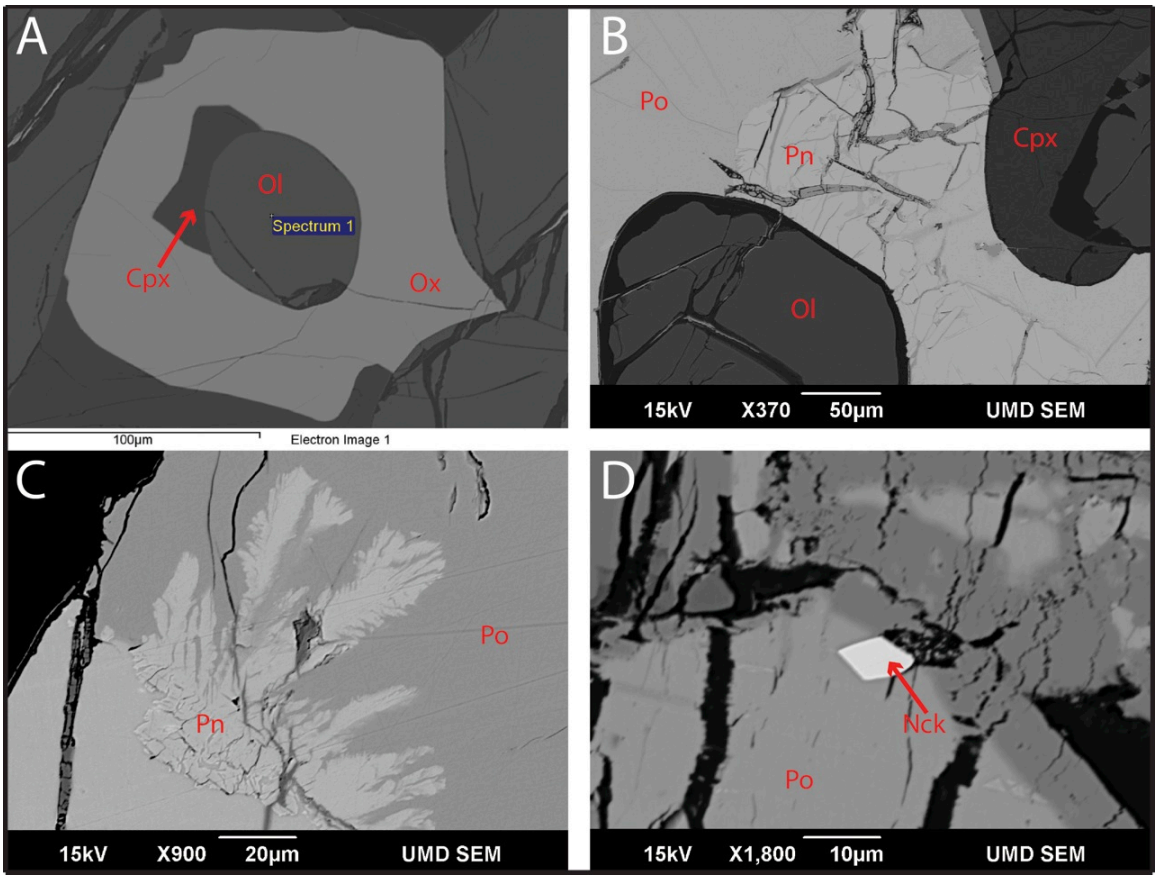

Figure 35: Thick section sample DNR-8. Image 35-A shows a well-rounded olivine (Ol) completely surrounded by oxide (Ox) and a small, anhedral clinopyroxene (Cpx) grain. Image 35-B shows pentlandite (Pn) in a channel-like structure between olivine and clinopyroxene. Image 35-C shows characteristic pentlandite "flames" extending outwards into a pyrrhotite (Po) groundmass. Image 35-D shows a small, euhedral nickeline (Nck) crystal at the edge of massive pyrrhotite. Spectrum information for Image 35-A can be found below in Appendix 1 (table A10).

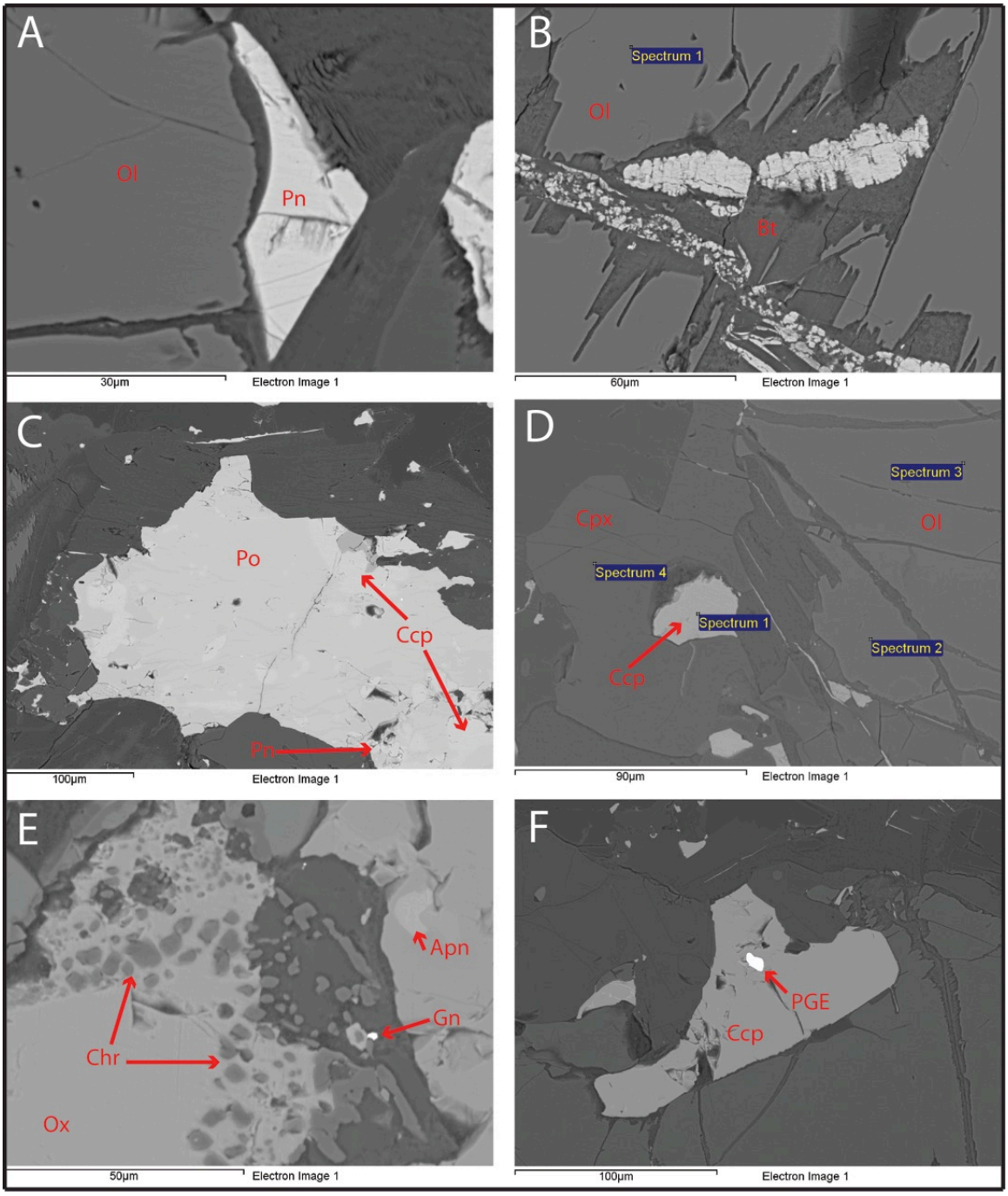

Figure 36: Thin section sample MB-07-07 (390'). Image 36-A shows a euhedral pentlandite (Pn) grain in close proximity to olivine (Ol). Image 36-B shows jagged olivine crystals next to biotite (Bt) and rounded, vein-hosted, sulfides. Image 36-C shows a large, multi-phase sulfide grain containing pyrrhotite (Po), pentlandite, and chalcopyrite (Ccp). Image 36-D shows olivine and clinopyroxene (Cpx) adjacent to chalcopyrite and thin sulfide stringers. Image 36-E shows rounded, fine-grained chromite (Chr) inside of oxide (Ox) along with a small galena (Gn) crystal and a rounded, heart-shaped argentopentlandite (Apnt) crystal. Image 36-F shows a small PGE grain inside chalcopyrite. Spectra information for images 36-B and 36-D can be found below in Appendix 1 (table A10).

6.6 Microprobe

Four thin sections and four polished thick sections were chosen for scanning electron microprobe analysis during two visits to the microprobe lab at the University of Minnesota-Twin Cities in the summer and fall of 2015. As stated above, these samples were chosen based on the data obtained from the SEM at the University of Minnesota-Duluth. During the first visit, samples were analyzed using two methods: spot analyses and wavescans. Spot analyses were used to examine olivine, clinopyroxene, and sulfides, specifically pentlandite. Olivine crystals were examined for their nickel, iron, and magnesium contents to calculate magnesium numbers average nickel contents. Using the same ideas described above in the SEM section, locations where olivine or clinopyroxene were in close proximity to pentlandite were examined to establish whether or not significant differences in nickel content could be detected between the edge and the core of these silicate phases. This was done using spot analyses that were measured at evenly-spaced intervals extending from the edge of a crystal to its center. Images and data from the spot analyses can be seen below in figures 37 to 39 and tables 5 to 7. Entire-spectrum wavescans were used to identify several unknown minerals in a few sections; this data can be seen below in Appendix 2 in tables A26-A29. Additional images and spot analyses can be seen below in Appendix 1 and Appendix 2.

The second visit to the U of M-Twin Cities was necessary because certain microprobe functions, notably the EDS detector, were not functioning during the first visit. After examining the data collected during the first visit, it was decided that additional data using the EDS detector, along with line scans and element maps, would help to further define the silicate-sulfide relationships within the samples. An example of the element mapping function can be seen below in figure 40. Additional line scans and element maps can be accessed below in Appendix 2.

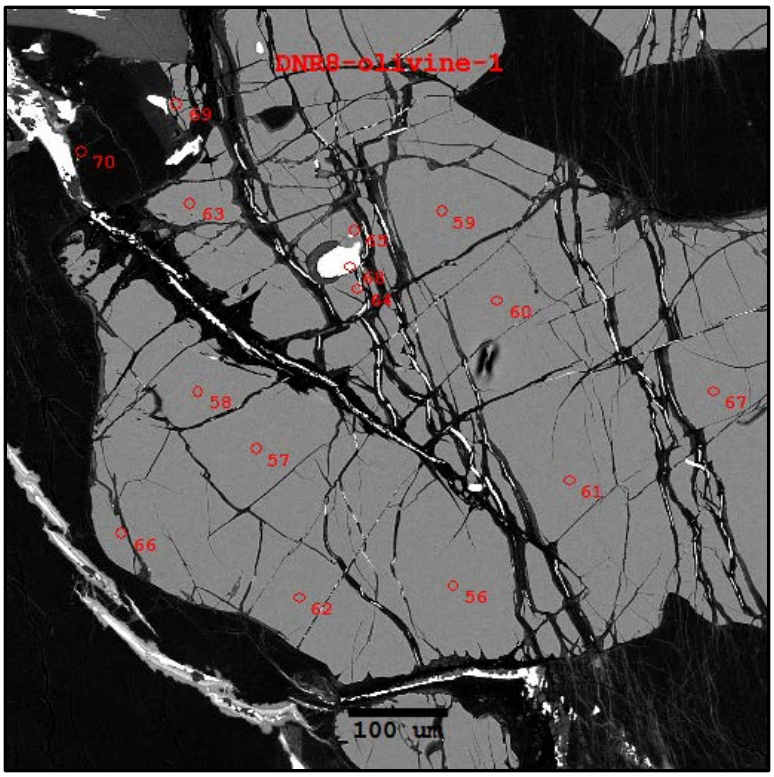

Figure 37: Olivine from sample DNR-8. Red dots correspond to numbers below in table 10.

Table 5: Quantitative data from an olivine crystal in sample DNR-8. Analysis numbers 68, 69, 70 are excluded because they did not measure olivine. MnO was not standardized and included in the analytical package for this particular suite of measurements. It is included in subsequent data sets. Values are given in weight percent by oxide.

Analysis	SiO_2	FeO	NiO	MnO	MgO	Total
56	36.32	31.15	0.20	N/A	31.10	98.77
57	36.25	30.90	0.18	N/A	30.97	98.30
58	36.22	30.97	0.19	N/A	31.07	98.45
59	36.24	30.89	0.20	N/A	31.15	98.47
60	36.20	30.89	0.19	N/A	31.21	98.49
61	36.14	30.98	0.18	N/A	31.09	98.39
62	36.16	30.85	0.18	N/A	31.06	98.26
63	36.25	30.85	0.18	N/A	31.09	98.37
64	36.26	31.00	0.19	N/A	31.09	98.55
65	36.37	31.02	0.18	N/A	31.17	98.73
66	36.20	30.43	0.19	N/A	31.16	97.99
67	36.29	30.94	0.18	N/A	31.13	98.54

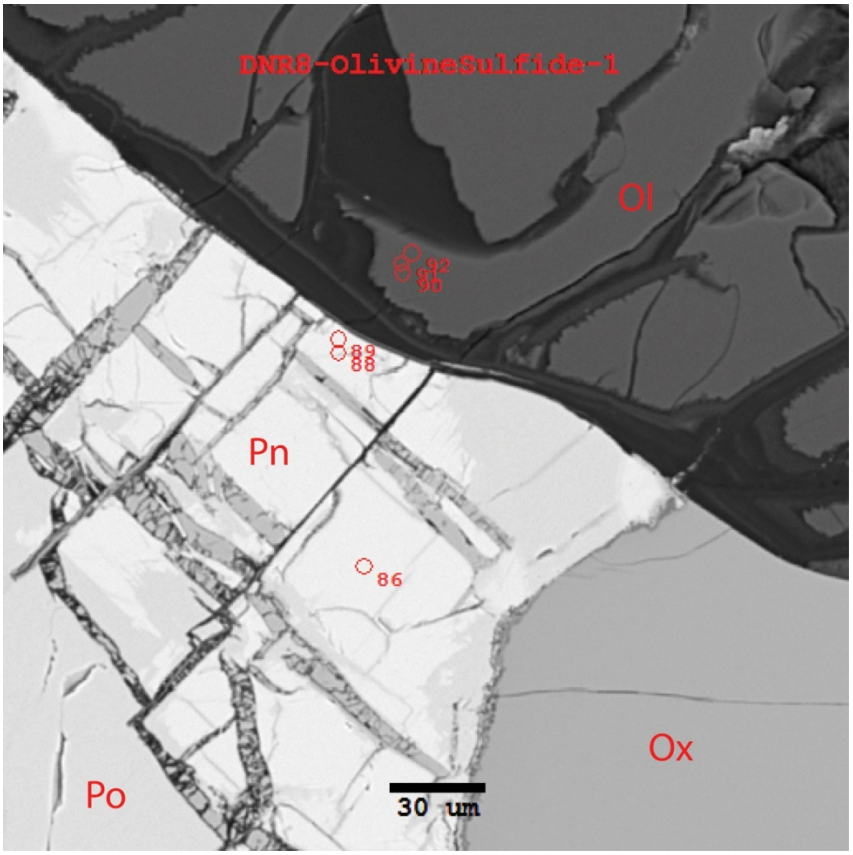

Figure 38: Olivine (Ol) and pentlandite (Pn) from sample DNR-8. Also visible are pyrrhotite (Po) and oxide (Ox). Red dots correspond to numbers below in table 6-A and 6-B.

Table 6A: Quantitative data from pentlandite in sample DNR-8. Values are given in weight percent by element. Analysis numbers 87 and 89 are excluded due to analytical error.

Spot	Zn	Pb	Fe	Co	Ni	Cu	S	Total
86	0.00	0.11	31.15	1.95	34.09	0.05	31.97	99.32
88	0.03	0.19	32.50	1.51	33.87	0.03	30.63	98.77

Table 6B: Quantitative data from an olivine crystal in sample DNR-8. Values are given in weight percent by oxide.

Spot	SiO2	FeO	NiO	MnO	MgO	Total
90	37.40	29.30	0.27	0.38	32.29	99.64
91	37.33	28.87	0.25	0.37	32.05	98.88
92	37.23	29.90	0.24	0.38	31.91	99.66

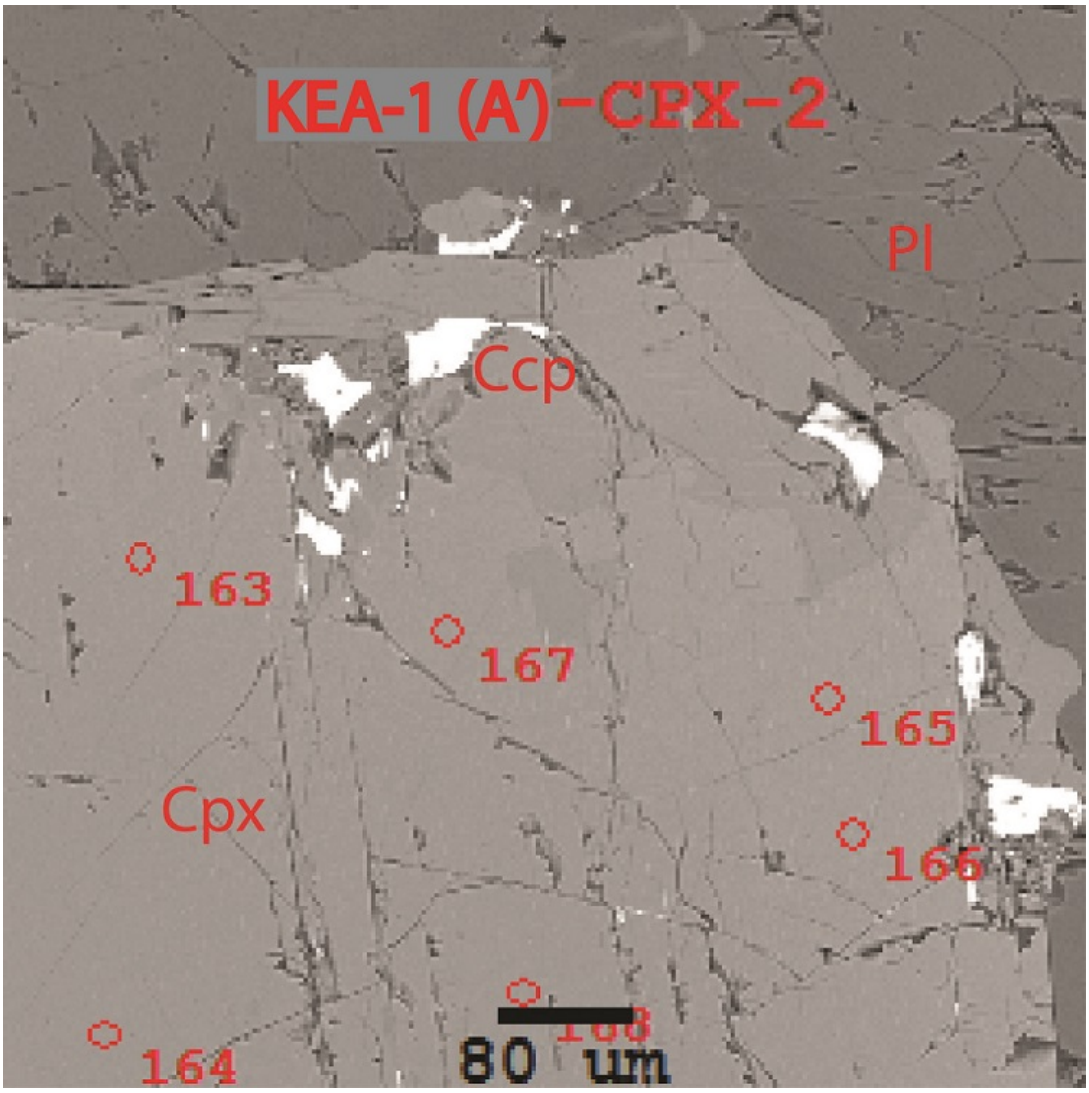

Figure 39: Clinopyroxene (Cpx) from sample KEA-1 (A'). Also shown are plagioclase feldspar (Pl) and chalcopyrite (Ccp). Red dots correspond to data below in Table 7.

Table 7: Quantitative data from clinopyroxene in sample KEA-1 (A'). Values are given in weight percent by oxide. Analysis 163 is likely from a different phase due to its lower magnesium oxide content and higher aluminum oxide and silicon dioxide contents.

Spot	SiO2	TiO2	Al2O3	FeO	NiO	MgO	CaO	Na2O	Total
163	52.14	0.30	1.75	19.13	0.07	20.85	2.00	0.14	96.38
164	51.19	0.32	1.39	19.29	0.07	23.85	2.00	0.02	98.12
165	51.12	0.60	1.02	21.87	0.06	22.36	1.83	0.02	98.88
166	50.57	0.68	1.06	21.42	0.08	22.28	2.06	0.02	98.18
167	51.77	0.29	1.14	20.55	0.04	22.79	2.09	0.04	98.71
168	50.19	0.71	1.16	20.07	0.07	23.70	1.93	0.06	97.89

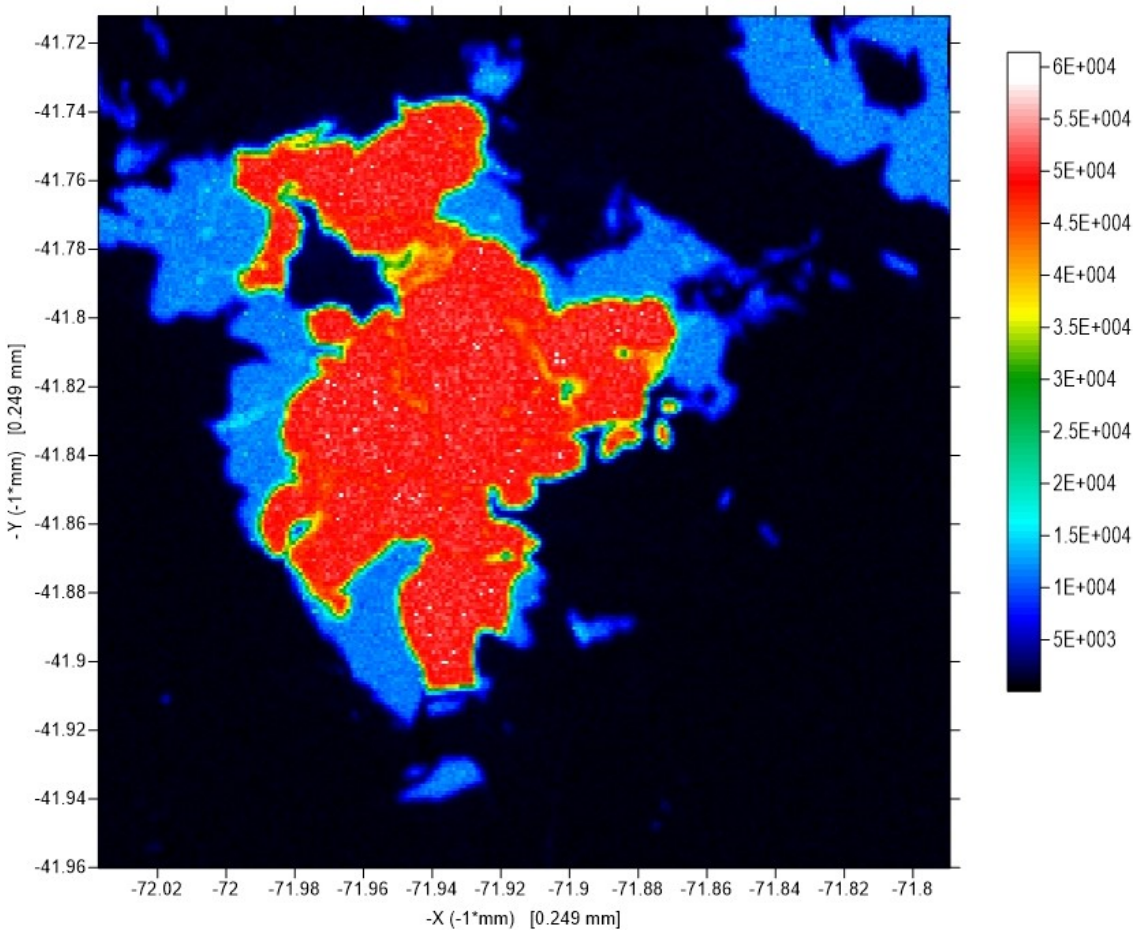

Figure 40: Microprobe element map showing Ni in a multi-phase sulfide grain from polished section sample KEA-1 (C'). The color scale at right shows the number of counts of Ni per pixel that were seen using the mapping feature on the U of M microprobe. Additional element maps can be seen below in Appendix 2 in figures A17-A21.

6.7 Ni and Cu Isotopes

6.7.1 Nickel

$\delta^{60/58}$Ni values were measured in the SESAME lab at the University of Indiana-Bloomington. Isotopic values were statistically measured against the NIST SRM 968 standard and are reported here in the typical delta notation with error bars between 0.06 and 0.18 ‰.

The 25 data points have an overall range of 1.2 ‰, with a minimum value of -0.97 ‰, a maximum value of 1.55 ‰, and an overall average value of -0.23 ‰ (figure 41). The value of sample StE-1, 1.55 ‰, is a significant outlier by several orders of

magnitude due to extreme mineralogical and geological differences between that sample and typical basal Duluth Complex material. If StE-1 is excluded, the adjusted maximum value is 0.22 ‰, while the overall average value changes to -0.3 ‰ (n=24). A much more detailed analysis of the Ni isotopic data can be found in the discussion section.

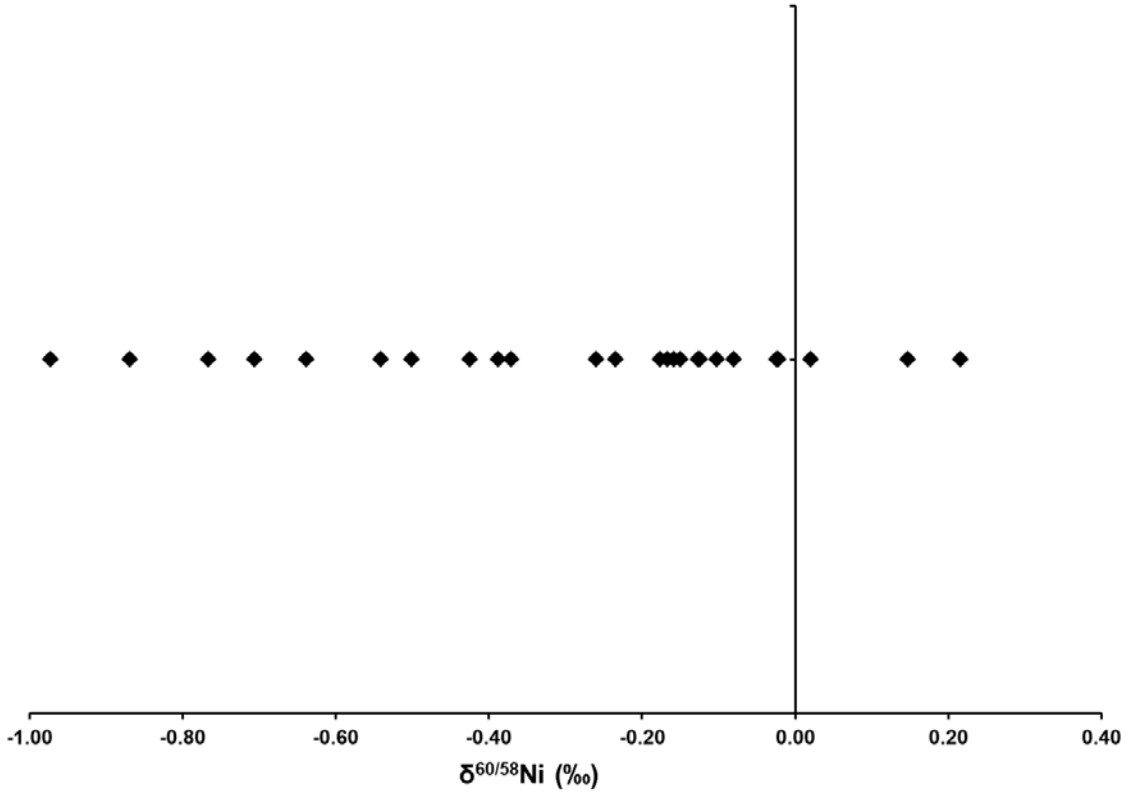

Figure 41: $\delta^{60/58}$Ni values from 24 samples; not shown is the value from StE-1 (1.55 ‰).

6.7.2 Copper

$\delta^{65/63}$Cu values were measured in the Yale Metal Geochemistry Center at Yale University. Cu isotopes were measured against the NIST SRM 3114 Cu standard and are reported here in the typical delta notation with average error bars of ± 0.1 ‰. The 28 data points have an overall range of 2.63 ‰, with a minimum value of -1.28 ‰, a maximum value of 1.36 ‰, and an average of -0.20 ‰ (figure 42).

Unlike the $\delta^{60/58}$Ni values, where 24 of the 25 values were measured from Duluth Complex samples, six of the 28 $\delta^{65/63}$Cu values were measured from material sourced from very different bedrock and ore deposit types. Excluding the values from exotic, non-Duluth Complex material, the overall range is 1.64 ‰, with the same minimum value (-

1.28 ‰), a maximum value of 0.36 ‰, and an average of -0.35 ‰ (n=23). These values will be interpreted in the discussion section below.

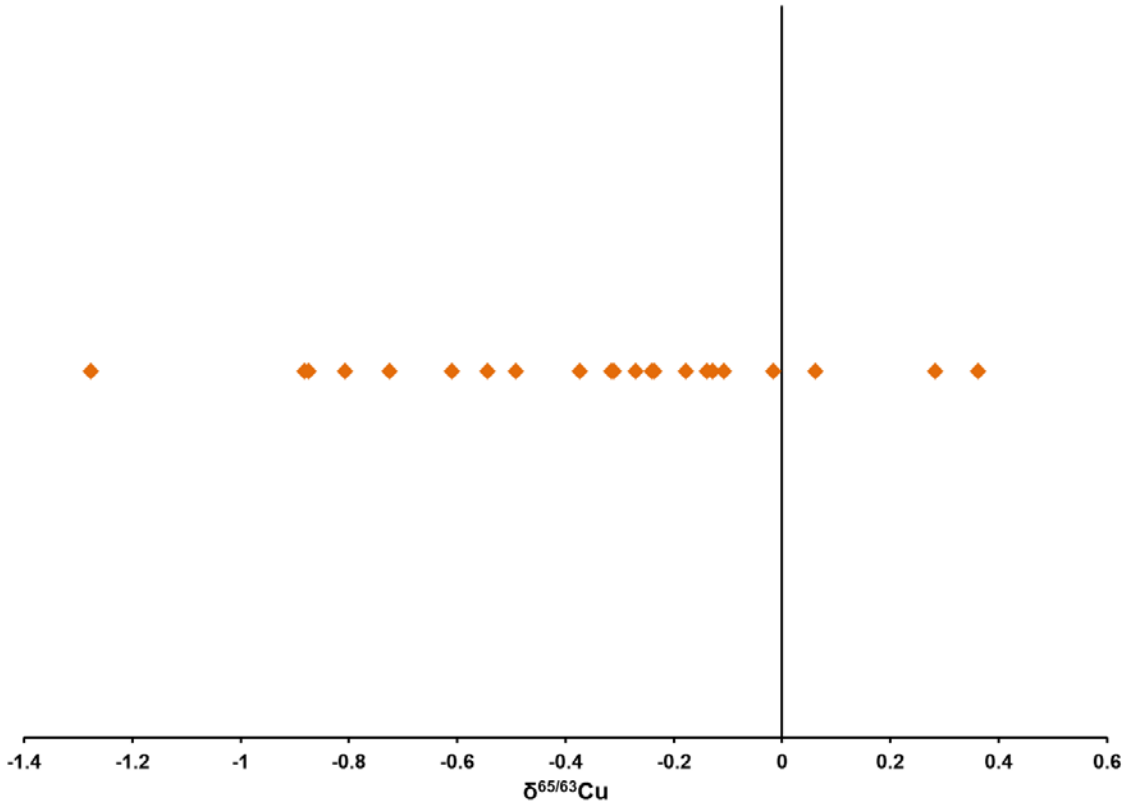

Figure 42: $\delta^{65/63}$Cu values from the 22 Duluth Complex samples. The six values measured from other samples can be seen in table A9 in Appendix 1.

7. Discussion

The basal intrusions of the Duluth Complex and its associated Cu-Ni-PGE mineralization have been studied using whole rock and isotope geochemistry, petrography, reflected light microscopy, and other analytical techniques. The results will be discussed with a focus on the fractionation of Ni and Cu isotopes in basal Duluth Complex material as a function of sample type, mineralogy, and other variables. These findings will be put into the context of the controlling processes that likely govern the fractionation of nickel and copper in both high and low-temperature environments.

7.1 Nickel Isotopes

Ni isotopic values obtained from Duluth Complex material show a total spread of 1.19 ‰, with a minimum value of -0.97 ‰, a maximum value of 0.22 ‰, and an overall average of -0.3 ‰ in the 25 measured samples (see figure 41). Grouping the values based on their sample type and mineralogy reveals significant differences between sulfide-bearing samples, sulfide-barren “olivine” samples, and highly weathered, secondary oxide-rich samples (figure 43). The nine samples containing sulfides are isotopically light, with a minimum value of -0.97 ‰, a maximum value of 0.15 ‰, and an overall average of -0.38 ‰. In contrast, the five sulfide-barren “olivine” samples are near the bulk silicate earth range (BSE; 0 to 0.1 ‰; Gueguen et al., 2013), with a minimum of -0.15 ‰, a maximum of 0.22 ‰, and an average of -0.03 ‰. Finally, the five secondary oxide-rich samples are also isotopically light, with a minimum value of -0.87 ‰, a maximum value of -0.23 ‰, and an average of -0.50 ‰.

Based on these data, it is clear that sample material from the basal Duluth Complex with different mineral assemblages have different Ni isotopic values. Specifically, samples rich in sulfides and secondary oxides are isotopically light, while sulfide-barren “olivine” samples show values comparable to bulk silicate earth signatures. Based on these observed trends, it is speculated that two or more fractionation processes led to these distinctly different isotopic signatures and probably correspond to different stages in the evolution of Cu-Ni-PGE mineralization in the Duluth Complex: a high-temperature fractionation during the initial crystallization of the host rock and formation of the sulfides, and a low-temperature fractionation during the

surficial weathering and alteration of exposed material. These two mechanisms will be evaluated below.

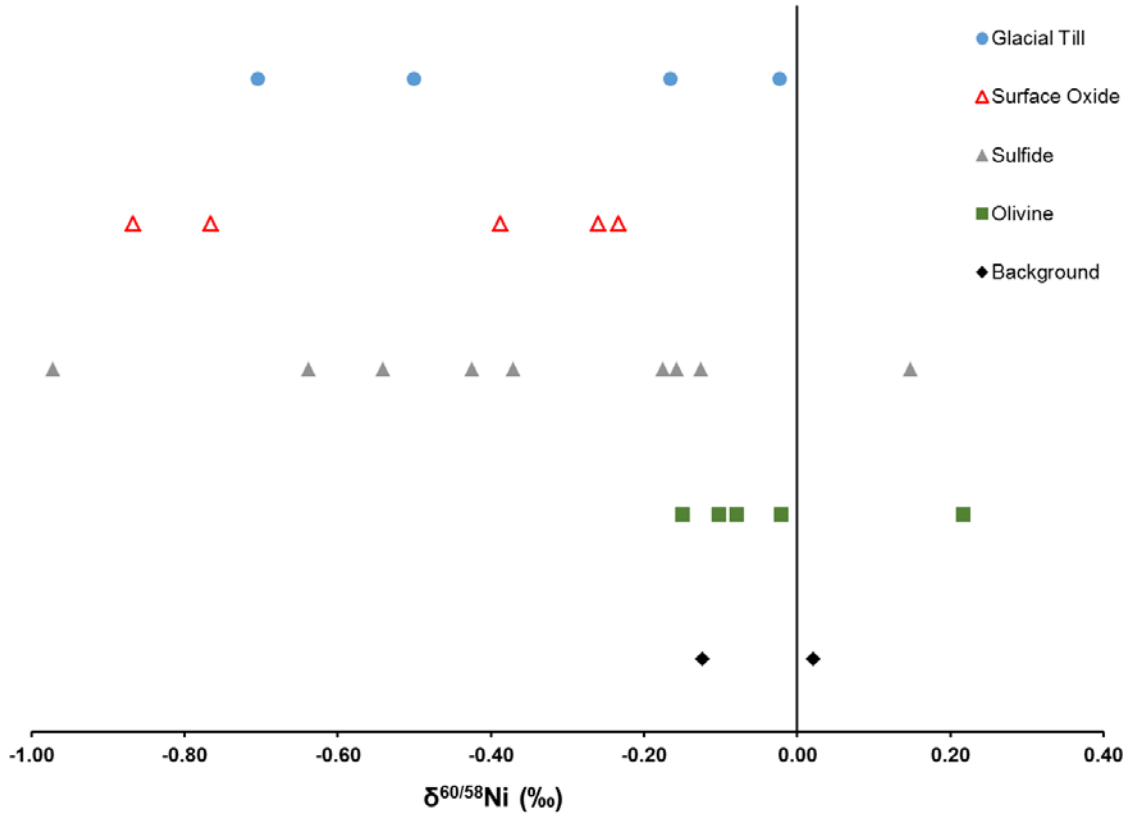

Figure 43: $\delta^{60/58}$Ni values for 25 samples divided based on mineralogy and sample type. 'Background' values were collected from O1-C (Archean greenstone, Newton Belt) and O12 (unmineralized silicate-rich weathered material).

7.2 Primary Fractionation

To gain a better understanding of the $\delta^{60/58}$Ni isotope results, it is necessary to discuss the geochemical processes that control the distribution of nickel-bearing minerals in Duluth Complex rocks. In the collected material, there are three main sources of nickel: silicate, sulfide, and primary/secondary oxides.

7.2.1 Comparison to Published Data

A number of other studies have used $\delta^{60/58}$Ni values to examine a variety of terrestrial materials, ranging from komatiite-hosted nickel sulfide deposits to ferromanganese crusts and manganese nodules. Hofmann et al. (2014) observed that

komatiite-hosted nickel deposits in Zimbabwe show $\delta^{60/58}$Ni values from -0.47 to -0.28 ‰. This narrow spread is interpreted to be a direct result of the sample material chosen for analysis, which was massive or net-textured nickel sulfide ore containing between 8.72 and 23.83 weight percent nickel. Another study by Hiebert et al. (2014) observed a much larger fractionation in 2.7 Ga komatiite-hosted nickel ore in the Hart deposit within the Abitibi greenstone belt. Unlike the Hofmann study, Hiebert et al. (2014) measured Ni isotope values in a greater variety of sample material, including sulfide-barren komatiite, disseminated sulfide, and semi-massive/massive sulfide. The sulfide-barren material ranges from -0.10 to 0.15 ‰, while the disseminated and semi-massive/massive material showed values between -1.06 and 0.12 ‰. Based on the analysis of Ni and S content, Hiebert et al. (2014) concluded that the light isotope of Ni was preferentially incorporated into sulfide liquid from the komatiitic magma, while the sulfide-barren komatiite retained a value more consistent with the bulk silicate earth due to the extremely high overall nickel content of the melt.

Apart from the recent work by Hiebert et al. (2014) and Hofmann et al. (2014), the study by Gueguen et al. (2013) was instrumental in demonstrating the likelihood of a primary, initial fractionation in igneous rocks by measuring Ni isotopes in a wide variety of terrestrial materials (see figure 8). In addition to measuring sulfide-rich and sulfide-barren komatiites, Gueguen et al. (2013) also measured serpentinite, dunite, peridotite, olivine crystals, and basalt. The sulfide-rich komatiite showed similar values to Hiebert et al. (2014) and Hofmann et al. (2014), but other materials all had $\delta^{60/58}$Ni between -0.15 and 0.25 ‰, suggesting a Ni silicate-rich melt rather than the Ni sulfide-rich melt in the komatiite. Ni isotope data obtained from this project show broad agreement with those measured by Gueguen et al. (2013), Hiebert et al. (2014), and Hofmann et al. (2014), as shown below in figure 44.

7.2.2 Nickel in Silicate

During the initial crystallization stages of basaltic magma chambers, it is widely accepted that the first phase to crystallize is olivine. Due to the simple structure of olivine and the presence of both Mg^{2+} and Fe^{2+} cations, a small amount of Ni^{2+} is included in the M1 and M2 sites of the crystal lattice (Henderson et al., 2001). Typically, olivine in ultramafic rocks (dunite, peridotite) has a slightly higher Ni concentration than olivine in mafic basalts and gabbros, with values up to 1.4 wt % NiO reported in the ultramafic Kevitsa intrusion (Yang et al., 2014).

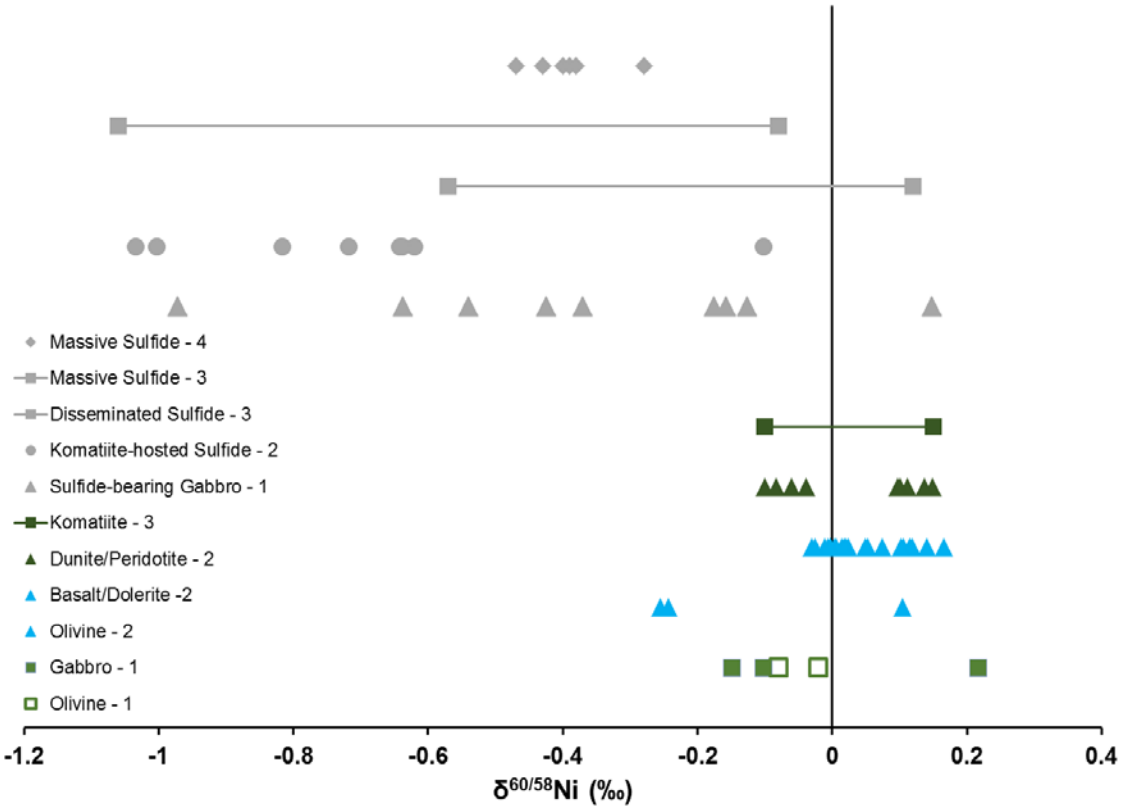

Figure 44: $\delta^{60/58}$Ni values from this study (Olivine/Gabbro, Sulfide) compared to published data. **1**: Values measured during this study **2**: Gueguen et al., 2013. **3**: Hiebert et al., 2014. **4**: Hofmann et al., 2014.

Olivine in typical layered mafic intrusions contains between 0.1 wt % and 0.2 wt % NiO, but occasionally up to 0.3 wt % (Li et al., 2003; Sobolev et al., 2007). In the Duluth Complex, olivine has been previously analyzed via microprobe by White (2010). Along with data obtained during this study, a dataset of over 2000 individual analyses display an average value of 0.14 wt% NiO, with a maximum value of 0.43 wt% and a minumum value of 0.002 wt% (Hauck, 2015; Peterson, 2015; figure 45). The data suggest a strong positive correlation between Mg # and NiO (wt. %), indicating the possibility of early, Mg-rich olivine incorporating more NiO, while late, Fe-rich olivine contains less NiO.

Apart from the data in figure 45, a significant amount of experimental work has been done to calculate the partition coefficient (K_D) for Ni between olivine and silicate melt at varying temperature and pressure conditions. Originally measured by Hart and Davis (1978) and Takahashi (1978), K_D values vary significantly from study to study, largely due to differences experimental designs and the starting compositions of the

sample material. Ultimately, the amount of interaction, including the exchange of Ni^{2+} between olivine and the silicate melt, depends on the starting composition of the liquid, especially the MgO content, and the temperature and pressure conditions (Takahashi 1978; Kinzler et al., 1990; Filiberto et al., 2009; Li and Ripley, 2010; Matzen et al., 2013).This suggests that ultramafic and komatiitic olivines would have higher average NiO contents than olivines from mafic basalts and gabbros. This has been proposed by Matzen et al. (2013), who note that when a deep-sourced partial melt from a peridotitic mantle source is transported to near-surface temperature and pressure conditions, the first olivines to crystallize have elevated NiO contents, while later olivines that formed at lower temperatures are relatively enriched in FeO.This result is corroborated by Filiberto et al. (2009), who also noticed that increasing the Ni content of their experimental melt, based on a predicted lunar composition, increases the olivine stability field, allowing a longer reaction time between the olivine phenocrysts and the liquid. This finding was confirmed by electron microprobe measurements, where higher temparture, early olivines have significantly higher NiO contents relative to glass than lower temperature, late olivines. A similar approach was used by Bulle and Layne (2015; 2016) who used secondary ion mass spectrometry (SIMS) to confirm this idea in olivine from Voisey's Bay, Canada. These findings are broadly consistent with the microprobe data from Duluth Complex olivines, where higher Fo compositions have higher NiO contents (figure 45).

Although olivine is the primary silicate host for Ni in the Duluth Complex, several other phases, including clinopyroxene (CPX) and biotite, are known to incorporate small amounts of Ni^{2+} (Marma, 2004; SRK consulting, 2007; White, 2010; Warren et al., 2015). Along with the olivine measurements shown in figure 45, microprobe data for clinopyroxene were collected (figure 46). Like olivine, the clinopyroxene data plot roughly between 35 and 60 for Mg #, but clinopyroxene appears to incorporate much less NiO on average than olivine. Additionally, although both data sets display an overall positive correlation between Mg # and NiO (%), the clinopyroxene data group into 2 or possibly 3 populations. Specifically, for the Mesaba deposit samples, the NiO content is consistently below 0.04 %, regardless of whether the CPX is an early (Mg # ≥ 50) or late (Mg # 35 to 45) cumulate, with one notable outlier. For I deposit samples, there is a slight negative correlation between Mg # and NiO (%).

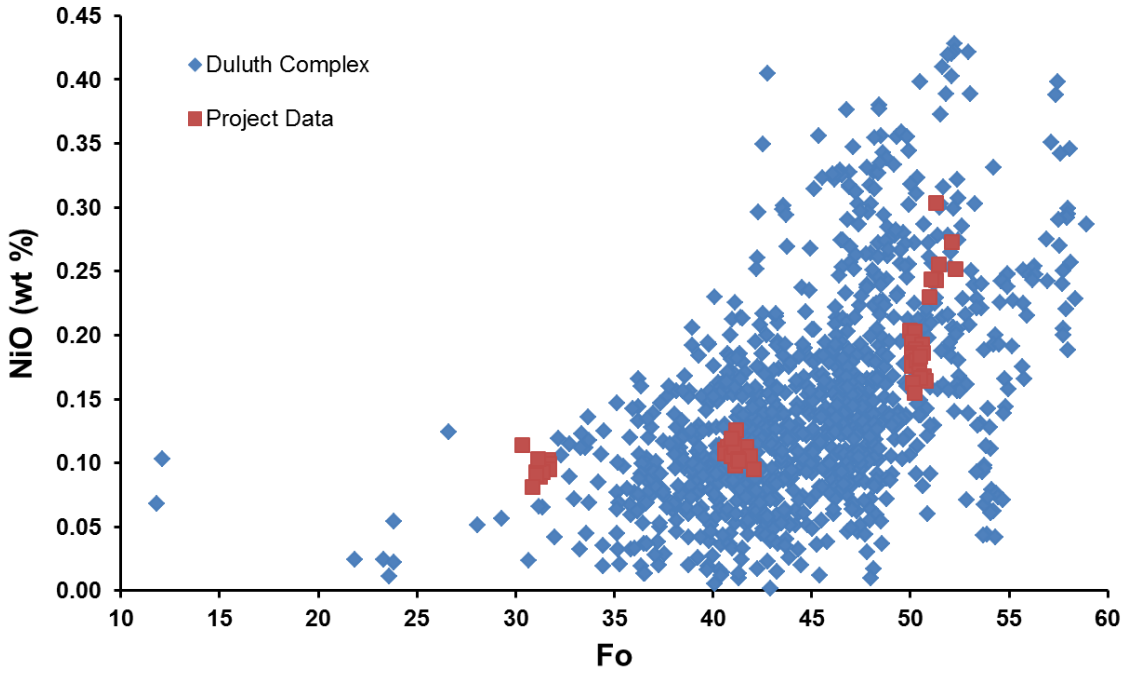

Figure 45: Fo vs NiO (wt. %) for olivine in basal Duluth Complex rocks where Fo is the forsterite content in measured olivine. Values in blue were collected by electron microprobe from the I deposit by White (2010), Peterson (2015) and employees of Duluth Metals LLC. Values in red were collected during this project in samples from the II and Mesaba deposits.

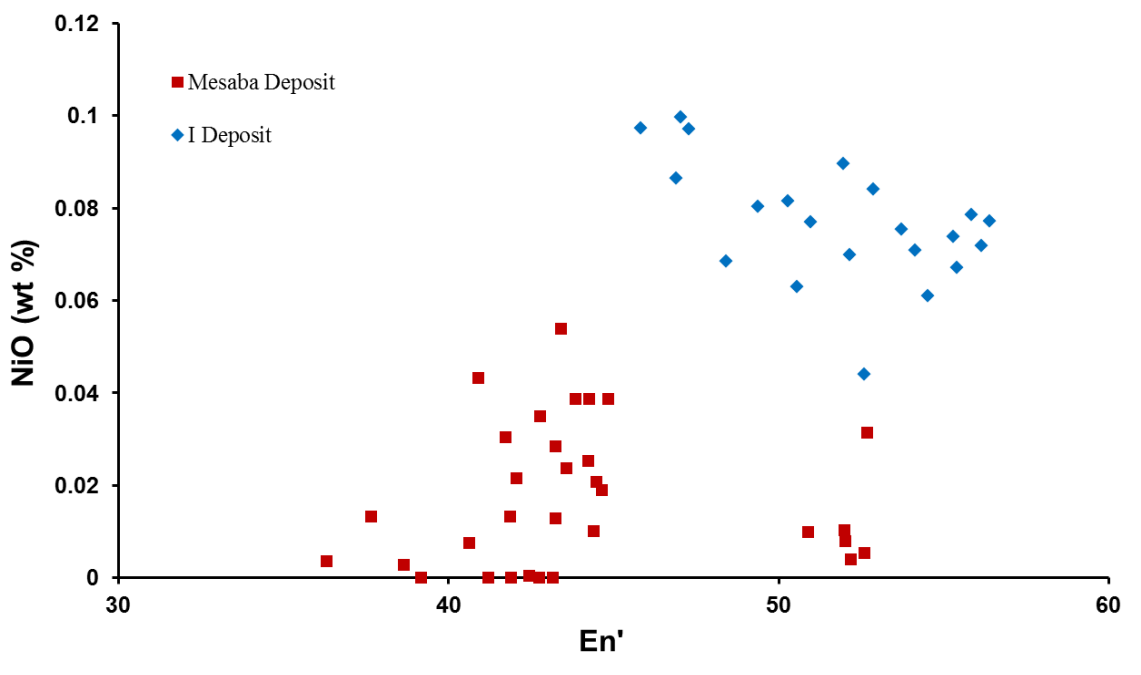

Figure 46: En' vs NiO (wt. %) for clinopyroxene from the Mesaba deposit and the I deposit. The data plot in 2 to 3 groups indicating mineralogical differences between the deposits and within the Mesaba deposit. Each data point has an error of ± 0.02 % NiO associated with it.

This implies late clinopyroxenes incorporate more nickel than early clinopyroxenes, but more data are required to confirm this assertion.

Apart from olivine and CPX, several other common igneous silicate minerals may incorporate trace amounts of nickel. A recent study by Warren et al. (2015) analyzed biotite crystals in units associated with the Sudbury Igneous Complex and reported values up to 2400 ppm nickel. Another study analyzed NorthMet material for the Polymet mining company and reported NiO contents of several silicate phases, including olivine (0.082 % median), clinopyroxene (0.016 % median), biotite (0.058 % median), orthopyroxene (0.016 % median), and plagioclase feldspar (0.016 % median; SRK Consulting, 2007). Based on these data, it is evident that non-olivine, non-sulfide minerals in the Duluth Complex may contain a small, but significant amount of nickel. It is possible, therefore, that they may influence the Ni isotope values for a given sample in the basal Duluth Complex. However, due to a lack of data in the literature, these values will not be considered in this study.

Despite the large experimental dataset on nickel exchange during olivine-melt interaction, there have not been any experiments performed that investigate nickel isotopic fractionation within olivine. Although our data indicate a minor fractionation trend of nickel into olivine, the overall lack of data in the literature makes it difficult to draw any definitive conclusions. The available information suggests that during crystallization, olivine incorporates nickel during its interaction time with the melt, which can lead to differences in NiO content between the core and rim of olivine crystals (Matzen et al., 2013; Yang et al., 2014). This idea was reinforced by Bulle and Layne (2015), who found differences of up to 200 ppm between the core and rim of olivine crystals in the Eastern Deeps Intrusion at Voisey's Bay. Thus, an early olvine with core to rim differences in Ni content could have a different $\delta^{60/58}$Ni value than a late-phase olivine that has less time to interact with the melt. Furthermore, it is possible that an initial fractionation of Ni into Mg-rich, early olivine cumulates is effectively overprinted by system equilibration during the long interaction time, especially if differing amounts of Ni are incorporated into the crystal rim. This would result in isotopic values around the bulk silicate earth range from 0 to 0.1 ‰, which have been documented in this study and others (figure 8; figure 44). However, a detailed isotopic analysis of olivine crystal separates would be required to further refine this hypothesis. Regardless, the Ni isotopic fractionation of 2.1 ‰ for mafic, igneous rocks in the literature must occur during the later formation of sulfides or secondary minerals that incorporate nickel.

7.2.3 Nickel in Sulfide

In contrast to the silicate minerals described above, sulfides are by definition metalliferous and contain a much larger amount of nickel. Accordingly, a different process governs the formation of magmatic sulfide deposits and likely the isotopic fractionation of nickel. A significant amount of research has been conducted on magmatic sulfide deposits and is discussed in detail by Naldrett (2004). The theoretical and empirical work presented by Naldrett (2004) indicates that at some mid-point during the crystallization history of a given magma chamber, sulfide droplets from an immiscible sulfide-oxide liquid within the silicate melt are concentrated in one place and later solidfy, forming magmatic sulfide deposits. The precise timing of these events depends on a series of factors, including fO_2 and the total sulfur content of the melt, more commonly referred to as "sulfur saturation." Once this saturation point is reached, sulfide droplets begin to form, and the immiscible sulfide liquid effectively separates from the silicate melt due to density differences or other factors (Naldrett, 2004). In the Duluth Complex, previous research by Ripley (1981; 1986; 2013), Ripley and Al-Jassar (1987), and Ripley and Li (2003), concluded that the sulfur for the Cu-Ni-PGE deposits was sourced from the underlying Virginia Formation (VF). Partial melting of the VF added a large amount of sulfur to the melt, eventually resulting in sulfur saturation, which led to the creation of the Cu-Ni-PGE deposits in the basal Duluth Complex.

Within the basal Duluth Complex Cu-Ni-PGE deposits, zones of massive, semi-massive, and disseminated sulfide have been documented (e.g. Weiblen and Morey, 1980; Severson and Hauck, 1990; Severson, 1994; Zanko et al., 1994). In all zones, the dominant Ni-sulfide is pentlandite, although minor talnakhite has been identified in other studies. Gueguen et al. (2013) noted that Ni isotope values in samples from komatiite-hosted sulfide deposits decrease as the sulfide content increases, although only six Ni isotope values were collected. Hiebert et al. (2014) observed a nearly identical trend in similar sample material and collected a more robust set of data from a larger sample size that included massive, semi-massive, disseminated, and sulfide-barren komatiite (figure 44). A similar trend was observed in basal Duluth Complex material and can be see below in figure 47. Olivine-rich samples generally have Ni isotope values near the bulk silicate earth, while samples with greater amounts of sulfide have increasingly negative Ni isotope values. This evidence, combined with the results of Hiebert et al. (2014) strongly suggests that sulfide minerals preferentially incorporate the light isotope (^{58}Ni) relative to the heavy isotope (^{60}Ni). One explanation is that the closely-packed,

denser crystal lattices of sulfides prefers the lighter, smaller isotope compared to the larger, heavier one. This preference could be the result of any number of properties including bond strengths, vibrational differences, or space requirements (Kendall and McDonnell, 1998; Schauble, 2004).

7.2.4 Equilibration between the Sulfide and Silicate Melt

Based on previous studies and the information presented above, nickel can be found in two primary mineral types within the Duluth Complex: silicates and sulfides. Although these phases are controlled by different geologic and geochemical processes, it is possible that a certain amount of interaction between the two phases and the remaining melt occurs within the magma chamber during crystallization.

Naldrett (2004) describes this reaction for nickel using the following equations:

1. $NiO + 0.5\ S_2 = NiS + 0.5\ O_2$
2. $K_2 = (\alpha_{NiS}/\alpha_{NiO})*(fO_2^{1/2}/fS_2^{1/2}) = (\gamma_{NiS}/\gamma_{NiO})*(N_{NiS}/N_{NiO})*(fO_2^{1/2}/fS_2^{1/2})$

Equation 1 assumes that nickel is bonded to oxygen in the silicate melt and sulfur in the sulfide melt based on past studies from Shimazaki and MacLean (1976) and Rajamani and Naldrett (1978). Equation 2 is solved for the equilibrium constant (K_2) by using the activities (α) of the two products, the activity coefficients (γ) of each product, the mole fractions (N) of each product, and the fugacities of O_2 and S_2. These relationships were later used by Brenan and Caciagli (2000) as the basis for experiments to measure partition coefficient (K_D) values for olivine in equilibrium with sulfide liquids of varying compositions. They determined that the partition coefficient depends strongly on the amount of nickel in the sulfide liquid, which in turn allows the determination of the fO_2 at which the reaction no longer occurs. Furthermore, Brenan and Cacialgi (2000) determined that sulfide melts with a higher concentration of nickel result in a greater fO_2, which may lead to a greater opportunity for interaction between olivine and free nickel in the remaining melt.

In light of this information, the nickel content of the deposits in the basal Duluth Complex can be seen as a proxy in determining the amount of interaction, and subsequent equilibration, between olivine and the sulfide melt.

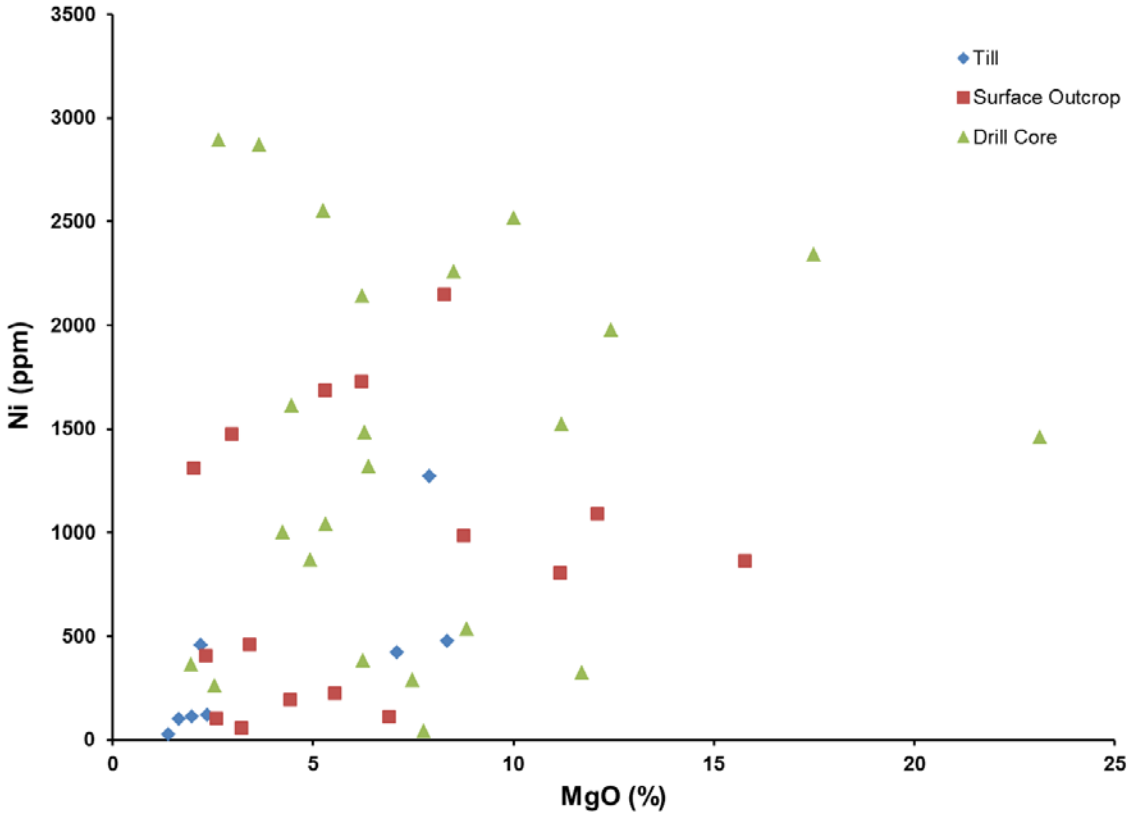

Figure 47: MgO (%) vs Ni (ppm) concentrations for till, surface outcrop, and drill core samples. Till and surface outcrop samples have positive correlations between MgO and Ni, while drill core material doesn't display a significant trend.

Figure 47 shows the MgO (%) vs Ni (ppm) content for Duluth Complex samples, and is divided based on sample type. There appears to be a positive correlation between MgO (%) and Ni (ppm) for the outcrop and till samples, while drill core samples don't display a clear trend. This suggests that other variables must control the nickel content of unweathered, sulfide-rich drill core. Although the MgO content in sample material does not appear to correlate with nickel content, it is possible that the isotopic fractionation could be affected. This idea is addressed below in figure 48, which shows that olivine-rich, sulfide-poor samples cluster between -0.1 and 0 ‰, while the oxide and sulfide-rich samples are much more variable and range from -0.97 to 0.15‰. Significantly, the MgO content does not show a significant correlation with different Ni isotopic values. This suggests the isotopic values must be controlled by a phase other than olivine.

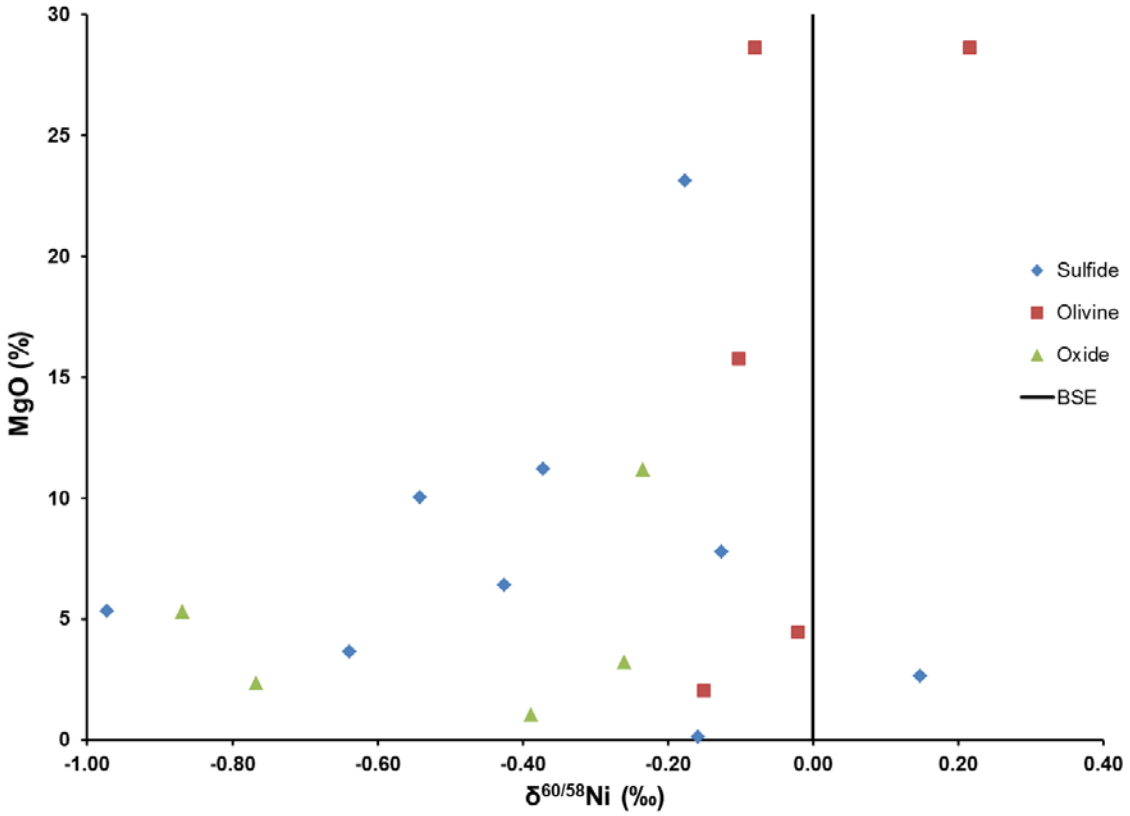

Figure 48: $\delta^{60/58}$Ni vs MgO (%) for sulfide, olivine, and oxide samples. A similar relationship to the one seen in figure 47 is show here between Ni isotope and MgO (%). Again, olivine isotopic values are clustered near the BSE value, while oxide and sulfide values do not greatly depend on MgO (%) values.

Figure 49 shows a weak negative correlation between Ni isotope and total Ni content, suggesting samples more rich in Ni-sulfide have more negative isotopic values. This finding is consistent with the idea presented by Hiebert et al. (2014), but more data is required to fully evaluate this hypothesis.

In addition to the isotope plots shown above, microprobe data shown in figure 50 strongly indicate the potential for interaction between the sulfide and silicate melt. In this image, a spot analysis was performed at the edge of an olivine crystal, followed by several more extending towards the center of the crystal. As the data in table 8 show, the amount of Ni in the olivine crystal is lower in the center of the crystal than at the edge, indicating an enrichment of Ni in the later stages of crystal growth. Possibly, this is an example of interaction between crystallized olivine and the nickel-rich residual melt. This would explain how the center and edges of an olivine crystal may contain different Ni isotopic signatures.

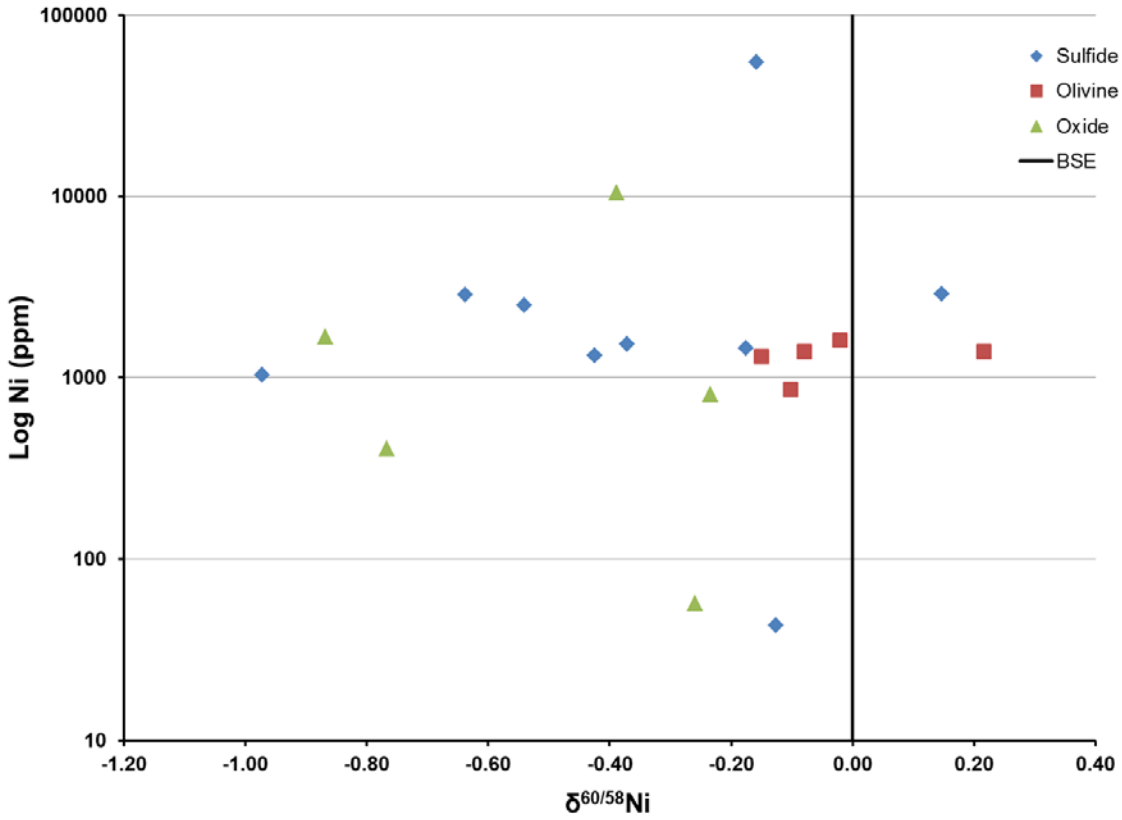

Figure 49: $\delta^{60/58}$Ni values compared to Log Ni (ppm) for samples grouped by mineralogy. Olivine-rich samples group near the bulk silicate earth range, while isotope values for oxide and sulfide-rich samples vary significantly.

Based on these data, nickel appears to undergo an initial high-temperature fractionation within a magma chamber during the crystallization of a mafic intrusion. This fractionation potentially occurs in three stages: a) an initial fractionation into olivine or other silicates, b) a second fractionation into sulfides, and c) a possible third fractionation as a result of reequlibration between sulfide and silicate. The first fractionation event into silicate minerals is very small, and results in Ni isotope values close to the bulk silicate earth range (0 to 0.1 ‰) as defined by Gueguen et al. (2013). The second fractionation into sulfide is much more significant, and leads to Ni isotope values in a relatively wide range from roughly -1.00 to 0.15 ‰ based on data from this study and others (Gueguen et al., 2013; Hiebert et al., 2014; Hofmann et al., 2014). This range may depend on the sulfide content of each sample, or else is a result of other factors that have not been identified here.

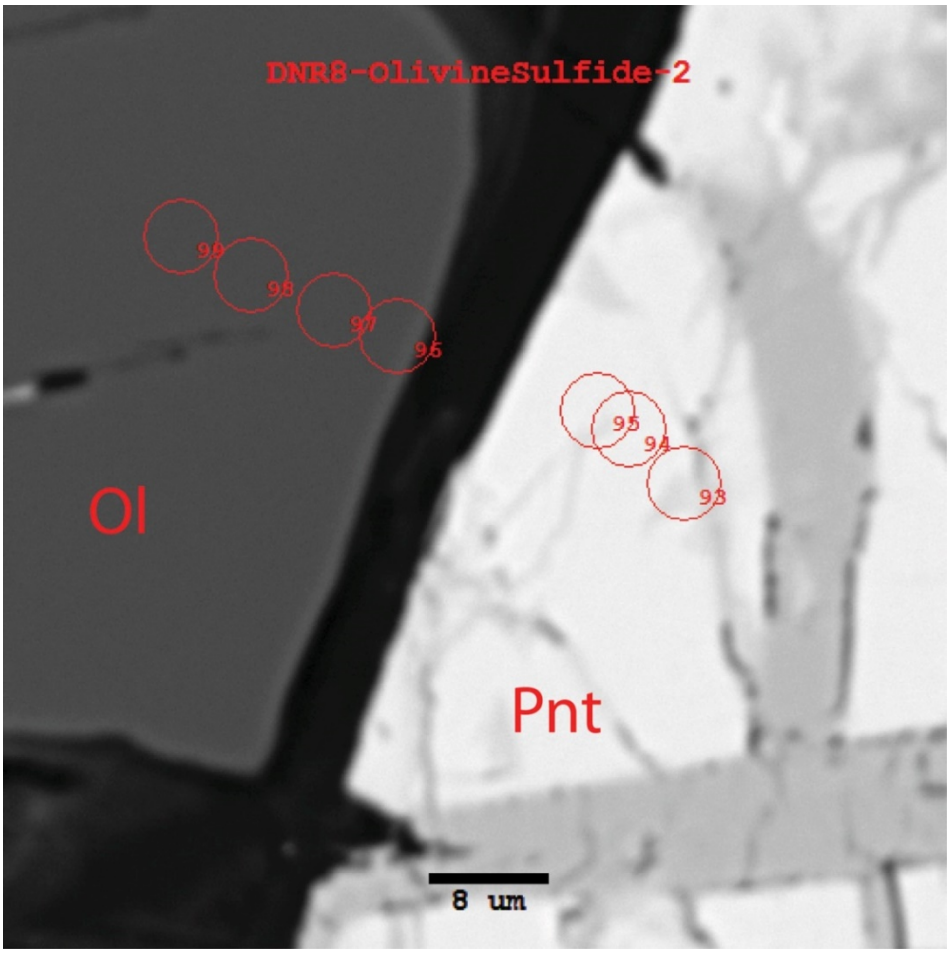

Figure 50: Olivine (Ol) and pentlandite (Pnt) from sample DNR-8. Red dots correspond to spot analyses below in table 8.

Table 8A: Quantitative data from a pentlandite crystal in sample DNR-8 (figure 50). Values are given in weight percent by element. Analysis number 95 is excluded due to analytical error. Analysis 94 has a low total content; this is likely due to the presence of an element that was not included in the analytical package.

Spot	Zn	Pb	Fe	Co	Ni	Cu	S	Total
93	0.01	0.09	31.73	1.28	34.42	0.05	32.73	100.31
94	0.00	0.18	36.36	1.21	24.84	0.19	33.21	95.99

Table 8B: Quantitative data from an olivine crystal in sample DNR-8 (figure 50). Values are given in weight percent by oxide.

Spot	SiO2	FeO	NiO	MnO	MgO	Total
96	36.58	30.05	0.30	0.34	32.04	99.32
97	36.70	29.90	0.26	0.33	32.00	99.18
98	36.73	30.26	0.24	0.33	31.94	99.50
99	36.61	30.08	0.23	0.34	31.63	98.89

The last fractionation event, the behavior of which depends on several variables within a given magma chamber (fO_2, fS_2, total S), could result in interaction between sulfides and olivine. This third fractionation is much less well defined, but could lead to a mixed signature recorded by the sample material. Essentially, bulk silicate earth olivine and Ni-light sulfide exchange nickel, resulting in a slightly negative whole-rock signature with an isotopic value inbetween the pure sulfide and olivine samples. These three primary fractionation events are complicated by the potential for secondary fractionation as discussed below.

7.3 Secondary Fractionation

After the Cu-Ni-PGE mineralization formed and the basal Duluth Complex fully crystallized, a lengthy time period of roughly 1.1 billion years passed. During this time, the intrusive rocks were altered and weathered to varying extents depending on geographic, stratigraphic, and topographic location. Sample material collected in many locations shows clear signs of oxidation and surficial weathering. As discussed in section 7.1, five samples chosen for Ni isotope analysis were sulfide barren and contained a significant amount of secondary oxides. These “oxide” samples are isotopically light, with a minimum value of -0.87 ‰, a maximum value of -0.23 ‰, and an average of -0.50 ‰. Four till samples with unknown compositions were also measured, showing a minimum value of -0.71 ‰, a maximum value of -0.02 ‰, and an average of -0.35 ‰. Unlike the unweathered samples discussed earlier, primary minerals are commonly altered during surficial weathering, leading to the creation of new secondary minerals. These phases often incorporate metals (Cu, Fe, Ni) that are released during redox reactions; accordingly, the potential for re-mobilization and possible secondary fractionation of nickel must be considered. These reactions, and the subsequent release of metals, will be considered in the context of a low-temperature fractionation.

7.3.1 Comparison to Published Data

In addition to measuring mafic and ultramafic rocks for Ni isotopes, Gueguen et al. (2013) also examined several other materials including Ni-contaminated soil (0.14 ‰), manganese nodules (0.36 ‰ and 1.03 ‰), and banded iron formation (0.46 ‰). Unlike the komatiite and basaltic samples, these materials are isotopically heavy,

suggesting a different process governs the fractionation of nickel during the formation of these materials. Several other studies by Cameron et al. (2009), and Gall et al. (2012, 2013), have investigated ferromanganese crusts and found a significant fractionation between 0.9 and 2.5 ‰. These crusts form on the seafloor, and are largely made up of detritus and minerals that precipitate directly from seawater in adsorption reactions. The isotopic compositions of river water and seawater have been investigated in detail by Cameron and Vance (2013; 2014). These studies determined that river water is isotopically heterogeneous, varying significantly from headwaters to the brackish water close to the sea. Specifically, river water measured by Cameron and Vance (2014) ranged from 0.29 to 1.34 ‰, revealing a significant concentration of isotopically heavy nickel in river water. Seawater was found to be much more homogeneous, but still isotopically heavier than river water, with a mean value of 1.44 ‰ across different oceans (Cameron and Vance, 2014). These values likely have a stong influence on the isotopic composition of minerals that precipitate out of the seawater and indicate low-temperature fractionation processes during surficial weathering.

Apart from values collected in natural samples, a recent study by Wasylenki et al. (2015) observed Ni isotopic fractionation in synthetic ferrihydrite, a secondary oxy-hydroxide phase that commonly forms as a by-product of water-rock oxidation reactions at the surface. During the creation of the ferrihydrite, samples of Ni-bearing solution were collected and measured for Ni isotopes along with the ferrihydrite, resulting in a unique set of solution (ave. 0.14 ‰) and solid (ave. -0.21 ‰) $\delta^{60/58}$Ni values during adsorption and coprecipitation reactions. These data suggest that secondary oxide phases can preferentially incorporate light nickel, while the heavy nickel remaining in solution is transported away by weathering and erosion into rivers, eventually reaching the ocean.The data discussed above are shown below in figure 51.

Ratié et al. (2015) examined the potential usage of the Ni isotopic system as an environmental tracer related to the effects of extreme tropical weathering in ultramafic terranes. Specifically, a variety of sample types displaying varying degrees of weathering were collected from an ultramafic massif in Barro Alto, Goiás, Brazil to study Ni metal cycling during geochemical weathering. Sample types and Ni isotopic values in this study included parental material (0.2 to 0.36 ‰), saprolite/laterite ore samples (-0.6 to 0.3 ‰), and soil (-0.19 to -0.02 ‰). In this case, the ultramafic host rock is isotopically heavy, while the secondary ore material includes both isotopically light and heavy samples.

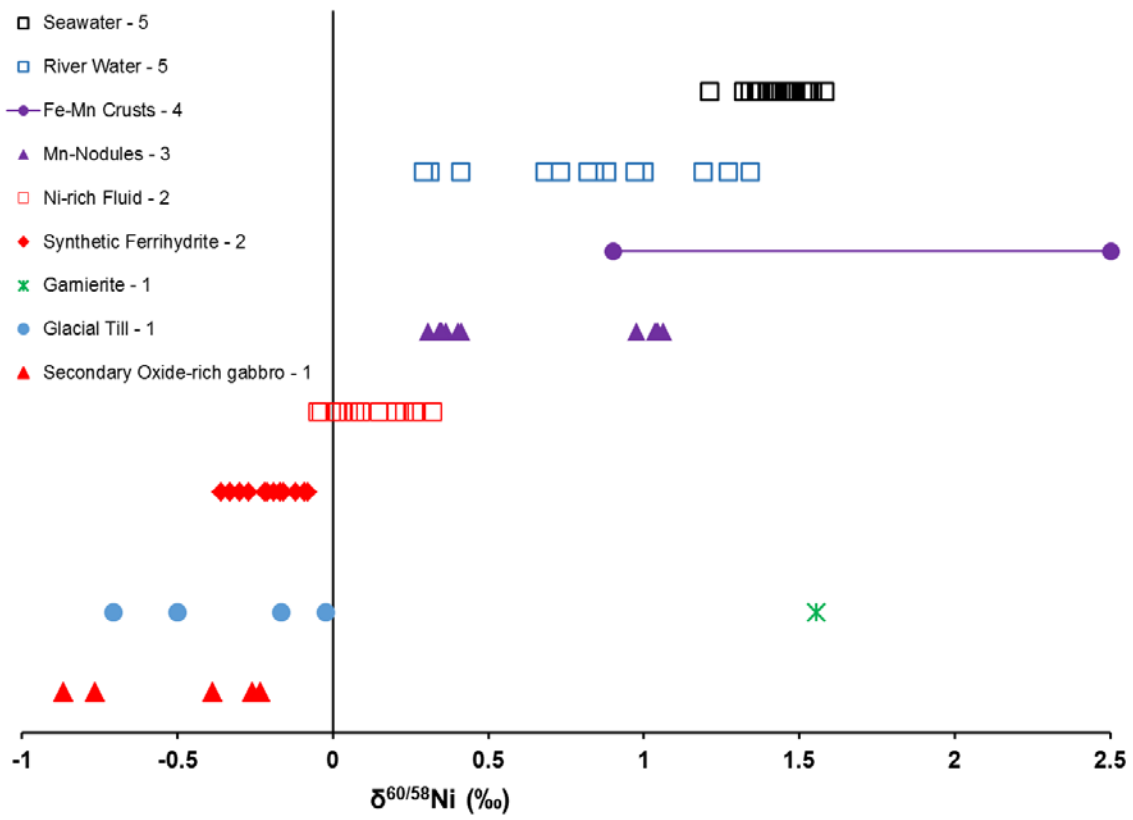

Figure 51: $\delta^{60/58}$Ni values from this study (secondary oxide-rich gabbro, till, garnierite) compared to published data. **1**: Values measured during this study **2**: Wasylenki et al, 2015. **3**: Gueguen et al, 2013. **4**: Gall et al, 2013. **5**: Cameron and Vance, 2014.

7.3.2 Weathering in the Duluth Complex

In the Duluth Complex, studies on the surficial weathering of rocks have been conducted since at least the mid-1970's, when the Minnesota Environmental Quality Board conducted a detailed investigation to determine the potential effects of Cu-Ni mining in the area (Minnesota Environmental Quality Board, 1979). During this review, the AMAX company placed a large volume of sulfide-bearing tailings into 6 large piles to study the effects of weathering and the impacts on water quality. This material was studied by Lapakko (1980), and Lapakko et al. (1986) in a number of detailed experiments regarding water quality, surficial weathering, and the possibility of acid mine drainage in northeastern Minnesota. Recently, the results of a 10-year series of experiments on Mesaba deposit material was published by Lapakko et al. (2013). In these experiments, sample tailings were placed in six small reactors and two humdity cells, which allow material to oxidize when in contact with both air and water. Over the

10-year period, oxidation products were periodically rinsed off and tested for metals along with the water that was in contact with the tailings. Olivine accounted for 9.8 % of all solid phases, and contained an average content of 0.15 % NiO. Additionally, the primary nickel sulfide phase, pentlandite, accounted for 0.02 % of all solid phases. This finding is consistent with the results of another study by SRK Consulting (2007), who characterized tailings material for PolyMet mining company. This report found that while pentlandite is the primary nickel sulfide, olivine contains up to 0.14 % NiO and biotite contains up to 0.13 % NiO, along with trace amounts in clinopyroxene, orthopyroxene, and plagioclase feldspar. Additionally, SRK Consulting (2007) suggests that nickel silicate minerals, specifically nepouite and Ni-kerolite, could be the controlling minerals for the solubility of Ni at moderate to low pH.

Based on the material presented above, it is clear that the primary nickel phases in the Duluth Complex are pentlandite and olivine, although several other phases, including biotite, also host nickel. During surficial weathering, oxidation reactions occur, leading to the creation of new, secondary phases, and the mobilization of nickel. A study by Li et al. (2012) discusses the disassociation of pentlandite, which occurs in the following series of reactions:

$$2\ Fe_{4.5}Ni_{4.5}S_8 \rightarrow 2\ Fe_3Ni_3S_4 + 3\ Fe^{2+} + 3\ Ni^{2+} + 8\ S^0$$
$$Fe_3Ni_3S_4 \rightarrow FeNi_2S_4 + 2\ Fe^{2+} + Ni^{2+}$$
$$3\ FeNi_2S_4 \rightarrow 2\ Ni_3S_4 + 3\ Fe^{2+} + 4\ S^0$$
$$2\ Ni_3S_4 \rightarrow 2\ NiS_2 + 4\ Ni^{2+} + 4\ S^0$$
$$NiS_2 \rightarrow Ni^{2+} + 2\ S^0$$

Although the later reactions in this series are stated to occur at pH values lower than 2, the release of elemental Ni^{2+} occurs in the very first reaction that breaks down pentlandite, which suggests that Ni^{2+} will be readily available for incorporation into secondary minerals. Lindsay et al. (2015) found that several Fe (III) (oxy)hydroxide and Fe(III) hydroxysulfates precipitate in the oxidation zone of sulfide tailings. Another study by Langman et al. (2015) found that nickel is released during the oxidation of pentlandite and then adsorbed or precipitated with secondary Fe-minerals. Additionally, Langman et al. (2015) noted that this reaction still occurs at near-neutral pH conditions, similar to those seen in the experiments by Lapakko et al. (2013). These secondary Fe-minerals include ferrihydrite, goethite, lepidocrocite, and jarosite, the first of which is mentioned by

SRK Consulting (2007) as being present in Duluth Complex material and a possible phase that incorporates nickel.

The weathering and alteration of olivine is relatively well-known, although the subsequent release of trace amounts of nickel is less well understood. Typically, olivine weathers or alters to iggingsite ($MgFe_2Si_3O_{10} \bullet 4(H_2O)$) after the completion of the following reaction, shown for the forsterite end-member (ten Berge et al., 2012):

$$Mg_2SiO_4 + 4\ CO_2 + 2\ H_2O \rightarrow 2\ Mg^{2+} + SiO_2 + 4\ HCO_3^- \Leftrightarrow 2\ MgCO_3 + SiO_2 + 2\ CO_2 + H_2O$$

Although this reaction does not include nickel, it can be assumed that Ni^{2+} behaves in the same way as Mg^{2+} because they occupy the same sites in the olivine crystal lattice (Henderson et al., 2001). This same idea is presented by Locsey et al. (2011), who found that elemental Mg^{2+} readily goes into solution following the oxidation of olivine during weathering.

In this study, material collected from surface outcrops was visually, chemically, and petrologically examined for evidence of oxidation and surficial weathering. Samples were loosely separated by the degree of oxidation, which was approximated by the presence of secondary oxide minerals in different parts of a given sample. The images shown below in figures 52 and 53 are representative of “highly weathered” samples that contain secondary oxide minerals along veins that run through an entire sample. Figure 53, in particular, shows oxide coatings and a large, multi-phase sulfide vein containing pentlandite.This is an example of how fluid infiltration and subsequent interaction with sulfides could release aqueous Ni^{2+}, which would be available for adsorption and precipitation into secondary phases.

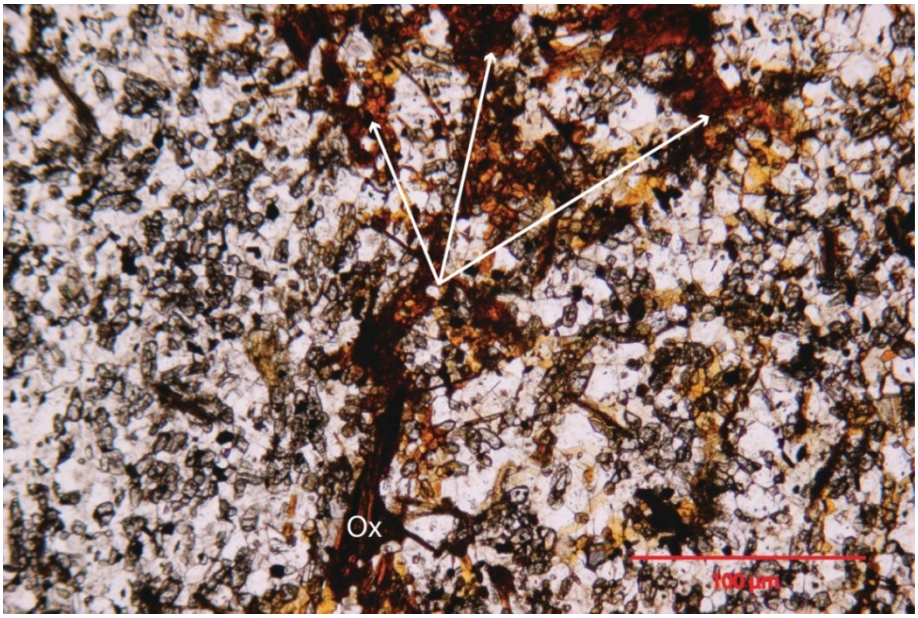

Figure 52: Transmitted light image collected from sample SP-4a. The oxide vein (Ox) in the center of the image branches out, creating 3 new fluid pathways. This allowed greater opportunity for interaction and the weathering of preexisting gabbroic minerals.

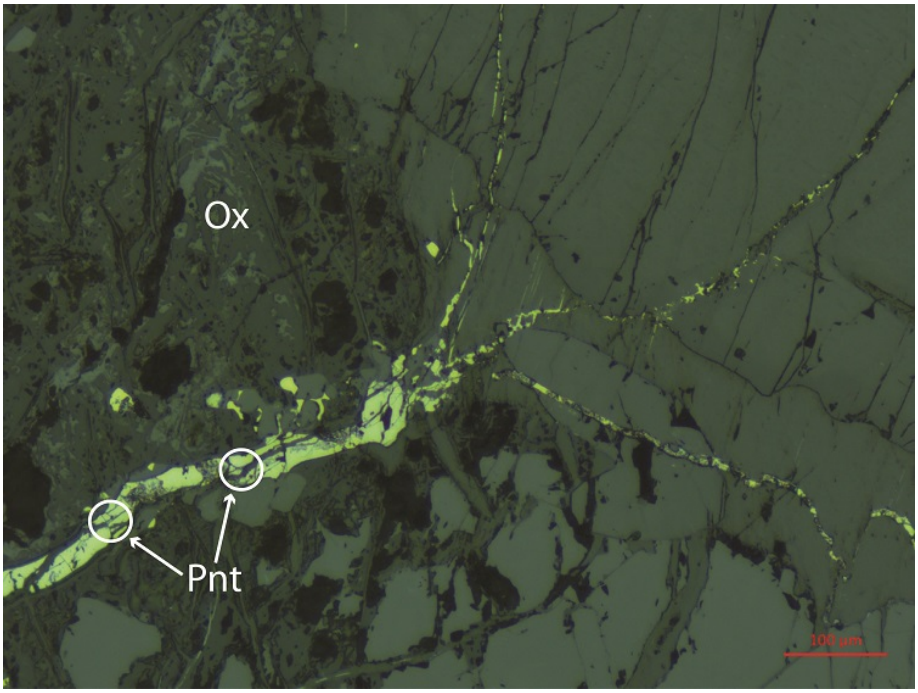

Figure 53: Reflected light image collected from sample PLM-2B. This image shows oxide (Ox) veins in close association with a large sulfide vein that contains small pentlandite (Pnt) crystals. Again, the large vein divides into 3 additional veins, like the example described in figure 52.

Along with the visual evidence shown in figures 52 and 53, the weathering of Duluth Complex rocks was also examined geochemically using the data in tables A2-1 and A2-2 (see Appendix 1). Major oxide data were normalized to the values from sample 10-599D, which are considered closest to the overall average for all the Duluth Complex samples analyzed. The data for 13 surface samples are plotted below in figure 54 in a typical spider diagram in the style of Rollinson (1993).

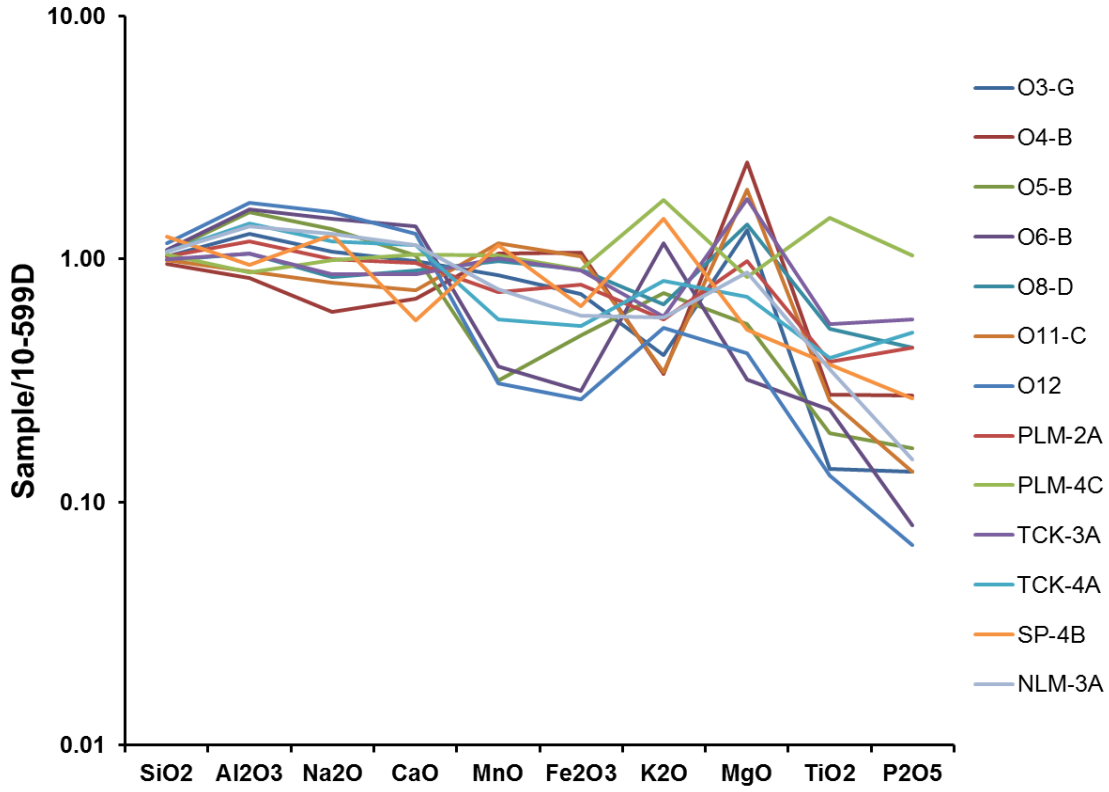

Figure 54: Spider diagram of major oxide data from 13 surface samples. The data from each sample are normalized to the data from sample 10-599D. Values are plotted on a logarithmic scale and sorted based on increasing degree of change.

Figure 54 shows that certain oxide species have a greater variance relative to others in surface samples, suggesting these samples have undergone differing degrees of weathering. While some oxides stay relatively constant, specific weathering reactions lead to the loss or gain of K_2O, MgO, TiO_2, or P_2O_5 in sample material. Specifically, the data remain close to the assumed average value for SiO_2, Al_2O_3, Na_2O, and CaO, whereas values for K_2O, MgO, TiO_2, and P_2O_5 appear to be depleted for the most part; MnO and Fe_2O_3 show variable depletion or enricment. The weathering of biotite to hydrobiotite and later clay minerals leads to the release of potassium and magnesium

(Velbel et al., 1985). The highly variable TiO_2 and P_2O_5 contents are likely a result of samples being relatively enriched or depleted in primary apatite or titano-magnetite. As the mineral content for specific samples is unknown, the potential contribution of these elements during weathering cannot be assessed. The MgO content is highly variable, and shows both enrichment and depletion across sample material. This is likely due to olivine-rich rocks altering to Mg-rich serpentine, while olivine-poor rocks alter to iddingsite and other relatively Mg-poor clay phases. The weathering of Mg or Fe-rich Chlorite to goethite, kaolinite, and other clay minerals, may have a strong influence on the Mg content of rock at the surface (Aspandiar and Eggleton, 2015). The potential for gain or loss of MgO in sample material during weathering could indicate the possibility of a weathering-induced fractionation of Ni; this idea will be addressed below.

7.3.3 Fractionation of Ni during Surficial Weathering

When samples were selected for Ni isotope analysis, it was determined that five of the surface outcrop samples contained no visible sulfide, but were especially rich in secondary oxides, along with olivine and other gabbroic phases. The measured Ni isotopic values are unique because they plot in a similar field to the sulfide-rich samples, but do not contain sulfide minerals. Thus, the fractionation during surficial weathering must involve another phase that preferentially incorporates light nickel (^{58}Ni). Although there are only five “oxide” data points, there are two distinct populations: a very light group (-0.87 and -0.77 ‰) and a moderately light group (-0.39, -0.26, and -0.23 ‰). The first group has values similar to the sulfide-rich samples, suggesting sulfides may be present in small amounts within those two samples. The second group, however, correlates with the values measured for synthetic ferrihydrite collected by Wasylenki et al. (2015) that have an average of -0.24 ‰. Combined with the values obtained from the Ni-rich fluid in this experimental study, these data indicate that when secondary oxides form, they preferentially incorporate light nickel, while the heavy isotope remains in solution. This idea is supported by the findings of Cameron and Vance (2014), who systematically measured Ni-isotope values for rivers and seawater, and Gall et al. (2011), who measured the values of seafloor ferromanganese crusts. Both the water and the secondary material have very heavy isotopic values, indicating certain mineral precipitates from heavy-Ni-rich fluids may be enriched in heavy nickel.

This hypothesis is supported by an additional sample composed of pure garnierite ($Ni_3MgSi_6O_{15}(OH)_2 \bullet 6(H_2O)$) that was analyzed during this study (figure 45).

The value obtained, 1.55 ‰, is distinctly different from all the other Ni isotopic data collected in this study from Duluth Complex material, and is in agreement with data published by Gall et al. (2011) and Cameron and Vance (2014). Garnierite is a secondary hydrous phyllosilicate that only forms in ultramafic laterite-type deposits that are highly enriched in nickel; thus, it is likely that a different process governs the fractionation of nickel in this environment. It is possible that the fluid involved in the oxidation process is so enriched in isotopically heavy nickel that garnierite, and other secondary nickel phases in laterites, naturally incorporate heavy nickel. These include a number of phases in the Yilgarn Craton documented by Butt et al. (2006), ranging from nickel sulfides (e.g. millerite, violarite) to nickel carbonates (e.g. takovite, kambaldite, otwayite). Due to the extreme climatic differences between lateritic environments and the basal Duluth Complex, it is likely that the formation of primary Ni silicates and the enrichment of heavy nickel in secondary minerals does not occur in significant amounts in northeastern Minnesota.

7.4 Nickel Fractionation – Conceptual Model

Based on the discussion above, it is suggested that the fractionation of nickel occurs in two main stages. The first stage occurs at high temperatures during the crystallization of Ni-sulfide, when light nickel is preferentially incorporated into sulfide. Sulfide-barren rocks measured in this study have an average Ni isotope value of -0.03 ‰, while sulfide-rich material averages -0.36 ‰. The precise cause of this preferential incorporation remains unknown, but may be a result of crystallographic differences between the structures of sulfide and silicate minerals, or other variables at the atomic level (vibration, bond length, etc.; Kendall and McDonnell, 1998; Schauble, 2004). The resulting melt after sulfide saturation may be enriched in heavy Ni, but no data has been collected at this point. The second stage occurs during alteration and surficial weathering, when nickel is remobilized and trapped in secondary phases. Surface rock samples containing abundant oxides and no sulfides have an average Ni isotope value of -0.5 ‰, suggesting a secondary incorporation of isotopically light nickel into secondary oxide. At the same time, it is possible that heavy nickel that doesn't precipitate into secondary phases remains in solution, based on the results of Cameron and Vance (2013, 2014), who measured the isotopic values of river water (0.84 ‰ average) and seawater (1.44 ‰ average). Finally, in nickel-rich ultramafic terranes

affected by deep, tropical weathering, water saturated with heavy nickel may lead to the precipitation of isotopically heavy, secondary nickel minerals. A visual representation of this model is shown in figure 55. This model was created using data from Gall et al. (2013), Gueguen et al. (2013), Cameron and Vance (2013, 2014) and Wasylenki et al. (2015), as well as this study. In this conceptual model, nickel, with an isotopic value of BSE, is initially incorporated into olivine during the early stages of crystallization of a mafic intrusion. Upon reaching sulfide saturation, sulfide minerals segregate from the melt and preferentially incorporate light nickel. During surficial weathering, there is a preferential uptake of light nickel into secondary oxides. As a consequence, heavy nickel enters into solution, and eventually reaches groundwater, rivers, and oceans. Minerals precipitating from these waters (e.g. garnierite, manganese nodules) may further fractionate nickel, with the heavy isotope entering the minerals or materials. Additional fractionation events may occur in other environments, and further research will show if the range of isotopic values shown below will require modification.

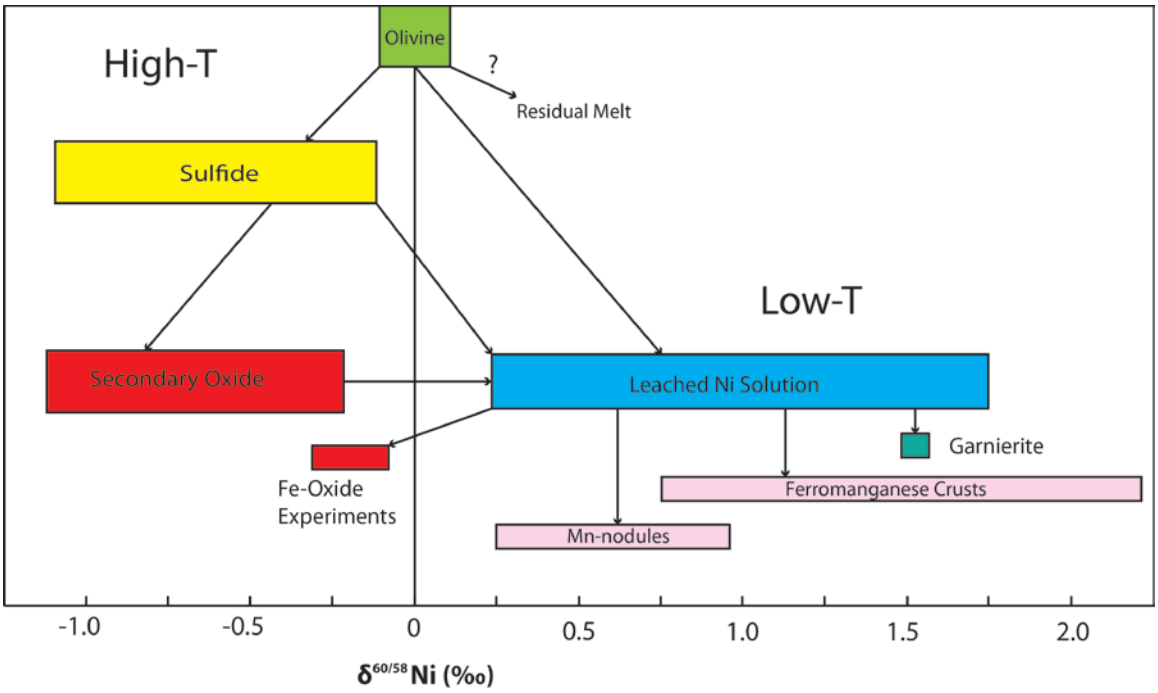

Figure 55: A conceptual model for the fractionation of nickel. In this model, the initial, high temperature fractionation into olivine and sulfide is followed by a secondary fractionation, where isotopically heavy nickel enters solution, while light nickel is incorporated into secondary oxide phases. The heavy Ni-rich solution may precipitate other phases, including garnierite and Mn-nodules that are enriched in heavy Ni.

7.5 Fractionation Factors for $\delta^{60/58}$Ni

Although there have been a number of studies involving nickel isotopes, none have calculated fractionation factors for the $\delta^{60/58}$Ni system. These factors have been used successfully in other stable isotope systems, especially $\delta^{18/16}$O, and indicate the relative magnitude of a given fractionation between materials, typically at a given temperature (Friedman and O'Neil, 1977):

$$\alpha_{A\text{-}B} = 1000 + \delta_A / 1000 + \delta_B$$

Typically, the two materials (δ_A, δ_B) represent the two phases incorporating the element of interest before and after a given reaction or process. For nickel, these are the liquid magma reservoir (δ_B) and a mineral, either olivine or sulfide (δ_A). The liquid magma, based on the work by Gueguen et al. (2013), represents the bulk-silicate earth (BSE) of the mantle, which has an estimated value of 0.05 ‰. The value for olivine, based on data collected in this study and by Gueguen et al. (2013), is -0.07 ‰. It should be noted, however, that early and late-forming olivine can vary significantly in composition as discussed above; thus, it should not be treated as a representative composition for all olivines. The value for sulfide, based on data collected in this study and by Gueguen et al. (2013), Hiebert et al. (2014), and Hofmann et al. (2014), is -0.47 ‰.

In addition to fractionation between magma and olivine/sulfide, the potential for a low temperature fractionation of nickel has also been discussed. This fractionation occurs in multiple materials during surficial weathering, including secondary oxide, fluid, and a range of other secondary materials including ferromanganese nodules and secondary nickel silicates (e.g. garnierite). The calculation of a fractionation factor for the reaction between bedrock and solid secondary phases would be extremely difficult due to the high variability in starting isotopic compositions, so it will not be attempted here. The reaction between bedrock and fluid, however, is possible because of the work by Cameron and Vance (2014). In this reaction, weathering of generic bedrock results in a fractionation of nickel between bedrock and fluid. Cameron and Vance (2014) measured $\delta^{60/58}$Ni for a number of rivers in different parts of the world, and produced a spread of values from 0.31 to 1.34 ‰, with an overall average of 0.84 ‰. This average will represent the overall fractionation that occurs when liberated Ni^{2+} enters fluid during weathering, and serves as δ_A. Estimates for bulk crustal compositions are possible due

to Gueguen et al. (2013), who published an estimate for the BSE, which represents a mantle-sourced mafic crust, and granite, which represents the most common bedrock type in continental crust. Additionally, the value for sulfide (-0.47 ‰) will represent sulfide-rich bedrock in a nickel-rich environment. These three values serve as δ_B in three separate calculations. The resulting fractionation factors are shown below in table 9.

Table 9: Fractionation factors calculated for different events using the standard fractionation relationship shown above.

No.	Fractionation Event	δ_A (‰)	δ_B (‰)	α_{A-B}
1	Magma → Olivine	-0.07	0.05	0.9999
2	Magma → Sulfide	-0.47	0.05	0.9995
3	Granitic Crust → Fluid	0.84	0.43	1.0004
4	Mantle-derived Crust → Fluid	0.84	0.05	1.0008
5	Sulfide-rich Bedrock → Fluid	0.84	-0.47	1.0013

The calculated factors are consistent with the idea that fractionation of nickel into sulfide leads to a preferential incorporation of light nickel, while the fractionation of nickel into fluid leads to an incorporation of heavy nickel. The fractionation factor for the magma/olivine event is so close to one that the two values are mutually indistinguishable, leading to the conclusion that olivine does effectively represent the BSE value described by Gueguen et al. (2013). These values may provide a base-level insight into the fractionation events, but additional data are required to confirm the validity of these fractionation factors.

7.6 Cu Isotopes

The 22 $\delta^{65/63}$Cu isotope values measured from Duluth Complex samples have an overall average value of -0.35 ‰, which is comparable to the average for Ni isotopes (-0.3 ‰). These values were measured to provide additional insight into the metal speciation and fractionation within mineralized basal Duluth Complex samples during the formation and subsequent weathering of the intrusions. The Cu isotope system is significantly more complex due to the additional valence state differences of copper. Because copper was not examined in any primary silicate minerals during this study, the

fractionation of copper will only be considered for the formation of sulfides and subsequent surficial weathering.

The values are divided into three categories based on the amount of weathering of each particular sample (figure 56). These are drill core (unweathered), surface (weak to moderate weathering), and weathered (extreme weathering). The drill core samples are typically isotopically light, with a minimum value of -0.88 ‰, a maximum of 0.36 ‰, and an overall average of -0.35 ‰. The surface samples are also isotopically light, but to a much smaller degree, with a minimum value of -0.31 ‰, a maximum of -0.02 ‰, and an average of -0.14 ‰. There were only three samples that were highly weathered, but these are the isotopically lightest values, with a minimum value of -1.28 ‰, a maximum of -0.61 ‰, and an average of -0.87 ‰. The total Duluth Complex range of Cu isotopic values (-1.28 ‰ to 0.36 ‰) is loosely similar to the range for mafic intrusions (-1.06 to 0.16 ‰) published by Larson et al. (2003), but only 3 data points were measured in that study. Additional data published by both Larson et al. (2003) and Markl et al. (2006) for porphyry/skarn deposits share some similarities (-0.87 ‰ minimum), but many data points (n=10) plot above the maximum value of 0.36 ‰, indicating a clear enrichment of heavy copper in this type of deposit.

Primary, sulfide-bearing drill core material has similar isotopic values for both nickel and copper in the Duluth Complex. The values range from highly enriched in the light isotope to near zero, with a few samples enriched in the heavy isotope (figure 56). It is possible that sulfide minerals preferentially incorporate light copper in a similar way to nickel. Studies by Larson et al. (2003) and Markl et al. (2006) generally focused on a specific copper mineral and do not focus on primary, high-temperature fractionation in a magmatic environment. Larson et al. (2003) measured $\delta^{65/63}$Cu values in 3 locations and found a fairly wide spread from -1.06 ‰ to 0.16 ‰. Although this spread nicely matches the trend found in this study, Larson et al. (2003) specifically targeted chalcopyrite for analysis, in contrast to the bulk measurements in this study. Additional chalcopyrite samples measured by Maréchal et al. (1999) and Zhu et al. (2000) showed similar values, with an overall average of -0.12 ‰ in samples from Sudbury, the Stillwater Complex, and the Bushveld Complex. Larson et al. (2003) speculates that these values may represent the isotopic composition of the mantle, but hydrothermal alteration, surface weathering, or oxidation processes could affect the isotopic values, making a definitive conclusion difficult. Additional research with a specific focus on primary,

unaltered copper-sulfide minerals would be required to provide further insight into the fractionation of copper in basal Duluth Complex mineralization.

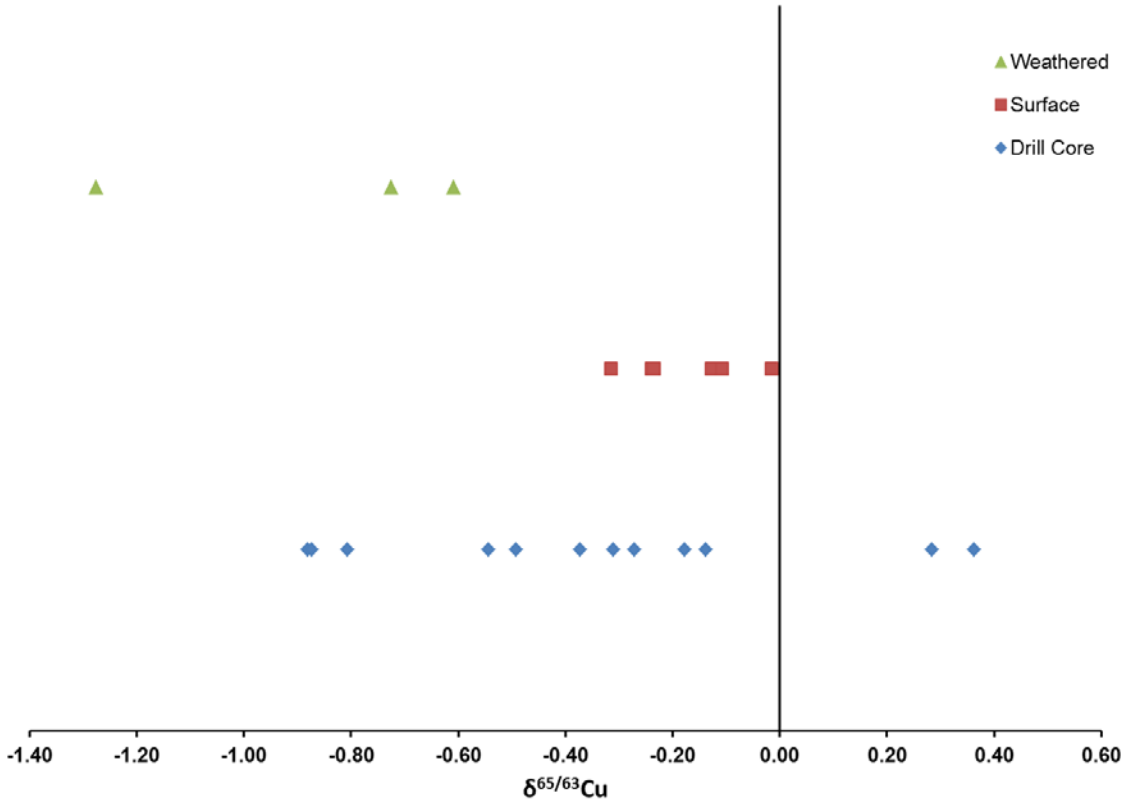

Figure 56: $\delta^{65/63}$Cu isotope values for Duluth Complex samples. “Surface” samples include material that is weakly or moderately weathered, while “Weathered” samples include material that was highly weathered. “Drill Core” samples are considered “unweathered” for the purposes of this study.

8. Conclusions

During the course of this project, a variety of samples were obtained from the basal Duluth Complex to investigate the potential for the isotopic fractionation of nickel, with the goal of producing a conceptual model for the $\delta^{60/58}$Ni system. These samples were chosen to represent primary and weathered sulfide-bearing rocks, sulfide-barren “background” rocks, and glacial till. The methodology and analytical methods utilized produced meaningful results, and a number of conclusions can be drawn regarding the questions put forth in the project goals section.

The intrusions of the basal Duluth Complex contain two primary sources of nickel: silicate and sulfide. Silicate minerals, especially olivine, represent an initial fractionation that occurs at high temperatures. It is possible that early and late-phase olivines are isotopically distinct, with late olivines incorporating slightly more ^{60}Ni, resulting in positive isotopic values above the BSE. Further research would be required to evaluate this idea. A second high temperature fractionation occurs when sulfide minerals preferentially incorporate isotopically light nickel. As a result, sulfide-bearing rocks produce distinctly negative isotopic values in contrast to the BSE isotopic values olivine-rich rocks. Following the complete crystallization of the intrusions, a third, low-temperature fractionation occurs. Based on this study, along with the work of Cameron and Vance (2014) and Wasylenki et al. (2015), it is likely that during surficial weathering, heavy nickel is dissolved and enters solution, while light nickel is preferentially incorporated into secondary oxide. Other secondary minerals, including garnierite, precipitate from the heavy nickel-rich fluid and incorporate heavy nickel, but there is no evidence of this process or these minerals forming in the Duluth Complex.

Through a detailed examination of the project data in the context of the above statements, a conceptual model for nickel fractionation in the Duluth Complex was developed (figure 55). The fractionation of ^{60}Ni and ^{58}Ni does not occur at comparable magnitudes of other stable isotope systems, but the resulting isotopic values in basal Duluth Complex rocks are distinct enough to warrant further investigation of this isotopic system in the context of magmatic and surficial processes.

8.1 Future Studies and Speculation

Although this study produced a number of useful results, it was unable to answer some of the questions posed in the project goals section. First, Ni isotopic values change from deposit to deposit (figure 57), but the size of the study area, differences in mineralogy, and the small number of samples make definitive statements about this question difficult. However, there appears to be a definite trend within South Kawishiwi Intrusion deposits. Isotopic values for a mixture of silicate and sulfide-rich samples change from near the Bulk Silicate Earth in the II and I deposits to distinctly negative in the Serpentine deposit. This may be linked to the ideas outlined by Peterson (2001) shown in figure 2 relating to the north-south formation of mineralization within the SKI. To investigate this idea fully, more samples would have to be collected from each

deposit, including sulfide-barren samples and mineralized samples containing varying amounts of sulfide. This would also provide more insight into the potential for interaction and possible nickel exchange between sulfide and silicate, along with isotopic differences between early and late phase cumulate olivine. This type of study would require the identification and separation of early and late(r) silicates, including olivine.

Another unanswered question relates to the potential usage of Ni isotopes as an exploration tool for mining companies.

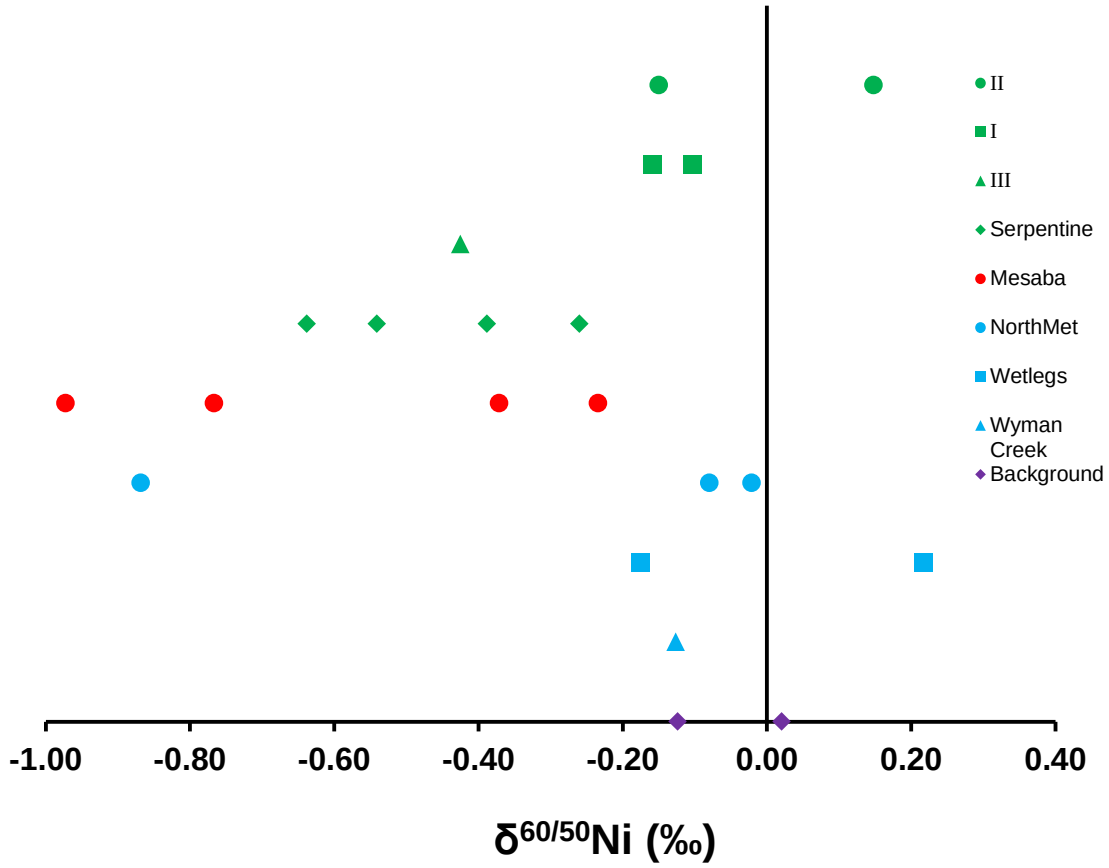

Figure 57: Ni isotope values by deposit. Values are arranged from north (III) to south (Wyman Creek) along the Y-axis, and further divided based on intrusion (South Kawishiwi, green; Bathtub, red; Partridge River, blue). The data for South Kawishiwi deposits (green) show a positive linear trend from roughly the Mesaba/Serpentine deposits to the III deposit. The data for Partridge River intrusion deposits do not show a clear trend and are generally clustered near the Bulk Silicate Earth range.

Only 4 till samples were analyzed, but they did demonstrate a notable spread of $\delta^{60/58}$Ni values. Two values are close to the BSE, but the other two clearly are influenced by the presence of either sulfide or secondary oxide in the source region. A systematic

sampling of till in the vicinity of Cu-Ni-PGE mineralization, along with material overlying sulfide-barren gabbro bedrock could provide answers. Additionally, examining oxidized surface material in the vicinity of known mineralization and in areas without mineralization could provide details about the relative effect of oxidation on isotopic values, and whether or not material at the surface is reflective of mineralization at depth. In an exploration setting, this information could be used to predict both the occurrence and sulfide content of potential magmatic Ni-rich sulfide deposits. Essentially, a more negative $\delta^{60/58}$Ni value would be reflective of the high concentration of sulfides necessary to produce the specific isotopic value. At this time, the lack of facilities for measuring Ni isotopes is currently impractical for commercial use.

In addition to work with Ni isotopes, material was collected to determine $\delta^{65/63}$Cu values in order to study fractionation events in the Duluth Complex. Obtained values are comparable with published data (Sudbury and Stillwater Complex magmatic sulfide; Larson et al, 2003). Recently, a study by Ripley et al. (2015) measured $\delta^{65/63}$Cu values in the Duluth Complex, along with the sulfide-bearing Tamarack and Eagle Intrusions, and the metasedimentary Thomson and Virginia Formations (figure 58). Although the average value for South Kawishiwi and Partridge River Intrusion mineralized material (0.015 ‰) is different than the average for values measured during this study (-0.39 ‰), the two data sets cover the same range and have similar maximum and minimum values. Intriguingly, the average values for Virginia + Thomson Formation material (0.96 ‰) and Eagle + Tamarack material (1.21 ‰) are significantly different than Duluth Complex rock, suggesting significantly different fractionation processes affect the material in those units. Ripley et al. (2015) cannot fully explain this difference, but speculates that two factors may influence the values: the style of mineralization, and the source of the copper in each unit. Regardless, additional future studies involving $\delta^{65/63}$Cu isotope values in high temperature magmatic sulfide deposits would certainly shed light on the involved processes.

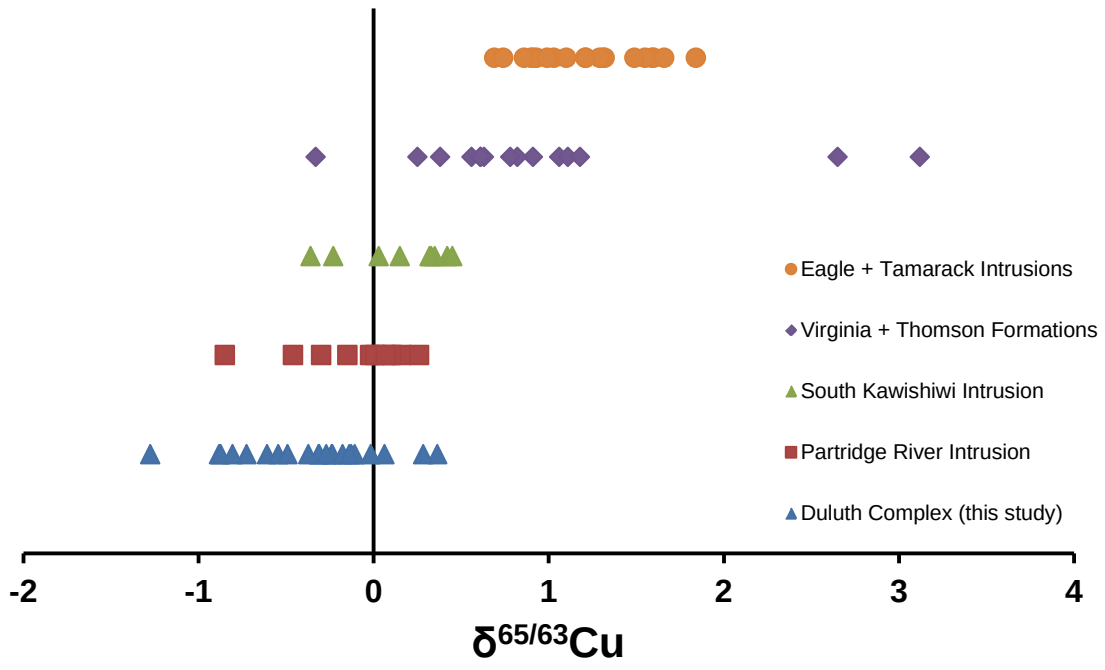

Figure 58: $\delta^{65/63}$Cu isotopic values measured by Ripley et al. (2015) compared to values measured in this study. All the data shown were collected by Ripley et al. (2015) apart from the values represented by the blue triangles. The values for the Eagle and Tamarack Intrusions, and the Virginia and Thomson Formations are grouped due to the similar averages and ranges of the datasets.

9. Works Cited

Albarede, F. and Beard, B. (2004). “Analytical methods for non-traditional isotopes.” *Reviews in Mineralogy and Geochemistry*, Vol. 55, pg. 113–152.

Anbar, A.D. and Rouxel, O. (2007). “Metal stable isotopes in paleoceanography.” *Annual Review of Earth and Planetary Sciences*, Vol. 35, 717–746.

Andres, U. (1977). "Liberation of apatite nepheline ore comminuted by penetrating electric
discharges." *International Journal of Mineral Processing* 4: 33-38.

Andres U. (1989). "Parameters of disintegration of rock by electrical pulses." *Powder Technology* 58: 265-269.

Andres, U., and Bialecki, R. (1986). "Liberation of mineral constituents by high voltage pulses." *Powder Technology* 48: 269-277.

Arribas, I., Bonilla, A., Rodriguez-Avello, A., Maortua, B. (2014). “Characterization of a high quality quartz sample processed applying high voltage (HV) fragmentation.” *Conference Proceedings, 14th International Multidisciplinary Scientific GeoConference SGEM*, Book 1, Vol. 3, pg. 839-850.

Asael, D., Matthews, A., Bar-Matthews, M., Halicz, L. (2007). “Copper isotope fractionation in sedimentary copper mineralization (Timna Valley, Israel).” *Chemical Geology*, Vol. 243, pg. 238-254.

Aspandiar, M.F. and Eggleton, R.A. (2015). “Weathering of chlorite: II. Reactions and products in microsystems controlled by solution avenues.” *Clays and Clay Minerals*, Vol. 50, No. 6, pg. 699-709.

Benko, Z., Mogessie, A., Molnar, F., Severson, M.J., Hauck, S.A., Raič, S. (2015). “Partial melting processes and Cu-Ni-PGE mineralization in the footwall of the South Kawishiwi intrusion at the Spruce Road deposit, Duluth Complex, Minnesota. *Economic Geology*, Vol. 110, no. 5, 1269-1293.

Bizzarro, M.; Birck, J.-L.; Chen, J.; Huss, G.; Lugmair, G.; Mostefaoui, S.; Papanastassiou, D.; Shukolyukov, A.; Quitte, G.; Tachibana, S.; Wadhwa, M. (2007). “Nickel Isotope Anomalies in Meteorites and the 60Fe-60Ni Clock.” *Workshop on the Chronology of Meteorites and the Early Solar System in Kauai, Hawaii.* LPI Contribution No. 1374, p.30-31

Brenan, J.M. and Caciagli, N.C. (2000). “Fe-Ni exchange between olivine and sulphide liquid: Implications for oxygen barometry in sulphide-saturated magmas.” *Geochemica et Cosmochimica Acta*, Vol. 64, No. 2, pg. 307-320.

Bulle, F. and Layne, G.D. (2015). “Element variations in olivine from the Eastern Deeps Intrusion at Voisey’s Bay, Labrador, as a monitor of assimilation and sulfide saturation processes.” *Economic Geology*, Vol. 110, pg. 713-731.

Bulle, F. and Layne, G.D. (2016). “Multi-element variations in olivine as geochemical signatures of Ni-Cu sulfide mineralization in mafic magma systems – examples from Voisey’s Bay and Pants Lake intrusions, Labrador, Canada.” *Miner. Deposita*, Vol. 51, pg. 49-69.

Butt, C.R.M., Nickel, E.H., Brand, N.W. “The weathering of nickel sulfide deposits and implications for geochemical exploration.” *in* Barnes, S.J. *ed*. “Nickel deposits of the Yilgarn Craton: geology, geochemistry, and geophysics applied to exploration.” *Society of Economic Geologists*, Special Publication No. 13, 210 pg.

Cabri, L.J., Rudashevsky, N.S., Rudashevsky, V.N., Oberthür, T. (2008). “Electric-pulse disaggregation (Epd), hydroseparation (Hs) and their use in combination for mineral processing and advanced characterization of ores.” *40th Annual meeting of Canadian mineral processors*, Ottawa, Ontario, Canada.

Cameron, V., Vance, D., Archer, C., House, C.H. (2009). “A biomarker based on the stable isotopes of nickel.” *Proceedings of the National Academy of Sciences of the United States of America*, no. 106, pg. 10944-10948.

Cameron, V. and Vance, D. (2014). “Heavy nickel isotopic compositions in rivers and the ocean.” *Geochemica et Cosmochimica Acta*, Vol. 128, pg. 195-211.

Chandler, V.W. (2002). “Geophysical characteristics of the Duluth Complex and associated rocks” *in* Miller, J.D., Green, J.C., Severson, M.J., Chandler, V.W., Hauck, S.A., Peterson, D.M., and Wahl, T.E. (2002). “Geology and mineral potential of the Duluth Complex and related rocks of northeastern Minnesota.” *Minnesota Geological Survey Report of Investigations 58*: 52-75.

Cook, D.L., Clayton, R.N., Wadhwa, M., Janney, P.E., Davis, A.M. (2008). “Nickel isotopic anomalies in troilite from iron meteorites.” *Geophys Res Lett*, Vol. 35, Issue 1, L01203.

Eckstrand, O.R. and Hulbert, L.J. (2007). “Magmatic nickel-copper-platinum group element deposits” *in* Goodfellow, W.D., ed. “Mineral deposits of Canada: A Synthesis of Major Deposit Types, District Metallogeny, the Evolution of Geological Provinces, and Exploration Methods.” *Geological Association of Canada*, *Mineral Deposits Division*: Special Publications No. 5, pg. 205-222.

Filiberto, J., Jackson, C., Le, L., Treiman, A.H. (2009). “Partitioning of Ni between olivine and an iron-rich basalt: Experiments, partition models, and planetary implications.” *American Mineralogist*, Vol. 94, pg. 256-261.

Finkelshtein G.A., Kurets V.I., Tsukerman V.A. and Isoitko, V.M. (1989). "Selectivity of disintegration by electric pulses." *Obogashchenie Rud* 4: 36-37. (in Russian)

Friedman, I. and O’Neil, J.R. (1977). “Compilation of stable isotope fractionation factors of geochemical interest.” *in* Fleischer, M. (ed.) (1977). “Data of Geochemistry, sixth edition.” *United States Government Printing Office*, Geological Survey Professional Paper 440-KK, 117 pg.

Gál, B., Molnár, F., and Peterson, D.M. (2011) “Cu-Ni-PGE mineralization in the South Filson Creek area, South Kawishiwi intrusion, Duluth Complex: Mineralization styles and magmatic and hydrothermal processes.” *Economic Geology*, Vol. 106, p. 481–509.

Gall, L., Williams, H., Siebert, C., Halliday, A. (2011). “Determination of mass-dependent variations in nickel isotope compositions using double spiking and MC-ICPMS.” *J. Anal. At. Spectrom.*, Vol. 27, pg. 137-145.

Gall, L., Williams, H.M., Siebert, C., Halliday, A.N., Herrington, R.J., Hein, J.R. (2013). “Nickel isotope compositions of ferromanganese crusts and the constancy of deep ocean inputs and continental weathering effects over the Cenozoic.” *Earth and Planetary Science Letters*, Vol. 375, pg. 148-155.

Gueguen, B.; Rouxel, O.; Ponzevera, E.; Bekker, A.; Fouquet, Y. (2013). “Nickel Isotope Variations in Terrestrial Silicate Rocks and Geological Reference Materials Measured by MC-ICP-MS”. *Geostandards and Geoanalytical Research*, Vol. 37, Issue 3, pg. 297-317.

Hart, S.R. and Davis, K.E. (1978). “Nickel partitioning between olivine and silicate melt.” *Earth. Planet. Sci. Lett.*, Vol. 40, pg. 203-219.

Hauck, S., Severson, M., Ripley M., Goldberg S. and Alapieti, T. (1997) “Geology mineralization of the Birch-lake area, South Kawishiwi intrusion, Duluth Complex.” *University of Minnesota Duluth*, Natural Resources Research Institute Report of Investigations NRRI/TR-97/13, 32 p.

Hauck, S. (2015). *Personal Communication.*

Henderson, C.M.B., Redfern, S.A.T., Smith, R.I., Knight, K.S., Charnock, J.M. (2001). “Composition and temperature dependence of cation ordering in Ni-Mg olivine solid solutions: a time-of-flight neutron powder diffraction and EXAFS study.” *American Mineralogist*, Vol. 86, pg. 1170-1187.

Hiebert, R.S., Rouzel, O., Houlé, M.G., Bekker, A. (2014). “Ni isotope fractionation between komatiite and sulfide mineralization at the Neoarchean Hart deposit, Abitibi greenstone belt, Canada.” *2014 Geological Society of America annual meeting*, Vancouver, British Columbia.

Hofmann, A., Bekker, A., Dirks, P., Gueguen, B., Rumble, D., Rouxel, O. (2014). “Comparing orthomagmatic and hydrothermal mineralization models for komatiite-hosted nickel deposits in Zimbabwe using multiple-sulfur, iron, and nickel isotope data.” *Mineralium Deposita*, Vol. 49, Issue 1, pg. 75-100.

Juillot F., Noel V., Morin G., Marchand C., Viollier E., Ona-Nguema G., Brest J., Marakovic G., Brown Jr. G (2015). “Fe and Ni cycling in mangrove sediments from New Caledonia.” *Goldschmidt Abstracts*, 1482.

Kendall, C. and McDonnell, J.J. (1998). “Isotope tracers in catchment hydrology.” Amsterdam: *Elsevier*, 839 pg.

Kinzler, R.J., Grove, T.L., Recca, S.I. (1990). “An experimental study on the effect of temperature and melt composition on the portioning of nickel between olivine and silicate melt.” *Geochemica et Cosmochimica Acta*, Vol. 54, pg. 1255-1265.

Kurets V.I., Usov A.F., Finkelshtein G.A., Shuloyakov A.D., and Shuloyakova, E.A. (1989)."Complex plant for disintegration and separation of rough crystals from productive ores." *Obogashchenie Rud* 4: 40-41. (in Russian)

Langman, J.B., Blowes, D.W., Veeramani, H., Wilson, D., Smith, L., Sego, D.C., Paktunc, D. (2015). “The mineral and aqueous phase evolution of sulfur and nickel with weathering of pyrrhotite in a low sulfide, granitic waste rock.” *Chemical Geology*, Vol. 401, pg. 169-179.

Lapakko, K.A. (1980). “Kinetics and mechanisms of the oxidative dissolution of metal sulfide and silicate minerals present in the Duluth Gabbro.” *University of Minnesota*, M.S. Thesis, 199 pg.

Lapakko, K.A., Eger, A.P., Strudell, J.D. (1986). “Low-cost removal of trace metals from copper-nickel mine drainage.” *U.S. Bureau of Mines*, Final Report, Contract J0205407, 103 pg.

Lapakko, K.A., Olson, M.C., Antonson, D.A. (2013). “Duluth Complex tailings dissolution: ten-year laboratory experiment.” *Minnesota Department of Natural Resources, Division of Lands and Minerals*, 54 pg.

Larson, P.B., Maher, K., Ramos, F.C., Chang, Z., Gaspar, M., Meinert, L.D. (2003). “Copper isotope ratios in magmatic and hydrothermal ore-forming environments.” *Chemical Geology*, Vol. 201, pg. 337-350.

Lee, I. and Ripley, E.M. (1995). “Genesis of Cu-Ni sulfide mineralization in the South Kawishiwi intrusion, Spruce Road area, Duluth Complex, Minnesota.” *Canadian Mineralogist*, Vol. 33, 723-743.

Li, C. and Ripley, E.M. (2009). “Sulfur contents at sulfide-liquid or anhydrite saturation in silicate melts: Empirical equations and example applications.” *Economic Geology*, v. 104, p. 405–412.

Li, C. and Ripley, E.M. (2010). “The relative effects of composition and temperature on olivine-liquid Ni-partitioning: Statistical deconvolution and implications for petrologic modeling.” *Chemical Geology*, Vol. 275, pg. 99-104.

Li, C., Ripley, E.M., Naldrett, A.J. (2003). “Compositional variations of olivine and sulfur isotopes in the Noril’sk and Talnakh intrusions, Siberia: implications for ore-forming processes in dynamic magma conduits.” *Economic Geology*, Vol. 98, pg. 69-86.

Li, H-x., Li, C., Zhang, Z-q. (2012). “Decomposition mechanism of pentlandite during electrochemical bio-oxidation process.” *Trans. Nonferrous Met. Soc. China*, Vol. 22, pg. 731-739.

Lindsay, M.B.J., Moncur, M.C., Bain, J.G., Jambor, J.L., Ptacek, C.J., Blowes, D.W. (2015). “Geochemical and mineralogical aspects of sulfide mine tailings.” *Applied Geochemistry*, Vol. 57, pg. 157-177.

Listerud, W.H. and Meineke, D.G. (1977). “Mineral resources of a portion of the Duluth Complex and adjacent rocks in St. Louis and Lake Counties, northeastern Minnesota.” *Minnesota Department of Natural Resources*, *Division of Minerals*: Report 93, 74 pg.

Locsey, K.L., Grigorescu, M., Cox, M.E. (2012). “Water-rock interactions: an investigation of the relationships between mineralogy and groundwater composition and flow in a subtropical basalt aquifer.” *Aquat. Geochem*, Vol. 18, pg. 45-75.

Maréchal, C.N., Télouk, P., and Albarède, F. (1999). “Precise analysis of copper and zinc isotopic compositions by plasma-source mass spectrometry.” *Chemical Geology*, Vol. 156, pg. 251-273.

Markl, G., Lahaye, Y., Schwinn, G. (2006). “Copper isotopes as monitors of redox processes in hydrothermal mineralization.” *Geochemica et Cosmochimica Acta*, Vol. 70, pg. 4215-4228.

Marna, J.C. (2004). “Magmatic and hydrothermal PGE mineralization of the Birch Lake Cu-Ni-PGE deposit in the South Kawishiwi intrusion, Duluth Complex, northeastern Minnesota.” University of Wisconsin, condensed version of Unpublished M.S. thesis. *University of Minnesota Duluth*, Natural Resources Research Institute Technical Report NRRI/TR-2003/39.

Matzen, A.K., Baker, M.B., Beckett, J.R., Stolper, E.M. (2013). “The temperature and pressure dependence of nickel partitioning between olivine and silicate melt.” *Journal of Petrology*, Vol. 54, No. 12, pg. 2521-2545.

Maurer, W.C. (1968). “Novel drilling techniques”. Oxford: Pergamon Press. 111 pg.

McDonough, W.F. and Sun, S.S. (1995). “The composition of the Earth.” *Chemical Geology*, Vol. 120, no. 3-4, pg. 223-253.

Miller, J.D, (2013). “Field guide to the copper-nickel-platinum group element deposits of the Lake Superior region.” *Precambrian Research Center Guidebook 13-01*: 245p.

Miller, J.D. (2015). *Personal Communication*.

Miller, J.D., Green, J.C., and Severson, M.J. (2002). “Terminology, nomenclature, and classification of Keweenawan igneous rocks of northeastern Minnesota” *in* Miller, J.D., Green, J.C., Severson, M.J., Chandler, V.W., Hauck, S.A., Peterson, D.M., and Wahl, T.E. (2002). “Geology and mineral potential of the Duluth Complex and related rocks of northeastern Minnesota.” *Minnesota Geological Survey Report of Investigations 58*: 5-19

Miller, J.D., Green, J.C., Severson, M.J., Chandler, V.W., Hauck, S.A., Peterson, D.M., and Wahl, T.E. (2002). “Geology and mineral potential of the Duluth Complex and related rocks of northeastern Minnesota.” *Minnesota Geological Survey Report of Investigations 58*: 207 p.

Miller, J.D. and Nicholson, S. (2013). “Geology and mineral deposits of the 1.1Ga midcontinent rift in the Lake Superior region – an overview.” *in* “Field guide to copper-nickel-platinum group element deposits of the Lake Superior region.” *Precambrian Research Center guidebook*, 13-01, pg. 1-50.

Miller, J.D. and Ripley, E.M. (1996). “Layered intrusions of the Duluth Complex, Minnesota, USA” *in* Cawthorn, R.G., ed. “Layered Intrusions.” Amsterdam: *Elsevier Science*, pg. 257-301.

Miller, J.D. and Severson, M.J. (2002). “Geology of the Duluth Complex” in Miller, J.D., Green, J.C., Severson, M.J., Chandler, V.W., Hauck, S.A., Peterson, D.M., and Wahl, T.E. (2002). “Geology and mineral potential of the Duluth Complex and related rocks of northeastern Minnesota.” *Minnesota Geological Survey Report of Investigations 58*: 106-143.

Miller, J.D., Severson, M.J., and Hauck, S.A. (2002). “History of geologic mapping and mineral exploration in the Duluth Complex” *in* Miller, J.D., Green, J.C., Severson, M.J., Chandler, V.W., Hauck, S.A., Peterson, D.M., and Wahl, T.E. (2002). “Geology and mineral potential of the Duluth Complex and related rocks of northeastern Minnesota.” *Minnesota Geological Survey Report of Investigations 58*: 21-51.

Miller, J.D. and Vervoort, J.D. (1996). “The latent magmatic stage of the Midcontinent rift: A period of magmatic underplating and melting of the lower crust.” *Institute on Lake Superior Geology*, *42nd Annual Meeting, Cable, WI*. Proceedings, Vol. 42, Programs and Abstracts, pt. 1, pg. 295-339.

Minnesota Environmental Quality Board. (1979) “Regional Copper–Nickel Study, Water Resources.” *Minnesota Environmental Quality Board*, St. Paul, MN. Vol. 3, Ch. 4. 217 pg.

Morand, P. and Allegre, C.J. (1983). “Nickel isotopic studies in meteorites.” *Earth and Planetary Science Letters*, Vol. 63, pg. 167–176.

Moynier, F.; Blichert-Toft, J.; Telouk, P.; Luck, J.M.; Albarede, F, (2007). “Comparative stable isotope geochemistry of Ni, Cu, Zn, and Fe in chondrites and iron meteorites.” *Geochemica et Cosmochimica Acta*, Vol. 71, pg. 4365-4379.

Naldrett, A.J. (2004). “Magmatic sulfide deposits: geology, geochemistry and exploration.” Berlin, Germany: *Springer*, 727 pg.

Noack, Y., Colin, F., Nahon, D., Delvigne, J., Michaux, L. (1993). “Secondary-mineral formation during natural weathering of pyroxene: review and thermodynamic approach.” *American Journal of Science*, Vol. 293, pg. 111-134.

Paces, J.B. and Miller, J.D. (1993). “Precise U-Pb ages of Duluth Complex and related mafic intrusions, northeastern Minnesota: Geochronological insights to physical, petrogenic, paleomagnetic and tectonomagmatic processes associated with the 1.1 Ga midcontinent rift system.” *Journal of Geophysical Research*, Vol. 98, No. B8, pg. 13997-14013.

Peterson, D.M. (2001). “Development of a conceptual model of Cu-Ni-PGE mineralization in a portion of the South Kawishiwi Intrusion, Duluth Complex, Minnesota.” *Society of Economic Geologists*: Second Annual PGE Workshop, Sudbury, Ontario.

Peterson, D.M. and Severson, M.J. (2002). “Archean and Paleoproterozoic rocks that form the footwall of the Duluth Complex” in Miller, J.D., Green, J.C., Severson, M.J., Chandler, V.W., Hauck, S.A., Peterson, D.M., and Wahl, T.E. (2002a). “Geology and mineral potential of the Duluth Complex and related rocks of northeastern Minnesota.” *Minnesota Geological Survey Report of Investigations 58*: 76-93.

Peterson, D.M. (2008). “Bedrock geologic map of the Duluth Complex in the northern South Kawishiwi intrusion and surrounding area, Lake and St. Louis Counties, Minnesota.” *Natural Resources Research Institute*, Map Series NRRI/MAP-2008-01, Scale 1:20,000.

Peterson, D.M. (2010). “The Nokomis Cu-Ni-PGE Deposit, Minnesota.” *Prospectors and Developers Association of Canada*, *Annual Meeting*. Powerpoint Presentation.

Peterson, D.M. (2015). *Personal Communication*.

Raič, S. (2013). “Arsenic-enriched Cu-Ni-PGE mineralization in Wetlegs, Duluth Complex, St. Louis County, Minnesota, USA.” Master’s thesis project. *Karl-Franzens University of Graz*, *Institute of Earth Sciences, Department of Mineralogy & Petrology*. 130 p.

Rajamani, V. and Naldrett, A.J. (1978). “Partitioning of Fe, Co, Ni and Cu between sulfide liquid and basaltic melts and the composition of Ni-Cu sulfide deposits.” *Econ. Geol.*, Vol. 73, pg. 82-93.

Ratié, G., Jouvin, D., Garnier, J., Rouxel, O., Miska, S., Guimarães, E., Cruz Vieira, L.,Sivry, Y., Zelano, I., Montarges-Pelletier, E., Thil, F., Quantin, C. (2015). “Nickel isotope fractionation during tropical weathering of ultramafic rocks.” *Chemical Geology*, Vol. 402, pg. 68-76.

Ripley, E.M. (1981). “Sulfur isotopic studies of the Dunka Road Cu-Ni deposit, Duluth Complex, Minnesota” *Economic Geology*, Vol. 76, pg. 610–620.

Ripley, E.M. (1986). “Origin and Concentration mechanisms of copper and nickel in Duluth Complex sulfide zones – a dilemma.” *Economic Geology*, Vol. 81, No. 4, pg. 974-978.

Ripley, E.M. (2013). “Sulfide saturation in mafic magmas: Is external sulfur required for magmatic Ni-Cu-(PGE) ore genesis?” *Economic Geology*, v. 108, pg .45–58.

Ripley, E.M., and Al-Jassar, T. (1987) “Sulfur and oxygen isotope studies of melt-country rock interaction, Babbitt Cu-Ni deposit, Duluth Complex: Minnesota.” *Economic Geology*, Vol. 82, pg. 87–107.

Ripley, E.M., Dong, S., Li, C., Wasylenki, L.E. (2015). “Cu isotope variations between conduit and sheet-style sulfide mineralization in the Midcontinent Rift System, North America.” *Chemical Geology*, Vol. 414, pg. 59-68.

Ripley, E.M., and Li, C. (2003). “Sulfur isotope exchange and metal enrichment in the formation of magmatic Cu-Ni-(PGE) deposits.” *Economic Geology*, Vol. 95, pg. 635–641.

Rollinson, H. (1993). “Using geochemical data: evaluation, presentation, interpretation.” *Longman Scientific and Technical*, London, U.K. 352 pg.

Rugel, G., Faestermann, T., Knie, K., Korschinek, G.,Poutivtsev, M., Schumann, D., Kivel, N., Günther-Leopold, I., Weinreich, R. and Wohlmuther, M. (2009). “New measurement of the ^{60}Fe half-life.” *Physical Review Letters*, 103, 072502.

Saini-Eidukat, B and Weiblen, P (1996). “Liberation of Fossils Using High Voltage Electric Pulses.” *Curator,* Vol. 39, pg.139-144.

Schauble, E.A. (2004). “Applying stable isotope fractionation theory to new systems.” *Rev. Mineral. Geochem.*, Vol. 55, No. 1, pg. 65-111.

Selfrag AG (2014). “Basic technology & application in geosciences.” *Powerpoint Presentation*.

Severson, M.J. (1994). “Igneous stratigraphy of the South Kawishiwi intrusion: Duluth Complex, northeastern Minnesota.” *University of Minnesota Duluth, Natural Resources Research Institute*, Technical Report NRRI/TR-93/34, 210 p.

Severson, M. J. (in press): Geologic mapping and structural analysis of the Peter Mitchell Mine: Natural Resources Research Institute, Technical Report NRRI/TR-96/04.

Severson, M.J.; Hauck, S.A. (1990). Geology, geochemistry, and stratigraphy of a portion of the Partridge River intrusion. *Natural Resources Research Institute*, Technical Report NRRI/TR-95/26, pg. 1-185.

Severson, M.J. and Hauck, S.A. (2008). “Finish Logging of Duluth Complex Drill Core (And a
Reinterpretation of the Geology at the Mesaba (Babbitt) Deposit)”, *University of Minnesota Duluth, Natural Resources Research Institute, Technical Report NRRI/TR-2008/17,* 68 p. + 94 plates.

Severson, M.J., Miller, J.D., Peterson, D.M., Green, J.C., Hauck, S.A. (2002). “Mineral potential of the Duluth Complex and related intrusions” *in* Miller, J.D., Green, J.C., Severson, M.J., Chandler, V.W., Hauck, S.A., Peterson, D.M., and Wahl, T.E. (2002). “Geology and mineral potential of the Duluth Complex and related rocks of northeastern Minnesota.” *Minnesota Geological Survey Report of Investigations 58*: 164-200.

Severson, M.J., Peterson, D.M., Ware, A, Boerst, K. (2013). “Cu-Ni-PGE deposits of the Duluth Complex – Geology and Development” *in* Miller, J.D. (2013). “Field guide to the copper-nickel-platinum group element deposits of the Lake Superior region.” *Precambrian Research Center Guidebook 13-01*: 99-158.

Shimamura, T. and Lugmair, G.W. (1983). “Ni isotopic compositions in Allende and other meteorites.” *Earth and Planetary Science Letters*, Vol. 63, 177–188.

Shimazaki, H. and MacLean, W.H. (1976). “An experimental study on the partition of zinc and lead between silicate and sulfide liquids.” *Mineralium Deposita II*, pg. 125-132.

Shuloyakov A.D., Lupal C.D., and Tarakanovsky, E.N. (1989). "Plant for preferred disintegration of geological samples (DIK-1M)." *Obogashchenie Rud* 4: 45 (in Russian).

SRK Consulting. (2007). “RS53/RS42 - Waste rock characteristics/waste water quality modeling – waste rock and lean ore – NorthMet project.” *SRK Consulting*, Project Number 1UP005.001, 846 pg.

Sobolev, A.V., Hofmann, A.W., Kuzmin, D.V., Yaxley, G.M., Arndt, N.T., Chung, S-L., Danyushevsky, L.V., Elliott, T., Frey, F.A., Garcia, M.O., Gurenko, A.A., Kamenetesky, V.S., Nikogosian, I.K., Rocholl, A., Sigurdsson, I.A., Sushchevskaya, N.M., Teklay, M. (2007). “The amount of recycled crust in sources of mantle-derived melts.” *Science*, Vol. 316, pg. 412-417 and pg. S1-S9.

Steiner, A. (2014). “Genesis of sulfide mineralization within the granite footwall of the Maturi deposit of the South Kawishiwi intrusion, Duluth Complex, NE Minnesota.” *University of Minnesota Duluth*, condensed version of unpublished M.S. thesis. 211 pg.

Takahashi, E. (1978). “Partitioning of Ni^{2+}, Co^{2+}, Fe^{2+}, Mn^{2+}, and Mg^{2+} between olivine and silicate melts: compositional dependence of partition coefficient.” *Geochemica et Cosmochimica Acta*, Vol. 42, pg. 1829-1844.

Tanimizu, M. and Hirata, T. (2006). “Determination of natural isotopic variation in nickel using inductively coupled plasma mass spectrometry.” *Journal of Analytical Atomic Spectrometry*, Vol. 21, pg. 1423-1426.

ten Berge, H.F.M., van der Meer, H.G., Steenhuizen, J.W., Goedhart, P.W., Knops, P., Verhagen, J. (2012). “Olivine weathering in soil, and its effects on growth and nutrient uptake in ryegrass (*Lolium perenne* L.): a pot experiment.” *PLOS ONE*, Vol. 7, Iss. 8, pg. 1-8

Twin Metals (2014). “Duluth Metals Announces SEDAR filing of updated AMEC Resource Study on Twin Metals.” *Twin Metals*. N.p., Accessed 11-20-2015. http://www.twin-metals.com/duluth-metals-announces-sedar-filing-of-updated-amec-resource-study-on-twin-metals/

Velbel, M.A. (1985). “Geochemical mass balances and weathering rates in forested watersheds of the southern Blue Ridge.” *American Journal of Science*, Vol. 285, pg. 904-930.

Velbel, M.A. (2009). “Dissolution of olivine during natural weathering.” *Geochimica et Cosmochimica Acta*, Vol. 73, pg. 6098-6113.

Wang, E., Shi, F., Manlapig, E. (2011). “Pre-weakening of mineral ores by high voltage pulses.” *Minerals Engineering*, Unknown volume, pg. 1-8.

Wang, E., Shi, F., Manlapig, E. (2012a). “Factors affecting electrical comminution performance.” *Minerals Engineering*, Vol. 34, pg. 48-54.

Wang, E., Shi, F., Manlapig, E. (2012b). “Mineral liberation by high voltage pulses and conventional comminution with same specific energy levels.” *Minerals Engineering*, Unknown volume, pg. 1-9.

Warren, M.R., Hanley, J.J., Ames, D.E., Jackson, S.E. (2015). “The Ni-Cr-Cu content of biotite as pathfinder elements for magmatic sulfide exploration associated with mafic units of the Sudbury Igneous Complex, Ontario, Canada.” *Journal of Geochemical Exploration*, Vol. 153, pg. 11-29.

Wasylenki, L.E., Howe, H.D., Spivak-Birndorf, L.J., Bish, D.L. (2015). “Ni isotope fractionation during sorption to ferrihydrite: implications for Ni in banded iron formations.” *Chemical Geology*, Vol. 400, pg. 56-64.

Weiblen, P.W. and Morey, G.B. (1980). “A summary of the stratigraphy, petrology, and structure of the Duluth Complex.” *American Journal of Science*, Vol. 280-A, pg. 88-133.

Weiblen, P.W. (1994). “A novel electric pulse method for obtaining clean mineral separates for geochemical and geophysical research.” EOS, *Transactions of the Americal Geophysical Union*, Vol. 75, 75 pg.

White, C. (2010). “The petrology, petrogenesis, and metallogenesis of the South Kawishiwi intrusion in the Nokomis deposit area, Duluth Complex, northeastern Minnesota.”
University of Minnesota Duluth, condensed version of unpublished M.S. thesis. 221 pg.

Yang, S-H., Maier, W.D., Hanski, E.J., Lappalainen, M., Santaguida, F., Määttä, S. (2013). “Origin of ultra-nickeliferous olivine in the Kevitsa Ni-Cu-PGE-mineralized intrusion, northern Finland. *Contrib. Mineral. Petrol.*, Vol. 166, pg. 81-95.

Zanko, L.M., Severson, M.J., and Ripley, E.M. (1994) “Geology and mineralization of the Serpentine copper-nickel deposit.” *University of Minnesota Duluth*, Natural Resources Research Institute Report of Investigations NRRI/TR-93/52.

Zhu, X.K., O’Nions, R.K., Guo, Y., Belshaw, N.S., Rickard, D. (2000). “Determination of natural Cu-isotope variation by plasma-source mass spectrometry: implications for use as a geochemical tracers.” *Chemical Geology*, Vol. 163, pg. 139-149.

10. Appendix 1

This section contains numerical data from geochemical and isotopic analyses, along with quantitative EDS data from the SEM and microprobe analyses. Additional images and spectra from XRD, SEM, and microprobe can be seen in Appendix 2 and the supplementary data file attached to this document.

Table A1-1: This table, along with Table A1-2, shows the samples that were processed and analyzed during the course of this project. Data types in this table include new sample material (thin and polished sections, EPD products), and numerical data (geochemistry and PGE Assay. Additional data types and information can be seen below in Table A1-2.

Sample	Deposit or Location	Thin Section	Polished Section	EPD	Geochemistry	PGE Assay
T4	II				X	X
O5-B	II				X	
O6-A	II	X				
O6-B	II				X	
O7-A	II					
DNR-8	II		X		X	
DNR-9	II				X	
T2	I				X	
T3	I				X	
O3-G	I				X	X
O3-H	I			X		
O4-B	I				X	
O8-D	I				X	x
KEA-1 (A')	I	X			X	
KEA-1 (B')	I		X			X
KEA-1 (C')	I		X	X	X	
DNR-10	III		X		X	
DNR-11	III			X	X	X
SP-2a	Serpentine					

Sample	Deposit or Location	Thin Section	Polished Section	EPD	Geochemistry	PGE Assay
SP-2b	Serpentine		X		X	X
SP-4a	Serpentine	X				
SP-4b	Serpentine				X	
DNR-1	Serpentine				X	
S1-11	Serpentine				X	
S4-11 (458-458.5')	Serpentine				X	X
S4-11 (458.5-459')	Serpentine		X			
TCK-1b	Mesaba					
TCK-1c	Mesaba	X				
TCK-2	Mesaba				X	
TCK-3a	Mesaba				X	
TCK-4a	Mesaba				X	
MB-07-01	Mesaba		X	X (2)	X	
MB-07-02	Mesaba	X	X (2)		X	
MB-07-07 (4-5')	Mesaba				X	
MB-07-07 (390')	Mesaba	X				
MB-07-07 (1106')	Mesaba		X		X	X
MB-07-07 (1110.5')	Mesaba		X	X (2)	X	
MB-07-16	Mesaba				X	
MB-07-22	Mesaba				X	
T9	NorthMet				X	
T10	NorthMet				X	
PLM-1	NorthMet				X	
PLM-2A #1	NorthMet				X	X
PLM-2B	NorthMet	X				
PLM-4B	NorthMet					
PLM-4C	NorthMet				X	
05-420c	NorthMet	X	X		X	
07-536c	NorthMet			X	X	
07-537c	NorthMet				X	

Sample	Deposit or Location	Thin Section	Polished Section	EPD	Geochemistry	PGE Assay
10-579c (15')	NorthMet			X		
10-579c (36')	NorthMet				X	X
10-590D (16')	NorthMet			X		
10-599D (165')	NorthMet		X		X	
DNR-2	Wyman Creek				X	
DNR-3	Wyman Creek	X	X			
DNR-4	Wyman Creek					
DNR-5	Wetlegs			X	X	
DNR-6	Wetlegs		X		X	
T1	Newton Belt				X	
O1-B	Newton Belt				X	
O1-C	Newton Belt					
T6	Jack's Rock				X	
NLM-3A	Nickel Lake				X	
T7	Bald Eagle				X	
O11-B	Bald Eagle			X		
O11-C	Bald Eagle	X			X	X
O12	Bald Eagle				X	
O13-B	Bald Eagle				X	
StE-1	St. Egidien				X	
Eagle-1	Eagle Deposit, MI					
Eagle-2	Eagle Deposit, MI					
SLC-88	Sturgeon Lake, ON, Canada					
O-528	Bingham Mine, UT					
O-574	Morenci, AZ					
G-11	Greens Creek, AK					
R-1	Rammelsberg, Germany					

Table A1-2: This table is a continuation of table A1-1, and includes information about which samples were analyzed using XRD, Ni and Cu isotopes, SEM, and Microprobe.

Sample	XRD	Ni Isotopes	Cu Isotopes	SEM	Microprobe
T4		X			
O5-B			X		
O6-A					
O6-B	X	X			
O7-A	X				
DNR-8			X	X	X
DNR-9		X			
T2		X			
T3			X		
O3-G			X		
O3-H					
O4-B	X	X			
O8-D			X		
KEA-1 (A')			X		X
KEA-1 (B')		X			
KEA-1 (C')			X		
DNR-10			X		
DNR-11		X	X		
SP-2a		X			
SP-2b			X	X	X
SP-4a					
SP-4b	X	X	X		
DNR-1					
S1-11		X			
S4-11 (458-458.5')		X	X		
S4-11 (458.5-459')					
TCK-1b	X				
TCK-1c				X	X
TCK-2	X	X	X		
TCK-3a	X	X			
TCK-4a			X		
MB-07-01		X	X		
MB-07-02				X	X
MB-07-07 (4-5')					
MB-07-07 (390')				X	X
MB-07-07 (1106')		X	X		
MB-07-07 (1110.5')				X	
MB-07-16					
MB-07-22					
T9		X	X		
T10					
PLM-1					
PLM-2A #1			X		
PLM-2B					

Sample	XRD	Ni Isotopes	Cu Isotopes	SEM	Microprobe
PLM-4B	X				
PLM-4C	X	X			
05-420c					
07-536c			X		
07-537c					
10-579c (15')		X			
10-579c (36')		X	X		
10-590D (16')					
10-599D (165')					
DNR-2			X		
DNR-3					
DNR-4		X			
DNR-5		X (2)			
DNR-6			X		
T1					
O1-B					
O1-C		X			
T6		X			
NLM-3A					
T7					
O11-B					
O11-C			X		
O12	X (2)	X			
O13-B					
StE-1		X			
Eagle-1			X		
Eagle-2			X		
SLC-88			X		
O-528			X		
O-574			X		
G-11			X		
R-1			X		

Table A2-1: Major and minor element by oxide; samples analyzed at ActLabs.

Sample	SiO2	Al2O3	Fe2O3(T)	MnO	MgO	CaO	Na2O	K2O	TiO2	P2O5	S	LOI	Total
	%	%	%	%	%	%	%	%	%	%	%	%	%
T1	62.13	14.17	5.61	0.05	1.98	2.31	2.70	2.19	0.54	0.19	0.02	6.75	98.63
T3	45.51	18.05	12.86	0.15	8.34	6.80	2.33	0.35	1.43	0.16	0.04	4.58	100.60
T4	44.34	16.05	13.27	0.13	7.91	5.70	2.18	0.39	0.89	0.19	0.13	6.96	98.00
T6	52.77	17.76	6.46	0.06	2.36	4.18	2.00	0.96	0.78	0.06	0.04	11.11	98.51
T7	44.83	19.48	11.24	0.12	7.10	6.16	1.94	0.51	0.87	0.08	0.03	8.64	101.00
T9	58.61	14.24	7.76	0.08	1.66	2.17	2.39	1.77	0.96	0.17	0.03	8.80	98.60
O1-B	49.45	13.54	13.03	0.20	6.90	11.47	1.14	0.48	1.35	0.13	0.09	3.09	100.80
O3-G	45.71	19.26	13.49	0.13	8.26	8.48	2.60	0.27	0.38	0.04	1.08	0.58	99.19
O5-B	47.52	23.68	9.12	0.05	3.41	8.95	3.22	0.49	0.53	0.05	0.37	3.56	100.60
O8-D	43.96	16.00	17.00	0.15	8.75	7.70	2.04	0.44	1.42	0.13	0.46	1.86	99.46
O11-C	44.06	13.44	19.26	0.18	12.1	6.39	1.93	0.23	0.73	0.04	0.69	1.35	99.72
O12	51.52	25.85	4.94	0.05	2.58	10.91	3.78	0.35	0.36	0.02	0.08	0.41	100.80
PLM-2A	45.54	17.88	14.69	0.11	6.20	8.33	2.42	0.38	1.04	0.13	1.15	2.23	98.96
TCK-4A	47.84	21.27	9.93	0.09	4.42	9.80	2.87	0.55	1.08	0.15	0.16	1.39	99.38
SP-2B	15.88	4.02	61.97	0.04	1.01	0.44	0.75	1.59	0.37	0.06	17.50	11.45	97.58
SP-4B	54.99	14.34	11.95	0.17	3.21	4.82	3.05	0.99	1.01	0.08	0.99	3.65	98.25
10-579c	46.98	15.81	13.15	0.14	4.46	7.35	2.95	0.91	4.53	0.92	1.12	0.11	97.31
MB-07-07 1106	42.06	15.49	18.57	0.17	6.23	3.06	2.06	3.00	0.40	0.05	4.61	7.15	98.24
MB-07-07 1110.5	58.29	14.30	5.12	0.11	1.95	11.36	2.37	1.04	0.44	0.20	0.84	5.21	100.40
S4-11	30.09	8.23	35.81	0.20	3.66	6.96	1.70	0.66	5.25	0.45	4.73	2.17	95.17
KEA-1 (C')	1.90	0.45	77.11	0.02	0.13	0.61	0.07	0.27	0.05	0.01	>20.00	13.09	93.71
DNR-2	34.50	0.94	43.38	0.40	7.76	9.03	0.24	0.15	0.05	1.08	4.11	1.55	99.09
DNR-6	43.30	17.91	18.18	0.12	5.26	8.49	2.66	0.71	1.21	0.21	3.02	1.25	99.30
DNR-8	40.73	7.93	21.61	0.22	17.49	4.63	1.29	0.49	2.13	0.18	1.43	1.28	98.00
DNR-10	6.37	3.83	81.34	0.26	4.93	0.65	0.08	0.03	5.92	< 0.01	0.30	-2.43	101.00
DNR-11	45.82	17.35	15.37	0.16	6.39	8.21	2.78	0.55	1.45	0.20	2.37	0.24	98.54

Table A2-2: Major and minor element by oxide; samples analyzed at the University of Western Ontario.

Sample	SiO_2	TiO_2	Al_2O_3	Fe_2O_3	MnO	MgO	CaO	Na_2O	K_2O	P_2O_5	Cr_2O_3	BaO	SrO	L.O.I.	Total
	%	%	%	%	%	%	%	%	%	%	%	%	%	%	%
T2	52.07	0.84	14.92	7.87	0.06	2.19	2.51	2.47	1.38	0.15	0.01	0.05	0.04	14.88	99.46
T10	63.48	0.68	13.06	5.92	0.07	1.38	2.55	2.97	1.87	0.17	0.01	0.05	0.04	7.43	99.68
O4-B	42.51	0.77	12.64	19.95	0.16	15.77	5.90	1.47	0.23	0.08	0.11	0.01	0.02	0.00	99.61
O6-B	48.69	0.66	24.33	5.35	0.06	2.02	11.70	3.56	0.78	0.02	0.03	0.02	0.05	2.37	99.64
O13-B	32.78	0.67	9.35	19.55	0.37	23.58	0.55	0.01	0.03	0.03	0.09	0.01	0.01	12.94	99.95
PLM-1	56.60	0.96	13.80	12.23	0.09	2.96	3.06	2.45	1.75	0.25	0.01	0.04	0.04	5.55	99.78
PLM-4C	46.25	4.09	13.29	16.95	0.16	5.30	8.98	2.40	1.18	0.31	0.02	0.03	0.02	0.85	99.80
TCK-2	56.83	1.22	13.81	10.37	0.09	2.32	2.68	2.28	1.61	0.20	0.02	0.03	0.03	8.11	99.59
TCK-3A	44.19	1.49	15.89	16.80	0.15	11.16	7.47	2.09	0.39	0.17	0.02	0.01	0.03	0.01	99.87
NLM-3A	47.74	0.97	20.66	10.98	0.11	5.54	9.80	3.07	0.39	0.05	0.04	0.01	0.04	0.00	99.40
05-420C	46.30	0.45	20.78	10.73	0.11	8.82	9.17	2.46	0.32	0.04	0.01	0.01	0.03	0.32	99.55
07-536C	46.41	0.62	21.46	9.68	0.11	7.48	9.45	2.29	0.55	0.04	0.01	0.01	0.03	1.31	99.46
07-537C	43.97	1.27	14.69	17.78	0.17	11.70	7.13	1.71	0.47	0.16	0.04	0.01	0.02	0.29	99.40
10-599D	44.45	2.76	15.13	18.75	0.15	6.30	8.62	2.42	0.67	0.30	0.02	0.01	0.02	0.00	99.60
MB-07-01	42.34	2.43	11.73	22.50	0.18	11.21	6.43	1.68	0.74	0.26	0.03	0.01	0.02	0.00	99.56
MB-07-02	46.29	1.40	16.38	18.54	0.11	6.24	5.94	2.57	0.50	0.16	0.04	0.01	0.03	1.33	99.53
MB-07-07 (390')	46.32	0.39	22.59	9.08	0.08	5.32	10.65	2.74	0.39	0.06	0.02	0.01	0.04	2.00	99.70
MB-07-16	55.21	0.68	14.99	8.81	0.02	2.55	0.38	0.89	4.74	0.10	0.03	0.05	0.01	11.15	99.59
MB-07-22	40.22	2.24	11.91	20.62	0.15	8.51	6.14	1.75	0.69	0.36	0.01	0.00	0.02	7.23	99.84
S1-11	41.96	2.19	12.63	23.09	0.17	10.01	6.84	1.75	0.61	0.24	0.04	0.01	0.02	0.19	99.75
KEA-1 (A')	51.25	1.75	9.76	16.00	0.18	12.43	5.17	1.52	0.82	0.27	0.08	0.01	0.03	0.44	99.71
DNR-1	28.88	1.10	11.17	40.57	0.01	4.24	2.53	1.47	1.46	0.09	0.03	0.04	0.02	6.63	98.24
DNR-5	39.22	1.36	5.61	23.80	0.22	23.13	3.12	0.28	0.32	0.16	0.29	0.01	0.01	2.05	99.58

Table A2-2 Cont.: Major and minor element by oxide; samples analyzed at the University of Western Ontario.

Sample	SiO_2	TiO_2	Al_2O_3	Fe_2O_3	MnO	MgO	CaO	Na_2O	K_2O	P_2O_5	Cr_2O_3	BaO	SrO	L.O.I.	Total
	%	%	%	%	%	%	%	%	%	%	%	%	%	%	%
DNR-9	47.73	0.89	23.68	8.87	0.07	2.65	10.31	3.38	0.58	0.12	0.05	0.03	0.05	1.23	99.64
StE-1	80.82	0.01	0.03	0.29	0.02	7.13	0.01	0.01	0.03	0.01	0.01	0.01	0.00	7.64	96.02

Table A3-1: Large ion lithophile, high field strength element, and high technology metal concentrations. Samples analyzed at ActLabs.

Sample	Rb	Cs	Sr	Ba	Zr	Nb	Hf	Th	U	Y	Tl	Ge	Ta
	ppm	ppm	ppm	ppm	ppm	ppm	ppm	ppm	ppm	ppm	ppm	ppm	ppm
T1	61	2.3	520	645	169	5	4.1	4.4	1.1	14	0.3	< 1	0.5
T3	11	1.1	269	155	97	5	2.1	2.0	0.5	10	< 0.1	1	0.6
T4	10	1.8	337	159	80	4	1.8	1.1	0.4	22	< 0.1	1	0.3
T6	31	2.3	231	369	107	6	2.6	2.5	1.1	9	< 0.1	1	0.5
T7	11	0.5	269	235	39	3	1.0	1.4	0.4	5	< 0.1	< 1	0.3
T9	63	2.9	319	544	176	10	4.9	5.2	1.6	12	0.4	2	0.9
O1-B	11	< 0.5	125	82	93	3	2.4	0.4	0.1	31	< 0.1	1	0.2
O3-G	4	< 0.5	295	98	24	1	0.5	0.4	0.1	2	< 0.1	< 1	0.9
O5-B	13	1.2	399	164	58	2	1.3	1.8	0.6	6	< 0.1	< 1	0.2
O8-D	13	0.9	265	151	85	6	2.0	1.0	0.3	12	< 0.1	1	0.7
O11-C	4	0.6	249	109	47	2	1.2	0.5	0.2	6	< 0.1	1	0.2
O12	2	< 0.5	426	133	11	< 1	< 0.2	< 0.1	< 0.1	< 2	< 0.1	< 1	< 0.1
PLM-2A	10	0.7	229	144	86	5	2.0	1.3	0.5	13	< 0.1	1	0.4
TCK-4A	12	1.3	331	180	101	6	2.4	1.6	0.5	16	< 0.1	1	0.5
SP-2B	50	2.0	43	211	61	3	1.3	3.1	1.2	7	0.2	< 1	0.4
SP-4B	48	3.2	225	245	143	6	3.6	2.6	0.7	15	0.8	2	0.6
10-579c	28	1.5	252	284	116	21	2.9	3.0	1.7	29	0.2	2	1.6
MB-07-07 1106	116	10.4	207	275	50	3	1.4	2.8	1.2	11	1.5	1	0.6
MB-07-07 1110.5	21	1.8	205	41	190	7	4.6	12.7	7.3	30	0.1	2	0.7
S4-11	16	0.6	137	226	182	23	4.3	1.8	0.7	27	< 0.1	1	2.0
KEA-1 (C')	12	0.6	9	25	5	1	0.3	0.4	0.1	< 2	0.1	< 1	< 0.1
DNR-2	6	1.9	77	24	11	< 1	0.3	0.6	0.3	19	< 0.1	2	0.3
DNR-6	15	0.9	275	191	119	7	2.8	1.5	0.5	18	< 0.1	1	1.4
DNR-8	16	1.8	126	154	139	9	3.0	1.3	0.5	17	< 0.1	1	0.7
DNR-10	< 2.0	< 0.5	9	6	33	5	1.2	< 0.1	< 0.1	< 2	< 0.1	5	0.6
DNR-11	12	0.8	358	214	88	5	2.2	1.3	0.6	15	< 0.1	1	0.4

Table A3-2: Large ion lithophile, high field strength element, and high technology metal concentrations. Samples analyzed at the University of Western Ontario.

Sample	Rb	Cs	Sr	Ba	Zr	Nb	Hf	Th	U	Y	Tl	Ge	Ta
	ppm	ppm	ppm	ppm	ppm	ppm	ppm	ppm	ppb	ppm	ppb	ppm	ppm
T2	111	3.55	450	927	461	13.2	8	8.6	2017	17	367	6	1
T10	63	1.04	195	432	273	5.3	5	3.9	968	9	200	5	1
O4-B	7	0.20	156	70	49	2.7	1	0.5	167	5	200	5	1
O6-B	58	7.74	483	234	75	4.0	1	0.7	229	11	200	5	1
O13-B	1	0.10	55	10	5	0.4	0	0.0	16	2	200	5	1
PLM-1	125	3.46	317	802	543	13.0	10	8.4	5063	28	462	7	1
PLM-4C	142	3.93	360	900	614	14.7	11	9.0	5427	32	513	8	1
TCK-2	129	3.92	302	797	659	4.7	11	7.6	3188	26	477	7	1
TCK-3A	21	0.86	260	265	211	11.4	4	2.2	737	22	200	9	1
NLM-3A	13	0.21	364	246	42	1.2	1	0.3	90	9	200	6	1
05-420c	11	1.13	291	165	37	1.9	1	0.4	143	5	200	6	1
07-536c	36	2.50	300	323	48	2.8	1	0.5	183	6	200	5	1
07-537c	14	0.55	152	115	88	5.1	2	0.8	252	11	200	5	1
10-599D	52	1.50	206	345	458	22.6	8	4.7	1583	47	200	10	2
MB-07-01	73	2.22	1	336	463	20.2	8	5.9	1810	41	200	12	2
MB-07-02	13	0.52	144	143	96	8.2	2	0.4	462	13	200	5	1
MB-07-07 (390')	23	0.62	329	187	86	3.9	2	1.0	327	8	200	5	1
MB-07-16	438	14.35	161	757	347	14.2	7	14.7	29684	48	5243	7	1
MB-07-22	68	2.40	299	358	470	23.7	8	6.2	1825	48	306	10	2
S1-11	55	2.10	326	302	382	19.4	7	3.6	1146	34	200	12	1
KEA-1 (A')	78	3.62	259	366	368	13.3	6	3.9	1002	29	238	9	1
DNR-1	65	1.10	124	416	159	5.6	3	10.2	716	11	224	7	1
DNR-5	33	3.13	136	205	212	10.7	4	1.9	603	23	200	13	755

Table A3-2 Cont.: Large ion lithophile, high field strength element, and high technology metal concentrations. Samples analyzed at the University of Western Ontario.

Sample	Rb	Cs	Sr	Ba	Zr	Nb	Hf	Th	U	Y	Tl	Ge	Ta
	ppm	ppm	ppm	ppm	ppm	ppm	ppm	ppm	ppb	ppm	ppb	ppm	ppm
DNR-9	28	1.83	462	394	139	2.1	2	1.5	557	14	200	5	1
StE-1 -1	9	6.13	1	5	N/A	0.0	N/A	N/A	8632	N/A	3161	5	1

Table A4-1: Rare earth element concentrations. Samples analyzed at ActLabs.

Sample	La	Ce	Pr	Nd	Sm	Eu	Gd	Tb	Dy	Ho	Er	Tm	Yb	Lu
	ppm	ppm	ppm	ppm	ppm	ppm	ppm	ppm	ppm	ppm	ppm	ppm	ppm	ppm
T1	17.7	41.4	4.3	17.4	3.1	0.7	2.1	0.3	1.7	0.3	1.0	0.2	1.0	0.2
T3	11.7	38.4	3.2	13.9	2.8	1.1	2.5	0.4	2.1	0.4	1.1	0.2	1.1	0.2
T4	9.1	20.2	2.6	11.1	2.2	0.9	1.8	0.3	1.6	0.3	0.9	0.1	0.8	0.1
T6	11.8	22.8	2.7	10.2	1.9	0.7	1.5	0.2	1.6	0.3	1.0	0.2	1.1	0.2
T7	4.9	13.5	1.3	5.5	1.2	0.6	0.9	0.2	0.9	0.2	0.5	0.1	0.6	0.1
T9	18.7	45.2	4.6	17.5	3.3	0.9	2.7	0.4	2.2	0.5	1.4	0.2	1.4	0.2
O1-B	5.5	15.2	2.3	12.5	3.9	1.3	4.7	0.8	5.5	1.1	3.4	0.5	3.5	0.6
O3-G	4.0	8.6	1.1	4.7	0.9	0.7	0.9	0.1	0.8	0.1	0.4	0.1	0.4	0.1
O5-B	7.2	15.7	1.9	8.0	1.6	1.2	1.3	0.2	1.2	0.2	0.7	0.1	0.6	0.1
O8-D	8.2	18.5	2.4	10.9	2.6	1.0	2.5	0.4	2.5	0.5	1.3	0.2	1.4	0.2
O11-C	4.0	8.9	1.2	5.6	1.3	0.6	1.2	0.2	1.2	0.2	0.7	0.1	0.7	0.1
O12	2.3	4.1	0.5	2.0	0.4	0.8	0.3	0.1	0.3	0.1	0.1	< 0.05	0.1	0.0
PLM-2A	9.5	21.3	2.8	12.8	2.9	1.1	2.7	0.4	2.7	0.5	1.5	0.2	1.4	0.2
TCK-4A	10.9	24.3	3.1	13.7	3.1	1.5	2.8	0.4	2.6	0.5	1.4	0.2	1.4	0.2
SP-2B	10.7	22.4	2.8	11.4	2.3	0.4	1.9	0.3	1.7	0.3	0.8	0.1	0.8	0.1
SP-4B	24.9	45.6	4.8	18.2	2.9	1.8	2.3	0.4	2.6	0.6	1.8	0.3	2.3	0.4
10-579c	27.2	64.1	8.5	38.8	8.3	1.7	7.3	1.1	5.8	1.1	2.9	0.4	2.5	0.4
MB-07-07 1106’	16.5	30.3	3.5	13.1	2.3	1.3	1.9	0.3	1.9	0.4	1.2	0.2	1.5	0.3
MB-07-07 1110.5’	30.2	61.1	7.5	30.8	6.0	1.7	5.1	0.8	4.7	1.0	2.8	0.4	2.8	0.4
S4-11	18.4	44.7	6.1	28.4	6.8	1.8	6.5	1.1	6.2	1.2	3.3	0.5	3.2	0.5
KEA-1 (C’)	1.4	2.9	0.3	1.1	0.2	< 0.05	< 0.1	< 0.1	< 0.1	< 0.1	< 0.1	< 0.05	< 0.1	< 0.04
DNR-2	12.8	21.5	2.4	10.0	1.9	0.6	2.3	0.3	1.9	0.5	1.4	0.2	1.0	0.2
DNR-6	14.5	32.2	4.1	18.2	4.2	1.5	3.9	0.6	3.5	0.7	1.9	0.3	1.9	0.3
DNR-8	11.6	26.9	3.5	16.4	3.8	1.2	3.7	0.6	3.4	0.7	1.8	0.3	1.9	0.3
DNR-10	1.1	2.6	0.3	1.6	0.5	0.1	0.4	< 0.1	0.3	< 0.1	0.2	< 0.05	0.2	< 0.04
DNR-11	12.2	27.7	3.6	16.4	3.9	1.5	3.5	0.6	3.2	0.6	1.8	0.3	1.7	0.3

Table A4-2: Rare earth element concentrations. Samples analyzed at the University of Western Ontario.

Sample	La	Ce	Pr	Nd	Sm	Eu	Gd	Tb	Dy	Ho	Er	Tm	Yb	Lu
	ppb	ppb	ppb	ppb	ppb	ppb	ppb	ppb	ppb	ppb	ppb	ppb	ppb	ppb
T2	29109	65154	7825	31833	6161	1825	5503	723	3774	739	2210	312	2089	328
T10	12343	42097	3320	13345	2681	817	2645	359	1915	376	1109	156	1050	162
O4-B	3762	8296	1084	4763	1082	592	1170	183	1064	212	607	83	550	87
O6-B	7164	14850	1941	8842	2262	1978	2546	422	2508	499	1394	194	1203	184
O13-B	1609	2697	334	1457	365	248	446	78	484	99	286	38	231	40
PLM-1	36364	87755	10122	41656	8392	2220	8214	1128	6113	1207	3508	493	3198	500
PLM-4C	40860	98045	11240	46176	9283	2421	9010	1245	6741	1314	3861	535	3479	554
TCK-2	32700	75096	8599	34667	6896	1902	6730	945	5261	1057	3131	449	2960	469
TCK-3A	17212	38216	4967	21770	5045	2460	5339	830	4745	942	2629	364	2344	367
NLM-3A	6066	11729	1526	7006	1770	2001	1992	321	1895	379	1088	149	955	154
05-420c	5056	9364	1157	5029	1104	1330	1203	183	1065	211	631	89	596	93
07-536c	6444	11537	1425	6087	1323	1688	1457	219	1250	254	731	100	667	110
07-537c	8046	17572	2266	10002	2292	932	2532	398	2332	476	1385	195	1277	207
10-599D	30962	70253	9180	40890	9827	3060	10739	1711	10139	2036	5800	800	5117	806
MB-07-01	29761	67446	8786	38525	9155	2978	9772	1529	9023	1790	5157	705	4526	705
MB-07-02	15125	28387	3330	13286	2651	2321	2821	433	2633	573	1834	286	1989	328
MB-07-07 (390')	8584	17478	2182	9227	1978	1810	2058	309	1746	341	972	130	836	132
MB-07-16	51349	100835	12809	50783	10360	2420	10508	1587	9164	1879	5762	850	5855	965
MB-07-22	35447	81350	10656	47083	11016	3283	11899	1841	10667	2112	5973	805	5051	763
S1-11	24554	56035	7319	32491	7673	2702	8221	1282	7547	1480	4261	587	3746	587
KEA-1 (A')	24526	54521	7021	30763	6820	1713	7297	1100	6279	1268	3674	508	3305	529
DNR-1	39518	81132	9922	39706	6432	1196	5798	609	2640	473	1338	167	1129	182
DNR-5	15829	36017	4715	21054	4902	1463	5242	816	4762	946	2716	382	2440	392
DNR-9	13235	28467	3620	15693	3475	2037	3652	546	3115	610	1730	236	1472	231

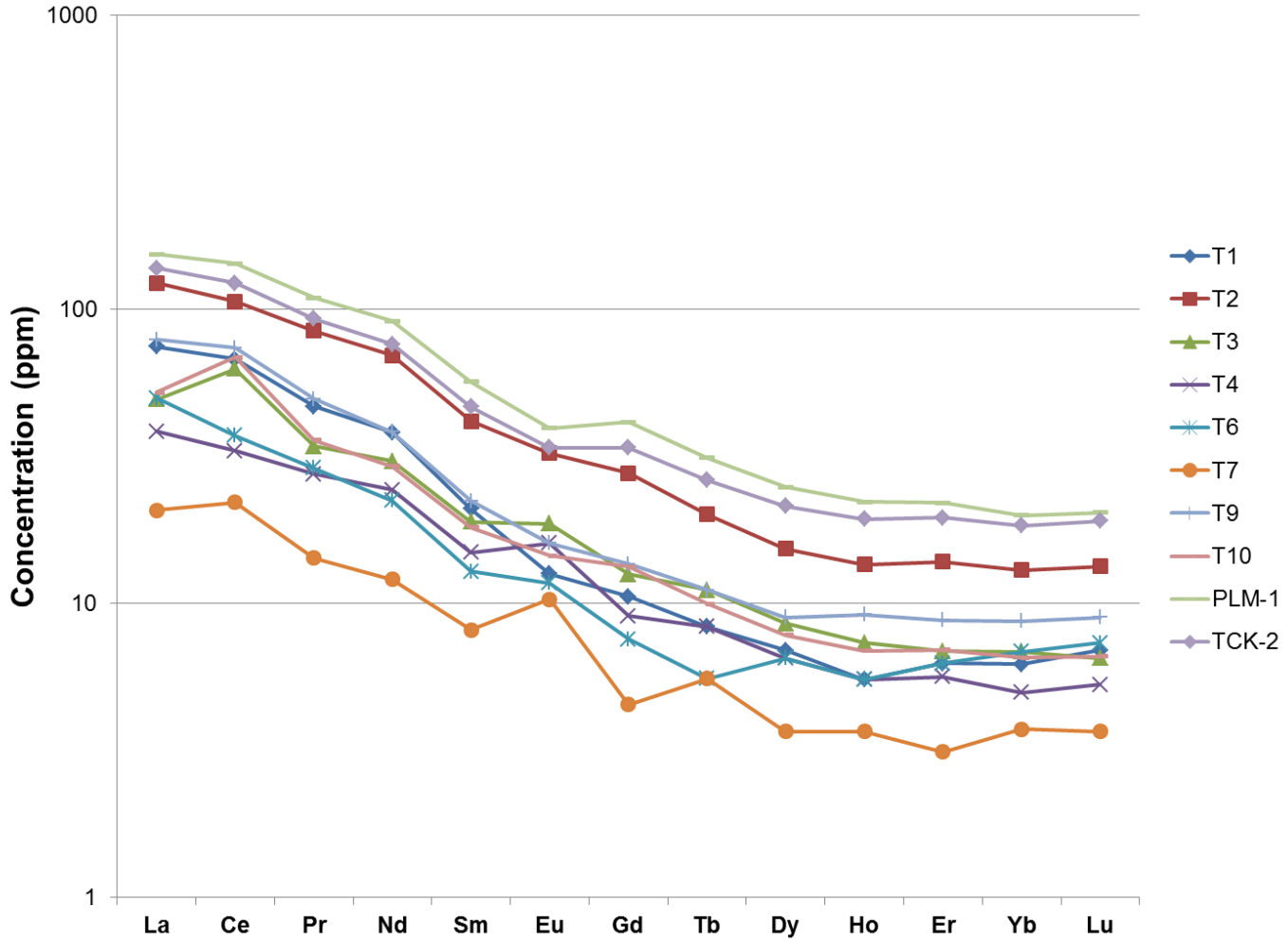

Figure A1: Spider diagram for glacial till samples collected in the basal Duluth Complex. Samples PLM-1 and TCK-2 are very fine grained, weathered material collected immediately above mineralized bedrock.

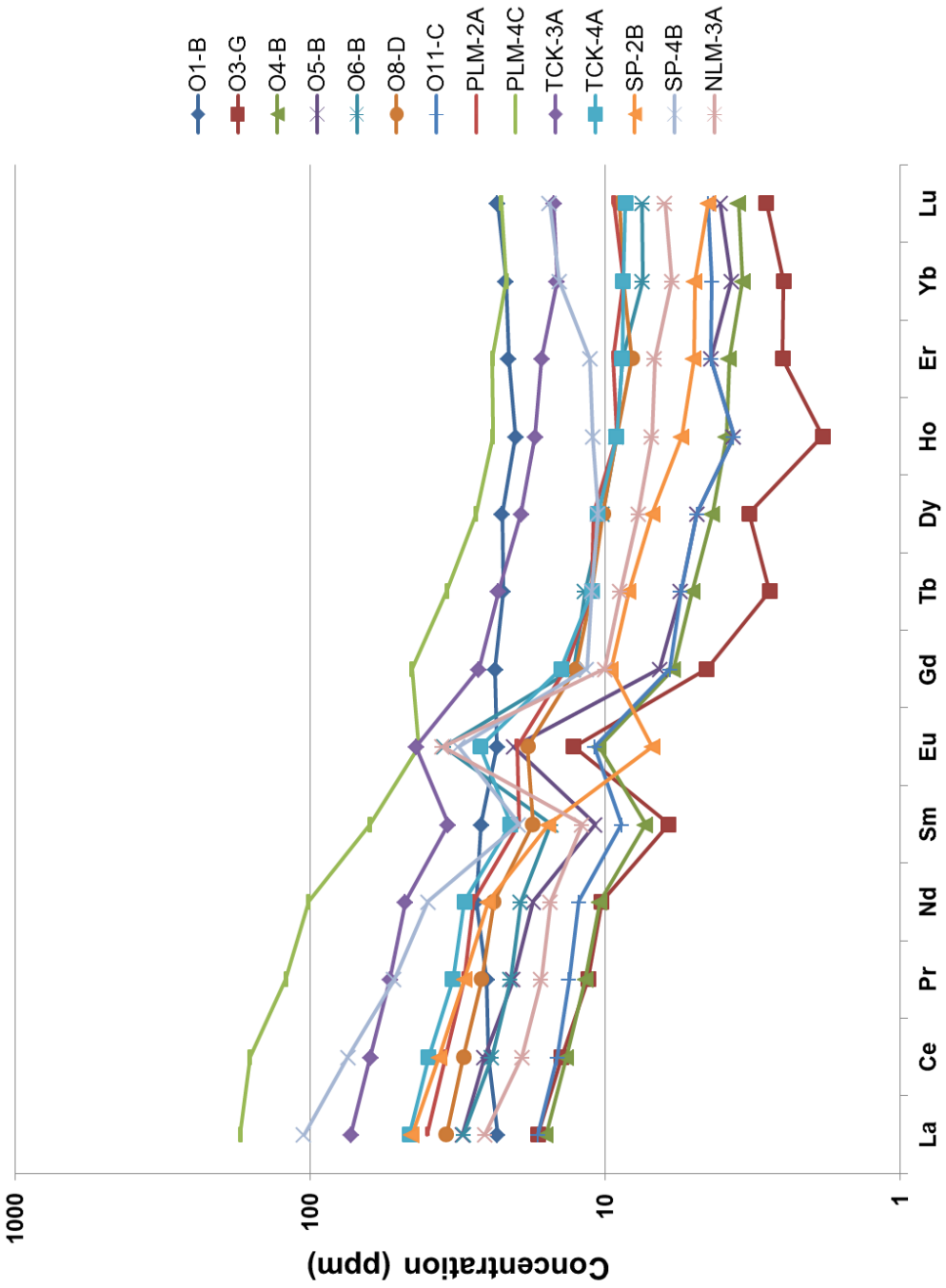

Figure A2: Spider diagram for surface outcrop samples collected in the basal Duluth Complex.

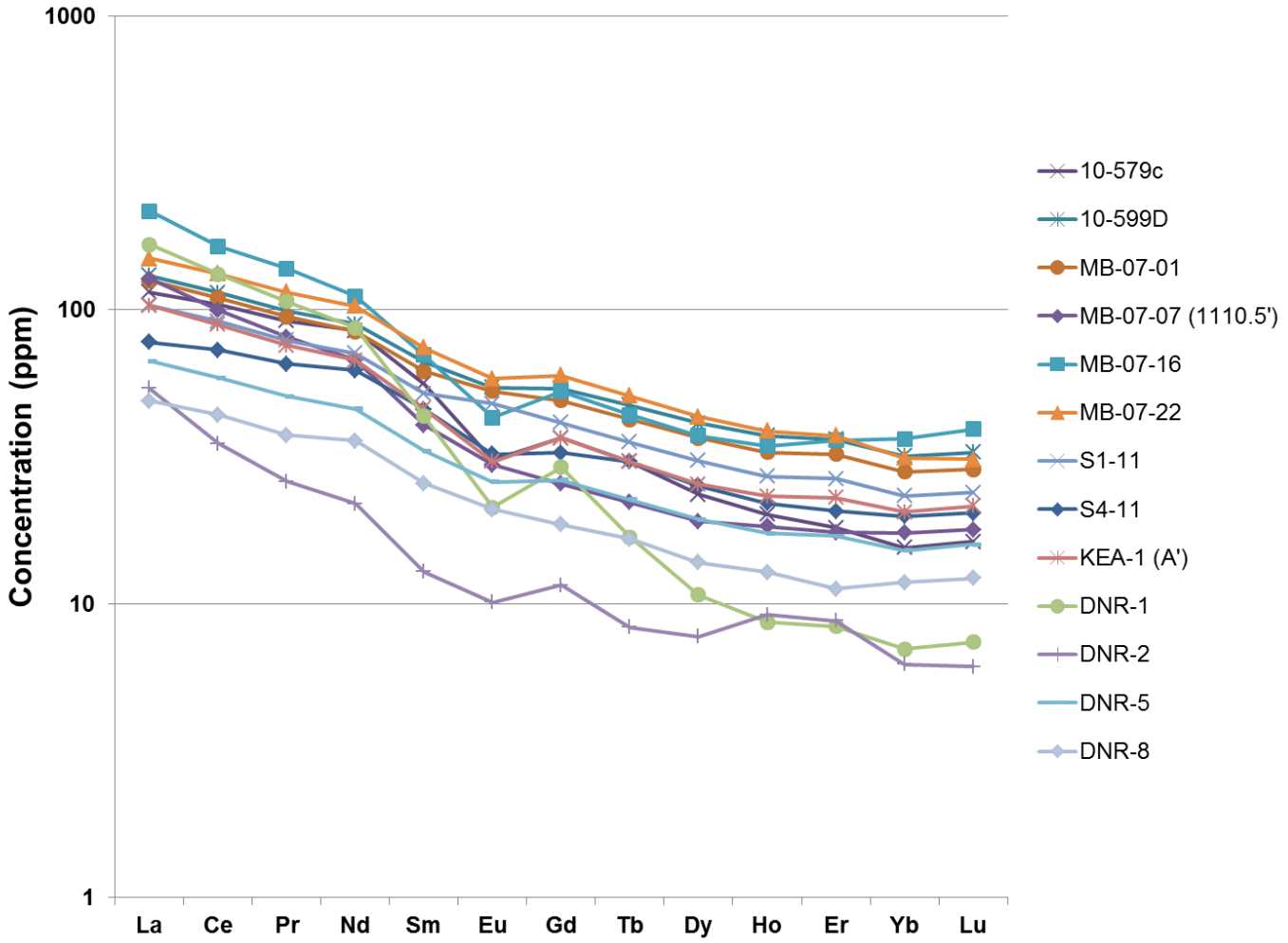

Figure A3: Spider diagram for drill core samples obtained from mining companies and the Minnesota DNR. These samples are grouped based on a relative depletion in europium relative to sample material in figure A4.

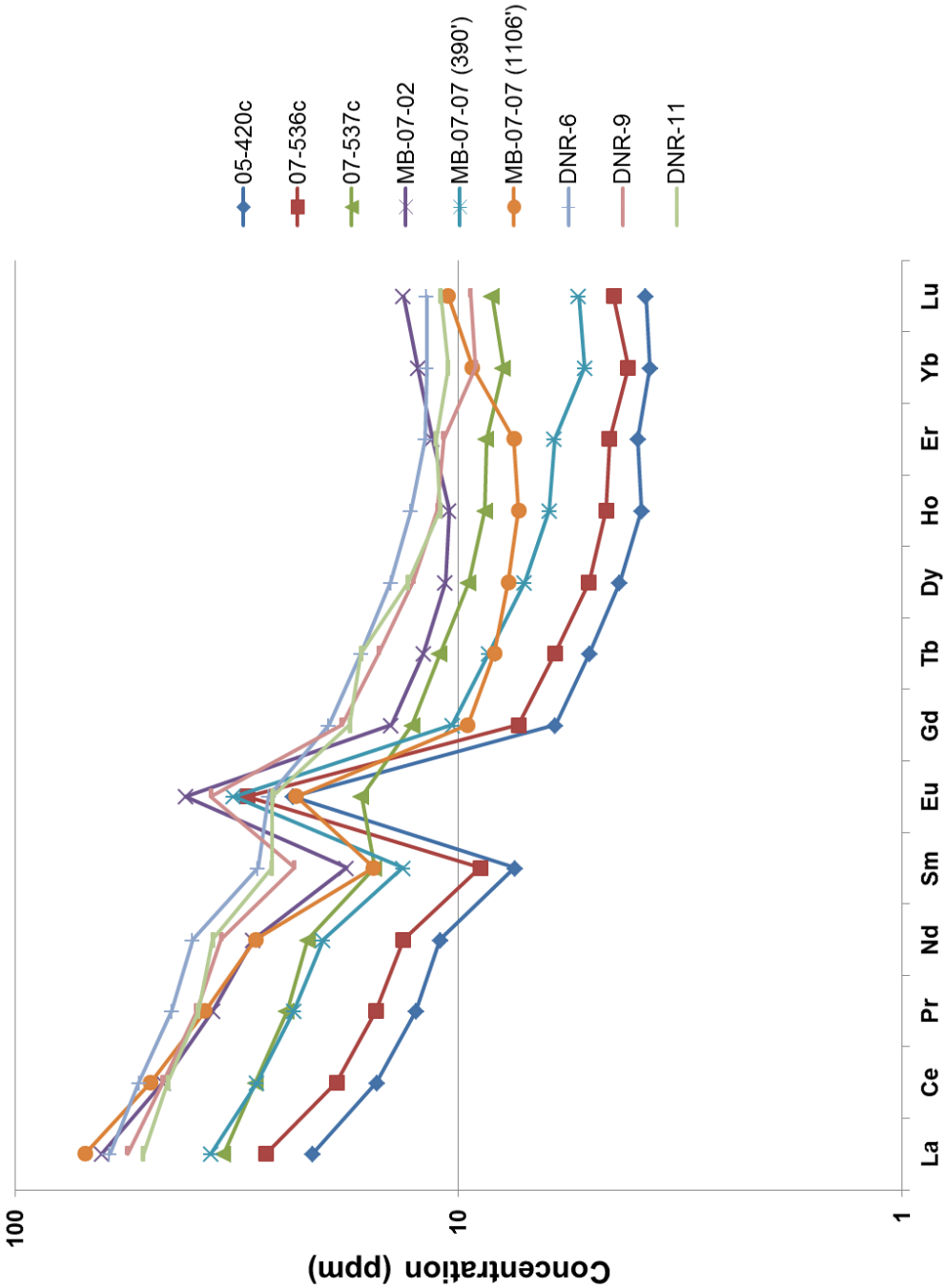

Figure A4: Spider diagram for drill core samples obtained from mining companies and the Minnesota DNR. These samples are grouped based on a relative enrichment in europium relative to sample material in figure A3.

Table A5-1: Transition and base metal concentrations. Ni, Cu, and Zn concentrations listed in table A2-E. Samples analyzed at ActLabs.

Sample	Sc	V	Co	Cr	Ga	Se	Mo	Cd	Bi	Pb	Sn	W	As
	ppm	ppm	ppm	ppm	ppm	ppm	ppm	ppm	ppm	ppm	ppm	ppm	ppm
T1	9	85	22	400	16	< 3	< 2	< 0.5	< 0.4	12	< 1	21	< 5
T3	10	122	97	180	19	< 3	< 2	< 0.5	< 0.4	< 5	< 1	57	< 5
T4	8	68	98	60	17	< 3	< 2	0.6	< 0.4	28	1	< 1	8
T6	7	65	29	70	21	< 3	< 2	< 0.5	< 0.4	15	1	< 1	< 5
T7	9	84	49	230	16	< 3	< 2	< 0.5	< 0.4	29	< 1	< 1	< 5
T9	10	131	35	160	19	< 3	< 2	< 0.5	< 0.4	13	3	43	12
O1-B	42	262	41	320	16	< 3	< 2	< 0.5	< 0.4	< 5	< 1	< 1	< 5
O3-G	6	40	133	170	16	< 3	< 2	< 0.5	< 0.4	< 5	< 1	165	< 5
O5-B	4	36	21	30	22	< 3	< 2	< 0.5	0.7	9	< 1	20	< 5
O8-D	14	97	91	130	16	< 3	< 2	< 0.5	< 0.4	9	2	57	< 5
O11-C	11	71	90	200	13	< 3	< 2	< 0.5	< 0.4	8	< 1	< 1	< 5
O12	3	60	23	230	24	< 3	< 2	< 0.5	< 0.4	< 5	< 1	< 1	< 5
PLM-2A	12	98	68	290	19	< 3	< 2	< 0.5	< 0.4	11	1	< 1	< 5
TCK-4A	9	75	37	50	22	< 3	< 2	< 0.5	< 0.4	< 5	< 1	< 1	< 5
SP-2B	3	93	373	210	6	23	13	2.6	< 0.4	7	< 1	31	11
SP-4B	19	167	20	240	22	< 3	5	0.8	0.6	30	2	< 1	7
10-579c	21	320	68	340	20	< 3	< 2	1.8	1.2	35	3	< 1	9
MB-07-07 1106	30	379	195	370	21	< 3	8	1.8	< 0.4	66	3	102	32
MB-07-07 1110.5	16	138	27	110	20	< 3	8	1.5	< 0.4	8	1	4	75
S4-11	33	359	83	60	20	< 3	2	3.2	< 0.4	19	5	148	7
KEA-1 (C')	< 1	21	> 1000	190	2	34	< 2	0.9	< 0.4	22	< 1	18	7
DNR-2	1	25	39	< 20	2	21	< 2	< 0.5	< 0.4	< 5	< 1	71	8
DNR-6	12	100	80	80	19	< 3	< 2	0.9	< 0.4	13	< 1	208	< 5
DNR-8	18	238	138	1290	14	< 3	< 2	0.6	< 0.4	12	1	1	< 5
DNR-10	16	649	157	190	29	< 3	< 2	1	< 0.4	< 5	2	56	< 5
DNR-11	14	131	69	140	20	< 3	< 2	< 0.5	< 0.4	< 5	< 1	< 1	< 5

Table A5-2: Transition and base metal concentrations. Ni, Cu, and Zn concentrations listed in table A2-E. Samples analyzed at the University of Western Ontario.

Sample	V	Co	Ga	Cd	Bi	Pb	Sn	W	As
	ppm	ppm	ppm	ppb	ppb	ppm	ppm	ppm	ppm
T2	245	65	29	333	< 9	32.7	2.4	1.3	14
T10	98	12	10	188	< 9	< 5.0	0.8	< 1.0	< 2
O4-B	116	133	9	62	24	< 5.0	0.6	< 1.0	< 2
O6-B	195	104	33	539	644	15.6	1.7	< 1.0	< 2
O13-B	156	121	5	34	< 9	< 5.0	0.2	< 1.0	< 2
PLM-1	269	96	23	484	125	13.5	2.3	1.5	11
PLM-4C	311	110	26	524	132	14.7	2.5	1.7	13
TCK-2	304	63	25	592	350	27.9	10	1.7	17
TCK-3A	302	242	27	241	43	< 5.0	1.5	< 1.0	2
NLM-3A	454	103	33	76	11	< 5.0	1.2	< 1.0	0
05-420c	113	139	28	68	< 9	< 5.0	1	< 1.0	< 2
07-536c	142	113	29	297	62	9.7	1.6	< 1.0	< 2
07-537c	129	97	11	96	< 9	< 5.0	0.7	< 1.0	< 2
10-599D	527	240	31	563	147	11.7	4.9	1.1	6
MB-07-01	475	336	28	495	193	13.7	3.4	1.6	17
MB-07-02	354	131	16	174	65	6.5	1.8	< 1.0	8
MB-07-07 (390')	96	179	32	216	147	6.6	1.6	< 1.0	< 2
MB-07-16	633	76	28	890	73	27.1	1.7	3.9	155
MB-07-22	384	488	26	467	141	13.6	5.1	1.0	18
S1-11	450	408	26	906	1417	13.8	3.1	< 1.0	6
KEA-1 (A')	405	206	22	479	444	31	2.2	< 1.0	< 2
DNR-1	225	291	11	190	73	< 5.0	1.2	< 1.0	28
DNR-5	530	372	17	203	33	< 5.0	1.4	1178	< 2
DNR-9	190	159	33	432	523	17.4	1.9	< 1.0	< 2
StE-1	24	4	0	417	< 9	< 5.0	0.3	< 1.0	3

Table A6-1: Ni, Cu, Zn metal values using different analytical techniques. Samples analyzed at ActLabs.

Sample	**Ni**	**Cu**	**Zn**	**Ni**	**Cu**	**Zn**	**Ni**	**Cu**
	ppm	ppm	ppm	ppm	ppm	ppm	%	%
Measurement Type	TD-ICP	TD-ICP	TD-ICP	FUS-MS	FUS-MS	FUS-MS	ICP-OES	ICP-OES
T1	113	21	74	100	20	70		
T3	477	1140	107	450	950	110		
T4	1270	4900	106	1180	4430	100		
T6	121	45	82	120	40	100		
T7	421	39	73	420	40	80		
T9	99	329	80	110	320	100		
O1-B	113	90	92	120	90	100		
O3-G	2150	5720	64	1030	2890	70		
O5-B	460	4230	31	450	3150	30		
O8-D	985	5660	78	990	4470	90		
O11-C	1090	6660	102	1020	3540	110		
O12	103	74	31	100	50	30		
PLM-2A	1730	>10000	75	1260	6620	80		1.08
TCK-4A	195	543	59	220	590	60		
SP-2B	9000	>10000	82	3350	8560	70	1.05	1.84
SP-4B	57	1610	224	60	1130	210		
10-579c	1610	8200	110	530	3550	120		
MB-07-07 1106’	2140	5410	458	1400	4760	480		
MB-07-07 1110.5’	362	1380	245	260	850	260		
S4-11	2870	>10000	162	670	6240	200		1.66
KEA-1 (C’)	>10000	3090	19	>10000	3660	30	5.51	
DNR-2	43	871	42	70	1170	50		
DNR-6	2550	>10000	110	780	4340	110		1.05
DNR-8	2340	7460	136	770	4990	160		
DNR-10	866	1030	170	960	1030	220		
DNR-11	1320	2280	94	570	1170	100		

Table A6-2: Ni, Cu, Zn metal values. Samples analyzed at the University of Western Ontario.

Sample	Cu	Ni	Zn
	ppm	ppm	ppm
T2	570	457	98
T10	14	24	29
O4-B	1341	864	69
O6-B	2857	1311	49
O13-B	43	290	40
PLM-1	2067	1474	130
PLM-4C	2362	1686	149
TCK-2	993	407	116
TCK-3A	1110	807	169
NLM-3A	264	225	113
05-420c	346	533	106
07-536c	371	289	108
07-537c	374	322	92
10-599D	3732	1482	202
MB-07-01	2914	1523	236
MB-07-02	760	383	108
MB-07-07 (390')	1539	1039	78
MB-07-16	294	261	713
MB-07-22	4037	2258	157
S1-11	3667	2516	226
KEA-1 (A')	3132	1975	179
DNR-1	3099	1000	89
DNR-5	829	1458	254
DNR-9	4449	2891	88
StE-1 -1	< 5	21011	8

Table A7: Au, Ag, Pt, Pd precious metal assay using different analytical techniques.

Sample	Au	Ag	Au	Pt	Pd
	ppb	ppm	ppb	ppb	ppb
	INAA	FUS-MS	FA-MS	FA-MS	FA-MS
T1	< 2	0.7			
T3	101	0.6			
T4	68	0.6	27	37	84
T6	24	0.5			
T7	39	< 0.5			
T9	2600	0.7			
O1-B	49	< 0.5			
O3-G	60	< 0.5	67	150	247
O5-B	74	0.6			
O8-D	184	1.0	46	154	305
O11-C	43	0.6	57	42	179
O12	< 2	< 0.5			
PLM-2A	140	0.7	74	250	1120
TCK-4A	< 2	0.6			
SP-2B	< 2	< 0.5	19	5.6	88
SP-4B	< 2	0.8			
10-579c	228	0.8	45	47	360
MB-07-07 1106	< 2	< 0.5	11	19	82
MB-07-07 1110.5	< 2	1.0			
S4-11	< 2	0.9	11	13	34
KEA-1 (C')	< 2	0.8	8	156	409
DNR-2	< 2	< 0.5			
DNR-6	18	0.5			
DNR-8	64	0.8			
DNR-10	11	< 0.5			
DNR-11	< 2	0.5	60	16.2	187

Table A8: $\delta^{60/58}$Ni values for 24 Duluth Complex samples and one secondary Ni ore sample from St. Egidien, Germany. Additional details about the samples can be seen above in tables 1-3 and tables A1-a and A1-b.

Sample	Sample Location	$\delta^{60/58}$Ni	2σ
T4	II	-0.02	0.11
O6-B	II	-0.15	0.10
DNR-9	II	0.15	0.09
T2	I	-0.71	0.06
O4-B	I	-0.10	0.06
KEA-1 (B')	I	-0.16	0.07
DNR-11	III	-0.43	0.06
SP-2A	Serpentine	-0.39	0.06
SP-4B	Serpentine	-0.26	0.06
S1-11	Serpentine	-0.54	0.06
S4-11	Serpentine	-0.64	0.06
TCK-2	Mesaba	-0.77	0.10
TCK-3a	Mesaba	-0.23	0.06
MB-07-01	Mesaba	-0.37	0.07
MB-07-07	Mesaba	-0.97	0.12
T9	NorthMet	-0.17	0.06
PLM-4C	NorthMet	-0.87	0.06
10-579c	NorthMet	-0.02	0.06
10-579c #2	NorthMet	-0.08	0.06
DNR-5	Wetlegs	-0.18	0.07
DNR-5 #2	Wetlegs	0.22	0.06
DNR-4	Wyman Creek	-0.13	0.06
O12	Bald Eagle	-0.12	0.18
O1-C	Newton Belt	0.02	0.08
T6	Jack's Rock	-0.50	0.06
StE-1	St. Egidien, Germany	1.55	0.06

Table A9: $\delta^{65/63}$Cu values for 23 Duluth Complex samples and 6 samples from other copper deposit types. Additional details about the samples can be seen above in tables 1-3 and tables A1-a and A1-b.

Sample	Sample Location	$\delta^{65/63}$Cu	2σ
O5-B	II	-0.31	0.12
DNR-8	II	-0.27	0.09
T3	I	0.06	0.12
O3-G	I	-0.13	0.07
O8-D	I	-0.24	0.13
KEA-1 (C')	I	0.36	0.11
KEA-1 (A')	I	-0.18	0.09
DNR-10	III	-0.81	0.07
DNR-11	III	-0.49	0.13
SP-2b	Serpentine	-0.61	0.15
SP-4b	Serpentine	-1.28	0.10
S4-11 (458-458.5')	Serpentine	-0.54	0.13
TCK-2	Mesaba	-0.72	0.18
TCK-4a	Mesaba	-0.02	0.29
MB-07-01 (584')	Mesaba	-0.88	0.10
MB-07-07 (1106')	Mesaba	-0.87	0.07
T9	NorthMet	N/A*	N/A*
PLM-2A #1	NorthMet	-0.11	0.14
07-536c	NorthMet	-0.31	0.07
10-579c (36')	NorthMet	-0.14	0.12
DNR-6	Wetlegs	-0.37	0.07
DNR-2	Wyman Creek	0.28	0.07
O11-C	Bald Eagle	-0.24	0.08
Eagle-1	Eagle Deposit, MI	1.36	0.08
Eagle-2	Eagle Deposit, MI	-0.16	0.08
SLC-88	Sturgeon Lake, ON, Canada	0.36	0.11
O-528	Bingham Mine, UT	0.12	0.06
O-574	Morenci, AZ	2.71**	0.05**
G-11	Greens Creek, AK	0.62	0.08
R-1	Rammelsberg, Germany	-0.18	0.09

*Sample was not measured due to issues with copper extraction and separation.

**Initial measurement, which was reportedly inaccurate. A second measurement could not be obtained due to instrument error.

Table A10: Quantitative EDS spectra data for thin and polished sections images shown above in figures 31 and 34-36 Values are listed in weight percent and are normalized to 100%. TCK-1c image C, spectrum 3 is omitted due to measurement error. TCK-1c image D, spectra 4-6 are also omitted due measurement error. Additional images and quantitative EDS data can be seen below in Appendix 2.

Sample, Image and Spectrum	O	Na	Mg	Al	Si	S	Ca	Mn	Fe	Co	Ni	Total
SP-2b												
A-1						43.08			27.39	4.22	25.32	100.00
TCK-1c												
A-1	33.69		15.19		16.53			0.43	34.17			100.00
B-3	36.09		15.14		16.13				32.63			100.00
C-1	35.78		15.23		16.18			0.40	32.41			100.00
C-2	36.13		15.13		16.05				32.69			100.00
C-4	46.89	5.31		14.66	26.25		6.50		0.39			100.00
C-5	41.55		14.08	0.39	24.44		0.69	0.35	18.49			100.00
D-1	34.88		14.62		16.19			0.45	33.85			100.00
D-2	35.76		14.51		16.09				33.63			100.00
D-3	36.21		14.31		15.66			0.48	33.34			100.00
D-7	45.85		14.55		19.58				20.03			100.00
DNR-8												
A-1	39.33		20.28		16.46				23.93			100.00
MB-07-07												
B-1	36.28		18.57		16.76			0.38	28.01			100.00
D-2	37.51		18.52		16.69				27.29			100.00
D-3	37.29		18.65		16.61				27.46			100.00
D-4	42.84		10.00	0.57	24.48		15.87		6.23			100.00

11. Appendix 2

This section includes selected images, element maps, line scans, and EDS quantitative data from SEM and microprobe analyses. Additional images, data tables, and other information can be found below in the supplementary data section.

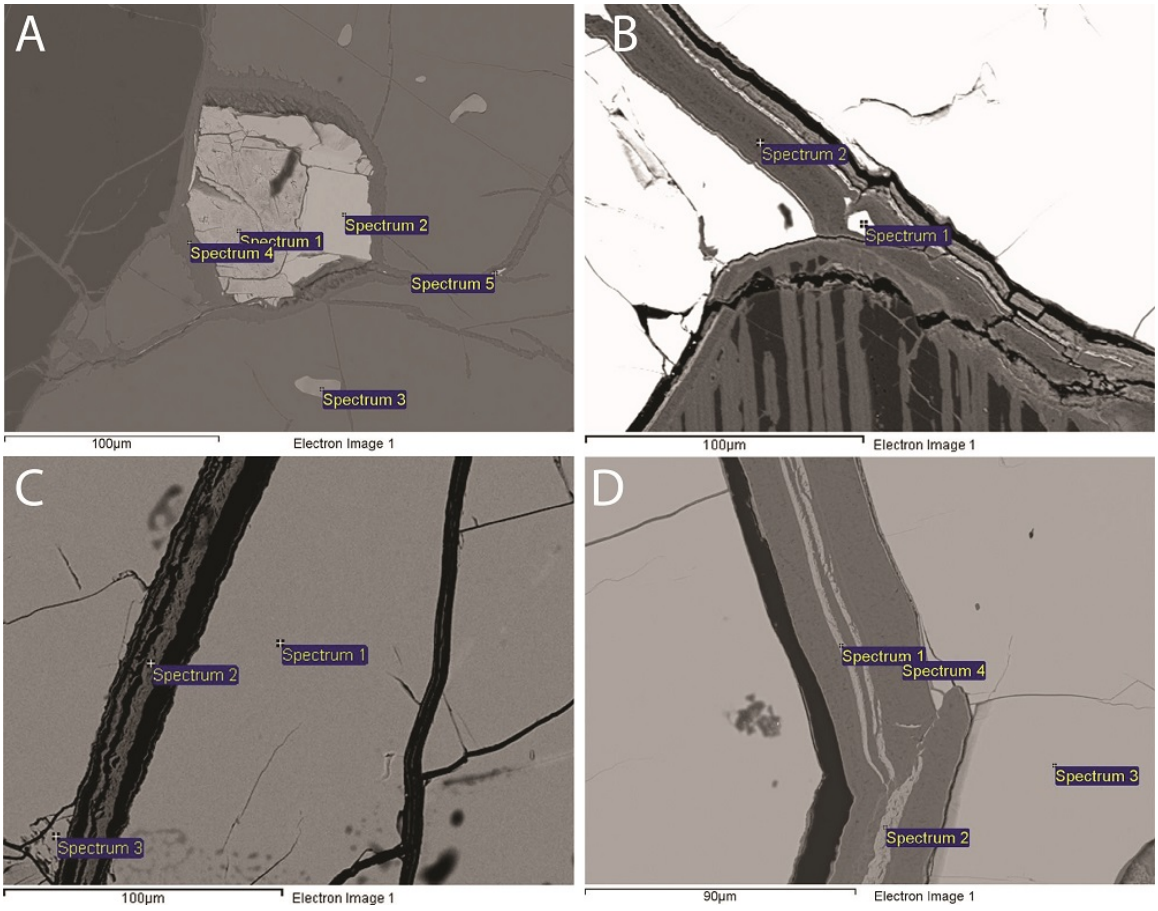

Figure A5: SEM images from sample SP-2b with additional spectra sites (see figure 31 A-D). Quantitative EDS data for the spectra sites can be seen below in table A11.

Table A11: Quantitative EDS data for images in figure A5. Table 11 is divided into two segments due to formatting constraints.

Image and Spectrum	O	Mg	Al	Si	Ti	V	Cr
A-1							
A-2							
A-3	27.80		8.09		3.78	2.09	18.25
A-4	42.70	6.59	4.90	15.70			
B-1							
B-2	42.38	7.22	5.55	14.59			
C-1							
C-2	27.96	0.99	0.72	2.66			
C-3							
D-1	27.79	0.94	0.90	3.07			
D-2	28.47	0.62	0.80	2.46			
D-3							
D-4	42.45	6.14	5.79	14.47			

Image and Spectrum	S	Fe	Co	Ni	Cu	Zn	Total
A-1	43.08	27.39	4.22	25.32			100.00
A-2	33.45	28.29			38.27		100.00
A-3		38.85				1.15	100.00
A-4		30.10					100.00
B-1	41.08	58.92					100.00
B-2		30.26					100.00
C-1	41.04	58.96					100.00
C-2		67.68					100.00
C-3	41.49	58.51					100.00
D-1		67.30					100.00
D-2		67.64					100.00
D-3	41.35	58.65					100.00
D-4		31.15					100.00

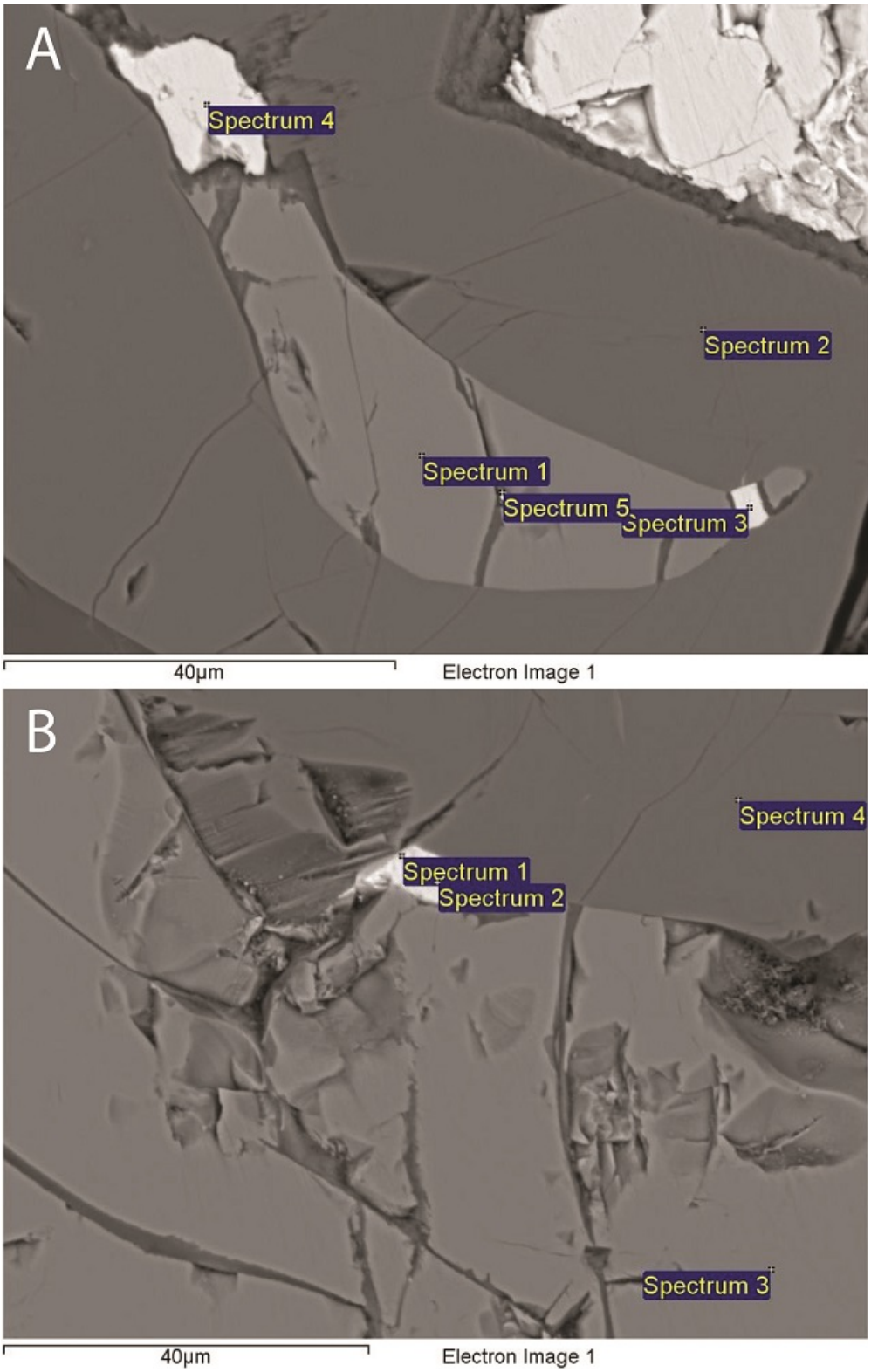

Figure A6: SEM images from sample TCK-1c with additional spectra sites (see figure 34 A and B). Quantitative EDS data for the spectra sites can be seen below in table A12.

Table A12: Quantitative data for figure A6. The data for spectrum A-5 was excluded due to high measurement error. The data for spectrum B-1 is likely inaccurate due to the presence of oxygen and magnesium in a sulfide measurement.

Image and Spectrum	O	Mg	Al	Si	S	Ca	Mn	Fe	Cu	Br	Total
A-1	33.69	15.19		16.53			0.43	34.17			100.00
A-2	40.96	14.13	0.45	24.70		0.63	0.37	18.77			100.00
A-3					33.12			28.16	38.72		100.00
A-4					34.38			37.79	27.83		100.00
A-5*											100.00
B-1**	3.23	0.41		0.82	30.16			23.36	42.01		100.00
B-2					33.61			28.69	37.71		100.00
B-3	36.09	15.14		16.13				32.63			100.00
B-4	41.21	13.87		24.49		0.72	0.37	18.47		0.86	100.00

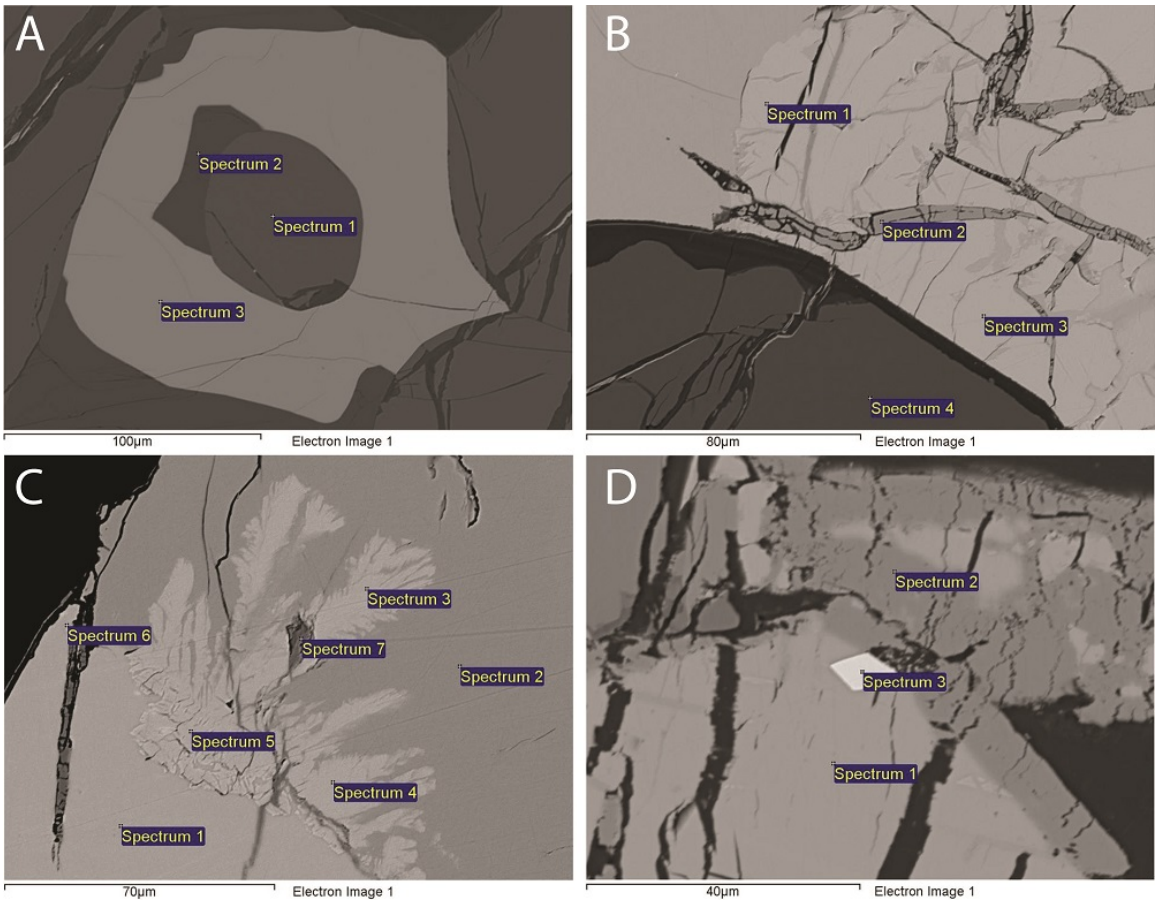

Figure A7: SEM images from sample DNR-8 with additional spectra sites (see figure 35 A-D). Quantitative EDS data for the spectra sites can be seen below in table A13.

Table A13: Quantitative data for figure A3. The data for spectrum B-4 and C-7 are likely inaccurate due to the mixture of oxygen, magnesium, silicon, and sulfur in the measurements.

Image and Spectrum	O	Mg	Al	Si	Ca	Ti	V	Cr	S	Fe	Co	Ni	Cu	As	Total
A-1	39.33	20.29		16.46						23.93					100.00
A-2	44.63	16.47	0.38	24.29	0.51					13.72					100.00
A-3	28.09	0.58	2.24			4.71	0.93	5.77		57.68					100.00
B-1									35.46	32.82		31.72			100.00
B-2	28.56									71.44					100.00
B-3									36.03	31.25		32.72			100.00
B-4*	39.87	20.74		7.51					17.19	23.26		16.66			100.00
C-1									33.60	27.68			38.71		100.00
C-2									41.58	58.42					100.00
C-3									35.06	30.03		34.91			100.00
C-4									35.12	28.94		35.94			100.00
C-5									35.55	29.42		35.04			100.00
C-6									33.32	27.44		12.56	26.44		100.00
C-7*	27.59								4.11	40.98		11.95			100.00
D-1									34.60	37.79			27.61		100.00
D-2	28.25									71.75					100.00
D-3										3.41	0.69	46.84		49.06	100.00

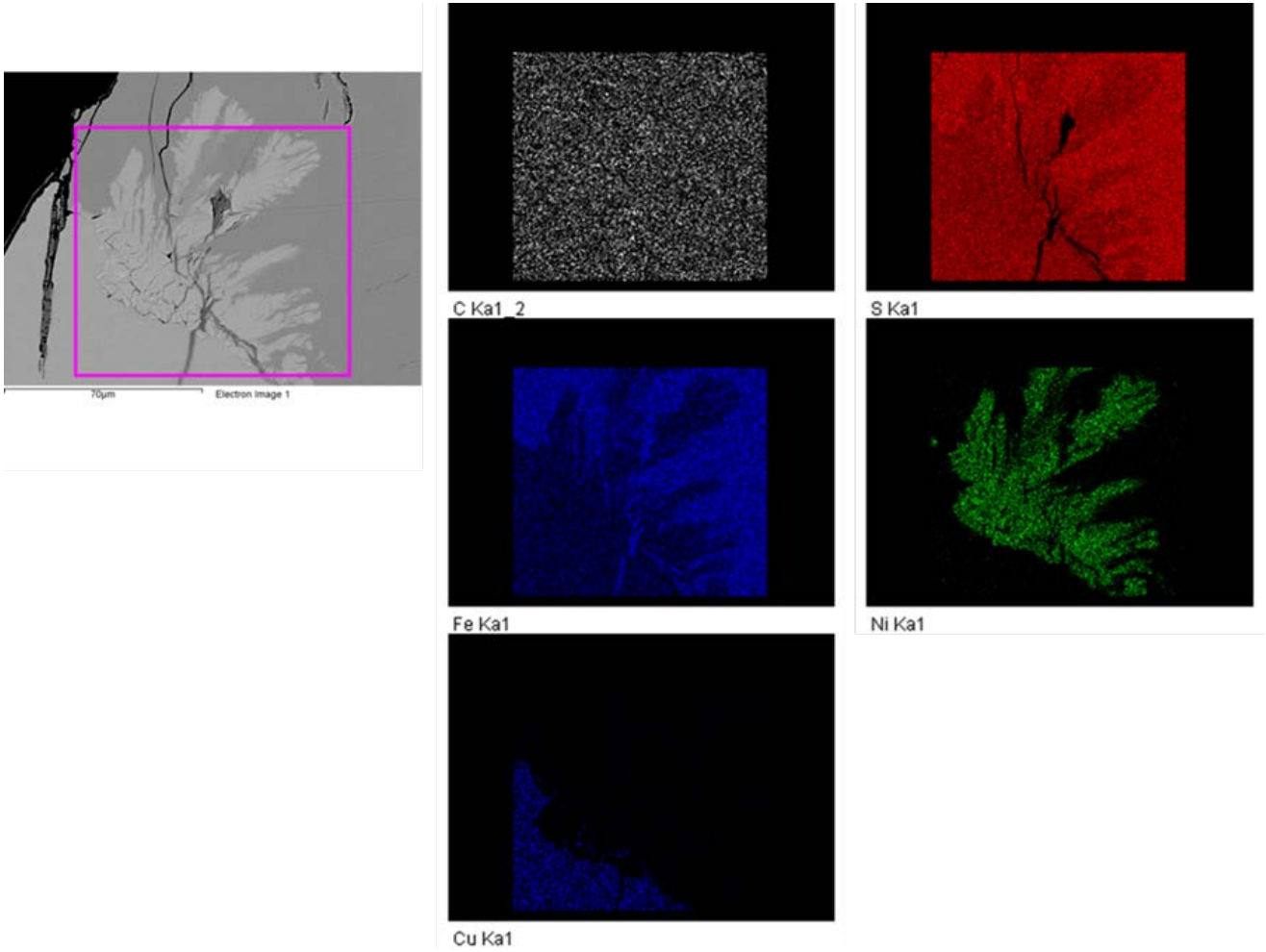

Figure A8: Element map for figure A7, image C. Elements include S (red), Fe (blue, middle), Ni (green), Cu (blue, bottom).

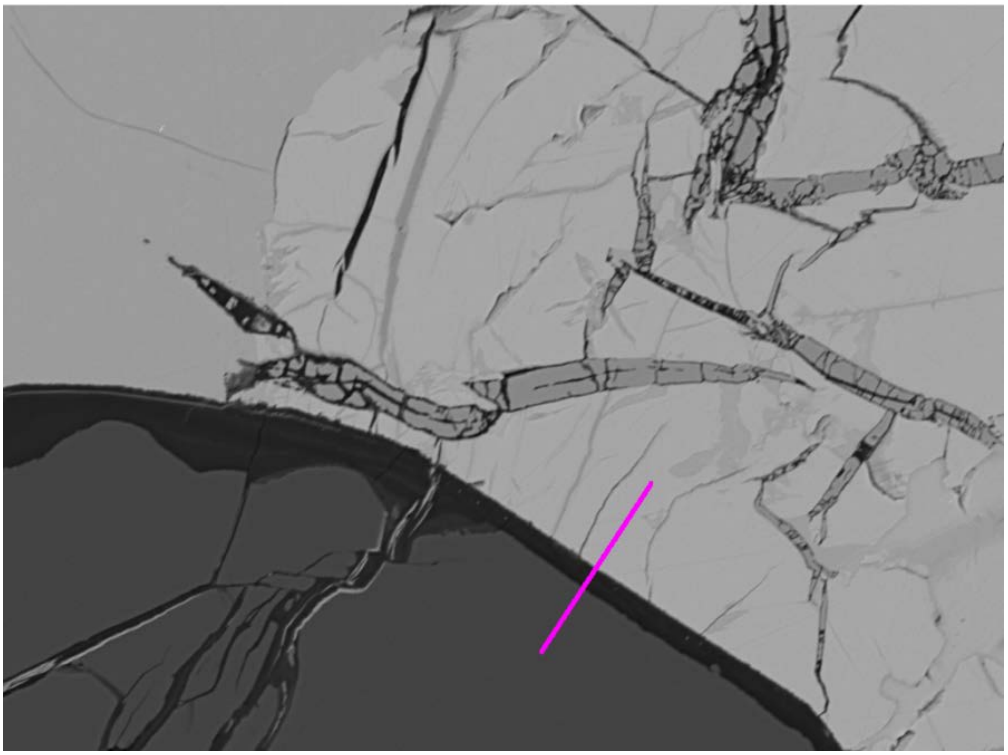

Figure A9: Line scan location image for figure A7, image B.

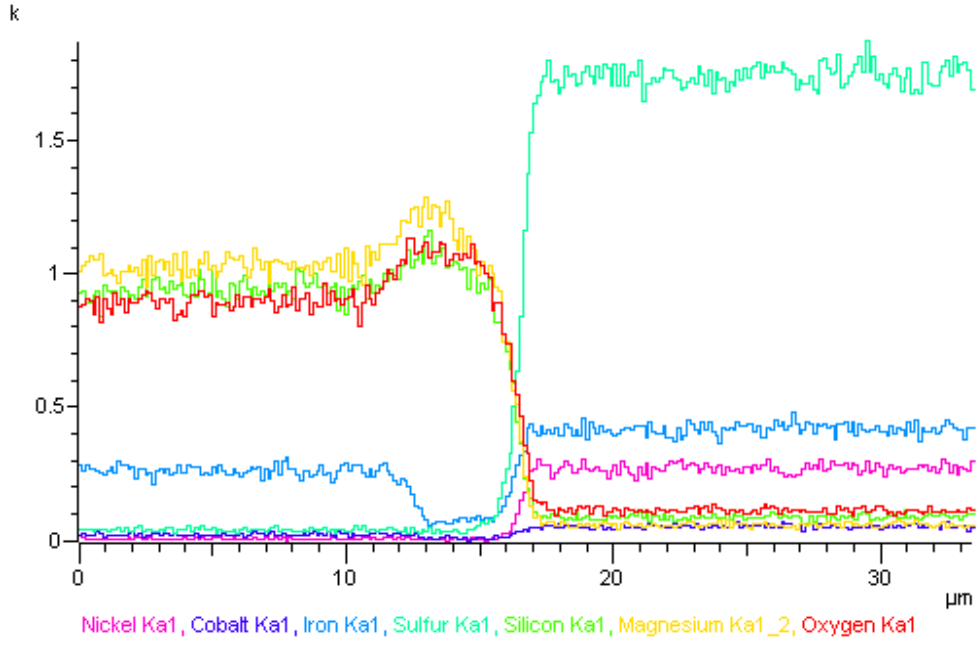

Figure A10: Stacked line scan spectra for location shown above in figure A9.

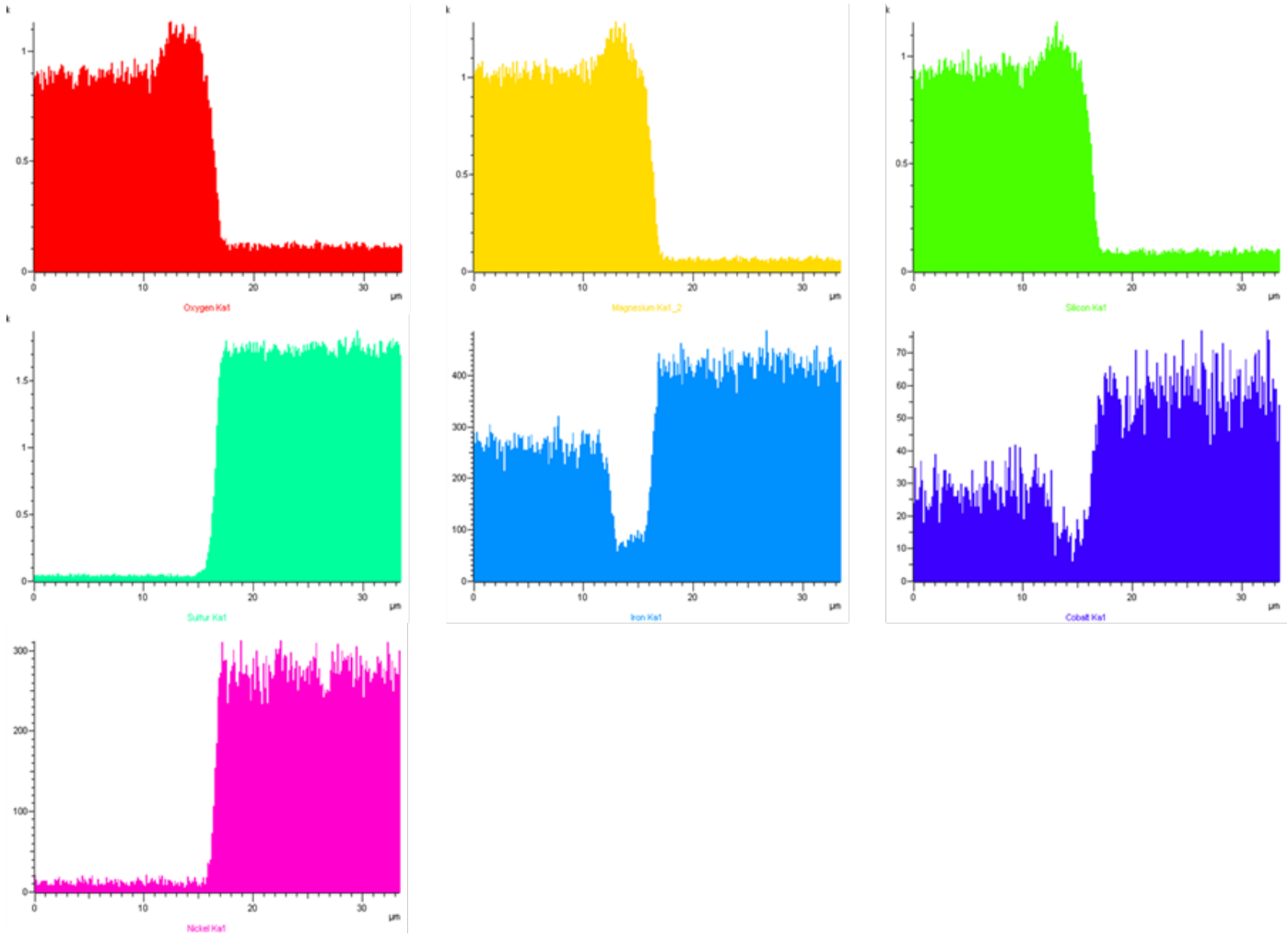

Figure A11: Individual element spectra for the line scan location shown above in figure A9. Element shown are: oxygen (red), magnesium (yellow), silicon (green), sulfur (teal), iron (blue), cobalt (dark blue), and nickel (pink).

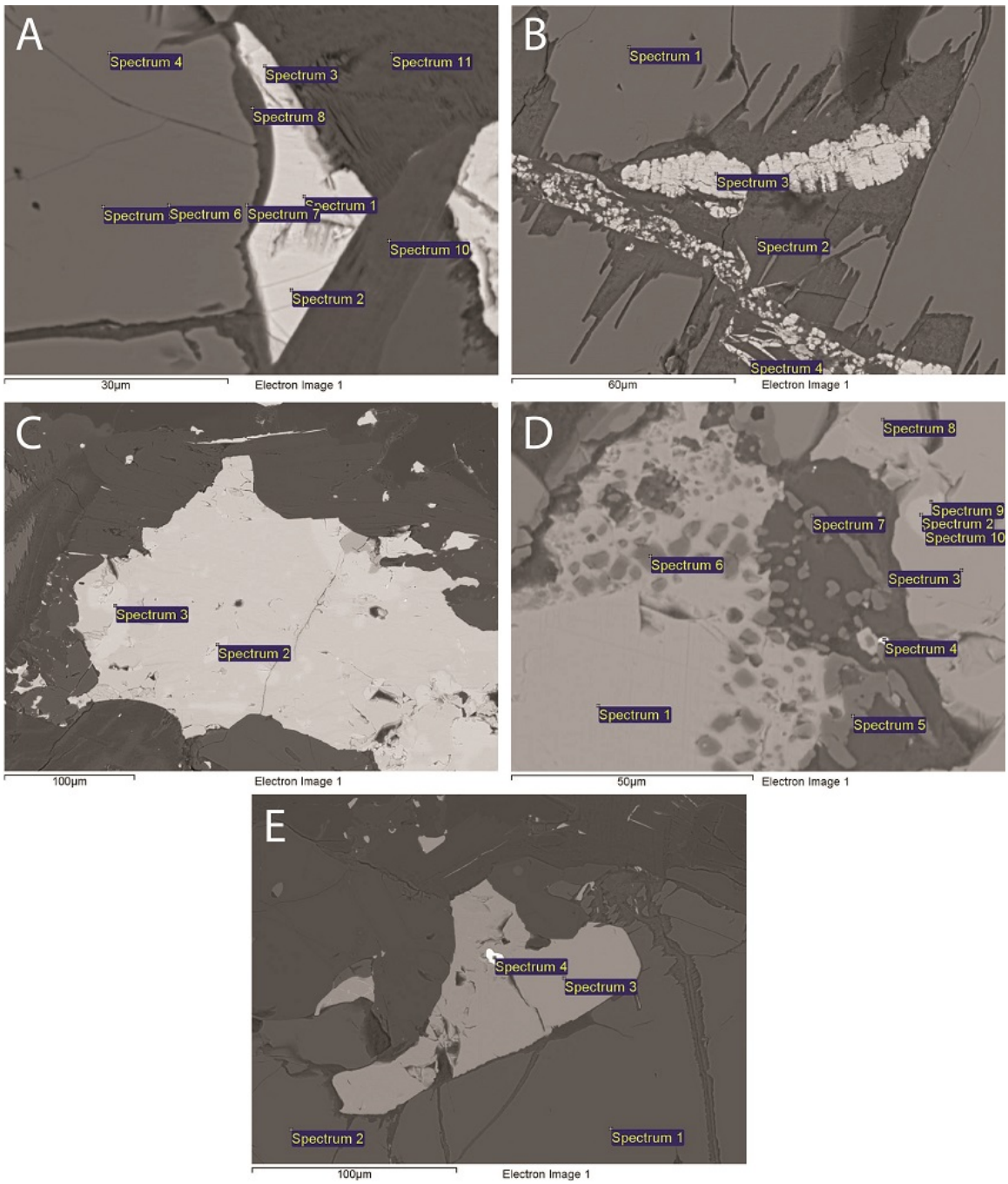

Figure A12: SEM images from sample MB-07-07 with additional spectra sites (see figure 36 A-C, E, F). Due to the mineralogical differences between the images, the quantitative EDS data for the spectra sites is split up and can be seen below in tables A14-A19.

Table A14: Quantitative data for figure A12, image A.

Spectrum	O	Na	Mg	Al	Si	Ca	K	Ti	S	Fe	Co	Ni	Total
1									35.39	33.52	1.42	29.22	100.00
2									36.01	33.82		30.18	100.00
3									36.86	33.85		29.29	100.00
4	37.74		18.28		16.57					27.40			100.00
5	37.70		18.16		16.44					27.69			100.00
6	37.58		17.99		16.41					28.01			100.00
7	38.15		17.08		16.26					28.51			100.00
8	45.63		14.96	2.83	14.26	0.24				18.11			100.00
10	43.62	0.54	12.80	8.33	17.74		7.05	1.72		8.19			100.00
11	44.01	0.73	12.99	8.23	17.87		7.08	1.55		7.55			100.00

Table A15: Quantitative data for figure A12, image B. The data for spectrum 4 is excluded due to measurement error.

Spectrum	O	Mg	Al	Si	S	Ca	Mn	Fe	Total
1	36.28	18.57		16.76			0.38	28.01	100.00
2	46.30	6.64	1.86	19.57		1.65		23.98	100.00
3					38.81			61.19	100.00
4* (Error)									

Table A16: Quantitative data for figure A12, image C. The data for spectrum 1 is excluded due to measurement error.

Spectrum	S	Fe	Co	Ni	Cu	Total
1*						
2	35.08	32.68	4.59	27.66		100.00
3	33.61	28.03			38.36	100.00

Table A17: Quantitative data for sulfide minerals in figure A12, image D.

Spectrum	S	Fe	Cu	Ni	Ag	Total
1	33.99	27.94	38.07			100.00
2	32.66	35.23		18.34	13.78	100.00
3	41.42	58.58				100.00
8	41.52	58.48				100.00
9	33.20	34.91		17.69	14.21	100.00
10	32.64	35.13		18.33	13.91	100.00

Table A18: Quantitative data for non-sulfide minerals in figure A12, image D. Spectrum 4 likely contains significant error due to the analytical beam including information from neighboring phases during analysis.

Spectrum	O	Mg	Al	Si	Ca	V	Cr	Fe	Se	Mo	Pb	Zn	Total
4*	6.73			1.05	1.73		0.63	2.23	5.57	16.50	65.56		
5	32.25	4.12	20.83			2.04	13.87	25.43				1.47	100.00
6	33.36	4.16	21.42			1.55	14.00	23.98				1.54	100.00
7	32.88	3.97	20.49		0.42	1.60	15.11	24.03				1.50	100.00

Table A19: Quantitative data for figure A12, image E. Spectrum 4 likely contains significant error due to the analytical beam interacting with neighboring phases during analysis.

Spectrum	O	F	Mg	Si	S	Mn	Fe	Cu	Pd	Bi	Total
1	36.69		18.74	16.64		0.40	27.52				100.00
2	37.44		18.74	16.65			27.17				100.00
3					33.41		27.82	38.77			100.00
4*	2.73	1.34					1.45		20.25	74.23	100.00

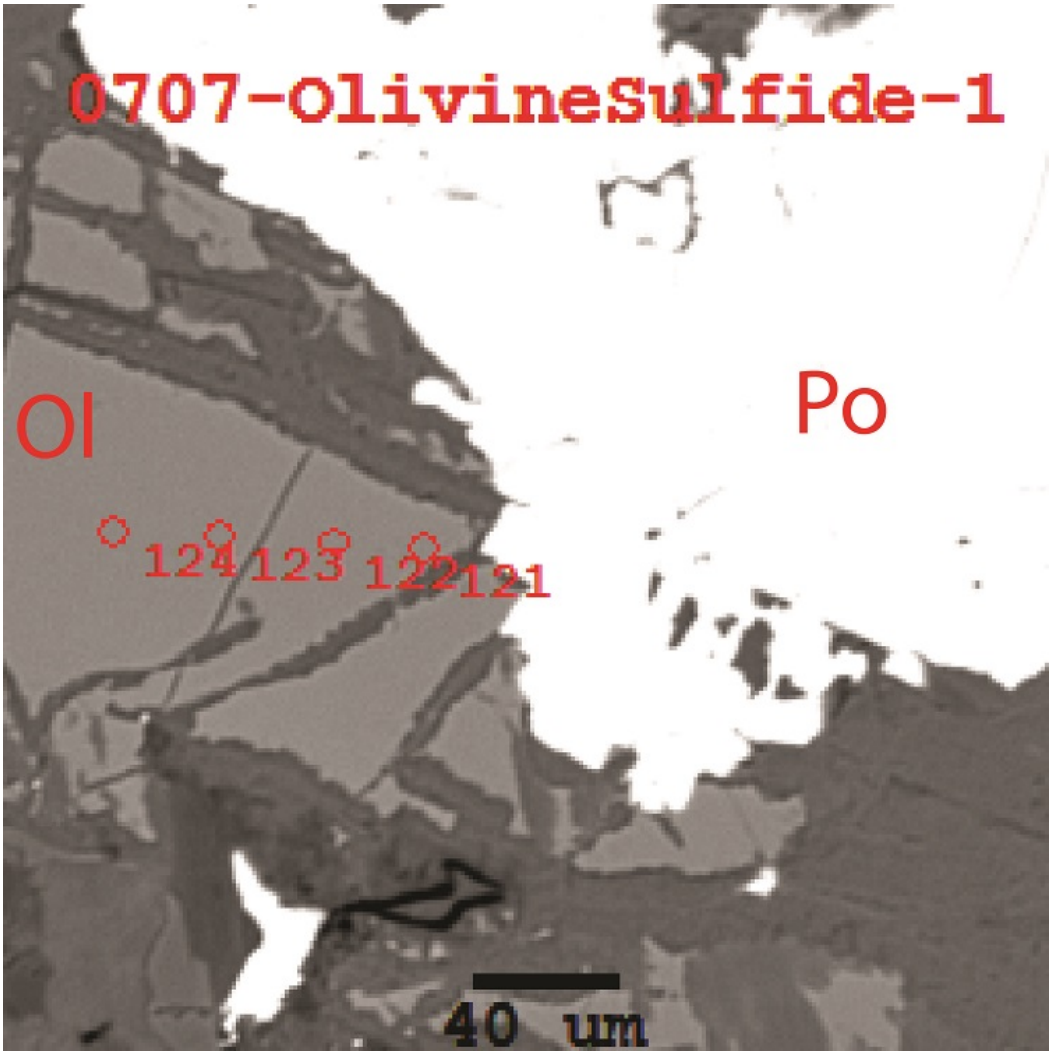

Figure A13: Microprobe image from sample MB-07-07 showing olivine (Ol) adjacent to pyrrhotite (Po). The quantitative data for this image are below in table A20.

Table A20: Microprobe data for the spot analyses shown in figure A13. The data for spot 121 has a low total due to the presence of elements that were not included in the analysis package.

Spot	SiO_2	FeO	NiO	MnO	MgO	Total
121*	31.88	27.21	0.03	0.21	15.80	75.12
122	34.38	37.23	0.12	0.47	26.15	98.36
123	34.36	37.01	0.10	0.43	26.31	98.21
124	34.28	36.91	0.10	0.45	26.31	98.05

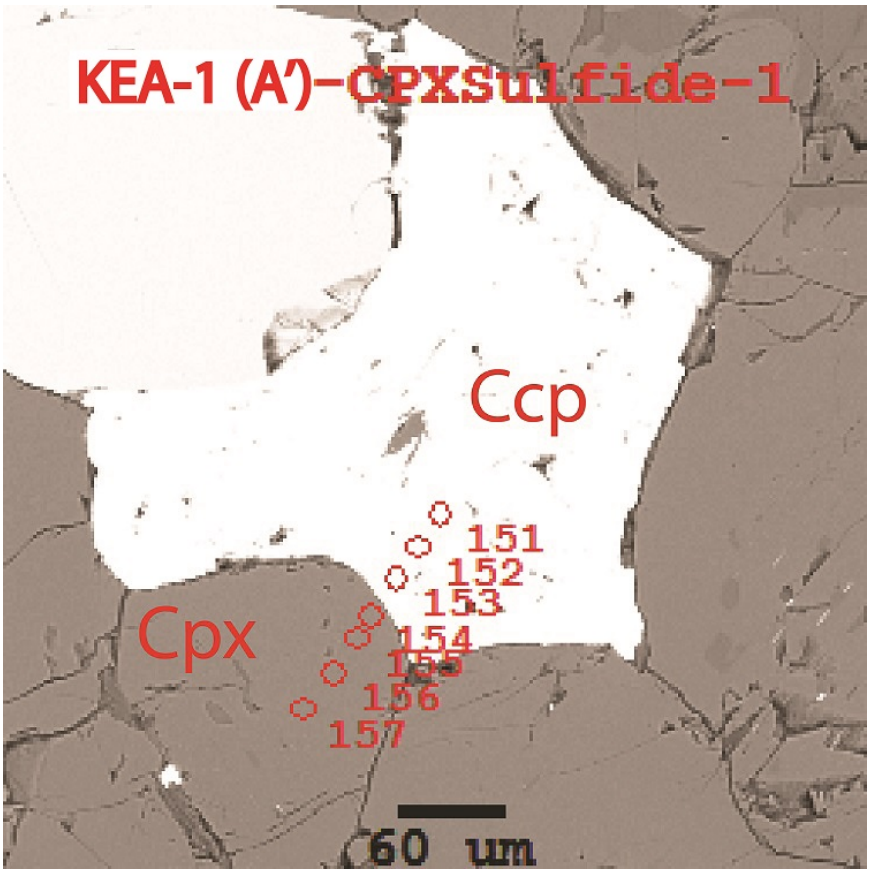

Figure A14: Microprobe image from sample KEA-1 (A') showing clinopyroxene (Cpx) adjacent to chalcopyrite (Ccp). The quantitative data for this image are below in tables A21 and A22.

Table A21: Microprobe data for spot analyses shown in figure A14. This table contains sulfide analyses. The data for spots 152 and 153 are missing due to measurement error.

Spot	Zn	Pb	Fe	Co	Ni	Cu	S	Total
151	0.07	0.12	30.80	0.05	0.02	33.53	32.96	97.54
152*								
153*								

Table A22: Microprobe data for spot analyses shown in figure A14. This table contains clinopyroxene analyses.

Spot	SiO_2	TiO_2	Al_2O_3	FeO	NiO	MgO	CaO	Na_2O	Total
154	49.37	0.34	0.68	24.65	0.10	20.85	1.10	0.02	97.11
155	54.59	0.17	0.72	23.51	0.07	22.06	1.53	0.07	102.72
156	52.05	0.08	0.49	24.03	0.09	21.21	0.93	0.00	98.88
157	51.48	0.13	0.57	23.93	0.10	21.26	0.97	0.02	98.44

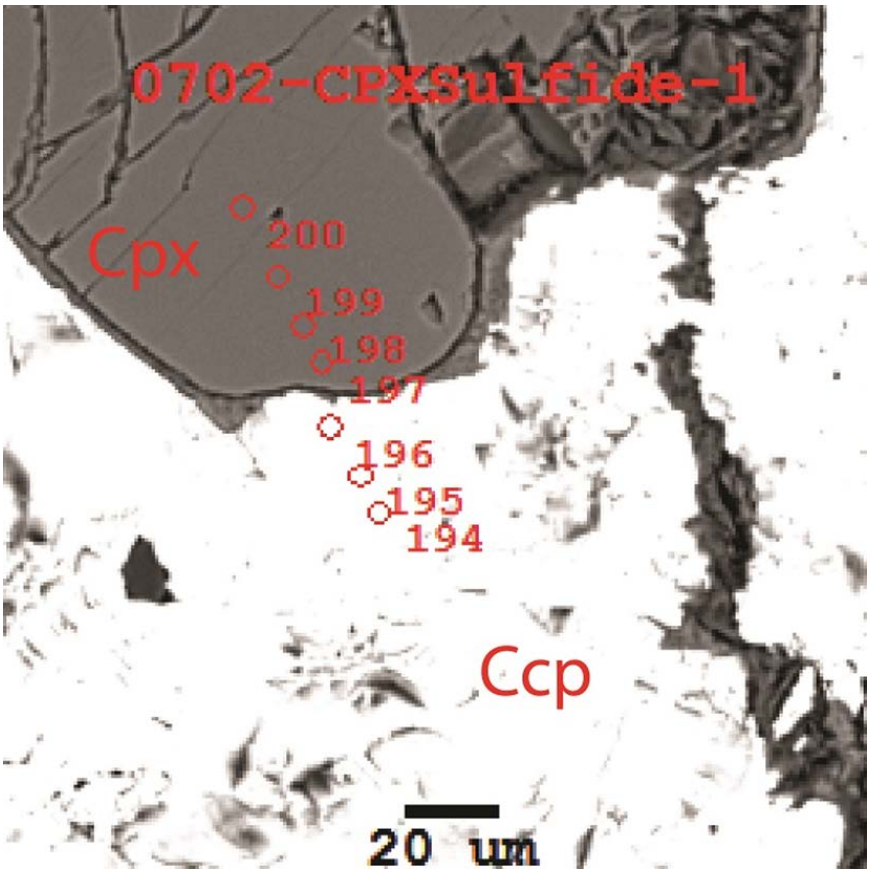

Figure A15: Microprobe image from sample MB-07-02 showing clinopyroxene (Cpx) adjacent to chalcopyrite (Ccp). The quantitative data for this image are below in tables A23 and A24.

Table A23: Microprobe data for spot analyses shown in figure A15. This table contains sulfide analyses. The data for spots 195 and 196 are missing due to measurement error.

Spot	Zn	Pb	Fe	Co	Ni	Cu	S	Total
194	0.01	0.11	42.30	0.04	0.00	22.94	33.70	99.10
195*								
196*								

Table A24: Microprobe data for spot analyses shown in figure A15. This table contains clinopyroxene analyses.

Spot	SiO_2	TiO_2	Al_2O_3	FeO	NiO	MgO	CaO	Na_2O	Total
197	47.25	0.14	1.05	30.14	0.00	17.17	0.32	0.00	96.08
198	47.77	0.14	1.39	29.15	0.01	17.60	0.33	0.00	96.38
199	47.89	0.17	1.31	28.69	0.00	18.06	0.37	0.00	96.48
200	48.16	0.24	1.38	28.26	0.00	18.18	0.36	0.02	96.61

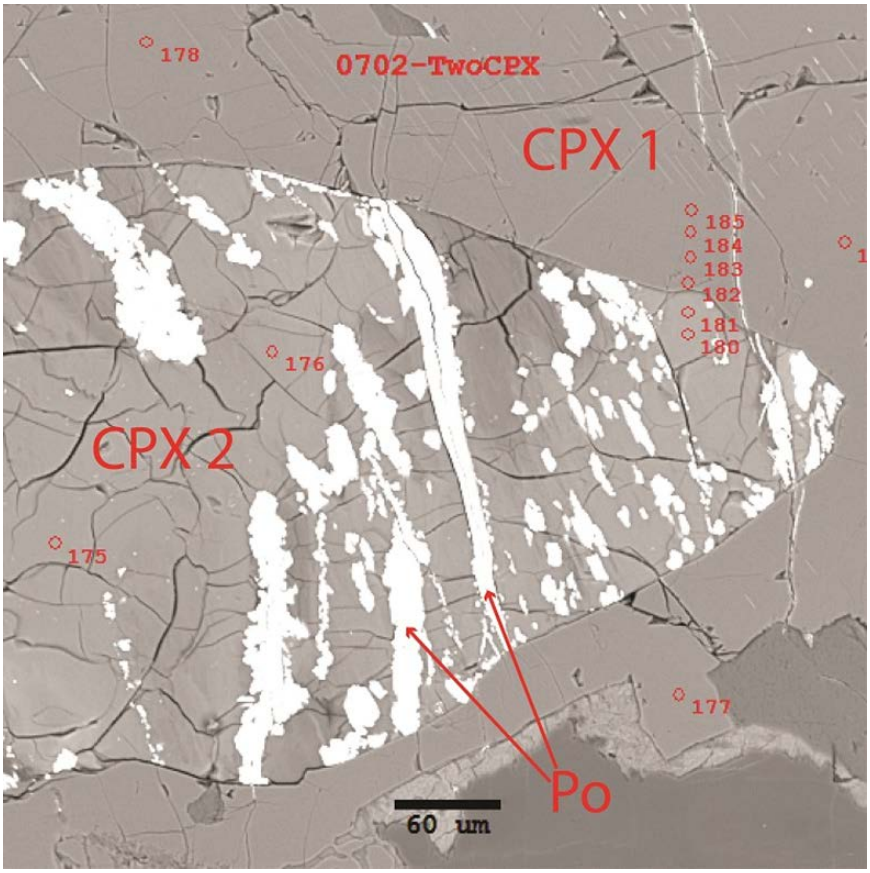

Figure A16: Microprobe image from sample MB-07-02 showing two clinopyroxene grains. The first one (CPX 1) is relatively homogeneous and sulfide-barren, while the second (CPX-2) is highly fractured and contains abundant sulfide. The quantitative data for this image are below in table A25.

Table A25: Microprobe data for spot analyses shown in figure A16. This table contains clinopyroxene analyses. The data for spots 175, 176, and 180-182 contain low totals possibly due to the presence of elements that were not accounted for in the selected analysis package.

Spot	SiO_2	TiO_2	Al_2O_3	FeO	NiO	MgO	CaO	Na_2O	Total
175*	41.95	0.10	3.99	30.03	0.00	5.53	3.36	0.09	85.04
176*	41.65	0.07	3.93	30.82	0.02	4.97	3.38	0.10	84.96
177	49.46	0.12	4.01	21.65	0.01	22.44	0.21	0.01	97.89
178	51.74	0.17	3.43	20.88	0.01	22.63	0.20	0.00	99.06
179	52.29	0.25	2.85	21.13	0.00	23.06	0.24	0.00	99.82
180*	43.22	0.00	3.88	34.29	0.00	2.46	2.88	0.08	86.81
181*	42.86	0.06	3.83	34.18	0.00	2.51	2.80	0.08	86.31
182*	42.21	0.06	3.86	33.67	0.02	3.13	2.78	0.08	85.80
183	52.00	0.16	2.36	21.12	0.01	23.43	0.24	0.00	99.31
184	51.63	0.17	2.68	20.92	0.03	23.30	0.24	0.03	99.00
185	51.19	0.35	3.40	21.17	0.01	22.95	0.24	0.00	99.30

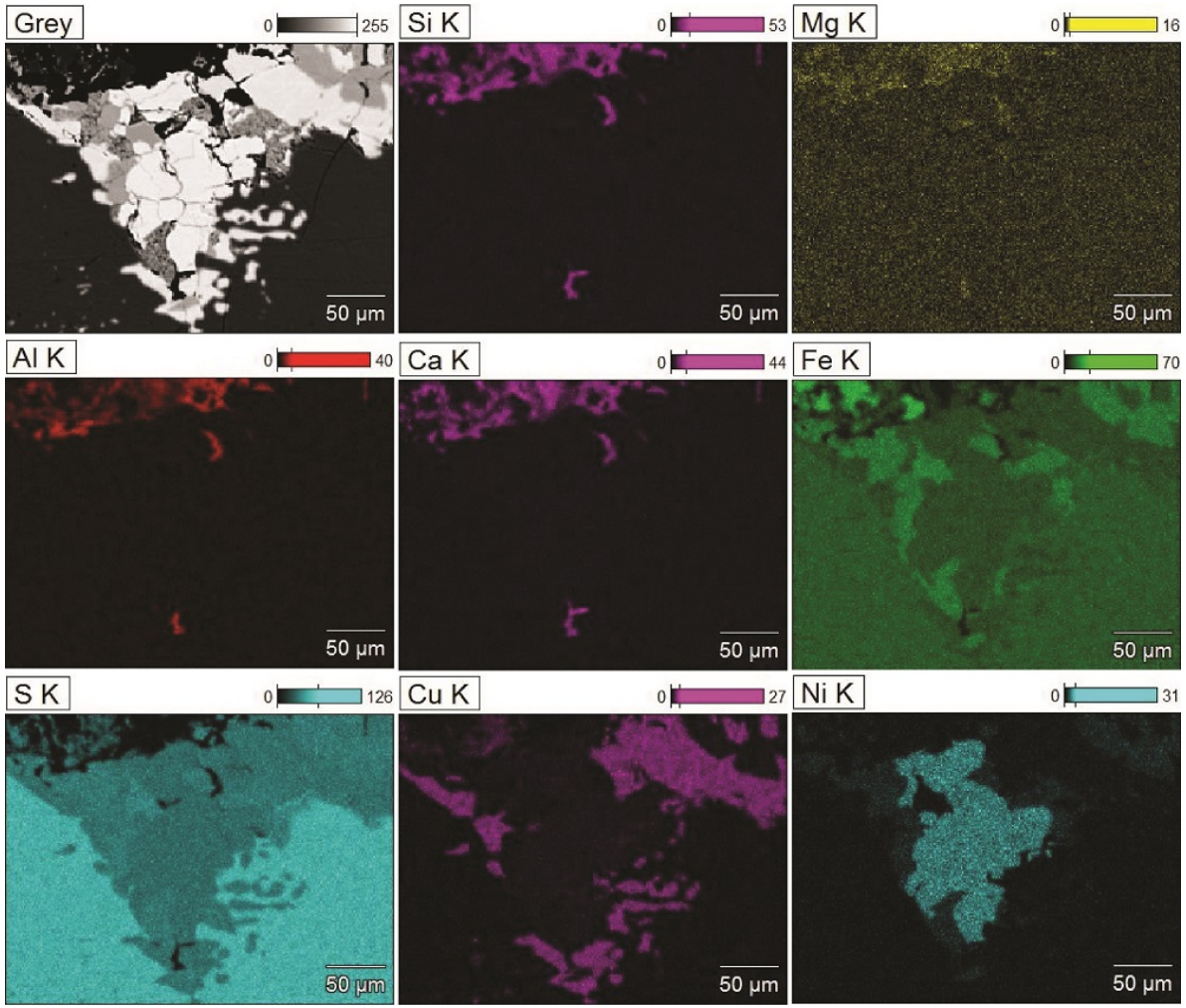

Figure A17: Microprobe element map of the multi-phase sulfide grain in sample KEA-1 (C') shown above in figure 40 and below in figures A18 to A21. The image labeled "Grey" is the greyscale microprobe image during analysis.

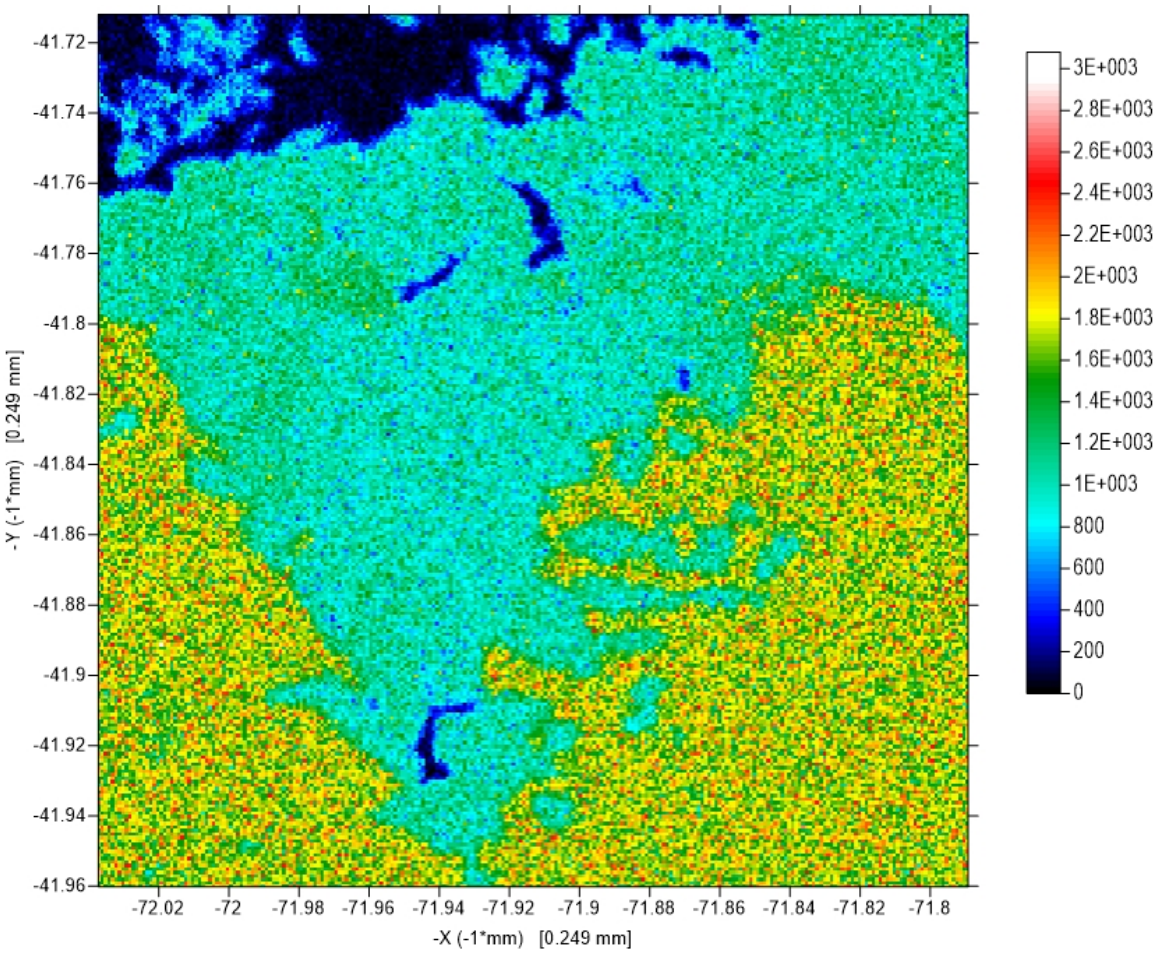

Figure A18: Microprobe element map for sulfur showing additional detail with the color bar scale. This image is the same multi-phase sulfide grain shown in figure 40 and figures A17 and A19 to A21.

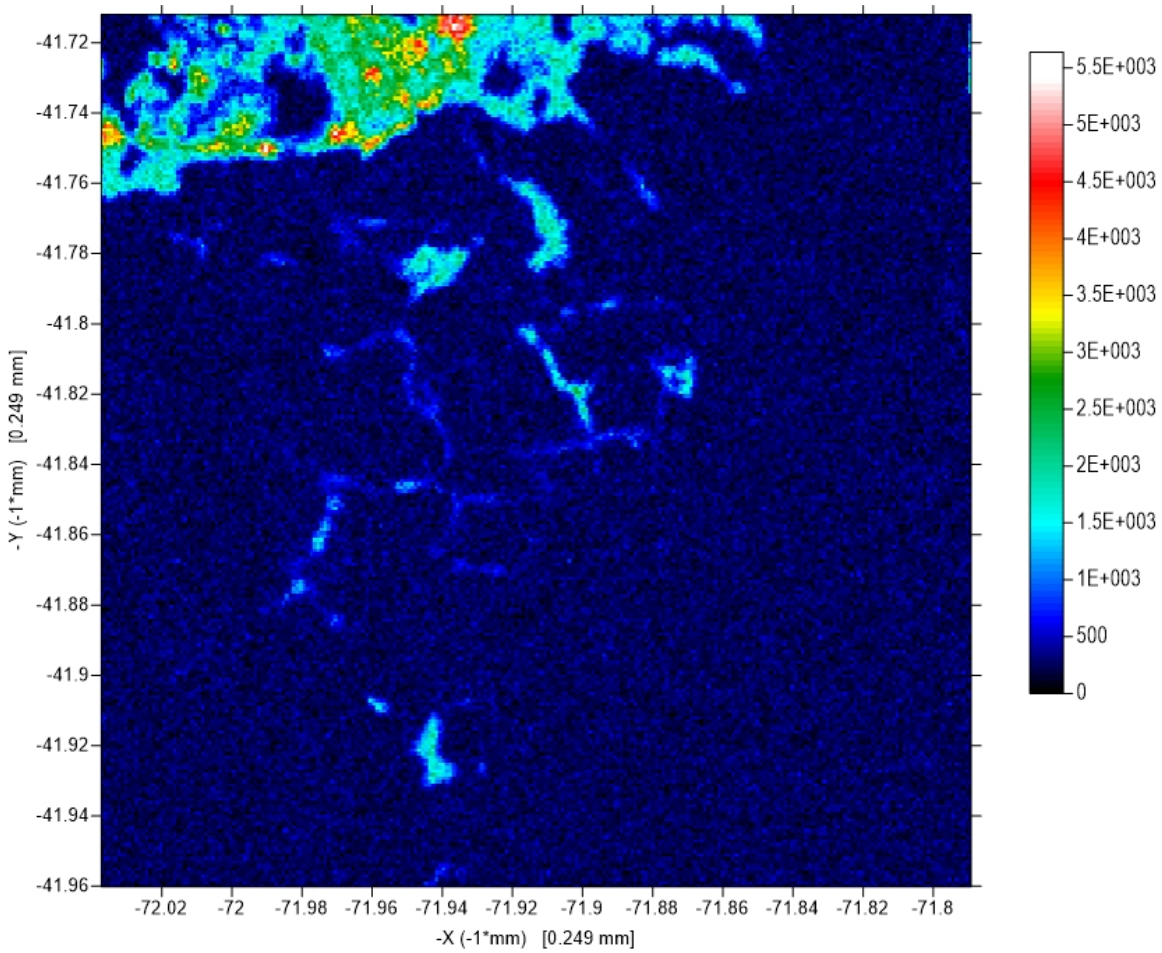

Figure A19: Microprobe element map for magnesium showing additional detail with the color bar scale. This image is the same multi-phase sulfide grain shown in figure 40 and figures A17, A18, A20, and A21.

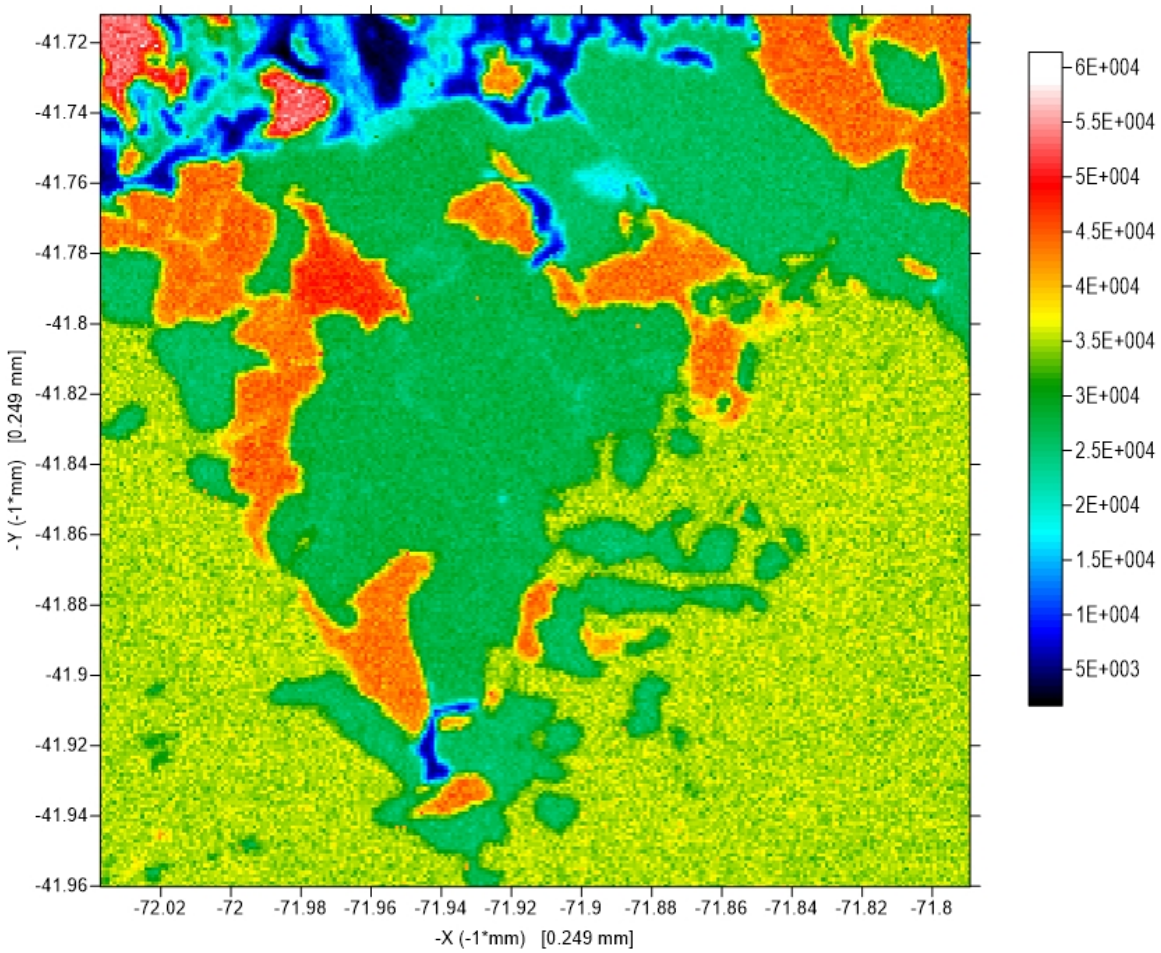

Figure A20: Microprobe element map for iron showing additional detail with the color bar scale. This image is the same multi-phase sulfide grain shown in figure 40, figures A17-A19, and figure A21.

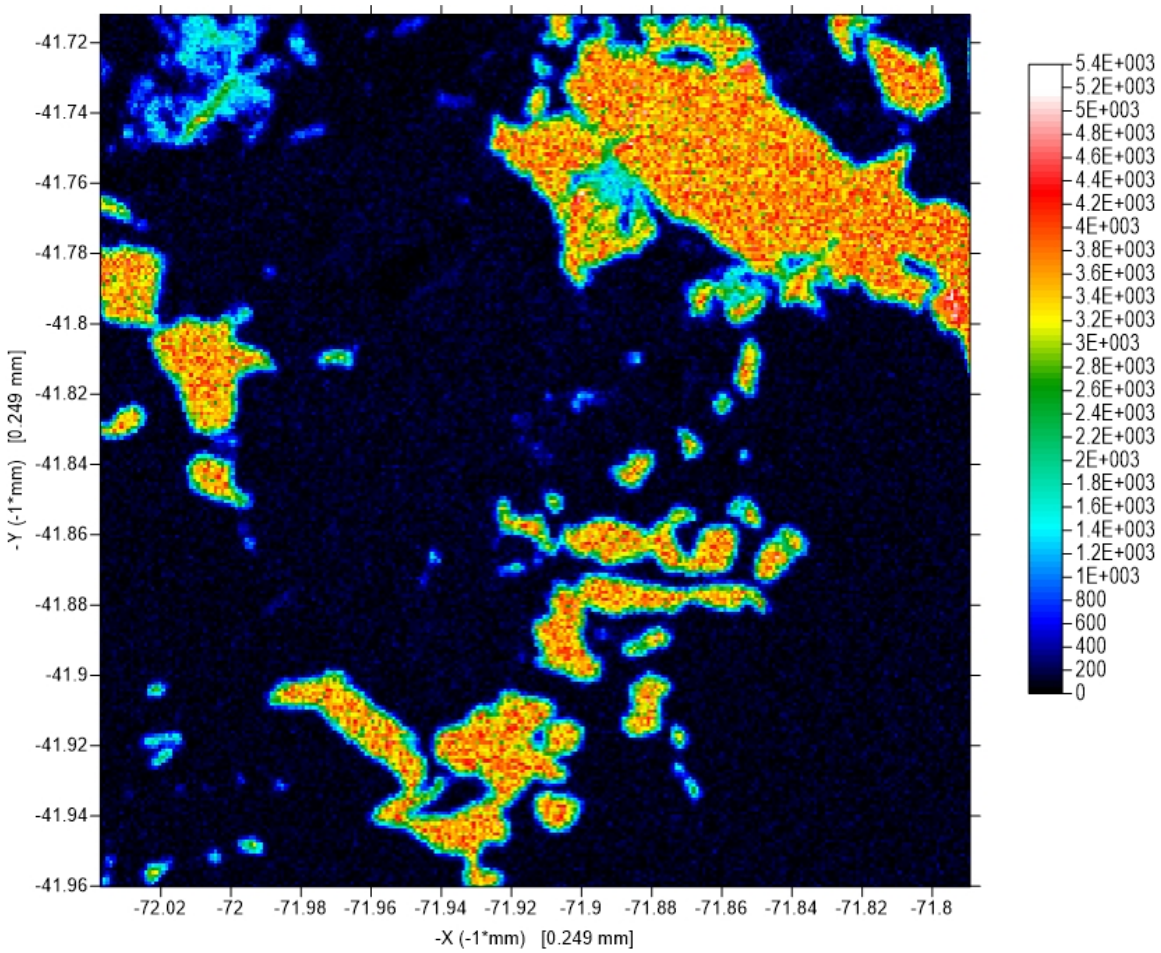

Figure A21: Microprobe element map for copper showing additional detail with the color bar scale. This image is the same multi-phase sulfide grain shown above in figure 40 and figures A17-A20.

This section includes tables of wave scan data measured during microprobe analyses of olivine, clinopyroxene, and sulfide. The data likely includes x-ray input from nearby phases as some sites of interest were extremely small in size, so the beam diameter was large enough to include information from other minerals. Further information about the sites and instrument specifications can be found in the supplementary data section.

Table A26: Microprobe wavescan data for sulfide-type phases. Data are shown in weight percent and normalized to 100.

Spot	Sample	Possible ID	Si	S	Fe	Co	Ni	As	Te	Ag	Total
1	MB-07-02	Ni Arsenide	1.24	19.21	54.68	0.89	10.58	11.39	2.00		100.00
2	MB-07-02	Pyrrhotite		36.78	62.18		1.04				100.00
5	MB-07-07	Ag Pentlandite		26.41	36.86		19.77			16.96	100.00

Table A27: Microprobe wavescan data for PGE-type phases. Data are shown in weight percent and normalized to 100.

Spot	Sample	Possible ID	S	Fe	Cu	Pd	Bi	Al	Cr	Total
3	MB-07-07	PGE	2.87	2.58	0.96	12.26	80.67			100.00
4	MB-07-07	PGE		1.35	1.11	15.79	80.41	0.22	0.82	100.00

Table A28-1: Microprobe wavescan data for a Pb-rich phase. Data are shown in weight percent and normalized to 100. This table is split up into table A28-1 and A28-2.

Spot	Sample	Possible ID	Si	S	Fe	Cu	Zn
6	MB-07-07	Pb/Zn?	2.57	4.10	9.44	0.85	1.77

Table A28-2: The continuation of table A28-1.

Al	Cr	Mg	Ca	V	Se	Pb	Total
4.53	2.53	1.18	2.71	0.77	1.86	67.69	100.00

Table A29: Microprobe wavescan data for a Cr-rich phase. Data are shown in weight percent and normalized to 100.

Spot	Sample	Possible ID	Si	S	Fe	Cu	Zn	Al	Cr	Mg	Ca	V	Total
7	MB-07-07	Chromite?		1.69	37.31	2.32	3.81	35.19	12.45	5.38		1.84	100.00
8	MB-07-07	Chromite?			40.11			35.02	13.83	5.93	3.08	2.04	100.00
9	MB-07-07	Chromite?	1.27		40.30		2.67	33.61	13.58	5.06	1.61	1.90	100.00

12. Supplementary Data

The attached compressed file contains additional analytical data that was collected during this project. This data includes all the XRD files, along with SEM and Microprobe data that was not shown in either the main body or the two appendices.

Physical samples, including till, surface, drill core, powder, EPD material, thin sections, and polished thick sections, are currently stored at the University of Minnesota Duluth in Heller Hall room 106. This storage location is subject to change following the submission of this thesis. Requests to access this material for further Ni or Cu isotopic work should be submitted to Dr. Christian Schardt.